

# **Different Mechanisms of Vortex Induced Vibration of Bridges**

by

José M<sup>a</sup> Terrés-Nicoli

Departamento de Mecánica de Estructuras e Ingeniería Hidráulica

Tesis preparada para la obtención del Grado de

**Doctor**

con Mención de Doctorado Europeo

E.T.S. Ingenieros de Caminos, Canales y Puertos

Universidad de Granada

Noviembre 2008

©José M<sup>a</sup> Terrés-Nicoli 2008

Editor: Editorial de la Universidad de Granada  
Autor: José María Terrés Nicoli  
D.L.: GR. 470-2009  
ISBN: 978-84-691-8582-7



# Resumen

Título de la Tesis:

**Diferentes Mecanismos de Vibración Inducida por Vórtices en Puentes**

Directores:

Miguel A. Losada Rodríguez (Universidad de Granada)

Gregory A. Kopp (The University of Western Ontario)

Candidato: José M<sup>a</sup> Terrés Nícoli

La mayor eficacia de nuevos materiales y metodologías de diseño hacen posible puentes de geometrías estilizadas y mayor flexibilidad. El Puente del Tercer Milenio en Zaragoza es un ejemplo de ello. La mayor flexibilidad de estas estructuras las hace más vulnerables frente a la acción del viento en general y a los fenómenos aeroelásticos en particular. La compleja aerodinámica de estas formas no está resuelta.

La vibración inducida por vórtices es un fenómeno aeroelástico que ha sido observado en distintos tipos estructurales: chimeneas de aireación, edificios, puentes, etc. En puentes puede afectar a su conjunto a través de la acción sobre el tablero, pilonas o arcos o parcialmente a cables u otros miembros en su estado final o durante la construcción. Así, este fenómeno fue responsable de vibraciones inaceptables en modos de flexión vertical en el Puente de Storebælt en Dinamarca poco antes de su inauguración.

El Puente de Storebælt es el objeto del núcleo de este trabajo que se centra en el estudio de los modos de vibración vertical y de torsión inducida por vórtices. La transferencia de energía y mecanismos de la interacción dinámica fueron investigados a partir de ensayos de un modelo de sección a escala 1:70. En este marco se diseñó y construyó un nuevo Túnel de Viento de Capa Límite en el Centro Andaluz de Medioambiente. El túnel fue equipado con un dispositivo de ensayo dinámico y estático de modelos de sección. Este sistema, diseñado según el estado del arte, además de puentes puede ser utilizado para ensayos diversos de distintos tipos de estructuras lineales. El nuevo túnel y el dispositivo de ensayo fueron evaluados satisfactoriamente mediante comparación con resultados de referencia del Túnel de Viento canadiense de ambos Puentes del Tercer Milenio y Storebaelt.



Los ensayos del modelo de sección del Puente de Storebælt, objeto de esta investigación, se llevaron a cabo en este túnel y en el Boundary Layer Wind Tunnel I de la Universidad de Western Ontario en Canadá. La respuesta general observada presentó una histéresis considerable, de modo que la amplitud de la respuesta depende sensiblemente si la velocidad crítica se fija aumentando desde velocidades menores o al contrario.

El inicio de la vibración se ha asociado al desprendimiento de vórtices en el borde de salida del tablero para ambos modos de vibración. No obstante, los mecanismos responsables de la evolución de la amplitud de las mismas difieren. Así, en el caso de la vibración en modo de torsión se han identificado estructuras asociadas a vorticidad moviéndose por convección con el flujo medio, como responsables de las vibraciones de máxima amplitud. El cambio en la estructura del campo de presiones, de la zona de separación en particular, a partir de un determinado ángulo de ataque se ha asociado con el origen de las estructuras señaladas.

La capacidad de disipación de energía del sistema ha sido caracterizada para las distintas fases de evolución de la respuesta. Esta caracterización permite la evaluación del nivel de amortiguamiento aerodinámico, concepto ampliamente utilizado en los modelos de predicción de la respuesta.

Finalmente y en contraste con los mecanismos de vibración anteriores que involucran al puente de forma íntegra, se presenta el caso una tipología particular de puentes en construcción. En concreto el estudio se centra en un problema recurrente de tableros formados por vigas doble T Vigas antes de que se ejecute la sola sobre la mismas. Se ha identificado la emisión de vórtices a sotavento del alma como responsable de vibraciones -en línea- en flexión lateral. Por último se proponen simples medidas aerodinámicas correctivas.

# Summary

## Different mechanisms of Vortex Induced Vibration in Bridges

Advisory committee:

Prof. Miguel A. Losada Rodriguez (Universidad de Granada)

Prof. Gregory A. Kopp (The University of Western Ontario)

Candidate:

José M<sup>a</sup> Terrés-Nícoli

The vortex induced vibration of the cylinder has been studied for over a century. Though significant progress has been done, there are fundamental questions that still don't have a clear answer. The aerodynamics of other bluff bodies with an afterbody involve mechanisms of different nature including the vortex shedding in the near wake responsible for the cylinder vibration. Such are, impinging shear layer instability, leading edge vortex shedding, trailing edge vortex shedding and the interactions between them. The present study focuses on the vortex induced vibration (VIV) of modern bridges.

In the framework of this work a new boundary layer wind tunnel was built at CEAMA, University of Granada. The wind tunnel was equipped with a rig for both dynamic and static testing of section models. The wind tunnel itself and the section model test rigs were benchmarked with available results from BLWTL, The University of Western Ontario for the two bridges being studied: the Storebaelt Bridge (Denmark) and the 3<sup>rd</sup> Millenium Bridge (Spain). The experimental work was carried in both wind tunnels I and II at the BLWTL and CEAMA wind tunnel I.

The interest in the above mentioned bridges have different nature. The Storebaelt bridge (1998) has a shape common nowadays in single deck long span bridges. Despite of the numerous studies that had been carried out, the Storebaelt Bridge exhibited unacceptable vertical VIV in March, 1998 when it was just about to be inaugurated. The 3<sup>rd</sup> Millenium deck cross section is fully curved incorporating carefully aerodynamically shaped leading and trailing edges in an attempt to reduced the vorticity generation.

Modern bridges have shapes that are cross between bluff bodies and airfoils. There is a need for fundamental physical investigation of the mechanisms that trigger the VIV of these shapes of complex aerodynamics. Some of the mechanisms involved are known to be motion induced; consequently, simultaneous measurements of force and response of the bridge undergoing both vertical and torsional VIV were carried out. The forcing was studied in detail looking at the simultaneous pressure field throughout the different phases of the response for increasing and decreasing wind speeds. The pressure field is analyzed in detail by means of the phase averaging technique.

It is observed that trailing edge vortex shedding is responsible for the onset of the torsional vibration. The build-up of larger amplitude oscillations is however due to a motion induced impinging shear layer instability on the upper flange of the leading edge. Such mechanism is observed triggering impinging leading edge vortices that are convected by the free stream and is indeed responsible for the enhancement of maximum amplitude oscillations. A constant  $2\pi$  phase is observed throughout the build-up stages between force and response consistent with the described mechanism.

The physics of the vertical VIV appears to be of a somewhat different nature. The onset of the oscillation appears to be caused by impinging shear layer vortices generated by motion induced instability at the natural frequency. A mechanism that has been referred to as vortex interaction of these vortices and those forming at the trailing edge may be held responsible for the build-up of maximum amplitude oscillation. An increasing phase is observed in the force with respect to the response reaching values of  $\pi/2$ .

Significant hysteresis was observed in both vertical and torsional response when the maximum amplitude oscillation wind speed was approached from higher and lower wind speeds. The nature of this hysteresis maybe related to the effect of the free stream wind speed in the instability of the motion induced structures. Nevertheless, the phenomena requires further investigation.

No VIV was observed in the tests of the 3<sup>rd</sup> Millenium Bridge. The spectra of hotwire measurements in the near wake did not show any peak that one could relate to vortex activity. Furthermore, the pressure measurements on the trailing edge did not present such peak neither. Finally a numerical simulation of the flow around did not show any significant vorticity in the near wake in good agreement with the experimental observations. The consistency of the experimental and numerical pressure field on the leading and trailing edges was remarkable. The design of the edges of the curved deck of the 3<sup>rd</sup> Millenium bridge proved to be successful in mitigating VIV.

The vortex induced vibration maybe observed in different bridge components other than the deck such as cables or at different stages of the construction. In contrast with the above mentioned phenomena, VIV of structural member of a Bridge under construction is studied. Evidence is presented of along wind VIV of slender beams set on top of the pylons waiting for the deck to sit over them. The design of such beams provides them with significant stiffness in vertical bending to support the deck while very little in lateral bending. It was found a computed modal frequency equal two twice the shedding frequency for the corresponding Strouhal number and measured wind speeds of anemometers nearby.

To the perfection of inexistence.



# Nomenclature

$\alpha$	angle of attack measured anti-clockwise
$\Delta A_i$	tributary area per unit length of pressure tap i
$\delta$	logarithmic decrement in percentage
$\varphi$	modal rotation
$\tilde{\varphi}$	root mean square of the rotation
$\rho$	air density
$\omega$	circular natural frequency of rotation
$\xi$	Damping ratio over its critical
$\phi$	phase within the cycle
$\lambda_L$	geometric scale
$\lambda_T$	time scale
$\lambda_V$	velocity scale
$\langle C_p \rangle_\phi$	phase averaged pressure coefficient, phase $\phi$
$A_i$	tap i of ring A
$B$	bridge width
$B_i$	tap i of ring B
<b>BLWTL</b>	<b>Boundary Layer Wind Tunnel Laboratory. University of Western Ontario</b>
$C_D$	drag coefficient
$C_i$	tap i of ring C

$C_L$	lift coefficient
$C_M$	moment coefficient
$C_p$	pressure coefficient
D	depth of the bridge's deck
d	depth of the leading and trailing edge wedges
DMI	Danish Maritime Institute, Denmark
DOF	degree of freedom
f.s.	full scale
FFT	Fast Fourier Transform
f <sub>s</sub>	sample frequency
f <sub>t</sub>	natural frequency of torsional oscillation
f <sub>v</sub>	natural frequency of vertical oscillation
I <sub>w</sub>	Turbulence Intensity alongwind
M	mass for the vertical degree of freedom
MMI	mass moment of inertia
m	mass per unit length
mmi	mass moment of inertia per unit length
n	shedding frequency
P <sub>i</sub>	static pressure on tap i
P <sub>o</sub>	free stream static pressure
PSD	power spectral density
Re	Reynolds number
Ref.	reference
rms	root mean square

St	Strouhal number
TMD/s	Tuned Mass damper/s
$T_0$	period of heaving or torsional oscillation, 1/f
t	sample time
u	longitudinal component of the velocity
U	mean wind speed
$\bar{u}$	mean of the longitudinal component of u
$\tilde{u}$	coherent or periodic mean of u
$\tilde{\tilde{u}}$	random component of u
u'	fluctuating component of u
V	free stream wind speed
v	vertical component of the velocity
$V_{cr}^-$	critical wind speed, that at which vortex induced oscillations reach its max. amplitude
$V_{cr}^+$	critical wind speed, that at which vortex induced oscillations reach its max. amplitude
$V_{or}^-$	reduced velocity of the onset of the vortex induced osc.
$V_{or}^+$	reduced velocity of the onset of the vortex induced oscillations
$V_r^-$	reduced decreasing velocity = velocity/(natural freq (tors. Or vertical * deck width))
$V_r^+$	reduced increasing velocity = velocity/(natural freq (tors. Or vertical * deck width))
WS	wind speed
$y_m$	model vertical displacement



$y_p$	prototype or full-scale vertical displacement
$y_r$	non dimensionalized vertical displacement
$z$	vertical direction perpendicular to the deck

Chapter 1: Introduction.....	12
1.1 Introduction .....	12
1.2 Bridge Aerodynamics.....	15
1.2.1 Vortex-Induced Response.....	16
1.2.1.1 Phenomenology.....	16
1.2.1.2 Build-up time.....	17
1.2.1.3 Modelling .....	18
1.2.3 Flutter Instability.....	19
1.3 Review of the aerodynamics of the Storebælt Bridge.....	20
1.3.1 Historical experimental work.....	20
1.3.2 Full-scale measurements.....	22
1.3.3 Summary .....	22
1.4 Study of the aerodynamics of the Third Millenium Bridge.....	23
1.4.1 The 3 <sup>rd</sup> Millennium Bridge Design.....	23
1.4.2 Experimental study.....	25
1.4.2.2 Aeroelastic model of the completed bridge .....	26
1.4.3 Results and discussion .....	27
1.4.4 Conclusions.....	31
1.5 Scope of the study .....	31
Chapter 2 .....	33

Vortex Induced Vibration of Bridges .....	33
2.1 Introduction .....	33
2.2 Bluff body aerodynamics: How Bluff?.....	36
2.2.1 The circular cylinder.....	37
2.2.1.1 The ensuing of VIV .....	39
2.2.2The Rectangular Prism and other bluff bodies .....	43
2.2.2.1 Flow structure around rectangular prisms .....	43
2.3Analytical models .....	52
2.3.1 Single oscillator models .....	52
2.3.2 Coupled oscillator models.....	55
Chapter 3 .....	57
Methodology.....	57
3.1 CEAMA New Boundary Layer Wind Tunnel (Laboratory?) .....	57
3.1.1 Framework and scope .....	58
3.1.2 Wind Tunnel Design.....	59
3.1.2.1 Design requirements .....	59
3.1.2.2 Wind Tunnel Specifications.....	61
3.1.2.2.1 Test Section .....	63
3.1.2.2.2 Contraction.....	65
3.1.2.2.3 Settling chamber.....	66
3.1.2.2.4 Inlet .....	68

3.1.2.2.5 Adapter – diffuser.....	68
3.1.2.2.6 Losses coefficients summary .....	69
3.1.2.2.7 Turbomachine.....	70
3.1.2.2.7 Drive and control system.....	72
3.1.3 Wind Tunnel Construction and Commissioning .....	75
3.1.4 Wind Tunnel Instrumentation .....	78
3.1.5 Wind Tunnel II .....	79
3.2 New CEAMA Section model test system .....	80
3.2.1 Section model testing.....	80
3.2.2 Test Rig frame.....	82
3.2.3 Dynamic section model testing rig.....	83
3.2.4 Static section model testing rig .....	84
3.3 Section models design .....	84
3.3.1 The Storebaelt Bridge 1:70 section model.....	86
3.3.2 The Third Millenium Bridge 1:70 section model.....	88
3.4 Experimental Set-up .....	90
Chapter 4: .....	91
Mechanisms of Vortex Induced Vibration .....	91
4.1 Introduction .....	91
4.2 Experimental work .....	92
4.2.1 Model Response: Displacements .....	92

4.2.1.1 Aeroelastic instabilities .....	92
4.2.1.2 Vortex-induced response .....	94
4.2.1.1.1 Vertical vortex-induced response .....	95
4.2.2 Torsional vortex-induced response .....	98
4.2.2.1 Hysteresis study .....	98
4.2.2.2 Description of the torsional response domains .....	101
BUILD-UP MECHANISMS .....	110
4.1 Maximum amplitude oscillations .....	110
4.2 Surface pressure field .....	111
Conclusions .....	113
Chapter 5 .....	115
Vortex induced vibration of bridge beams under construction.....	115
5.1 Summary .....	115
5.2 Case Scenario .....	116
5.3 Climate analysis: Wind .....	117
5.3.1 Mesoscale – general circulation in the region .....	117
5.3.2 Micro scale – local winds field .....	120
5.3.3 Summary .....	124
5.4 Pseudo-static analysis.....	125
5.4.1 Beam Aerodynamics.....	125
5.4.2 Standards review .....	127

5.4.2.1 ENV 1991-2-4:1995 .....	127
5.4.2.2 Spanish Road Bridge Design Standard, IAP-98.....	128
5.4.2.3 NBC 1995 – Part 4 Canadian Standard (National Research Council of Canada, 1995).....	129
5.4.3 Pseudo-static load in the collapse event .....	131
5.4.4 Stability Analysis .....	131
5.4.4.1 Overturning .....	132
5.4.4.2 Sliding.....	133
5.4.4.3 Summary .....	134
5.5 Aeroelastic Study .....	134
5.5.1 Beam dynamic characteristics .....	135
5.5.2 Vortex Induced Vibration analysis via vortex shedding.....	138
5.5.2.1 Description of the phenomenon .....	139
5.5.2.2 Analysis .....	140
Equivalent Force.....	143
5.5.3 Summary .....	144
5.6 Proposed Action.....	145
5.6.1 Aerodynamic .....	145
5.6.2 Structural.....	145
5.6.3 Monitoring .....	148
5.6.3.1. Real time measurement of local wind.....	148

5.6.3.2. Real time measurement of structural response .....	148
5.7 Conclusions.....	149
Chapter 6 .....	150
Conclusions, recommendations and future work.....	150
6.1 Structural response .....	150
6.2 Mechanisms of the flow-structure interaction.....	152
6.3 Future work .....	152
References .....	154

# Chapter 1: Introduction

## 1.1 Introduction

Bridges have been a part of every civilization's development since life began on this planet; sometimes spanning water, sometimes land. Amazing achievements in this regard were made around 480 BC over the Hellespont during the Persian Wars and 55 BC over the Rhine River during the Gallic Wars [1]. These links, these bridges, have often been targets in times of war, many times destroyed and rebuilt. Natural hazards (earthquakes, floods and wind) have also caused many to be destroyed.

Modern urban bridges, in the search for enhanced aesthetics, are repeatedly including structural and non-structural members of complex shapes for which the aerodynamics are not clear. That is the case of the innovative design of the 3rd Millennium Bridge to be built for the Expo 2008 in Zaragoza, Spain or the Storebaelt Bridge in Danmark, world span record at its time.

*The Wind* has caused serious damage and collapse. Some examples of this are [2,3]:

- Brighton Chain Pier (1836), twice.
- Menai Straits Bridge (1839), twice.
- Wheeling Bridge (1854)
- Lewiston Bridge
- Firth of Tay Bridge (1879) [4]
- Niagara-Clifton Bridge (1888)
- Shirling-Smith Bridge (1964)
- Plowden Bridge (1974)



- Tacoma Narrows Bridge (1940) [5]

Most of the research carried out in the field of bridge aerodynamics has focused on the prediction and mechanics of self-excited oscillations (flutter and torsional divergence) and buffeting motion since most of the cases mentioned above were related to self-excited oscillations. A better understanding of flutter instability allowed the development of numerical models, which can now predict flutter limits in reasonable agreement with wind tunnel test results in many cases. This is not the case for vortex-induced oscillations.

More recently, attention has been paid to the vortex-induced response of bridges. The following bridges are known to have had problems caused by vortex-induced oscillations:

- The Long's Creek Bridge (Canada) [6]
- Second Severn Bridge (UK) [7,8]
- Rio-Niteroi Bridge (Brazil) [9]
- Osteroy Bridge<sup>14</sup> (Norway)
- Wye Bridge (U.K.) [10]
- Waal River Bridge (The Netherlands) [10]
- Tokyo Bay Bridge<sup>15</sup> (Japan) [11]
- Dear Isle Bridge (U.S.A) [12]
- Kessock Bridge<sup>16</sup> (U.K.) [13]
- Storebælt Bridge (Denmark) [14,15,16]

The Storebælt Bridge is the focus of the present work. A brief description of the Storebælt Bridge is given in Appendix B. Some of the above mentioned bridges suffered from oscillations significant enough to require retrofitting. For the Storebælt Bridge, a passive aerodynamic control system was developed and installed.

---

<sup>14</sup> To the author's knowledge nothing has ever being published about this case.

<sup>15</sup> A remarkable event since it is a box girder bridge with a maximum span of 240 m.

<sup>16</sup> This is to the author's knowledge the only bridge known to have exhibited torsional vortex-induced oscillations.

Around the time of the inauguration of the Storebælt Bridge, in May 1998, the deck experienced vertical oscillations induced by “vortex shedding” which excited the 3<sup>rd</sup>, 6<sup>th</sup>, but mainly the 5<sup>th</sup> vertical modes of vibration. The wind speed was between 4 and 11 m/s and the turbulence intensity ( $I_t$ ) was in the range of 2 - 9 %. Figure [1-1] shows the significance of the amplitudes of motion, reaching a peak vertical displacement of 0.35 m [14]. Both pictures in Figure 1.1 were taken from the same site at approximately the maximum and minimum displacement from the at-rest position of the midspan. One can appreciate the importance of the oscillations by observing the marked vehicle near the midspan.

The oscillations experienced by the Storebælt Bridge and other modern bridges suggest that there is still a need for fundamental research into the mechanism of vortex-induced oscillations as well as to provide flow field measurements that may allow the development of numerical models. It has now been more than 60 years since bridge aerodynamics began its development. Research topics are now regularly related to serviceability limit states, long-term problems, refinement of predictions and numerical simulations of responses rather than related to the actual safety of the structure (ultimate limit states) as was the case after the saga of the Tacoma Narrows Bridge in 1940.



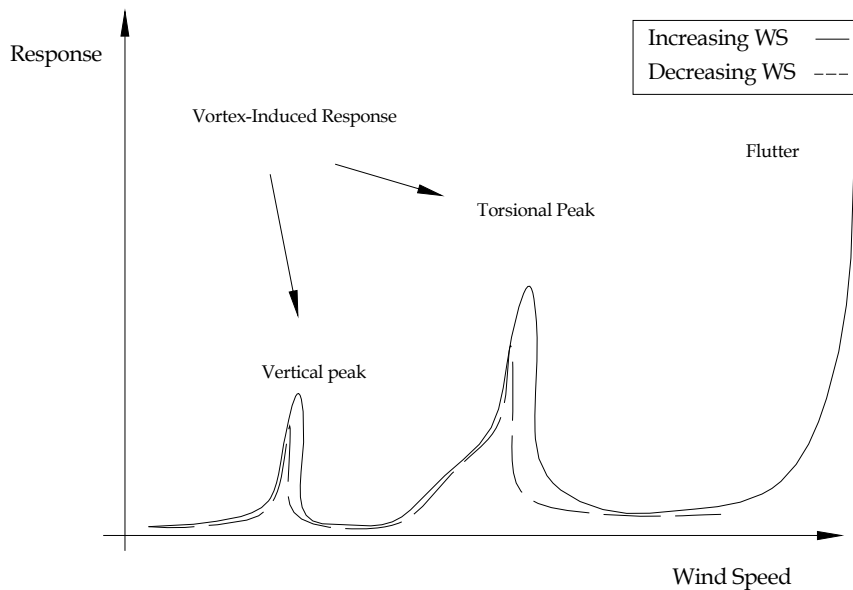
Figure [1- 1]: Vertical vortex induced oscillations observed in the Storebælt East Bridge [17]. May 1998. The marked vehicle is stationary. The location of the camera is the same for both images.

## 1.2 Bridge Aerodynamics

In this section a brief description of the wind effects for bridges is given, ignoring those related to elements others than the deck (e.g. pylons, cables, etc.). There are basically four types of responses or phenomena that one may find for a long span bridge deck under the action of the wind:

- Vortex-induced response
- buffeting response
- flutter instability
- torsional divergence

Figure [1-2] illustrates, superimposed, some of these responses of a bridge deck. Response is defined as displacement for vertical oscillations and rotation for torsional motions. It incorporates the differences found, in general, in the vortex induced vibrations when the wind speed was increased compared to that when it was decreased during the tests performed in this research. A detailed description of these differences is given in Chapter 3.



Figure

[1- 2]: Sketch of the general response of the Storebælt Bridge tests performed during this study. The dependence of the vortex induced response upon whether the wind speed was reached through an increase or decrease can be noted.

The collapse of the Tacoma Narrows' Bridge in 1940 helped to make wind tunnel testing a common practice in the design of long-span bridges. Typically section models are tested at an initial stage and later a full aeroelastic model study is performed.

Sometimes, taut strip models prove to be efficient [18]. Section model tests are used through out this research. A description of the model is given in Chapter 2. A review on section model testing was given by Hjorth-Hansen [19]. The issues concerning the similarity requirements in bridge aerodynamics are pointed out by Tanaka [20,21].

## 1.2.1 Vortex-Induced Response

### 1.2.1.1 Phenomenology

Many studies have been conducted on the geometries and mechanisms of the vortex shedding from bluff bodies. Currently, cross-sections of long and medium span bridges are becoming more streamlined. These shapes are a cross-between both categories (bluff bodies and streamlined), an example being the Tsing Lung Bridge<sup>17</sup> in Hong Kong [22], under design now. This bridge has a double box suspended girder deck where each box has a curved shape similar in some ways to an airfoil, although it has a sharp leading edge. The flow around it is highly complex. Issues such as Reynolds (Re) number effects, often neglected for bluff bodies, might be an issue [23].

The flow past a bluff body is characterized by vortices which are continuously being shed from the trailing edge of the bridge at a certain frequency. These vortices are often referred to as Kármán vortices. The pattern formed by them in the wake it is sometimes referred as Kármán's street. This frequency is represented by the dimensionless Strouhal number:

$$St = \frac{n \cdot D}{U} \quad (0.1)$$

where  $n$  is the frequency at which vortices are shed,  $D$  is the dimension of the object that characterizes the vortex structure and  $U$  is the mean wind speed. For bridges,  $D$  is typically the deck depth. Pairs of vortices leave the deck surface from both sides of the trailing edge alternatively. This causes a differential pressure field over the top and bottom surfaces inducing some motion in the deck. Vortices are, most likely continuously shed from the bridge deck no matter the magnitude of the velocity. The frequency at which these eddies are shed varies approximately linearly with the flow speed since  $St$  is approximately constant. At some point, this frequency might match that of a certain mode of vibration, either vertical or torsional, of the structure. Resonance can occur then as the bridge's motion locks-in at the shedding frequency of the flow. Within certain bounds, if the mean flow speed continues to increase, the frequency of the response remains unchanged. This is often called the plateau or synchronization range. The persistence of the synchronization over a wide range of wind speeds may cause fatigue problems, discomfort to users, or failure, depending on the amplitude of the vibrations. By increasing the velocity beyond the plateau range, frequencies are no longer in resonance and once again the shedding frequency increases linearly with the mean velocity and the response is no longer harmonic. During resonance, one may expect the amplitude to grow infinitely,

---

<sup>17</sup> A suspension bridge with a main span of 1418 m, Hong Kong.

except for the damping. However, vortex-induced vibrations are known to be self-limiting [24]. The amplitude of the motion increases with a constant flow speed when the state of synchronization is reached. One could state that the flow controls the response initially [25]. However, as the oscillations grow, the vortex shedding process changes. In other words, there is a type of feedback mechanism at work, by which we mean that any small change in the response will affect and change the flow field and vice versa when maintaining the same flow speed. In summary:

- the flow field can not adapt for all possible ranges of amplitude of the motion and maintain the same flow pattern or shedding frequency;
- the structural motion of the deck takes some time to build up;
- the pressure and velocity field around the deck results because of the flow past the deck body including that induced by motion of the structure.

There are different types and modes of vortex shedding and vortex structures around the deck. These depend on the deck geometry, the different flow mechanisms for generation, and the Reynolds number [24,26,27,28]. Motion induced vortices originating at the leading edge have been related to the forcing mechanism of the vortex-induced oscillation of some types of bridge deck cross sections [29, 30, 31]. An illustrated review can be found in [32].

Some of these different mechanisms or even combinations of them, can be involved in the vortex-induced response of a bridge deck. The mechanisms can be quite different depending on the shape of the cross section. For example, a box shape such as for the Sunshine Skyway Bridge can undergo torsional vortex-induced vibration due the resonance of the vortex-shedding at the trailing edge with the torsional natural frequency of the structure [33,34]. It will be presented here, that the phenomenology of the torsional vortex-induced vibration of the Storebaelt is quite different, involving a variety of mechanisms through the build-up phases of the response. Of course, the differences in the aerodynamics are not surprising, since the shapes of the decks are rather different, with the Sunshine Skyway being a bluffer section. Additionally, the edge and central barriers are solid in the Sunshine Skyway while these components of the Storebælt are porous. There are also structural differences such as the modal natural frequencies (higher for the Sunshine Skyway) or the higher mass and mmi of the Sunshine Skyway. These structural parameters will affect the vortex-induced response. For instance, assuming that the vortex-induced response is inversely proportional to the mass of the body, one can expect that the higher mass of the Sunshine Skyway imply lower vortex-induced oscillation amplitudes.

### 1.2.1.2 Build-up time

The (build-up) time required for the bridge to lock-in once the wind speed is in the range of the plateau, is believed to vary with different parameters such as:

- the history of velocity in time;
- the rate at which the velocity is increased or decreased;

- the sign of the rate of velocity change i.e. if the velocity was increasing or decreasing;
- the magnitude of the velocity within the plateau;
- the structural damping.

Thus, there is a hysteresis in the vortex-induced response. The hysteresis in the vortex-induced response of circular cylinders was studied by Brika and Laneville [35], who found different modes of vortex shedding.

### 1.2.1.3 Modelling

Reviews of vortex shedding from oscillating bluff bodies have been presented by Bearman [24] and Rockwell [26]. Based on the similarities with the Van der Pol oscillator, semi-empirical mathematical models have been developed for the prediction of vortex-induced oscillations [36]. For example, the model from Hartlen and Currie achieved the self-limiting and self-exciting characteristics of the motion for a circular cylinder [37].

Corless and Parkinson [38] have developed semi-empirical mathematical models for a square cylinder. Both the phenomena and existing models are discussed extensively in Parkinson [39]. Ehsan and Scanlan proposed a semi-empirical model for the vertical vortex-induced vibration of flexible bridges [40]. A generalized model for predicting such bridge responses using wind tunnel results, and based on Scanlan's model [41], was suggested by Larsen [25].

These lift-oscillator models assume a sinusoidal solution,

$$y_r = y_{r0} \cos(\omega t) \quad (0.2)$$

for the equation of motion of the vertical displacement,

$$M \cdot \ddot{y}_r + c \cdot \dot{y}_r + K \cdot y_r = F_L \quad (0.3)$$

where  $M$  is the mass of the body,  $c$  is the damping coefficient,  $K$  is the elastic coefficient,  $F_L$  is the lift force,

$$F_L = \frac{1}{2} \rho V^2 d C_L \quad (0.4)$$

and  $y_r$  is a non-dimensional vertical displacement. The lift coefficient is assumed to be influenced by the body's motion satisfying the characteristics of a Van der Pol oscillator [41]. Different expressions have been proposed for  $C_L$  including [25, 40, 41]:

- motion-induced force (reflecting an aerodynamic damping effect);

- a term reflecting the aerodynamic stiffness effects;
- a term that represents the force due to the shedding of vortices.

### 1.2.3 Flutter Instability

The flutter instability has been the topic of many studies during the second half of the 20<sup>th</sup> century, and it is still receiving the attention of many bridge aerodynamicists around the world. Flutter theory has its origins in the field of aircraft vibration [42]. Theodorsen in 1935 [43,44] gave a solution for the flutter of flat plates. Selberg [45] gave an approximation of Theodorsen's formulation for bridge decks under certain assumptions such as having a double beam cross section. It is known to give conservative values for small angles of attack (0° - 2° degrees). Scanlan's [46] model using flutter derivatives has become a standard procedure to obtain a very good estimate of the flutter limit. It requires wind tunnel testing in order to obtain the values of the aerodynamic derivatives for different wind speeds.

There are different kinds of flutter that occur in bridge aerodynamics: classical flutter and stall flutter. Classical flutter is often referred to simply as flutter. It happens when two degrees of freedom are coupled. As the wind speed increases, the first<sup>18</sup> vertical and torsional modal frequencies get closer. Both frequencies may change up to a certain value in between, or only one of them might vary. In the first case, the vertical frequency increases due to an increase in aerodynamic stiffness and the torsional one will be reduced by the effects of aerodynamic damping [47] (since the lowest torsional frequency is usually higher than the first vertical frequency). In some cases the torsional mode dominates and does not change its frequency of vibration while only the vertical one varies. When both match, resonance between both motions causes the response to grow *ad infinitum*. Thus, it is a self-excited oscillation where amplitudes grow rapidly causing the collapse of the structure. For the same geometry and flow conditions, the flutter limit for a coupled flutter will be higher for a higher frequency ratio<sup>19</sup>. In that case, one may expect it to take longer for both frequencies to come together. As a result of the interaction of the incoming flow with this "bluff" body, there is vortex shedding but the flutter mechanism is not believed to be related to it; the flow does not appear to control the motion.

Stall flutter is similar to that for aircraft. The lift force normally increases with increasing angle of attack. Due to the nonlinear characteristics of the system, the lift coefficient may drop abruptly in the vicinity of the stall leading to a rather unstable state. Stall flutter is also associated with strongly separated flows.

Compared to vortex-induced response, flutter instability is less sensitive to structural damping. However, the author observed some sensitivity for the Tsing Table [1- 1]: Observed vortex-induced response and aerodynamic instability limits in wind tunnel tests converted to full scale (from [51]).

---

<sup>18</sup> the lower respectively for vertical and torsional modes

<sup>19</sup> frequency ratio is defined as torsional frequency over the vertical.

**Taut Strip Model, 1:300,  $\delta=1.5\%$ ,  $L=6\%$**

Lung Bridge [48], where the flutter limit wind speed increased clearly with the structural damping. As well as vortex-induced response, flutter instability is highly sensitive to the turbulence intensity of the oncoming flow.

## 1.3 Review of the aerodynamics of the Storebælt Bridge

A description of the Storebælt Bridge is given in Appendix 1 where structural properties and geometric details are summarized.

### 1.3.1 Historical experimental work

The studies of wind effects on the Storebælt Bridge started when preliminary feasibility studies were carried out in late 1970's. Different cross-sectional configurations for both cable-stayed and suspended decks were tested in a wind tunnel [49]. In 1987 the Danish Government approved the construction of the whole Great Belt Link, which is comprised of a high level suspension bridge over the east channel. Section model tests were done in June 1990 at the Danish Maritime Institute (DMI) for 16 different cross sectional shapes of the box girder suspended deck [50]. Tests included determination of static force coefficients and the flutter instability limit. A cross section was selected<sup>20</sup> and further tests were carried out following a detailed structural analysis. With refined structural properties, the tender design cross section was tested with and without windscreens and at different erection stages of construction [51,52,53]. The option without additional windscreens exhibited a better buffeting and vortex-induced response, as well as a higher flutter instability limit. The scale of the section models was in every case 1:80. The aspect ratio of the model was between 6 and 7 (length over width). A summary of the main findings is given in Table [1-1].

---

<sup>20</sup> It was identified by "H9.1". It is the deck now spanning the Storebælt's strait.



<b>Vortex Induced Response</b>		
	Wind speed (m/s)	RMS Amplitude (m)
Vertical	7, 9	
<b>Aerodynamic Instability</b>		
	72	
<b>Full Aerolastic Model 1:200, <math>\delta=0.5\%</math>, <math>I_w=6 - 7\%</math></b>		
<b>Vortex Induced Response</b>		
	Wind speed (m/s)	RMS Amplitude (m)
Vertical (7 <sup>th</sup> mode)	10.9	0.163
Vertical (8 <sup>th</sup> mode)	12.7	0.154
<b>Aerodynamic Instability</b>		
	70	

A taut strip model was used to determine the response to three-dimensional turbulent boundary layer flow at the University of Western Ontario [52,53,54]. A 1:300 scale taut strip model was constructed and tested with exposures of turbulence intensities ( $I_w$ ) of 6, 9 and 12%. A summary of the main findings is given in Table [1-2].

A new wind tunnel of 13.6 m width test section was built for the testing of the full bridge aeroelastic model in 1991. The 1:200 scale aeroelastic model was tested under turbulent boundary layer flow of 7 and 6 % turbulence intensity ( $I_w$ ) [52,52]. A summary of the main findings is given in Table [1-2].

During the tendering process, a number of additional cross sections were suggested for the main span. These alternative 1:80 scale section models were tested at DMI's wind tunnel in smooth and turbulent flow. All alternate sections showed a worse behavior than the previously selected "H9.1"[55]. This study was followed by further tests of the taut strip model at BLWTL due to some discrepancy found between the aerodynamic derivatives obtained from the section model tests and the taut strip model tests. Supplementary section model tests were conducted at DMI to investigate the influence of vehicles on vortex shedding excitation and possibility of torsional instability of the section with wind screens [56]. Construction of the 1624 m main span suspension bridge started thereafter.

Section Model H9.1.  $\delta=1\%$ .1:80 scale

Vortex Induced Response. Test conditions:  $I_w=0\%$ ,  $\alpha=0$ .

Vertical Peak

Wind-speed (m/s)	Max. (m)	Min. (m)	Mean (m)	RMS (m)
3.69	0.216		-0.216 0	0.152

Torsional Peak

Wind-speed (m/s)	Max. (°)	Min. (°)	Mean (°)	RMS (°)
12.86		1.445	-1.426	0.015 0.996

Stability Limits (m/s)

$I_w=0\%$	68.84 (stable) - 73.88 (unstable)
$I_w=7.5\%$	68.84 (stable) - 70.52 (unstable)

## 1.3.2 Full-scale measurements

Through the final stages of construction, high amplitude vertical oscillations induced by vortex shedding were observed. Accelerations were monitored for the period between 14 Jan. 1998 and 16 May 1998 [57,58]. The main span was observed to experience locked-in vortex shedding 10 times during this period. All incidents occurred at wind directions near the perpendicular to that of the deck. The 5<sup>th</sup> mode of vibration was the one predominantly excited. The 3<sup>rd</sup> and 6<sup>th</sup> modes were also excited on a few occasions. Wind speeds were in the range of 4 to 10 m/s for all incidents, matching with the predicted values from the wind tunnel tests. The amplitudes were, however, higher than the predicted ones. Two reasons might be pointed out. First, the lower measured structural damping and, second, the lower than expected turbulence intensity levels.

**Table [1- 2]: Main findings of tests of a Taut Strip and a Full Aerolastic Model of the Storebælt Bridge (from [52,53,54,72]).**

A 1:60 scale model was tested in a wind tunnel to investigate the effectiveness of a guide vane system in the mitigation of the oscillations [59]. Guide vanes were found to be successful for the suppression of vortex-induced vertical oscillations. To the author's knowledge there has not been any wind tunnel study reported on the effect of this device on the flutter instability limit for this bridge. A numerical simulation model by Frandsen [17] showed a limit wind speed of 70 m/s without vanes and 65 m/s with them.

Simultaneous pressures and accelerations were recorded in a second campaign of full-scale monitoring [15,17]. The data collected correlated well with the full-scale data mentioned above. For oscillations in the 5<sup>th</sup> mode structural damping values as low as  $\delta=0.45\%$ <sup>21</sup> were found. A much higher correlation between pressures and accelerations at lock-in was measured than for outside of lock-in. Correlations between pressures at different locations on the top flange of the trailing edge were somehow insensitive to changes in wind direction. In contrast, pressure - acceleration correlations at this same location were highly affected by changes in this parameter. Due to some constraints, pressures were measured only at three locations and on all at the top flange, and not near the edges. As will be shown in the current investigation, and also according to the data of Larose [60], pressure in this area is not expected to play a significant role in the torsional response.

## 1.3.3 Summary

Extensive studies have been conducted for nearly two decades on the wind effects on the Storebælt Bridge. These studies included numerous wind tunnel tests of section models, a taut strip model and a full bridge aeroelastic model, as well as numerical simulations. Just before completion of construction, high amplitude (unacceptable) oscillations were observed. The amplitudes of these motions were higher than the predicted ones. Though this response was not of a catastrophic nature (as it was for Tacoma Narrows), they were

---

<sup>21</sup> Logarithmic decrement damping

unacceptable and mitigation solution had to be studied and implemented. This implied a subsequent higher cost of the project. Overestimation of structural damping, underestimated probability of occurrence of wind speeds with such low turbulence intensity and model scale effects might be pointed as possible explanations.

## 1.4 Study of the aerodynamics of the Third Millenium Bridge

### 1.4.1 The 3<sup>rd</sup> Millennium Bridge Design

The response to wind loading was investigated using both section and full aeroelastic models. The section model test program included the measurement of the pressure field on the two glass canopies over the sidewalks. The loads on the canopies computed from the pressure integration allowed for a considerable reduction in the assumed design loads. The obtained pressure field is compared, for validation purposes, with the one obtained from a numerical simulation. The overall performance under wind loading was satisfactory owing in part to the effect of the aforementioned canopies in improving the deck aerodynamics in addition to the inherent structural properties.

The Bridge (to be constructed for the 2008 World Exposition in Zaragoza, Spain) is an arch cable stayed bridge with a 216m main span and 27m symmetrical side spans. It is an innovative bowstring design having a high performance white concrete arch supporting a considerably wide deck of over 44m in width (see Figures 1 and 2). Its length falls within the longest of its type, just under the 304m of the proposed Indian River Inlet Bridge in Delaware, USA [1]. The width of the deck requires a significant separation between the legs of the “basket-handle” arch and therefore at the location of the arch bearings, the deck includes an intermediate support. The inclined arch legs follow the same vertical curvature of arch and provide an anchorage for several cables.

The typical cross section is presented in Figure 2. It consists of two side boxes connected by cross diaphragms every 6m, which is the same longitudinal separation between suspender cables. It can be observed that the lines of the boxes and diaphragms all follow the same curvature forming a remarkably streamlined shape. It is certainly becoming less unusual to find these bodies with shapes between bluff and airfoil shaped decks in modern bridges; see for example the Stonecutters Bridge in Hong Kong [2].

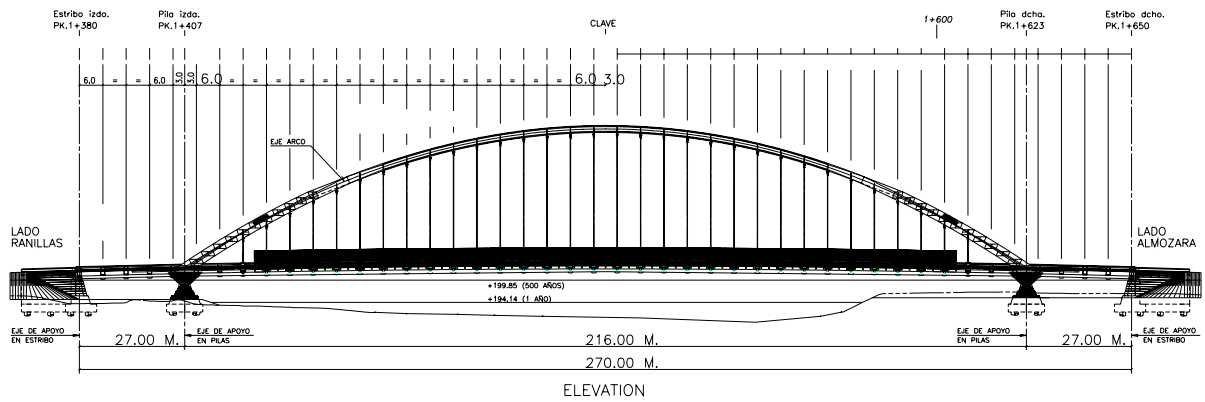


Figure 1.3. Elevation view of the 3<sup>rd</sup> Millennium Bridge (Zaragoza, Spain) showing the basic geometry.

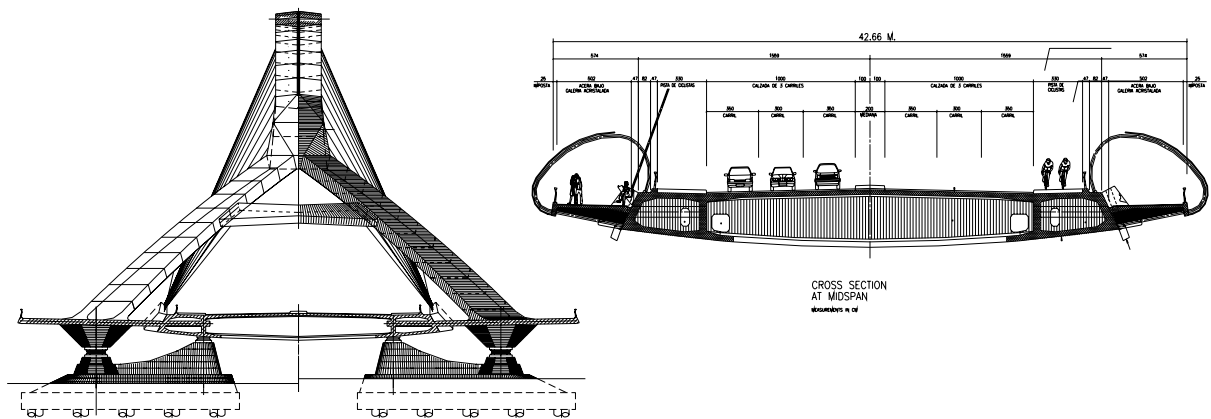


Figure 1.4. End view and deck cross section of the 3<sup>rd</sup> Millennium Bridge.

Located at both leading and trailing edges are the two cantilevers that support the canopies over the sidewalks. These canopies provide shelter to the sidewalks and also follow the curvature of the twin boxes and diaphragms. They result in smooth leading and trailing edges for the deck. The sidewalks are intended not only as a means for pedestrians and cyclists to cross the river but also as a recreational space where to sit and enjoy the look over the river through the glass canopies. Therefore, there is a need for ensuring the required comfort level within the canopy space for statistically appropriate wind speeds and their directions.

The arch's cross section is also streamlined with midspan dimensions of 540cm in width and 120-180cm in height (with an aspect ratio of  $W/H=4.5$ ). The elongated octagonal shape is anticipated to help in reducing the along wind response and hence in not exciting the considerable inertia of the heavy concrete arch.

## 1.4.2 Experimental study

The wind effects were investigated experimentally using both sectional and full aeroelastic models. The design of the models was a challenging task, given the shapes presented above and the desired mechanical performance.

The Section model was built at the CEAMA (University of Granada) and tested both at CEAMA in the new Boundary Layer Wind Tunnel I [3] and at The University of Western Ontario in Boundary Layer Wind Tunnel II (BLWT II, High Speed Test Section) [4]. The new facility at CEAMA may be unfamiliar to the reader and is described below. The wind tunnel is shown in Figure 3 is a conventional open circuit, closed section, suction-type wind tunnel. Its bi-dimensional 4:1 contraction follows a settling chamber which includes a typical flow conditioning system (honeycomb + screens) and leads the flow into the 15m x 2.15m x 1.8 m (L · H · W) test section. The pressure drop is generated by an 11 Al-alloy bladed fan, powered by a 160 Kw motor. The motor is driven by a 200 Kw frequency inverter and controlled through a PLC system. The wind speed in the test section is controlled in a closed loop by using an encoder in the shaft and a free stream pitot tube.

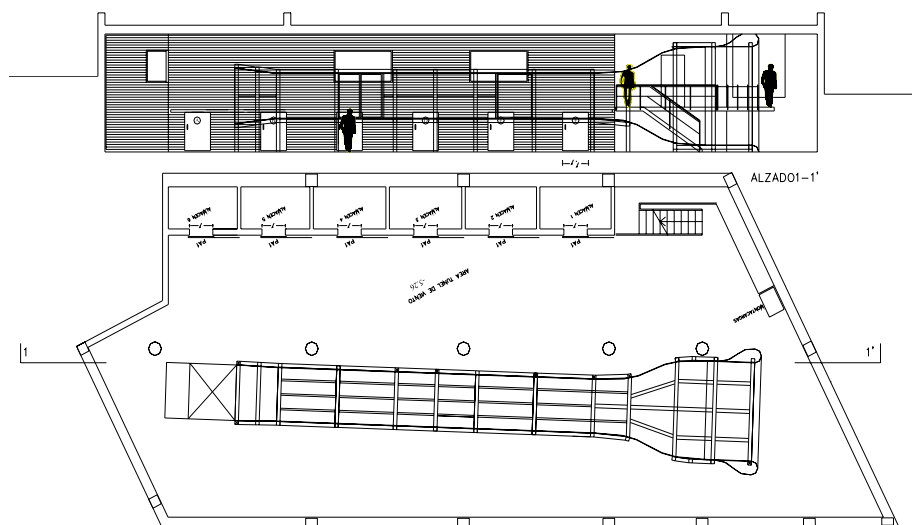


Figure 1.5: Plan and side view of the new Boundary Layer Wind Tunnel at CEAMA, University of Granada

### 1.4.2.1 Section Model

The section model was constructed at a scale of 1:70. Aluminum fiber composite diaphragms were inserted between the monolithic carbon fiber composite shell of the twin

boxes. The canopies along the span were made of polyamide (laser synthesized). Located at the midspan of the model were the corresponding leading and trailing edge pressure modules. These modules allowed for the measurement of the leeward and windward pressure field by means of short tubes connected to electronic scanners inside the twin boxes. The aerodynamic force coefficients were obtained for different angles of attack from  $-10$  to  $+10^\circ$  when the model was fixed and stationary. The model was ballasted to the scaled mass and mass moment of inertia (MMI) properties and mounted on a dynamic test rig in which the fundamental vertical and torsional modal frequencies were simulated. Given the prototype's deck and arch generalized mass and MMI, the selection of the target values for the section model is not straightforward. Therefore, different mass and MMI configurations were employed. The test program for the dynamic set-up included different structural damping ratios (0.15-0.8%), turbulence intensities (smooth - 5%), and loading history. The model was tested for different rates of change in mean wind speed as well as for increasing and decreasing wind speeds. This approach has been used quite successfully to demonstrate the sensitivity of bridge decks to vortex shedding (after, for example, [5]). A hotwire probe was located in the near wake through the stationary and dynamic tests in order to obtain information with regards to the associated vortex shedding frequencies.

Given the streamlined shape of the deck, special attention was paid to possible occurrence of Reynolds number effects. Hence, the deck and canopy surface was roughened thoroughly and the pressure and aerodynamic force coefficient tests were each performed for different wind speeds. The variation in the force coefficients observed for the higher wind speeds was within 5% for the integrated deck / canopy pressures and was found to be insignificant for the static force coefficient tests.

#### 1.4.2.2 Aeroelastic model of the completed bridge

The full aeroelastic model of the bridge was designed and constructed at the University of Western Ontario at a scale of 1:125 and tested in turbulent boundary layer flow at the Low Speed Test Section of BLWT II. The deck modules were designed of rapid prototyped ABS plastic and secured to an accurately machined central aluminum stiffness spine via magnesium cross beams. The arch was of similar construction. The stiffness spines were designed with span-wise variation in cross section, simulating the vertical, lateral and torsional stiffness of the deck and the vertical and lateral stiffness of the arch. The cable stays were modeled to approximate the mean drag force of the prototype, with both model and prototype cables in the subcritical Re number range. Their equivalent axial stiffness (AE) was provided by miniature extension springs. The fundamental mode shapes of the resulting model structure were checked using a set of accelerometers by exciting the corresponding mode in free vibration and analyzing the subsequent response. The first

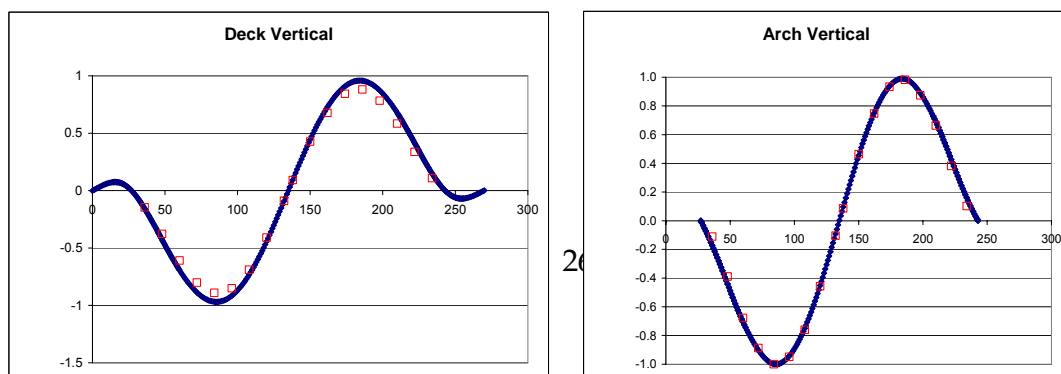


Figure 1.6: Comparison between prototype and model mode shape for Mode 1 - asymmetrical vertical bending.

mode, an asymmetrical vertical bending of both arch and deck, is compared to the prototype's mode in Figure 4.

The 3<sup>rd</sup> Millennium Bridge is in the wake of Zaha Hadid's "Pavilion Bridge". Therefore a "dummy" model of the building was included in the surrounding topographic model. Figure 5 shows the set-up of the model for the suburban exposure. Arch and deck were instrumented with strain gages in order to monitor both symmetric and antisymmetric modal response. Additionally, a set of accelerometers and laser transducers were used to measure vertical and lateral acceleration and displacement at midspan and the  $\frac{1}{4}$  point of both arch and deck.

The structural damping of the bridge model was quite low, with damping in the 0.67% to 0.74% range for vertical symmetric and antisymmetric bending modes of the deck respectively and 0.3% for the lateral bending mode of the arch. This level of damping is not unrealistic for a pre-stressed concrete deck structure and is considered to provide a conservative estimate of what may exist in the prototype. The frequencies of the important modes were reasonably well matched with the target values.

The completed bridge was tested for 15 wind directions: 0°, 40°, 50°, 60°, 70°, 80°, 90° (perpendicular to deck) under open country exposure ( $z_0=0.03\text{m}$ ,  $I_u = 15\%$ ) and 0°, 60°, 70°, 80°, 90° (perpendicular to deck) 100°, 110°, 120° under suburban exposure ( $z_0=0.3\text{m}$ ,  $I_u = 25\%$ ).

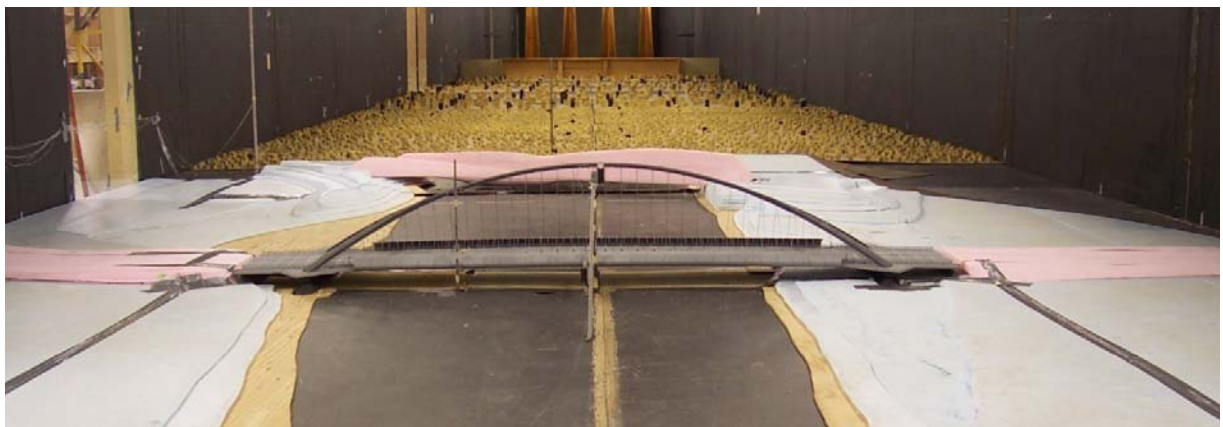


Figure 1.7. View of the full aeroelastic model (1:125 scale) in the wake of the complex shape of the Pavilion Bridge upstream.

### 1.4.3 Results and discussion

The aerodynamic force coefficients of the stationary model are listed in Table 1. There are no significant differences observed between smooth and turbulent flow results for any of the coefficients at small angles of attack. The coefficients differ for the two flow conditions only at high negative angles of attack. The coefficients show that there is a

positive slope in the aerodynamic lift and torsional force coefficient curves for small angles of attack. This is indicative of good aerodynamic stability characteristics.

Coef./Flow	SMOOTH	TURBULENT
$C_x(0^\circ)$	0.094	0.194
$C_y(0^\circ)$	0.113	0.110
$C_z(0^\circ)$	0.006	0.000
$\frac{\partial C_z}{\partial \alpha}$	7.78	7.11
$\frac{\partial C_M}{\partial \alpha}$	1.18	1.04

Table 1: Aerodynamic force coefficients of the stationary deck.

No flutter instability was observed in the section model tests up to a full-scale mean wind speed of 108 m/s. The gust wind speed for a 50 year return period at the bridge site and deck height is 41m/s (obtained from 55 years of data records). Vertical vortex induced vibration (V-VIV) was only observed at 22 and 56 m/s and torsional (T-VIV) at 32m/s in smooth flow conditions. Coupled response between the V-VIV and T-VIV occurred at windspeeds between 32 and 56 m/s. No VIV response was observed when turbulence intensity was higher than 1.5%. A typical result for long (450s f.s.) sampling time at each increasing and decreasing stationary wind speed is presented in Figure 6. No hysteresis was observed in neither the vertical or torsional response of any of these tests. The frequency ratio between the selected torsional and vertical modes of vibration was 1.2.

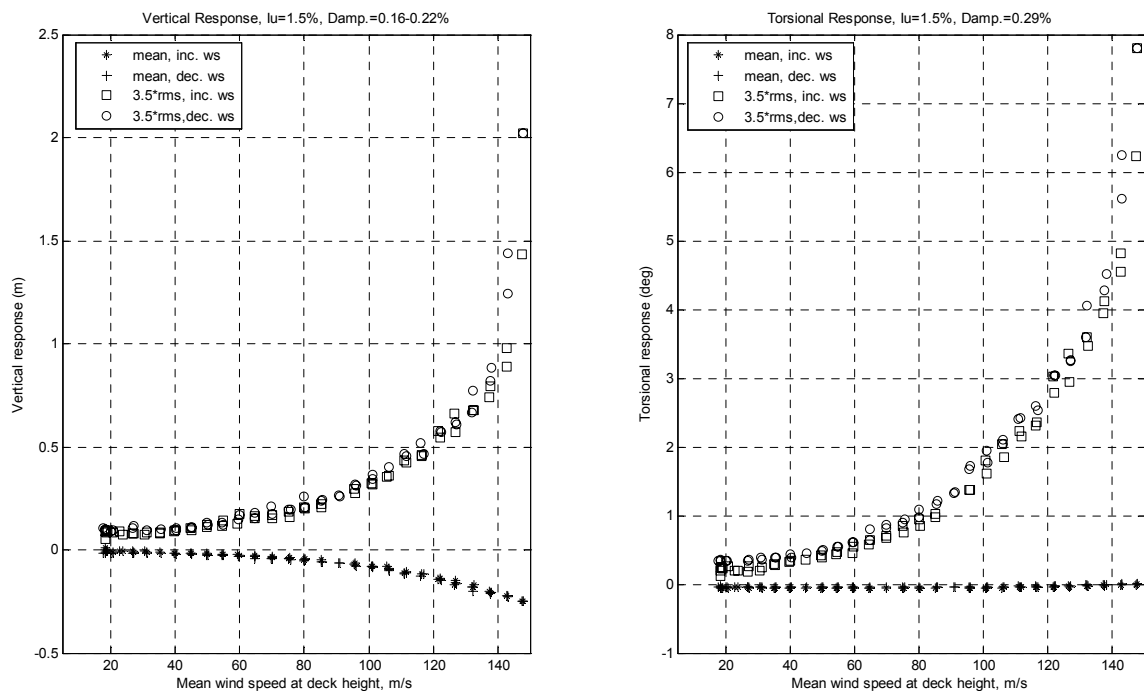




Figure 1.8: Typical response observed in low turbulent flow with low structural damping for increasing and decreasing wind speeds.

The mean pressure field on the canopies is presented in Figure 7. The small pressure gradient observed suggests that the shape follows the flow structure smoothly having boundary layer separation only at the top. The force coefficients computed by integrating the corresponding pressure fields are  $C_D=0.48$ ,  $C_L=0.42$  and  $C_M=0.02$  for the windward canopy and  $C_D=0.38$ ,  $C_L=-0.20$  and  $C_M=-0.04$  for the leeward one. The centre of rotation for the  $C_M$  calculation was located at the end of the supporting tube on the deck surface which is at the edge of the upper surface of the twin boxes. No peak was observed in the spectra of the pressures on the outer surface of the leeward canopy. Similarly, no distinct peak was observed in the spectra of the hotwire measurements performed at one deck width downstream of the trailing edge.

The experimental pressures are compared with a preliminary numerical simulation for validation purposes only (see Figure 8). Good agreement is observed on the basic features of the numerical simulation at a 1:70 scale using steady state Reynolds Averaged Navier Stokes (RANS) equations and Reynolds stress model (RSM). As for example, the differential  $C_p$  on tap 20 (windward canopy) from the section model tests, +1.26, compares well with the +1.15 obtained from the numerical model. The maximum velocities in the sheltered area under the leeward canopy ranged from 2 to 3m/s for a 13.7 m/s free stream wind speed. No vortex structure was identified in the wake of the simulated flow field.

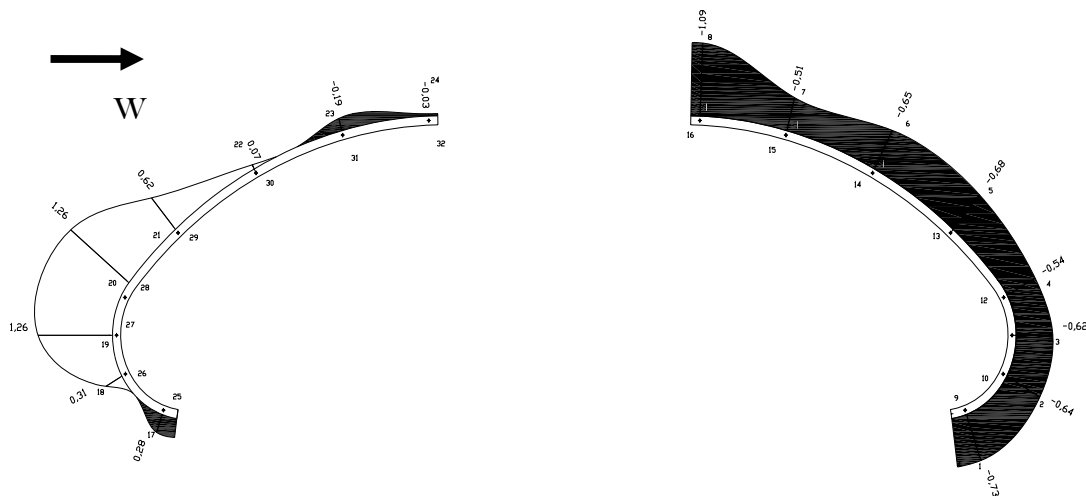


Figure 1.9: Differential pressure coefficients on the canopies. The shaded areas represent suction (negative pressure).

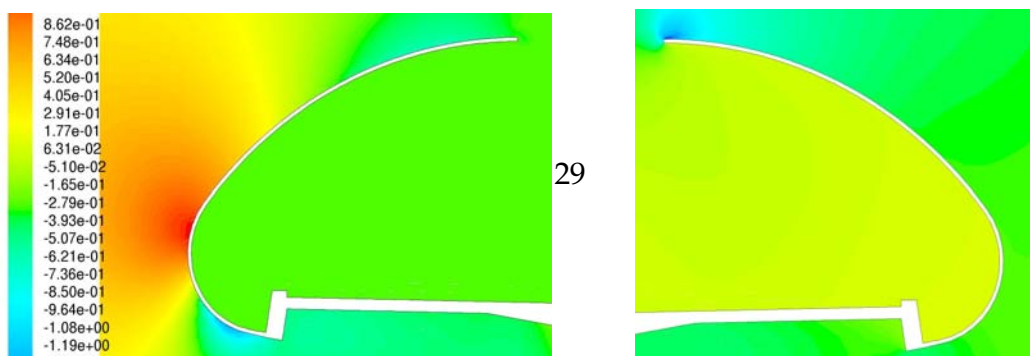


Figure 1.10 Pressure coefficient distribution on the windward (left) and leeward (right) canopy from numerical model.

No significant dynamic response was observed in any of the tests of the aeroelastic model in either exposure, partly due to the considerable mass and stiffness provided by the concrete structural members and the distinctive aerodynamic shapes of both arch and deck cross sections. This improvement in the response in comparison to the observed behaviour of the section model is likely due to the combined effects of turbulence, realistic levels of structural damping and the three dimensional representation of the structure and the local terrain (see Figure 9 below).



Figure 1.11: View of the 1:125 full aeroelastic model of the 3rd Millennium Bridge in the UWO, BLWT II Low Speed test section.

No evidence of torsional flutter or vertical galloping instabilities was observed, confirming the good aerodynamic behaviour observed in the section model.

All responses were characterised by turbulent buffeting up to mean hourly wind speeds at the top of the arch of approximately 65 m/s.

All dynamic responses exhibited a velocity-squared

relationship with wind speed, which is consistent with an aerodynamically well-behaved structure. The increase in dynamic response in the suburban exposure over that in the open country exposure was approximately proportional to the corresponding increase in turbulence.

The arch, located 35m above the deck surface forms a tight triangular stress path with the somewhat wide (46m) deck and cable stays. Movement of the heavy concrete arch could induce inertial loads at a level which would be of concern if it were to be excited by wind. This was not observed in the aeroelastic tests of the full structure. The reduced drag from the elongated octagonal shape of the arch's cross section is partly responsible for the stability of the arch. This streamlining is carried throughout the structure, as shown in Figure 10, one can fit a NACA 8320 airfoil section at 8° angle of attack to the actual deck section shape. The similarity is remarkable.

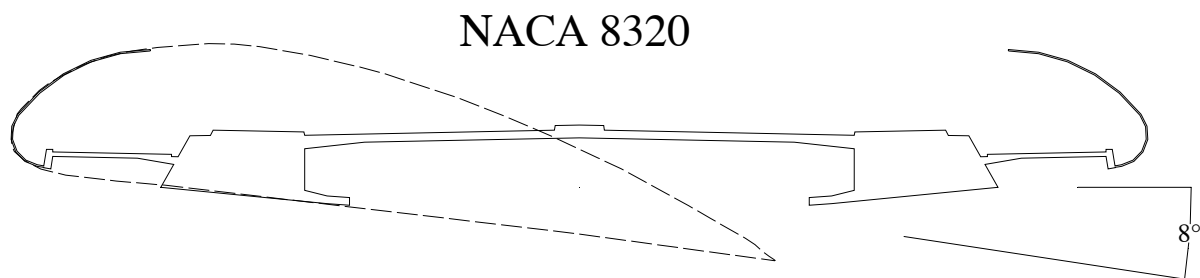


Figure 1.12: A NACA 8320 airfoil profile match remarkably well with the shape of the deck and side canopies.

### 1.4.4 Conclusions

The results from the section and full aeroelastic models confirm a good aerodynamic performance. The loads on the glass canopies obtained from the pressure integration allowed for a considerable reduction from the preliminary design loads. These canopies prove to be useful in providing shelter to the sidewalks and present favourable aerodynamic features. No significant vortex activity is believed to occur in the near wake. The streamlined canopies are anticipated to play a major role in enhancing the aerodynamics of the already streamline deck's cross section. The 3<sup>rd</sup> Millennium bridge is an example of how enhanced esthetics and aerodynamic performance come together naturally.

## 1.5 Scope of the study

The present work is framed within the field of modern bridge aerodynamics. Modern bridges are often complex in shapes which differ from traditional bluff forms. The aerodynamics of these shapes are not simple and involve mechanisms of flow structure interaction of different nature. The overall aerodynamics of an state of art Bridge (Third Millenium Bridge) have just been reviewed. The limitations of common section model testing have been put to test. The more fundamental work investigates the mechanisms of VIV of a complete long span Bridge, (Storebaelt).

It is the aim of the present work to aid in the understanding of the behavior of long span bridges in wind during **vortex-induced oscillations**. The present work may aid designers in understanding the phenomena. It is hoped that this will eventually lead to more effective mitigation measures. In addition, the results that will be presented may help in the development of numerical simulations of vortex-induced response. A better understanding,

and the development of such computer simulations, might reduce the number of wind tunnel tests in future projects.

A 1:70 scale section model of the Storebælt East Bridge was designed and tested. The hysteric nature of both torsional and vertical vortex-induced oscillations were studied in detail. The pressure field around the deck at different stages of the torsional vortex-induced response is presented; in particular, phase averages of the pressures around the deck at different stages as well as the resulting force coefficients ( $C_m$ ,  $C_l$ ,  $C_d$ ) are presented. The correlations between pressures along the deck were measured to see how they change through the different phases of motion. This work describes how the flow field around the bridge deck evolves during the different phases of the torsional vortex-induced response.

Finally a case study involving vortex induced vibration bridge beams under construction is presented in contrast with the above.



# Chapter 2

## Vortex Induced Vibration of Bridges

Vortex induced vibration (VIV) is an aeroelastic phenomena responsible of failures in structures of many kinds. The prediction of this response is not simple and normally requires wind tunnel tests. Available methodologies occasionally still fail in predicting it. The present work focuses on limited characteristics of VIV in Bridges. The Vortex Induced Vibration of Bridges is framed here within the so-called Bluff Body Aerodynamics field. The available literature and analytical models and techniques are reviewed.

### 2.1 Introduction

The vortex-induced vibration is a complex phenomenon involving disciplines such as fluid mechanics, dynamics of structures or vibration theory that is being studied through the use of mathematical, experimental and computational models. It is of interest for many research areas: wind-excited oscillations of bridges, cables, chimneys, vibration of hydraulic infrastructures, marine technology: offshore and harbour structures or industrial systems, i.e. engine design. Among the body shapes susceptible of suffering vortex induced vibration (VI-bodies, after (Sarpkaya T. A., 2004)), the cylinder is clearly the one that has attracted most interest. The literature on the vortex-induced vibration of the cylinders is vast, some excellent reviews are presented in (Sarpkaya T. A., 2004), (Williamson & Govardhan, 2004) and (Bearman P. , 1984). The problem is not solved even for the case of the cylinders where a lot of progress has been made but there is a number of unknowns that remain (see Section 2.2.1). Some of them are even related to the **actual nature of the physics** behind the phenomenon, others are related to the effect of certain intrinsic parameters or characteristics: body shape, body surface finish, turbulence intensities and scales, mass and damping independently, hysteresis, aspect ratio, blockage, Reynolds number, fluid's viscosity or experimental uncertainties (Schewe parameters). Most of the work has been carried out to study the vertical mode of vibration induced by the fluctuating surface pressure caused by the shedding of vortices into a vortex street. However, the

vortex-induced response of bluff bodies other than cylinders can involve other types of vortex structures and modes of vibration such as motion induced vortices or vortices travelling across bodies with long chord lengths (Komatsu & Kobayashi, 1980), (Terrés-Nicoli J. , 2002) that may excite other modes as torsional modes, for example.

In the search of better aerodynamic performance: lower drag, higher torsional stiffness and reduce vortex-shedding, modern bridge deck's cross sections have evolved through time becoming more streamlined. The resulting cross sections have changed from bluff bodies to shapes which are not airfoils but certainly not precisely bluff bodies; they are cross-between both categories (Wyatt, 2003). The flow is even more complex in the case of two of these curved shapes similar in some ways to an aerofoil but with a blunt leading/trailing edge and a gap in the middle. Such is the case of some twin box girder bridges such as the Stonecutters or the Tsing Lung bridge, both to be erected in Hong Kong (Figure 2.1). In this sense, the case of modern bridge decks can be quite different from typical Kármán vortex shedding, involving streamlined shapes with blunt edges, long afterbodies including obstacles (i.e. crash barriers) and oscillating leading and trailing edges. The aerodynamics of these shapes have not been fully resolved. In addition, issues such as Reynolds ( $Re$ ) numbers effects in the experimental or numerical testing, often neglected for bluff bodies, might be an issue (Schewe & Larsen, 1998).

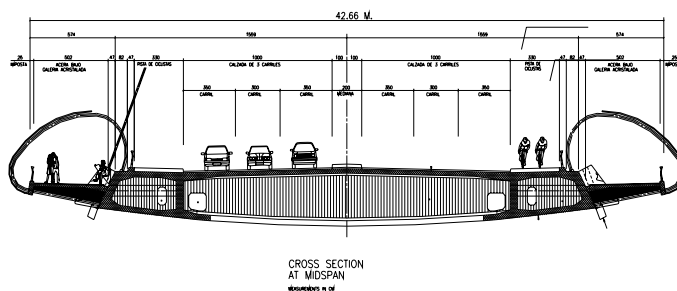


Figure 2. 1: Cross section of a modern twin box girder suspension bridge designed in Hong Kong (above) and the new Third Millenium Bridge in Spain (below).

There have been some attempts to classify bluff bodies for vortex-induced response regarding their cross-sectional shape (Shirashi & Matsumoto, 1983), (Matsumoto, 1999), (Komatsu & Kobayashi, 1980). For example, Matsumoto classified the response of square, rectangular and hexagonal cross sections with symmetrical nosings. Different mechanisms involving motion induced vortices and/or Kármán vortices are involved in the vortex-induced response depending on cross sectional shape.

The design of long span suspension bridges is governed by the study of the wind effects. There are different wind effects on bridges and its elements (pylons or cables), that one could divide into two groups, those that compromise ultimate limit states of the design and those related to serviceability limit states. The flutter instability which caused the well known collapse of the Tacoma Narrows Bridge in 1940 falls into the first group. This phenomenon, largely studied in aircrafts, has been the topic of many research projects since that and other structural failures in bridge engineering. There is a good understanding of the phenomenon provided that a semi-empirical formulation developed by Scanlan (Scanlan R. H., 1951.), (Simiu & Scanlan, 1996) let us predict the flutter limit with the aid of a few tests on a section model. Some numerical simulation have succeeded as well in predicting the flutter limit of certain bridges (Robertson, Sherwin, & Bearman, 2003), (Frandsen J. , 2004), (Larsen & Walther) though the predicted pressure and velocity field is to be investigated yet. Hence, the fundamentals of the physics of the fluid-structure interaction need to be further explained still. In the other group, the vortex-induced oscillation of long span bridges compromise serviceability limit states of design due to discomfort or long term fatigue of the materials mainly. A few years ago, the need to investigate the nature of this vibration was stated clear when in 1998, just before its inauguration, the 3.2billion USD Storebaelt Bridge and, at that time, longest span bridge in the world, exhibited unacceptably large amplitude vortex-induced vibration (Frandsen J. , 2001). The vibration was observed under the effect of moderate winds (5-10m/s) of remarkably low turbulence intensity (as low as 2%) and directions close to the perpendicular to the bridge's axis (Frandsen J. , 2001), (Larsen & al., Vortex shedding excitation of the Great Belt East Bridge, 1999), (Larsen, Eisdahl, & Andersen J., 2000). The deck's design was retrofit by adding guide vanes along the main span (at the lower corners E and F in Figure 4.1) with the subsequent additional considerable cost. This failure may serve as an example to confirm the need to investigate the driving mechanisms of the dynamic fluid-structure interaction specially when at the beginning of this century bridges of twice that span and higher are being proposed (Messina Strait 3300m, Sunda Strait, 3500m or Gibraltar Strait 5000m). Indeed, there have been quite a number of bridges which are known to have suffered problems related to vortex-induced oscillations.

- The Long's Creek Bridge (Canada), (Wardlaw, 1992)
- Second Severn Bridge (UK), (Scruton, 1948), (McDonald, 2001.)
- Rio-Niteroi Bridge (Brazil), (Battista, 2000)
- Osteroy Bridge<sup>22</sup> (Norway)
- Wye Bridge (U.K.), (Holmes J. D., 2001)
- Waal River Bridge (The Netherlands), (Holmes J. D., 2001)
- Tokyo Bay Bridge<sup>23</sup> (Japan), (Fujino & Yoshida, 2002)

---

<sup>22</sup> To the author's knowledge nothing has ever being published about this case.

<sup>23</sup> A remarkable event since it is a box girder bridge with a maximum span of 240



- Dear Isle Bridge (U.S.A), (Kumarasena, 1989)
- Kessock Bridge<sup>24</sup> (U.K.), (Owen, 1996)
- Storebælt Bridge (Denmark) (CBR., Measurements of Vortex Shedding Excitation, 1998), (Frandsen J. , 2001), (Larsen & al., 1999)

Among these are the Tokyo Bay Bridge in Japan, with a maximum span of only 240 m, and the Kessock Bridge in the U.K. which exhibited the previously unobserved torsional vortex-induced response.

The Storebaelt Bridge in Denmark is the focus of the present work. The cross section of the Storebaelt is similar to many other modern long span suspension bridges and the number of experimental, numerical and full-scale studies that have been carried out is remarkable. For the present study, a section model was tested under low turbulence, steady, wind of increasing and decreasing speeds. Detailed surface pressure field and deck's motion were obtained simultaneously for a sufficient number of increasing and decreasing wind speeds. As an attempt to deal with the fascinating feedback between body motion and vortex motion, the focus of the present work is the investigation of the modelled phenomenon with no meaning to extrapolate the analysis to the full-scale case, though every effort was made to model that in the experiments. It is the aim of this fundamental study to provide some insights into the mechanisms of the fluid-structure interaction responsible for the vertical and torsional vortex-induced response that may aid in the understanding of the phenomenon and the further development of analytical and numerical models. An extended report of the research on the torsional mode can be found in (Terrés-Nicoli J. , The torsional Vortex-Induced Vibration of the Storebælt Bridge. Master of Engineering Science Thesis. , 2002).

## 2.2 Bluff body aerodynamics: How Bluff?

When studying the airflow around a body we may divide such flow field in two regions: one in which the body disturbs the approaching flow and that in which it is not (Zdravkovich, Flow around Circular Cylinders: Vol 1: Fundamentals, 1997). Within the latter we can identify a sub-region where the air velocity is lower than the free stream windspeed ( $U_\infty$ ), the wake. In there, the flow is referred to as separated. The flow separation originates when the boundary layer over the body can not cope for the adverse pressure gradient derived from the shape and subsequent circulation and therefore separates ( $U < U_\infty$ ). These bodies that impose the flow separation are referred to as **Bluff Bodies** in contrast with the streamlined airfoils which shapes are designed so that the flow hardly separates (obviously at low angles of attack). Bluff bodies exist with sharp edges that impose the separation point or rounded forms around which the separation point change its location depending on many parameters like surface roughness, turbulence intensity,

---

<sup>24</sup> This is to the author's knowledge the only bridge known to have exhibited torsional vortex-induced oscillations.

viscosity, windspeed etc. The disturbed flow by bluff bodies has many similarities. The circular cylinder is clearly the one that has attracted more attention.

Most of the forms in civil engineering and architecture have traditionally been considered bluff bodies. However, more recently, rounded shapes are becoming more common in bridges and buildings. The question remain on the flow similarity, i.e. Re number effects, of these shapes becoming less “*bluff*” or as posed by Wyatt, (Wyatt, 2003), How bluff is bluff?.

Notwithstanding the above, a The 3<sup>rd</sup>Millenium Bridge presented in Chapter 1, has remarkably rounded shapes of structural and non structural elements. This flow field around it presented very low vorticity in the wake. No significant energy peak was found in the hot wire spectra and consistenly exhibited negligible vortex induced response (Figure 1.8).

## 2.2.1 The circular cylinder

The circular cylinder is undoubtable the body that has attracted more attention in fluid mechanics. The literature on the VIV of the circular cylinder is vast, starting in the second half the 19<sup>th</sup> century with the pioneering work by Lord Rayleigh and Strouhal among others in the field of sound engineering<sup>25</sup>. The flow structure around the circular cylinder depends basically on the transition for increasing Reynolds numbers (Re) of the flow regimes in the wake (W), free shear layers (SL) and boundary layers (BL) up to a fully turbulent state (Zdravkovich, Flow around Circular Cylinders: Vol 1: Fundamentals, 1997). It can be postulated that most of the elements of interest in Civil and Environmental Engineering, and Architecture, submerged in atmospheric boundary layer flows corresponding to Re numbers ranging from 0.1 to  $100 \cdot 10^6$ . The above mentioned Re number is defined as:

$$R_e = \frac{U_\infty \cdot D}{\nu}$$

where  $U_\infty$  is the free stream wind speed, D the cylinder diameter and  $\nu$  is the kinematic viscosity of the air, hereinafter  $1.51 \cdot 10^{-5}$  (m<sup>2</sup>/s, at 20°). Different flow structures are originated at the different regimes mentioned above. Furthermore, the body motion gives rise to certain patterns in the flow which differ to those corresponding to the above mentioned regimes. These flow structures have been termed 2S (2 vortices shed per oscillation cycle) 2P (2 pairs of vortices per cycle), and P+S (one pair one side a one vortex on the other and therefore unable to induced vibration (Williamson & Govardhan, Vortex-induced vibrations, 2004). It is noted that the latter two differ from the classical Karman vortex street. The range of Re of interest in the studies of processes near the surface of the earth correspond to strong vortex shedding for  $300 < Re < 2.5 \cdot 10^5$  (so called subcritical regime) and regular vortex shedding for  $Re > 3.5 \cdot 10^6$  (fully turbulent

---

<sup>25</sup> The so called Aeolian tones of strings producing sounds in the wind while undergoing VIV gained the attention of Greek ancient cultures.

supercritical regime) and a transitional regime at the boundary layers in between, see Figure 2.2 (Blevins, Flow induced vibration, 1990).

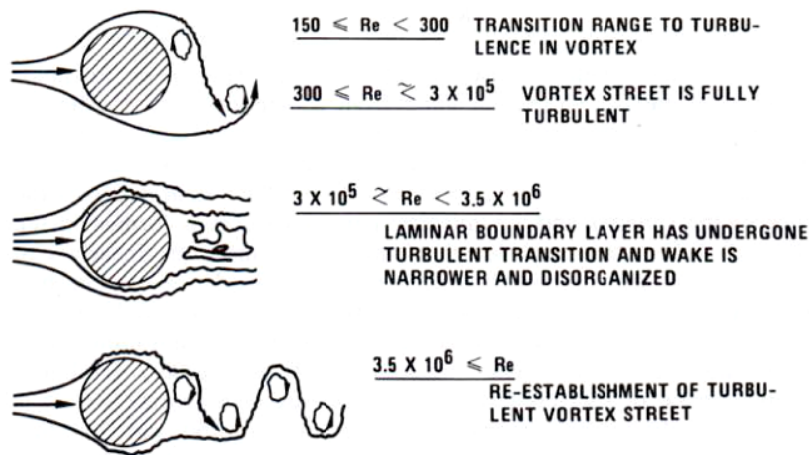


Figure 2. 2: Circular cylinder flow regimes of interest in Civil and Environmental Engineering (Blevins, Flow induced vibration, 1990).

The study of the vortex strength and structure passed the cylinder is important in the study of VIV irrespective of the corresponding mode. However the mechanisms of vortex creation are yet not fully solve. A detailed study of creation of vorticity is presented in (Saffman, 1995). One of the first evaluation of the vorticity in the near wake is made based on the generation of circulation at the shear layer at the boundary layer separation. Roshko (Roshko, 1954), proposed that the rate of circulation,  $\Gamma$ , produced at shear edge is,

$$\frac{d\Gamma}{dt} = \frac{1}{2} U_s^2$$

where  $U_s$  is the velocity at edge, "S" in Figure 2.2. And the circulation defined as,

$$\Gamma = \oint U ds$$

from which the above rate can be obtained, by considering  $d\Gamma = U ds$ . The amount of circulation in the wake vortices is evaluated as a fraction,  $\alpha$ , of the total circulation produced at the shear layers,  $\Gamma_T$ ,

$$\Gamma_T = \alpha \cdot \frac{1}{2} (k \cdot U_\infty)^2$$

where  $U_s$  is presented as fraction of the free stream velocity,

$$U_s = k \cdot U_\infty$$

Such relationship between the velocities leads to a pressure coefficient at the separation point of,

$$C_{p_s} = 1 - k^2$$

by simple application of the Bernoulli's equation considering constant pressure. The pressure coefficient above is defined here and hereinafter as,

$$C_p = \frac{P_s - P_\infty}{\frac{1}{2}\rho U_\infty^2}$$

it follows from **second last** equation that

$$U_s^2 = U_\infty^2(1 - C_{p_s})$$

on the other hand, the circulation in the wake can be estimated from the strength and rate of the vortices shed in to it,

$$\Gamma_T = f_s \Gamma_v$$

where  $\Gamma_v$  is the circulation of each vortex in the wake. The balance presented above can finally be presented as (Bearman P. , 1984),:

$$\alpha = \frac{2S_t \Gamma_v}{U_\infty D(1 - C_{p_s})}$$

where  $S_t$  is the Strouhal number or non-dimensional shedding frequency,

$$S_t = \frac{f_s D}{U_\infty}$$

Davies (Davies, 1976) accounted for the production of circulation due induced by the fluctuating component and concluded it could be neglected. Estimates of the fraction  $\alpha$  range from around 0.5 for the stationary cylinder compared to the higher value of 0.66 of the oscillating case (Sarpkaya T. A., 2004). Davies observed a much lower value of 0.26 for a stationary D-shaped body, compared to 0.24 of the oscillating wake (Davies, 1976). This balance has given physical ground to a number of classic analytical models. More recently detailed numerical simulations of the near wake flow structure around the oscillating cylinder have allowed for more accurate limited estimates of the vortex forces accounting for another source of vorticity generated by a secondary flow when the shedding occurs near the BL (Koumaoutsakos & Leonard, 1995).

### 2.2.1.1 The ensuing of VIV

An elastically mounted cylinder restrained from along wind response is considered throughout this study in a similar arrangement as shown in **Figure 3**. The along wind or drag induced response is considered therefore restrained hereinafter.

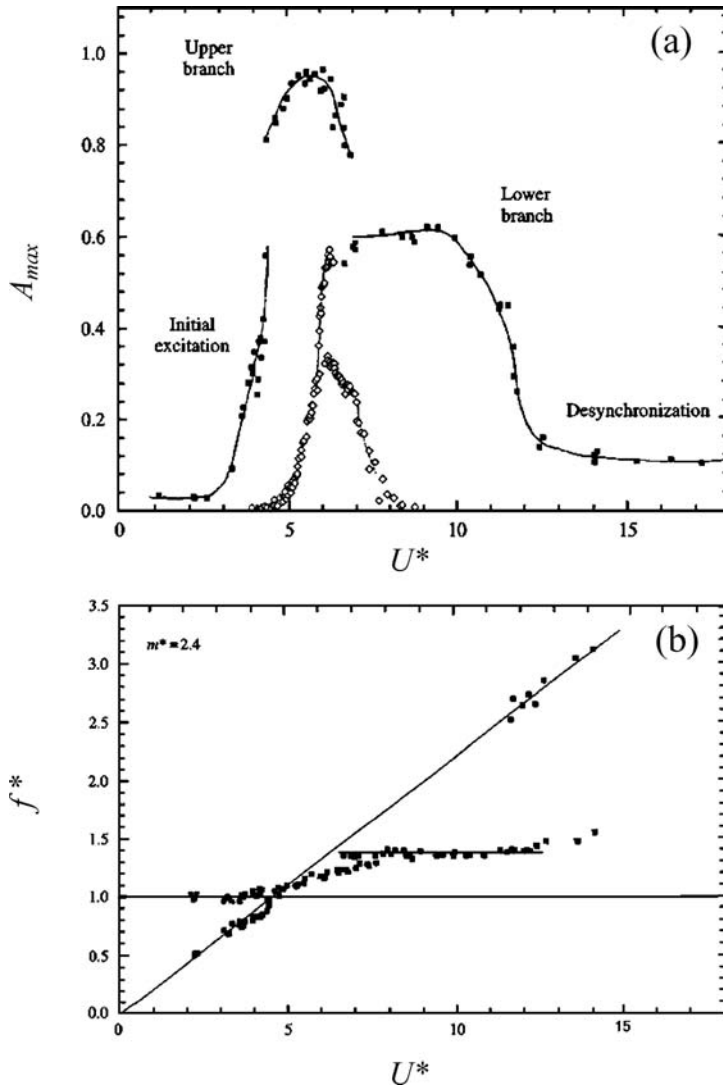


Figure 2.3: Williamson's circular cylinder observed response for low mass-damping (solid) with Feng's well known data (open) (Khalak & Williamson, 1999) and (Williamson & Govardhan, Vortex-induced vibrations, 2004).

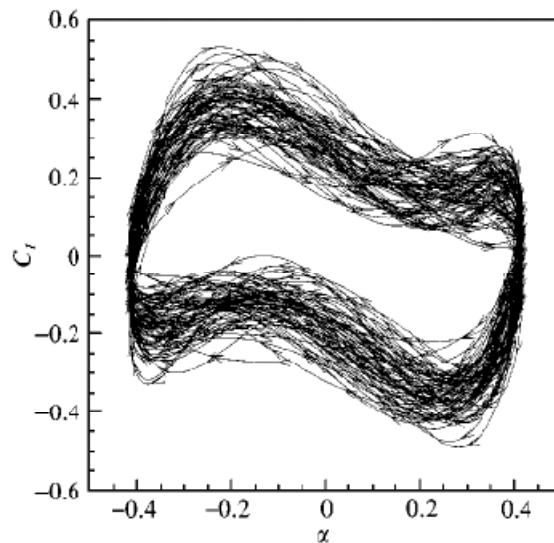
The frequency of the flow structures related to different phenomena in the wake, shear and boundary layers vary with  $Re$ . The flow structures interact with the cylinder inducing a fluctuating pressure field on its surface. Resulting from this interaction when the frequency in the flow structures get any close to the cylinder modal frequency is resonant vortex induced response (VIV). We shall consider the  $Re$  ranges where regular vortex shedding occurs. The shedding frequency ( $f$ ) varies with the  $Re$  number as give by the previously defined  $St$  number. This relationship is shown in Figure 2.3.

The vortex shedding frequency,  $f_s$  correspond to a complete shedding cycle, one shedding event at each shear layer (which may correspond to either one or two vortices depending on the shedding mode (2S or 2P)). Consequently a fluctuating lift force is generated at that same frequency and a fluctuating drag force  $2 \cdot f_s$ . The first is responsible for across wind or normal VIV and the latter for along-wind or in-line vibrations at the corresponding

frequencies (Bearman P. , 1984), (Blevins, Flow induced vibration, 1990) and (Bishop & Hassan, 1963). The in-line vortex induced response of bluff bodies has normally received relative less attention.

The typical response of a circular cylinder in a transverse mode is presented in Figure 2.2 (Khalak & Williamson, 1999). The response of a configuration with significant less mass and damping is presented in contrast with the well know response from Feng of a higher order of magnitude of such parameter. The initial branch of the response curve is associated with 2S shedding modes, whereas the upper and lower are related to 2P modes.

Figure 2.4: Phase plane portrait of lift coefficient and non-dimensional displacement obtained from Govardhan& Williamson data (Govardhan & Williamson, 2000) presented in (Blackburn, Govardhan, &



Williamson, 2000).

The enhancement of maximum amplitude vibration is associated with changes in the timing of the vortex formation (Zdravkovich, 1997), (Chyu & Rockwell, 1994), or similarly in the phase of the vortex force of (Khalak & Williamson, 1999). This transition has a hysteric nature in contrast with intermittent transition between the upper and lower responses which is due to changes in the of  $180^\circ$  in the phase of the total force (Khalak & Williamson, 1999) and not the timing of the vortices as it was initially expected. The phase is referred to here as the phase angle by which the force leads the response ( $\phi$ ). The measured phase becomes close to  $90^\circ$  at maximum amplitude oscillations for high mass-damping ratios (see Figure 2.3). Different Lissajou (phase plane diagrams) for the different response branches are available in (Khalak & Williamson, 1999) and (Blackburn & Henderson, 1999). This value corresponds to a typical resonant response (Den Hartog, 1984). Notwithstanding, phase becomes  $180^\circ$  for low mass-damping maximum amplitude vibrations which would be consistent with small deviations of the force frequency around the natural for a low damped oscillator. The precise value of the phase angle  $\phi$ , has a significant effect in the response. This can be simply illustrated by the solution for single degree of freedom mechanical system as shown in Figure 2.4. It can be observed in this

Figure that abrupt changes in the phase ( $\pm 180^\circ$ ) can be expected at resonance for low damped systems. The phase smoothly approaches  $90^\circ$  as the damping tends to the critical value.

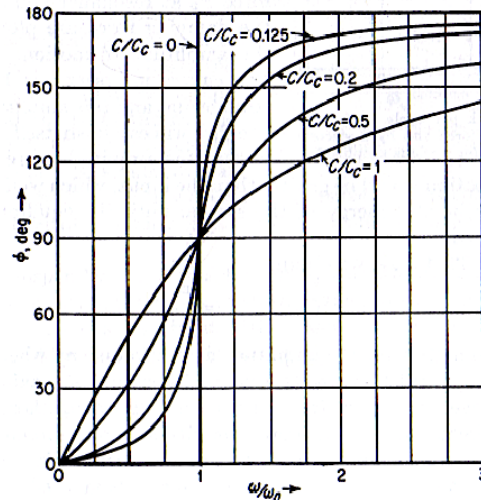


Figure 2. 5: Phase solution of damped single degree of freedom mechanical system as a function of the frequency and the damping.

The study of the forces of the mechanical system will be described analytically in detail in [section](#). The force shall be decomposed in different parts with respect to the aforementioned phase. There have been some attempts to give physical explanations to the different components. In this context, and **added mass** concept is introduced corresponding to the force component in phase with the acceleration. Consequently it can be referred to as an inertial term which can take positive and negative values there affecting the nature and magnitude of the response. Many features of this “virtual mass” or of the nature of the in-phase force components are question of debate (Williamson & Govardhan, 2004), (Sarpkaya T. A., 2004).

The synchronization range is defined as range of reduced wind speeds at which actual vibration frequency matches the wake (or more generally, flow) excitation frequency whatever the mechanism is. The width of this range increases as the mass-damping becomes lower. Similarly, a reduction of this product implies an increase in the maximum amplitude attainable. A critical mass concept has been proposed based on numerical simulations with mass tending to zero. Consequently a limit of reduced mass of 0.54 (critical mass) would make the lower branch (higher Re end) of the synchronization range to tend to infinity. Significantly, such value of reduced mass is common in the design of civil engineering structures. If such a critical mass exist a body undergoing VIV with this reduced mass would resonate infinitely with unlimited upper end reduced wind speed.

The maximum amplitude attainable is certainly one of the features of this phenomena that attracts more interest from the engineering design view point. The maximum amplitude of vibration of a system of given mass and damping, is normally estimated via the well know Griffin plot, however, there is no final explanation for such relationship. Whether such

amplitude depends of a certain product of mass and damping (Scruton or Scott-Griffin numbers) or depends on each parameter independently is still a question of debate.

It is observed that the ensued vibration helps a the flow couple along the span of the body. Considerable increase is observed in the correlation of the pressure traces along the span of the vibrating body relative the stationary state. A correlation length can be defined as:

$$L = \int_0^{\infty} R_z(p, z) dz$$

where R is the non dimensional cross correlation of a pressure measured at two points of the cross section separated a distance z along the span,

$$R_z(p, z) = \frac{\overline{p(z_0)p(z_0 + z)}}{\overline{p(z_0)^2}}$$

The investigation of this length can help in validating the selected aspect ratio and ensure bi-dimensionality of the experimental set-up.

Significant knowledge has been accumulated over nearly 150 years of work on the circular cylinder. Nevertheless there are fundamental questions for which response is yet not final such as what is the maximum attainable amplitude of an elastically mounted cylinder under certain conditions? The bluff body aerodynamics is certainly built based on the circular cylinder experience, however it is not clear what features, characteristics and mechanisms can be carried across to other VIV systems and body shapes.

## 2.2.2 The Rectangular Prism and other bluff bodies

The square and rectangular prism are among the types of bluff bodies that have attracted more attention other than the circular cylinder. Compared to this, a distinct characteristic of the flow around prism is the fixation of the separation points at the blunt edges. Several studies, mainly in Japan, have been conveyed for different body types and vibration modes (Shirashi & Matsumoto, 1983), (Matsumoto, Recent study on bluff body aerodynamics and its mechanism., 1999), (Komatsu & Kobayashi, 1980), (Nakamura & Nakashima, 1986), (Okajima, 1982). It is noted, that these prisms are often referred to as “rectangular” or “square” cylinders.

### 2.2.2.1 Flow structure around rectangular prisms

For the most part, studies have focused on rectangular cylinder of different chord to thickness (depth)ratio,  $c/D$  while less attention has been paid to triangular or other polygonal cross sections. The square prism may be considered as a particular case with  $c/D=1$ . The flow structure and its interaction mechanisms with the body surface much differ based on that parameter. The flow regimes can therefore be described based on that parameter so that for high Re numbers ( $>10^3$ ) (Parker & Welsh, 1983), (Mills, Sheridan, & Hourigan, Response of base suction and vortex shedding from rectangular prisms to transverse forcing, 2002):



A:  $\frac{c}{D} < 3.2$ : The shear layers do not reattach but only change their curvature

B:  $3.2 < \frac{c}{D} < 7.6$ : the shear layers periodically reattach and separated letting the flow fluid in the separation bubble interact with the flow structures in the near wake at the trailing edge.

C:  $7.6 < \frac{c}{D} < 16$ : shear layers are always attached at some point upstream of the trailing edge. The separation bubble structure varies randomly generating irregular vortex shedding.

D:  $\frac{c}{D} > 16$ : the structure is similar to the previous but the vortices over the surfaces diffuse so that the flow developed over them reaches a state close to fully turbulent .

As for the Strouhal number, it is agreed

$0 < \frac{c}{D} < 1.0$ : approximately  $St=0.13$

$1.0 < \frac{c}{D} < 3.2$ : progressively decreases from 0.13 to 0.065

$3.2 < \frac{c}{D} < 7.6$ : steady increase from 0.15 ( $c/D=3.2$ ) to 0.07 for  $c/D=7.6$ . Note the significant jump in the shedding frequency around  $c/D$  of about 3.2.

$7.6 < \frac{c}{D} < 16$ : no regular vortex shedding for large  $Re$  is observed.

$\frac{c}{D} > 16$ : the shedding corresponds to that of an airfoil

These values are consistent from the proposed universal  $St$  number proposed by Nakamura (Nakamura & Nakashima, 1986) of  $0.6D$  for  $c/D$  values in the range of 2.0 to 8.0. As for example, the  $St$  number that corresponds to  $c/D=7.6$  could be estimated as,  $0.6/7.6=0.07$ . Nakamura based such relationship in the number of vortices that reach the trailing edge from the leading edge, based on the chord length.

It has been described in the previous section how different shedding modes (2S, 2P, P+S) result from the interaction of the two shear layers past a circular cylinder. It is noticed that the flow structure around a body shape such as a rectangle with  $c/D$  of for example 7 shall involve the two shear layers at the trailing edge and another pair located at the leading edges which oscillate periodically impinging over the surface which complicates the flow structures interacting with the trailing edge phenomenon. The case of a body shape which

may incorporate more edges such as hexagon is consequently anticipated furthermore complicated.

Unlike the circular cylinder, a stationary rectangular prism may involve 3 different mechanisms of flow instabilities responsible for the different vortex structures (Naudascher & Wang, 1993) (Naudascher & Rockwell, Flow Induced Vibrations, 2005). The VIV of rectangular cylinder is associated with vortices of different sources which may or may not included Kármán vortices (Nakamura & Nakashima, 1986). These mechanisms shall be classified based on the  $c/D$  ratio and turbulence intensity of the upcoming flow (see Figure 2.5):

**I: LEVS, Leading Edge Vortex Shedding:** This is observed for low ratios from 0 up to 2 or 3 depending on the turbulence intensity. The formerfor higher for higher intensities. The separated shear layers do not reattach and interact with each other given rise to vortices that shed in a similar manner to that of a circular cylinder.

**II: ILEV, Impinging Leading Edge Vortex:** This is related to the vortices that have its origin in the instability of the impinging shear layer rolling up over the body surface. This flow instability is well known in jets and flows past cavities (Naudascher & Wang, 1993). The corresponding Strouhal number to the shedding of vortices is defined as:

$$St = \frac{f_s d}{U}$$

where  $f_s$  is the shedding frequency,  $d$  is the cavity dimension and  $U$  is the free stream wind speed. It is noted here that in contrast with the circular cylinder Kármán vortices, the nature of these vortices are related to a single shear layer instead of two.  $St$  is found constant a around a value of 0.6.

Naudascher (Naudascher & Rockwell, 2005) further précised  $St$  based on (Shirashi & Matsumoto, 1983) for the different modes in Figure 2.5:

$$St_n = (n + \epsilon) \frac{D}{c} \frac{U_c}{U}$$

where  $n$  is the mode and  $U_c$  is a convective wind speed at which the ILEVs may travel which as well as  $\epsilon$  depends on the particular flow conditions. Based on the above mentioned shedding frequency (0.6) the following critical wind speeds are proposed for the onset of the oscillation with the first modes (Shirashi & Matsumoto, 1983):

$$U_{CR} = \frac{1}{0.6} \frac{c}{D} \frac{1}{n}$$

for vertical motion and similarly for the torsional mode:

$$U_{CR} = \frac{1}{0.6} \frac{c}{D} \frac{2}{2n-1}$$

based on the arrival on the vortices from the leading edge to the trailing edge. It is noted that the convective speed is implicit in the latter expressions through the 0.6 coefficient.

The impinging shear layer instability is definitely demonstrated in the flow visualisations of

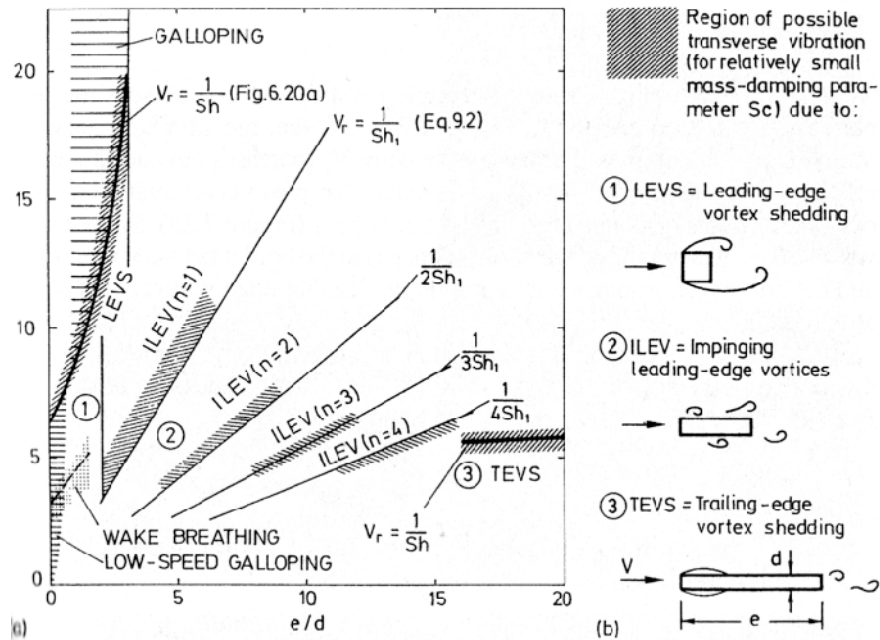


Figure 2. 6: Regimes and instabilities mechanisms classifications for rectangular prisms based on their  $c/D$  ratio, after (Naudascher & Rockwell, 2005).

a rectangular prism with and without a splitter plate on the leeward side (Naudascher & Wang, 1993). The vortex formation seems unaffected by the presence of the splitter plate confirming the distinct nature of these vortices compared to the Kármán street vortices. In fact, Matsumoto et al. found that not only the mechanism was unaffected but significantly amplified (Matsumoto, Shirashi, Shirato, Stoyanoff, & Yagi, 1993).

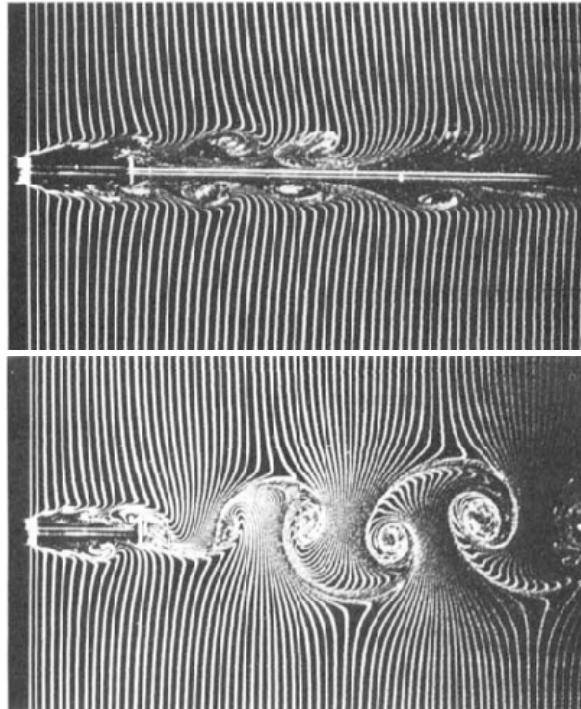


Figure 2. 7: Flow structure of ILEV present with and without a splitter plate installed in the near wake of an H cylinder. (Nakamura & Nakashima, 1986).

It was observed that the first mode ( $n=1$ ) of ILEV was observed no matter what Re numbers whereas the higher modes were not observed for high Re numbers. This attracted the attention of different studies which, in fact, detected such weaker modes by means of control mechanisms. The control was demonstrated with perturbing leading edge motion and sound fields (Naudascher & Wang, 1993). Similarly, the impinging shear layer instability vortices or ILEV were expected for  $c/D$  ranges from 2 to 8 whereas latter studies reviewed this range,  $2 < c/D < 16$ .

III TEVS, Trailing edge vortex shedding. This mechanism is based on the interaction of the corresponding two free shear layers. As  $c/D$  is increased over 7.6 the boundary layers approach a fully turbulent state near the trailing edge. Regular vortex shedding is observed for chord to thickness ratio above  $c/D > 16$ . It has been observed that this mechanism plays an important role in the formation of ILEV.

Particular effects of sound perturbations on impinging shear layer instabilities were studied in (Parker & Welsh, 1983). A more recent review is available in (Mills, Sheridan, & Hourigan, 2002). It is observed that applied perturbations have two significant effects on the ILEV formation: it phase locks the mechanism to the perturbation frequency on one hand and on the other it reduces the length scale moving the reattachment point upstream. Consequently, the shear layer curvature is increased and so is the strength of the vortex structures derived and the pressure coefficient. It is understood that the effect of cross perturbations triggering ILEV is the nature of the motion induced vortices described by Komatsu and Kobayashi (Komatsu & Kobayashi, 1980). Mills, Sheridan and Hourigan

observed that there are preferred perturbation frequencies ( $St_p$ ) based on  $c/D$  that give peak base pressure coefficients. They postulated a **vortex interaction mechanism** triggered by the velocity perturbations across the mean flow. It is suggested that certain perturbation frequencies would phase lock both shedding at the leading edge and trailing edge. Therefore, depending on the  $c/D$  ratio ILEV would interact with TEV leading to a much stronger base pressure coefficient (see Figure 2.5).

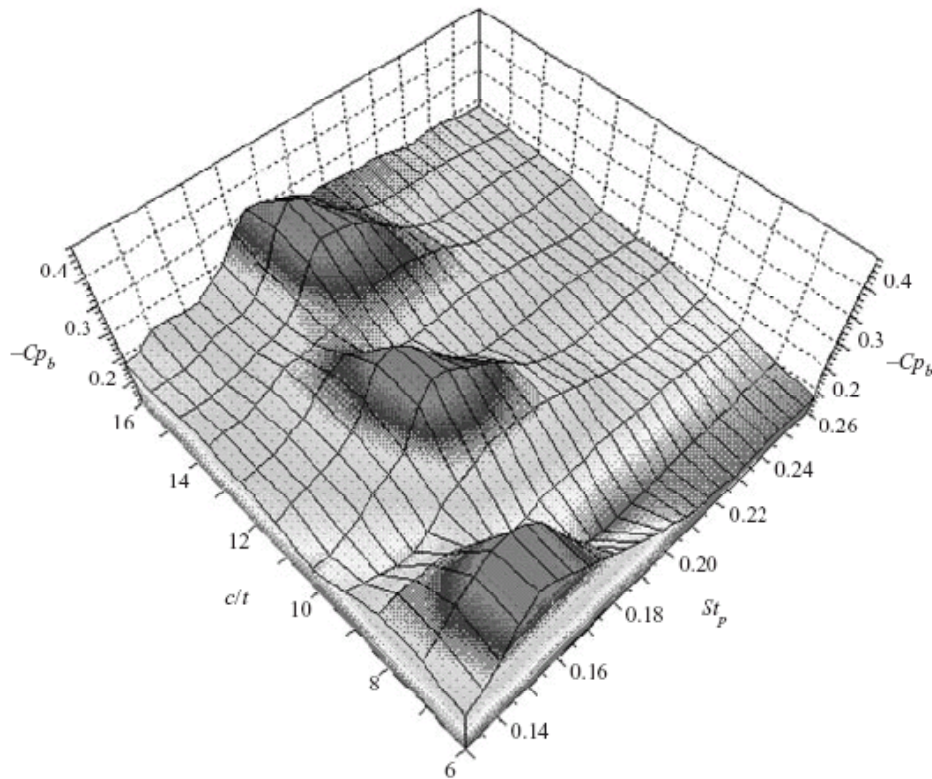


Figure 2. 8: Observed base pressure coefficient for different  $c/D$  ratios ( $c/t$  in the Figure) for different perturbation frequencies  $St_p$  (after, (Mills, Sheridan, & Hourigan, 2002)).

This hypothesis of LE and TE vortex interaction was further proved with the analysis of the flow field obtained for the  $c/D=7^{26}$  case presented in Figure 2.6 below (Mills, Sheridan, & Hourigan, 2003), (Mills, Sheridan, & Hourigan, 2002). The vorticity contours in this Figure clearly show a vortex being convected from the upper surface leading edge reaching the trailing edge and coupling there with a vortex that is being shed from the trailing edge. Resulting from this interaction much greater base pressures are observed reaching peak values of more than twice the pressure without the triggering perturbation. This interaction produces peak pressures only for certain ranges of chord over thickness ratio which are  $4.0D$  apart as can be shown in Figure 2.5. This is consistent with measured spacing between ILEV of  $3.8D$  in previous work (Naudascher & Rockwell, 2005).

<sup>26</sup> It is noted here that such chord to thickness ratio corresponds for example to the Storebaelt Bridge Deck cross section.

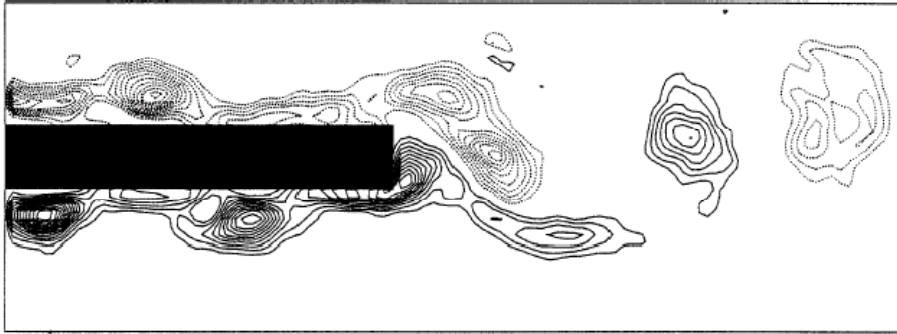


Figure 2. 9: Vorticity contours obtained by means of PIV for a rectangular prism of a chord to thickness ratio of 7 (Mills, Sheridan, & Hourigan, Response of base suction and vortex shedding from rectangular prisms to transverse forcing, 2002).

Note that  $c/D$  ratios in the range of the peaks in Figure 2.5 are rather common in modern bridge decks. As an example, the Storebaelt Bridge presents a  $c/D$  of 7.05.

There are two flow conditions parameters other than the referred  $Re$  number that significantly affect the previously described mechanisms: the angle of attack and the turbulence intensity.

Minor deviations in the angle of attack ( $4^\circ$ - $16^\circ$ ) of the rectangular cylinder cause variations in the  $St$  number defined in Eq. . The modified  $St'$  Strouhal number can be similarly defined as (Naudascher & Rockwell, 2005),

$$St' = 0.6 \frac{D'}{c} \frac{1}{\cos \alpha}$$

where  $\alpha$  is the angle of attack and  $D'$  is defined as,

$$D' = c \sin \alpha + D \cos \alpha$$

The effect of turbulence intensity and length scale is addressed in (Saathoff & Melbourne, 1997). It is found that an increase in either the turbulence intensity or the integral length scale increases the magnitude of the pressure fluctuations. The increase in turbulence intensity causes a decrease in the reattaching length and as a consequence of that and similarly to the effect of cross velocity perturbation an increase in the vortex strength. The larger length scale implies higher spanwise correlation of the vortices, which again increases the pressure fluctuation.

The effect of turbulence length scale on the nature of motion induced vortices like the derivated from impinging shear layer instability is worth of consideration in bridge aerodynamics. The test of section models in wind tunnels (presented in detail in Chapter 3), is performed systematically in the design phases of modern bridges. Scales of 1:40-1:100 which allow to properly model every detail are normally used. It is noted here that the proper modeling of turbulent lengths at that scales is not possible if not complicated in normal test section sizes and arrangement. Consequently and among other matters one should examine carefully results obtained with this technique which may involve impinging shear layer instabilities.

There are previous attempts of classifying cross sections with respect to their critical wind

Figure 2. 10:Critical wind speed observed for rectangular cylinders (from (Komatsu & Kobayashi, 1980)).

speeds other than they presented in Figure 2.4 (Naudascher & Wang, 1993)based on the above mentioned motion induced vortices (ILEV) Komatsu and Kobayashi were among the first (Komatsu & Kobayashi, 1980). Their model proposed the different modes in Figure 2.7 attending at the measured pressure traces and their phases with respect to the response. A criteria based on the cases where the total work done by the fluid onto the prisms being positive is presented as the lines in Figure 2.7. It is observed that the modes are similar to those in Figure 2. 4 though the actual coefficients differ from those.

Mode (n)	(Shirashi & Matsumoto, 1983)	(Komatsu & Kobayashi, 1980)
1	$V_{CR} = 1.67 \frac{B}{D}$	$V_{CR} = 2.4 \frac{B}{D} + 0.5$
2	$V_{CR} = 0.83 \frac{B}{D}$	$V_{CR} = 1.2 \frac{B}{D} + 0.5$

Table 2- 1: Comparison of linear relationships for critical wind speeds based on chord to thickness ratio.



Another analysis (Shirashi & Matsumoto, 1983) proposed a classification into 3 groups attending to the onset critical wind speed. Such classification, presented in Figure 2.8 is similar in nature to Naudascher's LEVS, ILEV and TEVS in Figure 2.4. The first and third group presents peak response at  $1/St$ , higher than the onset windspeed. The second group presents onset wind speeds related to the arrival of ILEV to the trailing edge (Eq.). Naudascher's review is all consistent with this classification. It is noted that this classification is very similar to (Naudascher & Rockwell, Flow Induced Vibrations, 2005) and consistent with (Komatsu & Kobayashi, 1980). However, the latter present somewhat different linear relationships for the Group 2 or ILEV (see table below). Furthermore, there is no reference to TEVS regime or Group 3 in (Komatsu & Kobayashi, 1980).

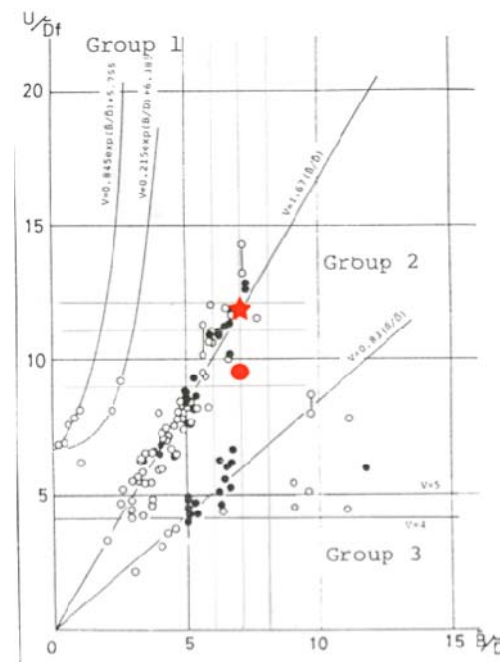


Figure 2. 11: Critical wind speed based on the slenderness or chord to thickness ratio for a variety of shapes (Shirashi N. a., 1983).

Based on the study of the local phase of pressure fluctuations at particular locations the dissipating or augmenting (damping or force) of the in phase component can be estimated. Miyata et al. (Miyata, Miyazaki, & Yamada, 1983) observed that for heaving VIV of bridge girders, the forcing (positive out phase component) was concentrated on the upper flange of the trailing edge whereas the damping was located at leading edge. The moment responsible for the torsional VIV was concentrated mainly at the trailing edge with little damping generated at the LE compared to the heaving response.

A number of parameters, referred to as Schewe parameters in section 2.2.2, are known to affect the vortex induced vibration of circular cylinder. The VIV response of rectangular and other prisms include particular extra parameters such as edge characteristics sharpness, alienation, planimetry ...



The circular cylinder VIV involves different modes of vortex shedding in the near wake as the driving mechanism. The mechanisms of VIV in bodies with a long after body such like rectangular prisms or bridge decks in general may involve several vortex-body interactions of different nature.

## 2.3 Analytical models

Considerable effort has been made to mathematically model the response of bluff bodies induced by vortex interaction. Most of the models that have been developed in the past are based in the cylinder case starting with the early studies: (Bishop & Hassan, 1963), (Hartlen R. T., 1970), (Parkinson G. , 1974) and (Blevins & Iwan, 1974). The most relevant outcomes are summarized here.

It has been pointed out in many of these references that current available models still lack from physical base of some the model parameters (Holmes 1977, Vickery).

The models can be basically divided in two types (Billah, 1989):

- Single degree of freedom models
- Wake body oscillator models

### 2.3.1 Single oscillator models

These models propose an equation of motion where the forcing part on the right hand side normally have 3 components:

- one proportional to the aerodynamic coefficient corresponding to the mode subjected to modeling ( $C_L$ ) which is normally referred to as *stationary* or assign to vortex shedding
- the other two normally motion induced:
  - o one proportional to the modal displacement
  - o the other proportional to the displacement velocity

There are basically two types of single degree of freedom models. The first are based on the traditional and practical concept of aerodynamic damping, also referred to as negative damping models. The second focus on modeling the actual force coefficient.

The displacement, of a body undergoing synchronized motion can be written as (i.e. vertical displacement)

$$y_r = y_{r0} \sin(2\pi f_{com} t)$$

where  $y_r$  is the reduced vertical displacement, defined as the ratio of the absolute measure of the displacement,  $y$ , and the thickness of the body,  $D$ ,

$$y_r = \frac{y}{D}$$

$y_{r0}$  is the amplitude (peak to peak) of the reduced displacement and  $f_{com}$  is the common frequency at which the excitation forces matches the natural lift frequency,  $f_l$  (Sarpkaya T. A., 2004). the equation of motion for the single degree of freedom (sdof) can be written as,

$$M\ddot{y}_r + c\dot{y}_r + Ky_r = F_L$$

where  $M$  is the generalized mass corresponding to the “ $y$ ”, lift or vertical mode,  $c$  is the viscous damping coefficient,  $K$  is the generalized stiffness or elastic coefficient and  $F_L$  is the lift force.

An example of linear oscillator of this type was proposed as a generalization of the well-know Scanlan’s flutter model of aerodynamic derivatives (Ehsan, 1990). The fluctuating force is presented as a function of time, the response and its time derivatives:

$$F_L = F_L(\ddot{y}_r, \dot{y}_r, y, U, t)$$

in particular the proposed equation of motion is of the form of,

$$M\ddot{y}_r + c\dot{y}_r + Ky_r = \frac{1}{2}\rho U^2 D \left[ Y_1\left(\frac{f_s D}{2\pi U}\right) \left(1 - \varepsilon \frac{y^2}{D^2}\right) \frac{\dot{y}}{U} + Y_2\left(\frac{f_s D}{2\pi U}\right) \frac{y}{D} + \frac{1}{2} C_L \left(\frac{f_s D}{U}\right) \sin(2\pi t + \phi) \right]$$

where  $Y_{1,2}\left(\frac{f_s D}{2\pi U}\right)$  are functions of a reduced shedding frequency or similarly  $2\pi St$ ,  $C_L$  is

the lift aerodynamic coefficient,  $\phi$  is the phase angle by which the force leads the response (just like the horse leads the cart, Sarpkaya dixit (Sarpkaya T. A., 2004)) and  $\varepsilon$  is a parameter that controls the nonlinear contribution of the aerodynamic damping term. It is noted that the force is made up of 3 terms. A term that is proportional to the response velocity and therefore named “aerodynamic damping” (in phase with the velocity of motion), a term that is proportional to the actual response “aerodynamic stiffness” (in phase with the displacement) and the actual aerodynamic force independent of the response. The  $\varepsilon$  parameter which was not present in an earlier (1981) version of the model ensures that the response is self limiting.

This expression has the form of the well know Van derPol oscillator (Van der Pol, 1920) except for the fact the fact  $Y_{1,2}$  are functions of the reduced velocity. A solution for the response amplitude and phase is proposed based on the model parameters  $Y_1$  and  $\varepsilon$ . These are obtained by parameter identification of a simple decay to resonance wind tunnel test. In this test a section model (see Chapter 3) undergoing VIV is forced to an amplitude over the undergoing fairly constant synchronized VIV. The model parameters can be estimated from the observation of the amplitude decay rate. The component due to

vortex shedding ( $\frac{1}{2}C_L(\frac{f_s D}{U})\sin(2\pi t + \phi)$ ) is neglected in the derivation of the solution. This was supported by experimental data in which this component proved to be very small compared to the motion induced components for large amplitude oscillations. The proposed model acknowledges the sensitivity to the model parameter estimation and flow interaction complexity.

Another model that has been widely use in the prediction of chimneys response and is the base of many standards is the one by Vickery or. Vickery's model incorporates spectral definition of wind forces narrow band and broad band in the pioneer line traced by Davenport in the early 60's (Davenport A. , 1961). This formulation conveniently incorporates the prediction of the buffeting response of cylindrical (Vickery & Basu, 1983). The equations are built in a random vibration framework similar to the one proposed by Davenport and based on a form of the equation of motion of the VIV system. The VIV model equation is formulated based on a similar Van derPol oscillator concept like the one just described. The forcing is defined as the sum of two terms, a so called "stationary" term due to vortex shedding and "motion induced term" defined as,

$$F_{\text{stationary}} = \frac{1}{2}\rho U^2 D C_L(t)$$

$$F_{\text{motion induced}}(t) = h_a y + k_a \dot{y}$$

where  $h_a$  and  $k_a$  are the corresponding contribution coefficients. The motion induced term is, like the previous model, a sum of an aerodynamic damping and stiffness. The aerodynamic stiffness term is not studied in great detail since its magnitude is neglectable compared to the structural stiffness. A non-linear aerodynamic damping based on previous results ensures the self limiting nature,

$$F_{\text{aero-damping}} = k'_a (\dot{y} - G\dot{y}^3)$$

where  $G$  is a constant. Such expression, originally proposed by Marris (Marris, 1964) is based on the well known Magnus effect and has been largely debated (Billah, 1989). The model was adapted for square prisms in boundary layer flows (Vickery & Steckley, 1993). The modified model makes use of directly measured aerodynamic damping values in through wind tunnel experiments.

It is remarked here that the aerodynamic damping is a concept that does not attend to a direct physical ground. Predictive models based on the aerodynamic damping like the one described above have been successfully and extensively used by practitioner engineers. It has served as a "black box" housing the multiple physical mechanisms of different nature that are involved in the VIV of bluff bodies. Further development of existing models would require a deeper understanding on the different mechanisms behind the "aerodynamic damping"; quoting Vickery,

"the negative damping model is a very useful predictor although it is not particularly appealing from a physical viewpoint" (Vickery & Steckley, 1993)

Similar models have been proposed based on experimentally obtained aerodynamic coefficients. Among the models of force coefficient, the method by Sarkaya 1978, proposes a force coefficient of the form of,

$$C_L(t) = C_{mh} \cdot \sin \Omega t - C_{dh} \cdot \cos \Omega t$$

where  $C_{mh}$  and  $C_{dh}$  are obtained from force oscillation tests for different reduced amplitudes. The resulting equation of motion is,

$$M \cdot \ddot{y}_r + c \cdot \dot{y}_r + K \cdot y_r = a \Omega^2 (C_{mh} \sin \Omega t - C_{dh} \cos \Omega t)$$

where  $a$  is a constant and  $\Omega$  is the ratio of the shedding to the natural frequency.

It is observed that the interaction mechanisms are captured via the forced oscillation experiments in order to obtain the coefficients. It is therefore expected that the coefficients will not carry across to other bluff body shapes and that the framework can be questionable if other mechanisms are involved.

## 2.3.2 Coupled oscillator models

These models consist of two oscillators compared to the single body motion one of the previous framework. The first being the body motion and the second normally and oscillator of the aerodynamic coefficient.

The model by Hartlen and Currie (Hartlen & Currie, 1970) are among the first of this type. A wake-oscillator model was built based on previous experimental results (Bishop & Hassan, 1963). The model successfully reproduces the inherent self-limiting and self-excited nature of the VIV of a cylinder. The model consist of two coupled oscillators,

$$M \ddot{y} + c \dot{y} + Ky = \frac{1}{2} \rho U^2 D C_L$$

$$\ddot{C}_L + (\text{damping term}) + (2\pi f_s)^2 C_L = (\text{forcing term})$$

both are reduced and simplified to the following system of two ordinary differential equations that constitute the model,

$$y_r'' + 2\zeta y_r' + y_r = a \Omega^2 C_L$$

$$C_L'' - \alpha \Omega C_L' + \frac{\gamma}{\Omega} (C_L')^3 + \Omega^2 C_L = b y_r'$$

where ' denotes a derivation with respect to a reduced time and  $\alpha, \gamma, a$  and  $b$  are model parameters;  $a$  is defined as:

$$a = \frac{\rho D^2}{8\pi^2 St^2 M}$$

and the ratio  $\alpha/\gamma$  is directly related to the lift coefficient amplitude, obtained experimentally;  $b$  is set to fit the experimental evidence. If the right hand side of the  $C_L$

oscillator is set 0 implies the cylinder is rigidly mounted ( $y'=0$ ). It is noted that the oscillator frequency in that configuration would be  $f_s$ ,

$$f_s = \frac{St \cdot U}{D}$$

which is in good agreement with the Strouhal relation.

The model gave new and promising perspective to the analytical formulation of VIV, though it failed to predict key features of the interaction such as the non-linear nature or the phase jump.

A similar coupled oscillator model was developed by Iwan and Blevins with a different approach (Blevins & Iwan, 1974). An attempt was made to have the model parameters selected based on approximate and simplified physical analysis of the flow structure in the near wake<sup>27</sup>. The autonomous wake oscillator is a form of the momentum equation (y-component) from which the net force on the cylinder is also derived ( $F_i$ ). A simplified model of flow structure in the near wake control volume allows for the computation of the different terms in the momentum balance. It is noted that the fluid force on the cylinder is part of both oscillators and acts as coupler. This is simply derived accounting for the relative motion of the cylinder and the vertical component of the flow in the control volume on one hand and of the relative angle on the other (two last terms of the wake oscillator eq below).

$$\ddot{z} + K' \frac{u_{co}}{D} 2\pi f_s z = (a_1' - a_4') \frac{U}{D} \dot{z} - a_2' \frac{\dot{z}^3}{UD} + a_3' \ddot{y} + a_4' \frac{U}{D} \dot{y}$$

$$\ddot{y} + 2\zeta \cdot 2\pi f_n \dot{y} + (2\pi f_n)^2 y = a_3'' \ddot{z} + a_4'' \dot{z} \frac{U}{D}$$

where  $a_{1,2,3,4}$  and  $K$  are the different model parameters. It has been argued that this model based on the actual analysis of the near wake flow structure justifies the wake oscillator nature though this is still a controversial (see for example (Sarpkaya T. , 1979) or (Bearman P. , 1984) among others).

---

<sup>27</sup> Special thanks are given here to Dr. Blevins for his encouragement and for providing the doctoral Dissertation in which the models is described

# Chapter 3

## Methodology

The methodology followed throughout this work is presented and framed in this Chapter. The nature of the method described herein has been primarily experimental. However certain numerical and analytical procedures were used as well. These are described with the corresponding results in the body of Chapters 4 and 5.

As a result of the experimental set-up required for the study, a new testing facility was designed and built: the boundary layer wind tunnel of the Andalusia Environment Centre (CEAMA). Different experiments were carried in it and in both Wind Tunnel I and II at the Boundary Layer Wind Tunnel Laboratory (BLWTL) at The University of Western Ontario (Davenport A. , Isyumov, King, Novak, Surry, & Vickery, 1985). The new wind tunnel at CEAMA was successfully benchmarked against results from BLWTL wind tunnels.

The experimental program involved both dynamic and static testing of section models of the Storebøelt Bridge in Denmark and the 3<sup>rd</sup> Millennium Bridge in Spain. Resulting from this work, an innovative dynamic and static rig was designed for the wind tunnel at CEAMA. Preliminary tests were performed initially to verify these experimental set-ups. Results checked well against available results from the design stages of the Storebøelt bridge (DMI and SINTEF, 1993), (King, Larose, & Davenport, A Study of Wind Effects for The Storebaelt Bridge Tender Design, 1990).

This work focuses on modern bridges made of efficient materials with complex shapes and details. Hence the design of section models of these relatively light bridges becomes challenging.

Details of these model designs, the experimental facilities, test rig set-ups, and instrumentation involved in this study are presented here.

### 3.1 CEAMA New Boundary Layer Wind Tunnel (Laboratory?)

### 3.1.1 Framework and scope

Despite of the escalating development of computational fluid dynamics (CFD), wind tunnels are still essential in wind engineering research. In fact, these facilities are sometimes the only capable tool given the complex nature of the three-dimensional, highly turbulent flows around moving complex shapes of some building and bridges.

Though common from the very early times in the aviation industry, wind tunnels only became used regularly in Civil Engineering in the second half of the last century. These wind tunnels differ, however, from those used in the aeronautical or automotive industry in their specialization in simulating *atmospheric boundary layer* (ABL) flows. In contrast, aeronautical wind tunnels focus on the simulation of highly uniform low turbulence flows. Consequently, their design is significantly different.

The specific study of wind loading of structures gathered more interest with the development of less stiff and lighter structures in the 19<sup>th</sup> and 20<sup>th</sup> century. These studies sometimes even involved some early stages testing of models in uniform laminar flow in aeronautical wind tunnels. Major Failures in Civil Engineering due to wind effects such as the popular collapse of the Tacoma Narrows Bridge (1940) in the U.S. or the Ferrybridge Cooling Towers in the U.K. (1965) among many others, transformed the way wind loading had been dealt with in the design of Architectural and Civil Engineering infrastructure (Terrés-Nicoli J. M., 2002), (King J. P., 2003). The first example is a consequence of the lack of knowledge of the dynamic nature of the wind-structure interaction. The latter, for which uniform flow was considered, derives from the poor understanding and significance of the spatial structure of the wind (the atmospheric boundary layer).

The need for the detailed study of these structures in turbulent boundary layer flows was then found decisive for the design. In this regard the work done around the 50s such as the valuable contributions from the Technical University of Denmark (Jensen & Niels, 1963) followed by the pioneering work from Davenport in Canada (Davenport A. , 1961) and (Davenport & Isyumov, 1967), or Cermark in the US (Cermark, 1971) set the basics of the current methodologies at boundary layer wind tunnels. The 1958 paper by Jensen was significantly clear referring to the previous work done in the field (Jensen, 1958):

*“These investigations, however, are to some extent misleading, because the test procedure, especially the model law, has been wrong. It may seem strange that within a vast research field incorrect model-laws have been applied, but the explanation is both simple and not very flattering: the model tests have practically never been checked by full-scale tests in nature.*

*The natural wind is turbulent, and the phenomena dealt with take place in the boundary layer of the wind, and as should be emphasized, are highly dependant on the nature of this boundary layer.”*

While there are a number of aeronautical wind tunnels in Spain, the **CEAMA Boundary Layer Wind Tunnel** is the first of this type. A new wind engineering laboratory was created around both wind tunnels I and II. The later (CEAMA WTII) is a 1:5 scale replica of the first that was initially built to make final adjustments in the design of key elements of wind tunnel I and to optimize the use of the available space. Made entirely transparent, it is now available for science shows and engineering students.

## 3.1.2 Wind Tunnel Design

### 3.1.2.1 Design requirements

The facility design program targeted a wind tunnel for the basement level of the CEAMA building in Granada, Spain. Fig 3.1 shows the plan and side views of the space available. The overall dimensions of the room are  $34 \cdot 11.5 \cdot 4.75$  m (length·width·height). The wind tunnel design aimed for the model testing in the field of civil and environmental engineering. In particular, in order of relevance for the design project, the anticipated use of the wind tunnel is:

- a. Model test of section models of slender line-like structures such like: bridges, towers, cables, masts. This design target is framed within the scope of the present research work. Section model testing normally implies the test of models in both stationary and dynamic set-ups. Consequently, the wind tunnel has to be equipped the corresponding two test rigs (see Section 3 for more details). The target scales range from 1:50-1:80 for modern mid and long span bridges. The motivation for these studies is the determination of structural loads in the form of pseudo static terms. These account for the dynamic component of the response and together with the structure's modal analysis, let the structural engineer compute the overall response of the bridge. Though section model tests can't account for the effect of other structural members such as pylons, arches or cables they provide good estimates of the overall aerodynamics that govern the response in cost and time competitive manner. Furthermore, through this methodology it is possible to identify aeroelastic effects at early stages of the design. A collection of wind tunnels used for section model testing of bridges is listed in (Ito, 1992).
- b. Model test of buildings in simulated atmospheric boundary layer (ABL). The target scales for both balance and pressure model tests are 1:300 - 1:500. The motivation for these studies is normally the definition of the structural wind loads and determination of corresponding response. In these tests, attention is paid to the study of Ultimate Limit States (ULS) and Serviceability Limit States (SLS). The first involves the determination of pseudo-static loads per floor that account for the dynamic component and in a way that can be use by the structural engineers. Other typical studies involve the measurement of the pressure field on the façade. (ASCE, 1999), (AG Davenport Wind Engineering Group, 2007). The study of SLS involves the measurement of wind speeds in the plaza around the building and the determination of acceleration levels in the top floors.
- c. Wind field studies. Such normally involve the test of physical models of entire regions or limited areas with complex topography. Reccomended scales for these studies range minimum of 1:3000 - 1:4000 (ASCE, 1999), (Plate, Engineering Meteorology: Fundamentals of methodology and their applications to problema in environmental and civil engineering, 1982).The motivation derives from urban planning programs, wind energy sitting studies or environmental analysis.



- d. With a lower weight in the design program it is intended to pursue the capability of model studies of aerodynamic performance of ambient anemometers, sails and descent skiers.

In order to achieve the performance needed to comply with the facility application just set the following required specifications are established:

1. Wind tunnel type (Barlow, Rae, & Pope, 1999). Briefly, wind tunnels can be classified by
  - 1.1. Circuit: open or closed (single or multiple returns)
  - 1.2. Test section design, size and shape: open or closed, vertical or horizontal, long or short, rectangular square or rounded.
  - 1.3. Speed range: subsonic, sonic, transonic and ultrasonic
  - 1.4. Power system: suction or blower, multiple or single fan units, direct or transmission drive, centrifugal or axial
  - 1.5. Application for which is designed: aeronautical, climatic, automotive, aero-acoustic ...

The required performance for the CEAMA wind tunnel could be achieved with any of the above types. As for what respects to the speed range, a low speed wind tunnel is adequate (25 - 50 m/s). Though velocity scales can be used satisfactory in many cases it is sometimes desired more dynamic pressure ( $q = \frac{1}{2}\rho U^2$ ) in the flow. This can result from the resolution demanded in a particular instrument, to excite more response in an aeroelastic test or simply to raise the Reynolds number of the simulation.

2. Test section dimensions.
  - 2.1. Width: limited by the final available power for the required operational speed, a minimum dimension will be required to achieve proper aspect ratio for section model testing of bridges. A length of the order of 5 times ( $A = 5$ )<sup>28</sup> is understood to sufficiently accommodate for the span-wise scales of the turbulence required for the 2-dimensional nature of the simulation (King J. P., 2003). Given the desired length scales for these models mentioned before, this would lead to a required width of around 2m or more for modern bridges. This would also be sufficient for models of building and their surroundings (500m radius) at the scale mentioned before of around 1:500.
  - 2.2. Height: also limited by power available to the minimum required for the design requirement b, and c and d where possible. It is known complicated to reproduce the characteristics of the turbulence in the ABL at scales larger than say 1:300. It is reasonable not to expect building heights higher than 300m to be built in the near future in Europe. In this context a wind tunnel height of at least 1.5 m is required.

---

<sup>28</sup> The aspect ratio ( $A$ ) is defined as the length over the chord of the model

2.3. Length: this dimension is governed by the required scale of the simulated ABL, around 1:400. It is known that approximately 10-11 times the simulated boundary layer thickness is required to properly simulate the ABL with the different available techniques (Schlichting & Gersten, 2001), (Plate, Engineering Meteorology: Fundamentals of methodology and their applications to problems in environmental and civil engineering, 1982). At the above-mentioned scale, this leads to a required length of approximately 10-15m, assuming that the boundary layer is developed with passive devices<sup>29</sup>.

The above-mentioned design requirements are constrained by the funding<sup>30</sup> and space available. The balance between both led to the engineering solution presented in the following section.

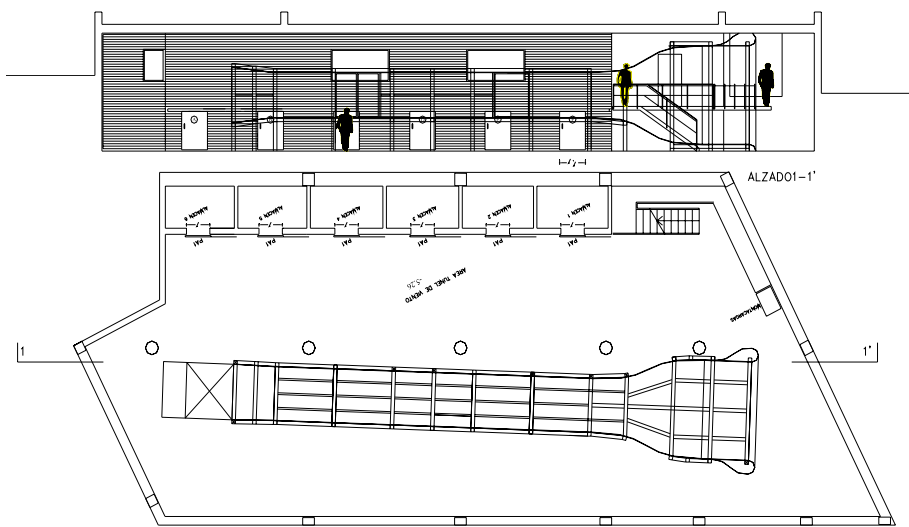


Figure 3.1 Plan and side view of the new Boundary Layer Wind Tunnel at CEAMA, University of Granada

### 3.1.2.2 Wind Tunnel Specifications

The description of the whole facility, including the design of the dynamic and static rigs for section model testing is given here. Complete information on the wind tunnel design can be found in (Terrés-Nicoli & Losada Rodríguez, 2002) and (Terrés-Nicoli J. M., 1999). More details of the dynamic and static rig for section models of bridges can be found in (Terrés-Nicoli J. , Design of Section Model Bridge Test Rig, 2006).

<sup>29</sup> Rather than active methods by means of matrices of jets calibrated with different flow rate and such like the one at the University of Toronto in Canada (Simiu, E., & Scanlan, R., 1996)

<sup>30</sup> The CEAMA Boundary Layer Wind Tunnel and its basic operational instrumentation was funded by the European Union FEDER program, Application 422.D.663.02 -Scientific Equipment

The wind tunnel type was decided according to the above mentioned design requirements and arguments related to:

- Space available and its aerodynamic, thermal, lighting and acoustic conditioning
- Construction, maintenance and operation cost
- Flexibility, adaptability, versatility and user-friendliness of the design

The selection of the circuit type: open or closed is not straight forward (Barlow, Rae, & Pope, 1999). It is still topic of expert discussion in many wind tunnel designs. The final design decided was an open circuit, closed test section, suction, single axial fan, direct drive. Different changes to the rooms' architecture where required, an example being the columns' location.

In this particular design the open circuit proved to be significantly more cost-efficient in what respects to the construction and only slightly less in operation cost given the relatively low power. That is not the case in many aeronautical and multi-purpose wind tunnels. A wide angle diffuser is required for a blower design wind tunnel. Therefore, the turbomachine operating in suction rather than a blower was less demanding in overall length<sup>31</sup> even though it was less energy and cost efficient. Given the space limitations it was estimated that an open test section was not acceptable due to flow quality requirements.

A single large custom made axial fan was compared to a matrix of four smaller industrial ones. The single fan, motor and drive solution though less economic proved to be more efficient in terms of flow quality, energy, maintenance and operation.

Following the required length of the test section justified in the previous section, the total length available for all the other components is of approximately 34-15=19m. This space must be sufficient to allocate the inlet, settling chamber, and contraction upstream of the test section and the diffuser-adapter, turbomachine and diffuser downstream of it. Furthermore a certain separation is required upstream of the inlet and downstream of the discharge in order to adjust the corresponding head losses to an optimum value. The length of these components will result from their particular design requirements and more importantly, the test section power, which can be defined as:

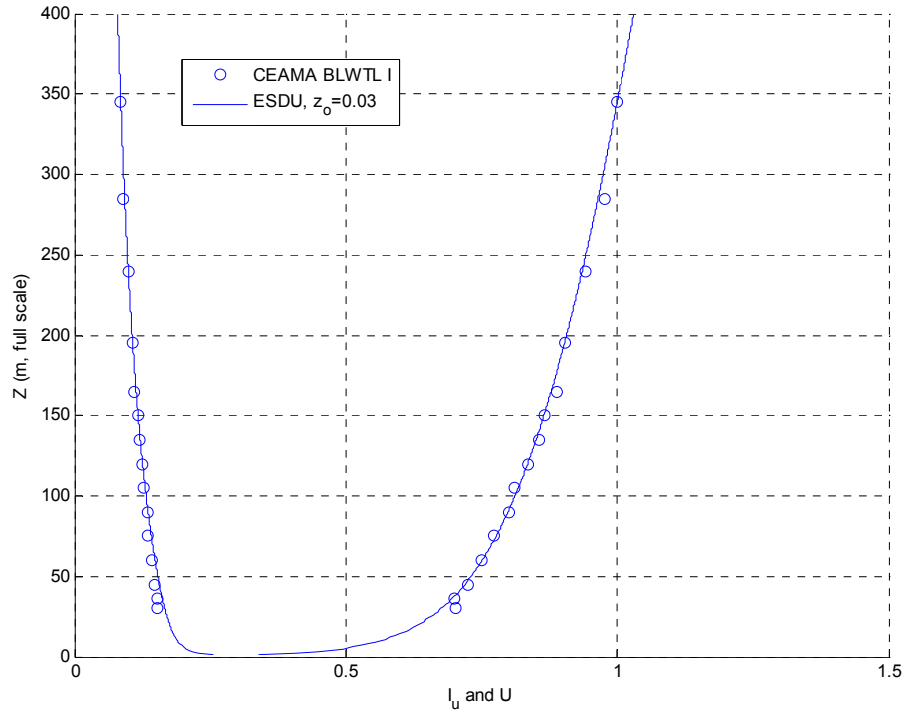
$$P_{ts} = \frac{1}{2} \rho U_{ts}^3 \cdot W \cdot H$$

where  $U_{ts}$  is the mean wind speed at the test section,  $W$ , the width and  $H$  the height.  $P_{ts}$  is useful as a design parameter of such components since it combines the value of the cross sectional ( $W \cdot H$ ) area with the air velocity ( $U_{ts}$ ) and the magnitude of the forces involved  $\frac{1}{2} \rho U_{ts}^3$ . It is also a measure of the energy per unit time that flows through the particular cross section of the corresponding component (in the present case the test section). From

---

<sup>31</sup> The overall length (34m) was the strongest space limitation. A blowing design for the present application would require the use of a wide-angle diffuser upstream of the settling chamber. The length of which would vary depending on the design around 2-3 m, which wasn't acceptable for the present design.

this jet power and each component design parameters, the reasoning leading to the final configuration of each is given below.



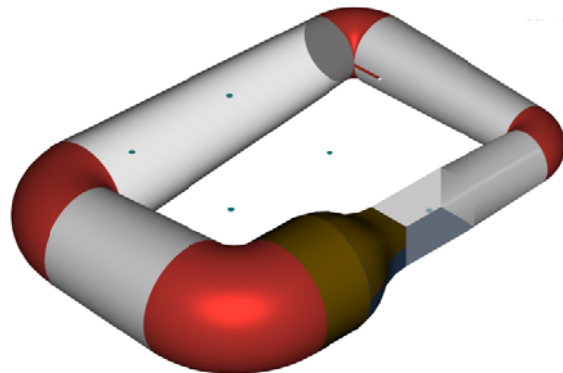
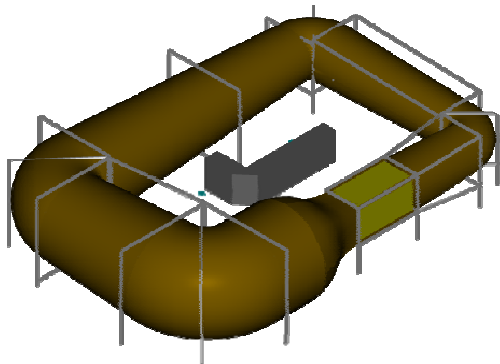
### 3.1.2.2.1 Test Section

Resulting from the design study and final adjustments (Terrés-Nicoli & Losada Rodríguez, 2002), the test section dimensions are,  $W=2.15$  m  $H=1.8$  m and a length of  $L=14.20$  m. This length is sufficient for simulating atmospheric boundary layer at scales of around 1:400, minimum (Counihan, 1967), (Plate, 1982), (Hunt & Fernholtz, 1975), (Irwin, 1981). A sample of simulated ABL following the methodology described in above mentioned references is presented in Figure 3.2. (show details of simulating components and picture of wind tunnel section?). The BL is simulated by using a combination of spires at the test section entrance and roughness elements along the test section floor. The first generate turbulent structures with decreasing scale with height. The roughness elements provide the necessary shear to properly decelerate the mean flow. Sometimes a third element, a barrier, is used at the entrance to enforce the proper mix of the flow structures generated by the roughness elements and spires. All these devices cause a somewhat considerable head loss along the test section which depends on the scale and type of targeted ABL. Such loss implies that a horizontal pressure gradient will be created. This is sometimes referred to as horizontal buoyancy. A slight test section expansion was therefore planned to compensate the loss in static pressure by decreasing the velocity or dynamic pressure,  $\frac{1}{2}\rho U^2$ . Such expansion is achieved by progressively increasing the roof height up

to a total 1.93m at the exit of the test section. The total estimated head loss in such operating conditions is: , including losses due to friction in walls and roof (0.13 for when operating empty). Finer adjustments based on the measure of the static pressure along the wind tunnel are however expected depending on operating wind tunnel conditions, i.e. type of simulated ABL. A fully automated height adjustable roof along the test section is proposed for further development. This system would be based on project specific pressure gradient measurements and based on this data the height of the test section along is adjusted. Such system would allow for gradient corrections at the end of the test section area where the building models and the surroundings are placed inducing significant pressure gradients.

The test section is planned with two differentiated test areas. One, 1.200m downstream of the test section inlet for the test of models in uniform flow such as section models of bridges, towers, cables and such. The two 2.500m long, PIV (Particle Image Velocimetry) suited, glass windows that enclose the testing area are designed with access slots that facilitate the installation of the necessary rigs, outside of the wind tunnel.

A second testing area, right upstream of the fan protection meshes and enclosed by solid 2.500 m long glass windows is planned for the test of models in boundary layer flow.



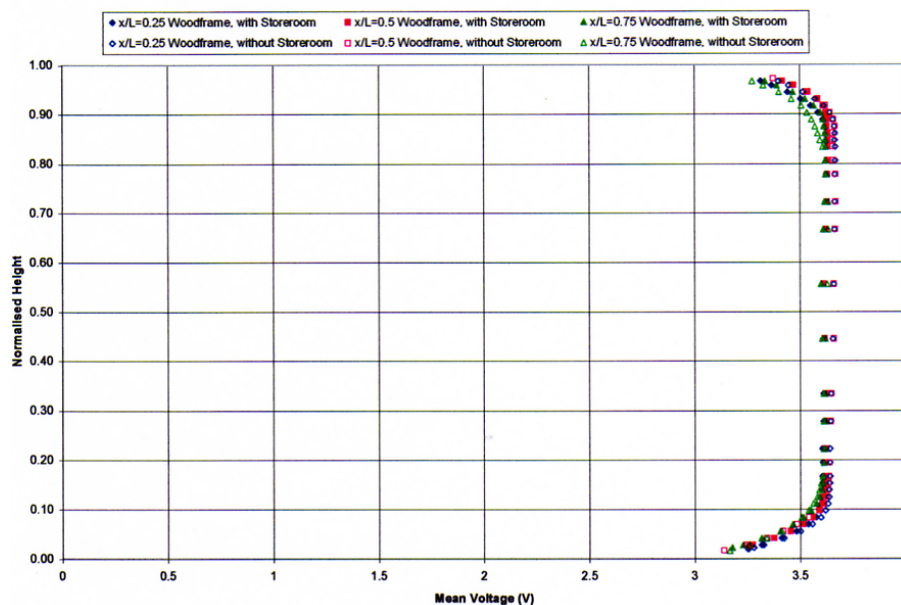
The test section interior is painted in flat black color to make it more suitable for flow visualization or laser light based measurements such as PIV or PTV (Particle Image Velocimetry or Particle Tracking Velocimetry).

Due to the major net pressure acting on the windows, given the significant pressure rise (up to 1KPa) the vibration of the glass was monitored with an accelerometer located at the center. The frequency and amplitude of such acceleration allowed to check the magnitude of the stress in the glass and that the boundary condition was actually performing as fully clamped at the four sides. The vertical connection was modified consequently (give peak Eq.).

The heat coming from the test section lamps can cause secondary convective air circulation at low windspeeds. Dissipative flat covers were used to minimized this effect. A LED illuminating system is proposed for further development.



The final wind tunnel design was slightly rotated with respect to the room and a lane of 600 mm diameter columns which position was modified to alleviate some of the architectural constraints (columns, walls, access and roof). Given these constraints, the final position was based on tests of a 1:5 scale model of the wind tunnel and the surrounding walls and roof. **Figure 3.5** shows a view of the acrylic wind tunnel (CEAMA Wind Tunnel II, CEAMA WTII). The measured profiles proved the location to be satisfactory (**Figure 3.6**).



**Figure 3.2** shows a 3D model of early-stage tentative design of a closed circuit option (Terrés-Nicoli J. M., 1999). The location changed afterwards. The final design of the CEAMA wind tunnel is presented in **Figure 3.1**. **Figures 3.3 and 3.4** show different views of a 3D representation of the final design for the CEAMA wind tunnel.

### 3.1.2.2.2 Contraction

The flow conditioning by means of honeycombs and screens requires a significant amount of energy loss. Therefore, given that losses are proportional to  $U^2$ , flow conditioning is performed at a much larger section. A contraction is hence needed to convey the fluid into the smaller test section, increasing the speed, maintaining flow quality and avoiding separation and relaminarization of the boundary layers.

A Bi-dimensional square to rectangular contraction with a 4:1 area ratio is designed following the methodology described in (Fang F. , 1997) further assessed in (Fang, Chen, & Hong, 2001). The effect of the contraction on turbulence is verified according to (Uberoi, 1956), (Hussain & Ranjee, 1976) and (Ranjee & Hussain, 1976). The cubic curves presented in drawing #8, appendix A are obtained from (Morel, 1975) using the parameters from (Fang F. , 1997). The contraction performance was finally checked satisfactory by means of a 1:5 model scale test (CEAMA WTII).

The contraction carries the flow from the square section of the settling chamber into the 2.15 by 1.8m rectangular test section ( $A_{TS} = 3.87m^2$ ). Therefore the resulting settling chamber section for a 4:1 contraction ratio is  $A_{SC} = 15.48m^2$ ,  $A_{SC} = 15.60m^2$  if one rounds up to a more convenient  $H_{sc}=3.95m$  side dimension. The inflection point location ( $\frac{x_m}{H_{SC}}$ ) and contraction length ( $\frac{L}{H_{SC}}$ ) are required to define Morel's cubics. Pressure gradients at the entrance and exit are checked in order to avoid separation of the boundary layers, specially at the entrance where the inertia is lower. The final contraction design had the following parameters:  $\frac{x_m}{H_{SC}} = 0.48$  and  $\frac{L}{H_{SC}}=1.2$  which ensured a favorable pressure gradient at the entrance ( $C_p$  of 0.5 compared to the allowable maximum of 0.619). This was in fact the limiting criteria for its design. The allowance at the exit was much greater, having a  $C_p$  of 0.15 compared to the much greater allowable of 0.6, Stratford criterion. The estimated non uniformity at the exit was close to 3%. Finally, the acceleration parameter is checked alright, lower than the allowable in order to prevent relaminarization (85 compared to 100).

The pressure loss coefficient of the above mentioned contraction designed is obtained from (Idelchik, 1986),  $K_c = 0.01$ .

### 3.1.2.2.3 Settling chamber

In this chamber or plenum the flow quality conditioning is performed by means of a honeycomb and two meshes. Based on the distance and orientation of the wind tunnel with respect to the wall before it, a turbulence intensity of 12% and integral length scale of 500mm ( $L_u = L_v = L_w$ ) are estimated at the inlet (Batill, 1984), (Farell, 1992). This was checked conservative through the positioning tests of the replica wind tunnel (CEAMA WTII).

A total length of 2.020m results available for this component once it is accounted for the test section, contraction, turbomachine, and adapter. A system of a single honeycomb followed by two meshes (or screens) is designed for the management of turbulence and flow conditioning.

The honeycomb (HC) hexagonal cells length and size ( $M_{HC}$  and  $L_{HC}$ ) are selected by maximizing the reduction in the incoming turbulence intensities  $I_u$ ,  $I_v$ ,  $I_w$ , and integral length

scales  $L_u$ ,  $L_v$ ,  $L_w$ , at a low energy loss ( $K_{sc}$ ) and turbulence production. The design windspeed for the honeycomb cells is 7.4m/s which corresponds to the 30m/s design wind speed at the test section and a flow rate of roughly 115m<sup>3</sup>/s. The honeycomb has two effects: it reduces the level of the incoming turbulence and produces turbulence itself of a smaller scales. The cell length is selected in order to ensure fully developed turbulent flow which reduces the production of turbulence compared with the laminar flow condition. A mesh size of 12.7mm was selected among the commercially available to ensure fully developed flow in a range up to  $V_{sc}=3.8$  m/s= $V_{ts}=15.4$  m/s, see (Lumley J.L., 1967). The selected honeycomb is made of aeronautical grade aluminum sheets of 0.071mm thickness which means a porosity of 0.9888 and a loss due to contraction of only 0.003 (Idelchik, 1986). A total loss of  $K_{hc}= 0,85$  is estimated based on the cell's length, Reynolds number and hydraulic diameter (Lumley J.L., 1967) and (Idelchik, 1986). The damping effect on turbulence leads to a reduction in turbulence intensity (including its own production) of 5.34% just downstream of the honeycomb with a length of 410mm. Similar performance could have been achieved with a more economic design using larger cells. Provided that the pressure rise at the fan could account for the corresponding higher losses, the resulting larger length required would lead to a higher wind speed threshold to ensure fully turbulent flow.

A set of two screens follow downstream of the honeycomb. Their purpose is to further damp the longitudinal turbulence intensity and reduce the non-uniformities in the flow. The screens damping coefficient was computed following (Schubaber, 1948) based on the pressure drop  $K_{sc}$  which was estimated upon the porosity and a experimental coefficient (Groth, 1988):

$$K_{sc} = c \frac{1-\beta^2}{\beta^2}; K_{sc1} = 0.65 \quad \text{and} \quad K_{sc2} = 0.25;$$

where  $c$  is the experimental coefficient, assumed equal to 0.45, (Groth, 1988)) and  $\beta$  is the porosity.

The positioning of the screens is such that the resulting integral scales downstream and upstream of it are within the following range:

$$3 < \frac{L_u}{L_D} < 10$$

The first screen (SC1) is consequently located 200mm downstream of the honeycomb end with a porosity of 64% followed 200mm downstream by a 80% porosity mesh (SC2). Their corresponding damping coefficients  $\sqrt{\eta}$  are 0.571 and 0.699 for SC1 and SC2 respectively:

$$\sqrt{\eta} = \frac{1}{1 + K_{sc}} \sqrt{\frac{3 + 2 \cdot K_{sc}}{3}}$$

similarly the integral length scales are obtained so that the resulting estimated flow conditions at the end of the settling chamber are (Groth, 1988), (Tan Atichat, 1982):



$I_u$	$I_v$	$I_w$	$L_u$
1.1%	0.8%	0.7%	

Further intensity decay is expected at the straight 1210mm end of the plenum downstream of SC2 up to 0.7%. The above mention turbulence management configuration is designed for wind speeds higher than 15m/s. A set of intermediate screens right downstream of the honeycomb and SC1 respectively is proposed for future development to ensure turbulent flow condition.

A set of two safety meshes are designed, SC3 and SC4. SC3 is located 100mm downstream of the end of test section, within the adapter-diffuser. Its purpose is to protect the fan from impacts from flying objects. The second, SC4, is located right at the downstream end of the wind tunnel for safety. A man entry hole is set for maintenance purposes. Both meshes have cell sizes of 50mm and 5mm wires which correspond to loss coefficients of  $K_{SC3} = K_{SC4} = 0.29$ .

#### 3.1.2.2.4 Inlet

The space available for the wind tunnel was tight with the targeted requirements. The final position and orientation of the wind tunnel with respect to the surrounding walls was studied carefully through a set of experiments in which WTII was conveniently enclosed in a replica of the room.

The inlet design was bell-shaped, given the short distance to the wall and the angle between them. A tubular aerodynamic design (see drawing in Appendix) with a diameter of 0.3 times the plenum dimension helped reducing the otherwise significant head loss and turbulent intensity. (Cataldo, 1991). The final distances to wall at the inlet range from a minimum of 2.5m up to a maximum of 4.5m, measured from the plane of the first frame were in any case higher than the 2m presented in (Cataldo, 1991) (see dwg. #). The estimated loss (Idelchik, 1986) based on an average ratio of these distances to the hydraulic diameter was  $K_N = 0.38$

#### 3.1.2.2.5 Adapter - diffuser

Up to this element every other length has been set according to its own requirements. The space left available is used to diffuse by expanding the cross section. This expansion is beneficial to the wind tunnel's overall performance for two reasons. Firstly, when the flow is conveyed into a larger section the wind speed is reduced and therefore energy is stored in pressure and the head loss is reduced. Secondly, a larger section can adapt to a higher diameter of turbomachine, which guarantees a better performance for a same fan's functioning point. The recommended maximum levels of expansion are set around  $4^\circ$  in order to avoid separation and maintain flow quality (Royal Aeronautical Society. Engineering Science Data Units, 1980). This angle is the actual walls' angle, which would correspond to a total aperture of twice that value, i.e.  $8^\circ$ . Based on these recommendations, a diffuser downstream of the test section adapts the 2.150 by 1.800m rectangular test section to the 2338mm diameter circular section of the

turbomachine fan with a length of 1.86m and an expansion ratio of 1.11. Such ratio leads to a pressure recovery coefficient of 0.17, computed as:

$$C_{Pr} = \frac{\Delta P}{\frac{1}{2}\rho U^2}$$

where  $\Delta P$  is the absolute pressure recovery,  $\rho$  is the air density and  $U$  is the air speed. The pressure loss coefficient can be derived from the average expansion angle and such pressure coefficient:

$$K_{Diff} = \alpha - C_{Pr}$$

where  $\alpha$  is the averaged expansion total angle. The shape is made of four triangular planes at the top and bottom and two sides connected by the same number of ruled surfaces.

A second diffuser is proposed for further development to be installed just downstream of the turbomachine. Its design shall be based on actual measured overall performance of the wind tunnel.

### 3.1.2.2.6 Losses coefficients summary

The **table** below shows the pressure loss coefficients referred to the section where they are located and to the test section as obtained by the corresponding area ratio:

$$K_{TS,i} = K_i \left( \frac{A_{TS,i}}{A_i} \right)^2$$

where  $K_i$  and  $A_i$  are the pressure loss coefficient and cross section of component “i” and  $K_{TS,i}$  and  $A_{TS,i}$  are those referred to the test section.

COMPONENT	$K_{TS,i}$
INLET	0.024
HONEYCOMB	0.053
SCREEN #1	0.041
SCREEN #2	0.016
CONTRACTION	0.01
TEST SECTION	0.13 (0.51) <sup>32</sup>
SCREEN #3	0.32

<sup>32</sup> Operating simulating a 1:400 boundary layer

ADAPTER-DIFFUSER	0.02
OUTLET	0.97
SCREEN #4	0.3104
<b>TOTAL K</b>	<b>1.89 (2.27)</b>
Total $\Delta P$ at 30m/s	852 Pa
ABL simulation	1023 Pa

### 3.1.2.2.7 Turbomachine

This component is design to transfer the energy that is lost through all the mentioned wind tunnel components to the flow. Such machines capable of transferring either energy or force to the flow are termed turbomachines.

Firstly the convenience of an enclosed turbomachine system based on one single blower is compared to a multiple matrix design. An array of 9 or 4 industrial standard small size turbomachines appears as clearly more economical option. However, a carefully designed adapter would be needed to ensure the proper junction of the individual jets. This element would require extra length in the already tight design. Furthermore the overall efficiency of such fans made of bent-aluminium blades is of the order of 10% lower than a customly designed cast aluminum blades unit. A more complicated and less precise power and control would drive the multiple fans. A more robust solo custom turbomachine was finally selected compared to the multiple system where the breakdown of any of the 4 or 9 units would lead to the malfunction of the whole facility.

Following the dynamic similarity principia, the performance curves of the turbomachine are derived from the following nondimensionals (Csanady, 1964):

$$\Omega = \frac{N \cdot \sqrt{Q}}{E^{\frac{3}{4}}}$$

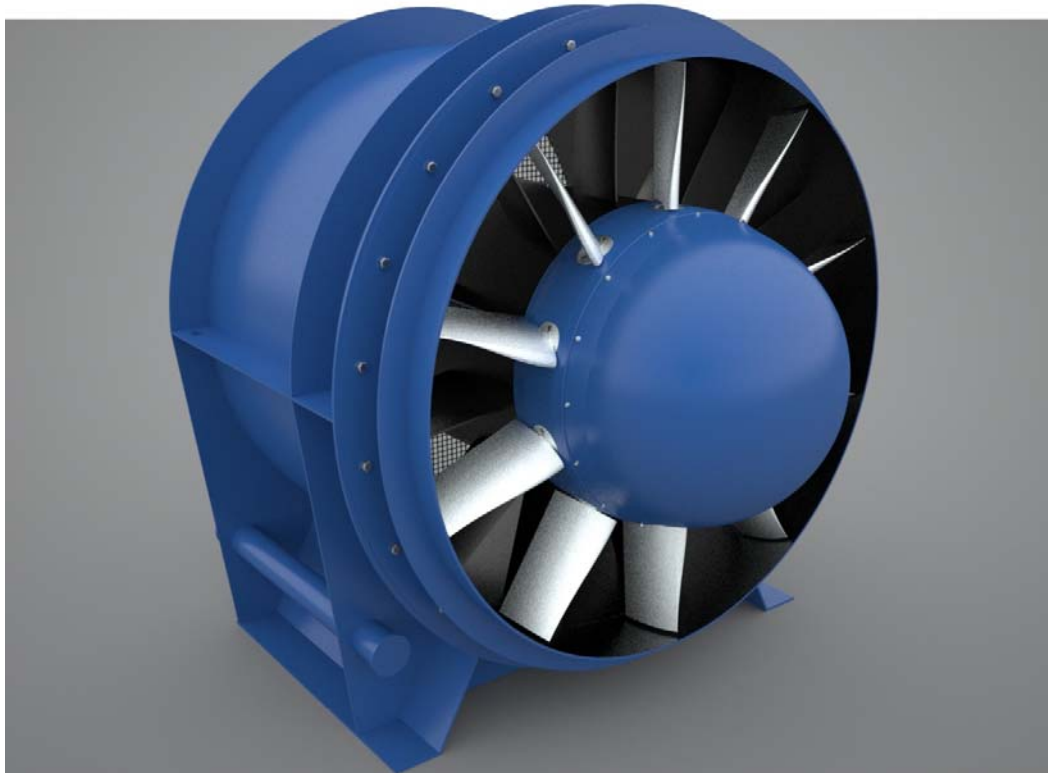
the *turbomachined specific number* optimum for flow-speed in which N is the speed of rotation in radians, Q the flow rate and E the energy in the flow which maybe as the gravity acceleration times the pressure head in meters.  $E = H \cdot g$  and  $H = \frac{P}{g\rho}$ . An 8 poles

induction motor is sought to rotate the blades in a direct drive configuration. Nevertheless the synchronous speed of the motor is 750 rpms, all calculations are made for the design point to be reached at 650rpm which guarantees a longer life and less maintenance. An specific number of 5.45 (6.29 for 750 rpm) is obtained which corresponds to radial compressors and fans and through Cordier diagram, to an specific diameter of  $\Delta=1.25$  (1.35 for 750 rpm) defined as:

$$\Delta = \frac{\Phi \cdot \sqrt[4]{H \cdot g}}{\sqrt{Q}}$$

where  $\Phi$  is the turbomachine diameter. Following the above, values in the range of 2.5 m are obtained for optimum diameters. A final diameter of 2238mm is selected after further fine tuning and considering the expansion limitations upstream of the turbomachine.

The study of the energy transfer in the turbomachine is performed and a subsequent design for the rotor and stator is produced in collaboration with ventilator specialist Turbolufitech TLT, Germany. The [figure](#) below shows the 10 blades rotor design upstream of the 11 guide vanes stator which compensate the swirl generated in the energy transfer by rotor - flow interaction. A higher number of blades such like the current contributes to a lower noise level for the same momentum transfer. It also alleviates the mechanical requirements and rotor stability. The blades are connected to the hub through a connection that allows to adjust the angle of attack during stand still. This would benefit further developments of the facility for which a change in the performance curve of the turbomachine might be sought. The nosecone is rotating and fixed the rotor. Its shape is aerodynamically optimized and it is designed as a light aluminum shell.



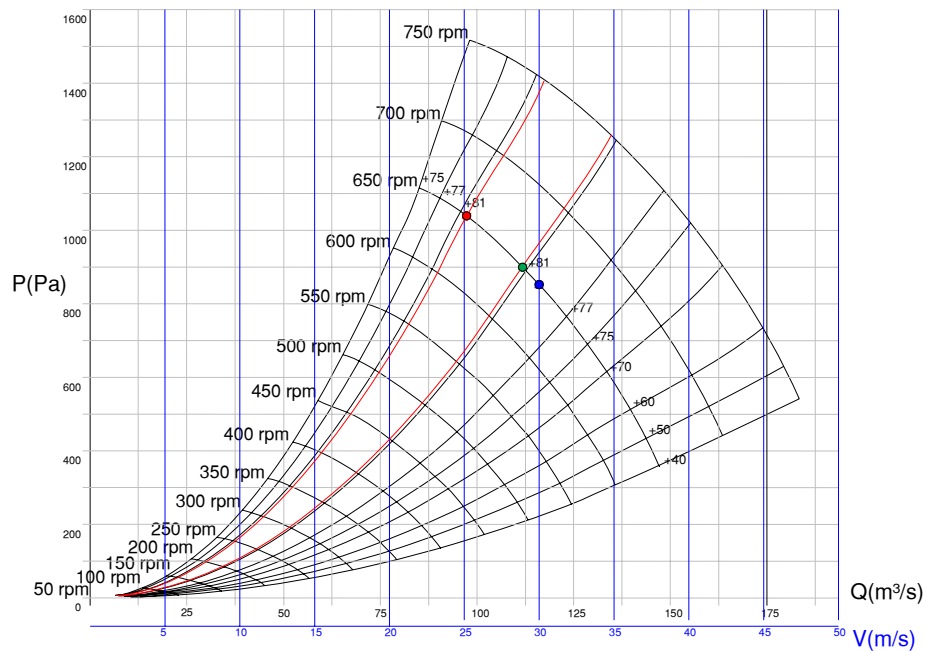
A power consumption of 114 Kw is estimated at the ventilator shaft to deliver the required torque. The hub is fixed to the shaft by a press fit mechalock SKF system. It is expected that the noise level from the fan will be lower than that generated at the motor (see next section).

The fan housing is designed with an internal hub diameter of 50% of the external, 1122mm. The stator guide vanes are integrated with the nozzle and flange so that this can support the motor by itself. Consequently no rear support is needed at B side of the motor which is beneficial for the flow quality. The fan housing is connected to the adapter-diffuser of the wind tunnel with a flexible expansion joint made tight with wrapping steel bandage. An aerodynamically shaped radial cabinet is set to house the power, control and monitoring coming from the motor to the outside of the housing. These cables finally reach the outside through an airtight cable seal system (ROXTEC®).

The resulting performance curves are presented in **Figure**. The design functioning point is achieved with blades at 4 degrees of angle of attack with an overall efficiency of nearly 81% (blue dot in the figure). It is however anticipated that the efficiency will be reduced in boundary layer simulation operating conditions due to the non-uniformity of incoming flow.

#### **3.1.2.2.7 Drive and control system**

The above-mentioned power at the shaft of 114Kw corresponds to a rated motor power of 124 Kw, assuming an efficiency of 90%. A nominal power of 160Kw is finally sought in a cast iron frame, size 315, to fit within the 1122mm diameter hub. An standard 8 poles (750rpm sync.) induction ABB® motor design is modified to fulfill the present requirements. Therefore, the shaft diameter is enlarged up to a fully rounded 90mm. This larger diameter reduces the shear stress and consequently allows the torque transmission via the mentioned press fit system. The flange designed is also modified to converge to the needs of the supporting nacelle flange. The standard motor fan on the B side is removed so that it the motor is surface cooled by the actual wind tunnel fan. The shaft is supported in the iron cast housing by means of two corresponding SKF bearings (6319 and 6316).



It is recommended that some allowance is also attained in between the motor power and that available from the drive system. The motor is then driven by a 200Kw Allen-Bradley frequency converter equipped with a line filter. This converter is controlled by the PLC (programmable logic control) system.

The PLC is located next to the frequency converter within a cabinet of approximately 2000·1800·500mm. Both are separated by a steal plate to prevent noise in the PLC control and monitoring signals.

A high precision, 1024-counts-per-revolution, encoder is required to guarantee fine control capabilities of the wind tunnel wind speed (Leine & Leine ®). The converter hence powers the motor at 380V from 0-50Hz depending on the measured 0-750rpm. The measured rpm regime is then compared to the command rpm given via the PLC. The frequency of the power is adjusted consequently. Such closed loop rpm control has a precision of 0.1%. Alternatively the signal coming from a pitot tube can also be used in the same fashion to directly command the desired wind tunnel wind speed. The resolution decreases however given the poorer resolution of the corresponding pressure measurement.

The motor is equipped with double temperature sensors (PT100) at each winding. The condition of these bearings is monitored via acoustic sensors which allow to correlate the dB measured in the bearing cast to the ball and grease conditions (SPM®, shock pulse method). The bearings are also equipped with double PT100 sensors.

The pressure difference between a point located 30mm upstream the blades leading edge and a set of averaging multipoint half way downstream of the nacelle to the end of the fan housing is measured. Such measure by means of a differential pressure transducer is connected to a switch which allows to stop the operation in the case that the stall pressure gradient is approached. This could, for example, happen due to large pressure waves caused by the breakage of a large model or sudden considerable blockage or release of it. The consequent significant pressure gradients may cause the stall of the fan blades and the rotor unbalance. The switch is set to a limit of 2000Pa and is connected to relay that manages the feed of power to the motor. The temperature sensors are similarly managed with pre-alarm (60°) and alarm (120°) levels and connected to that same relay in the event of an alarm.

A set of two SPM accelerometers are used to monitor the vibration of both the wind tunnel and the turbomachine. The first accelerometer is located centered right under the end of the test section at the ABL testing area. It serves to monitor unwanted vibrations of different sources such as turbomachine flexible joint malfunction, frame failure or structural deterioration, major model breakage or even a persons' fall down. The turbomachine's accelerometer is located at half height on one of the sides. Both sensors are set with a pre-alarm and alarm threshold of 4.5 and 11mm/s.

Every signal cable is screened, grounded and kept physically separated from the noise source of the power cables.

A number of safety stops connected to the drive relay are located strategically around the wind tunnel room: section model testing area, ABL testing area, drive system cabinets and entrance. Safety and flashing lights together with a warning message are automatically displayed at the entrance triggered by the wind tunnel operation.

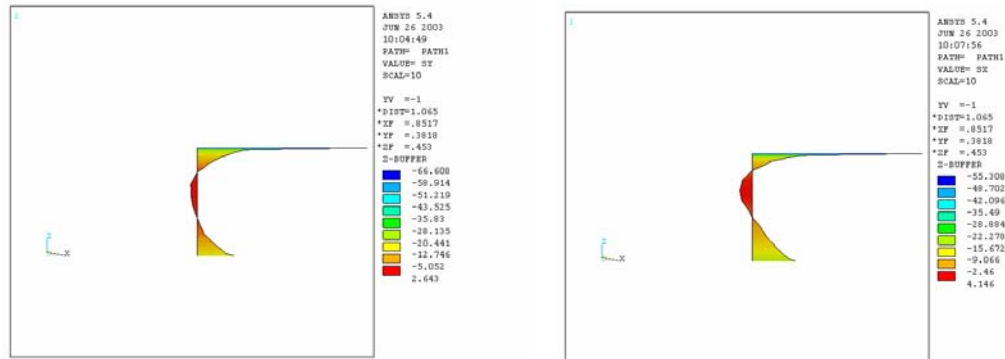
It is worth of noting that all the logic operations for the control and monitoring of the different signals are made electronically at the SCADA unit (supervisory control and data acquisition) rather than via software at the control computer. The information is only displayed at this computers' interface where the user commands are also acquired. It is understood that results in a more robust system independent of the computer operation. (table with signal arrangement?)

An armoured concrete foundation is design to support the 6300kg<sup>33</sup> dynamic mass of the vibrating turbomachine. The asymmetric loading state with the pads close to the edges are out the scope of the current code and formulations available for the analysis of this kind of massive foundations. A finite model was used to simulate the stress state under this loading and to locate the tractions that are known to exist in this massive blocks. The armour was positioned consequently at the referenced height which in fact did not differ much from that recommended in the Eurocode for the symmetrical case (CEN , 2004). The figure below shows the stress state resulting from the numeric simulation right under the pads.

---

<sup>33</sup> 4700Kg from the housing , nacelle, stator and rotor and 1600Kg from the motor

The turbomachine seats on the foundation through a set of four viscoelastic dampers (GERB®) which reduce the transmission of dynamic loading to the foundation and building.



### 3.1.3 Wind Tunnel Construction and Commissioning

This section will examine the major milestones, technological solutions, materials, difficulties, and procedures that lead to the construction, calibration and start up of the wind tunnel design detailed in the previous section.

The final design shown in [Figure 3.1](#) was built at the lower level of the Andalusian Environment Centre (Centro Andaluz de Medio Ambiente, CEAMA). The room was modified to some extent to adapt to the wind tunnel needs. The span between the support columns was extended so that only one set of larger diameter columns was needed. The final position of the wind tunnel was confirmed by scale model tests of the Wind Tunnel II with and the surrounding walls of WTI made of wood at the corresponding scaled distances. The wind tunnel was finally positioned slightly tilted with respect to the line of columns in a compromise between the inlet, discharge and recirculation flow conditions while maximizing the test section length. It is observed that given the number of columns located on the recirculation path an their diameter (600mm), considerable vorticity will be shed into the room at frequencies of importance for the testing (0-10Hz). It is anticipated that the settling chamber elements will damp the energy content at this particular frequency. Some space was made available for storage at one of the sides. The space was divided in 6 small rooms is thought so that every accessory equipment, instrumentation, components, models and so is stored there and the recirculation path is kept free which will be beneficial for the preservation of the flow quality of the facility.

The wind tunnel shell is made of 241mm (8' by 4's) Canadian plywood panels supported by 6" sq. Swedish pine timber system. The contraction is however made of a set 8, 3.2mm, MDF board panels. The panels were laminated at the site over a mould in a similar fashion to the way boat hulls are built. Two moulds were built for the different contraction ratio of vertical and horizontal walls ([see picture below](#)). Given the importance of the contraction in the overall wind tunnel performance, a tolerance of 1mm maximum was threshold for acceptance with respect to the control points given every 100mm in plan. The inlet is aerodynamically shaped with 3.2mm TABLEX board which flexibility allowed for the



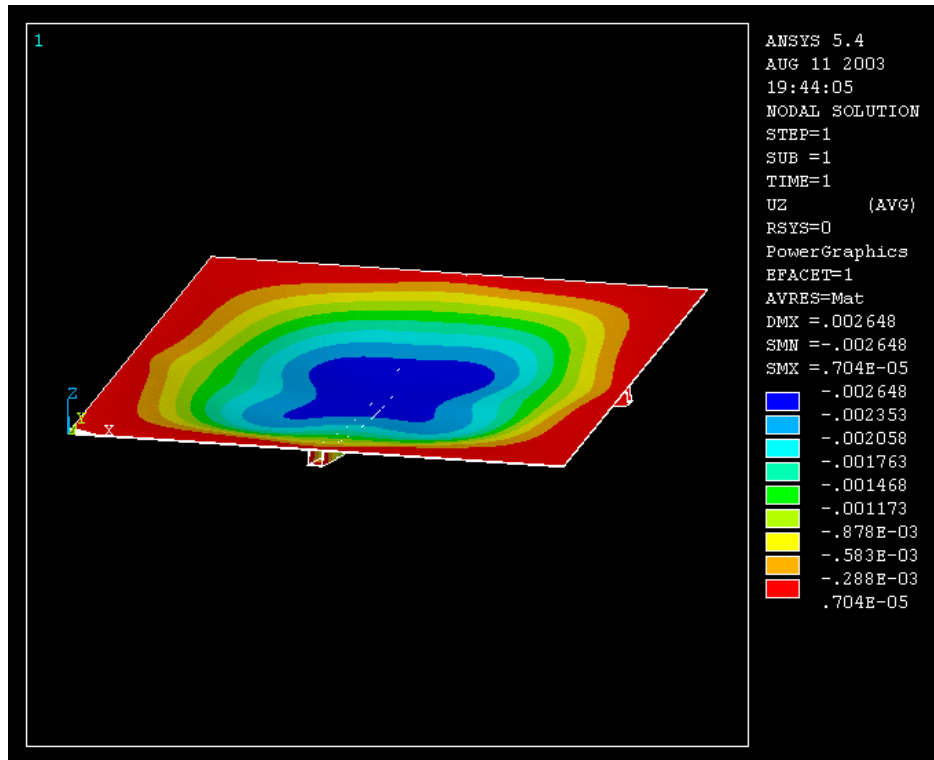
corresponding curvatures. Stiffening ribs provided support to the Tablex skins. A tolerance of 2mm was accepted with respect to Morel's curves give in drawing #8, appendix A.



The two test areas windows were perforated at their sides before the tempering. Flexible rubber washers were used with the bolts to fix the windows to the timber system. The section model test area windows included a central slot so that section models could be support from the outside. 8 mm thick high transparency glass was used to enhance their capabilities for laser measurements. The wind tunnel interior is painted in flat black for the same reason and to improve the conditions for different flow visualization techniques. The test section is provided with two double airtight gates to help the circulation of material such as the roughness elements as well as for safety reasons.

The turbomachine was assembled outside of the building given the space limitations. The motor was first positioned vertically and then the fan housing was lowered over it. The motor was then lifted inside and fixed by 8 M20 bolts. The rotor was then lower onto the shaft and fixed to it with the press fit system (mechalock, SKF). The connecting ring to the wind tunnel around the rotor was finally carefully positioned given that the maximum distance from tip of a blade to this ring is 7mm (2 pictures [figures](#)). The fully assembled and calibrated (mechanically balanced) turbomachine was positioned into place through an aperture in the roof made for this purpose. The 40cm waffle concrete slab was cut from the outside using a 1000mm diameter diamond head cutting disk over a precisely positioned railing. A set of steel U profiles around the four sides of the opening provided the slab with the required stiffness. It is intended to have an easy access to the turbomachine in case in the future it has to be lift up for maintenance or repair. A steel

plate provided with a set of two stiffening U-profiles is designed to sit on top and support the Chinese garden above which included stones of up to nearly 2000Kg. Figure shows the stress state of the plate under such loading. Given the consequent need of keeping the opening dimensions low, the gap left with respect to the turbomachine overall dimensions was of a few centimeters only (Figure). The turbomachine was dropped down on to a temporary timber support with an offset out of the wind tunnel axis and then rolled over the foundation and finally position and leveled on top of the dampers with hydraulic jacks. Connection of all the electrical power, signal and control cables followed.



Last before trial runs, the honeycomb is set into its position divided into 6 units enclosed 2mm steel frames within the settling chamber (see drawing 6, appendix A).

The preliminary commissioning of the facility comprised the following tasks:

- Power transmission check - ok
- Sensor measuring check one by one: the aim is to check that all sensors were measuring and that they were measuring correctly
  - Windings PT Sensors (2x3) - ok
  - A and B side bearings PT Sensors (2x2) - ok
  - Turbomachine accelerometer (1) - ok
  - Wind Tunnel accelerometer (1) - ok
  - Turbomachine Pressure gradient (1) - ok

- A and B side bearings dB sound pulse (1x2) - ok
- Relay aperture checks: the relays were tested giving alarm levels of the following sources
  - Temperature - ok
  - Vibration: the test included the monitoring of the wind tunnel and turbomachine accelerometer as well as a third one positioned in the center of the test section window. Significant vibration on the windows was measured possibly due to the net pressure on them. The clamp condition at the end was stiffened consequently and the maximum speeds tests were postponed.
  - Bearing shock - ok
  - Pressure gradient - ok
  - Emergency stops (4) -ok
- Sense of rotation check (CW). CCW rotation was observed the sense was changed at the frequency converter.
- Rotation command precision. RPM value measured with the encoder on the shaft rear end is cross-checked with a high precision stroboscope. A precision of 0.1% was confirmed - ok
- Computer interface and command and communication to the SCADA. The information presented in the computer interface is cross-checked with the measured values. The command logic is checked. (OK)
- The electrical brake, injecting DC into the windings was set to 5s and checked ok for the emergency stops.
- Power consumption control. The power actually supplied to the turbomachine at different regimes was measured. It was found that peak intensities at 650 rpm were 155A so that the corresponding peak power is 59 KVA.
- Wind speeds at the test section measurement and general aerodynamic evaluation through the performance curves (figure). The performance is found generally satisfactory. However, higher losses than calculated correspond (see red dot in figure). The flow conditions at the end and entrance are partly pointed out responsible for the higher losses. Different issues are identified through the maximum wind speed tests at roughly 30m/s. Considerable vibration is observed in a pipe on top of the discharge and on the panoramic windows of a viewpoint that looks to the wind tunnel from a room at another level in CEAMA.
- The wind speed across the test section is finally measured with hotwire anemometry and LDV to confirm the flow quality (figure).

### 3.1.4 Wind Tunnel Instrumentation

The new wind tunnel laboratory established is equipped with preliminary instrumentation for applied research in the field of bluff body aerodynamics:

- Electronic pressure scanning system (Esterline, former PSI). A chamber with a frequency controlled loudspeaker one end and pressure tube connections on the other end was built in order to test the tubing combinations with proper dynamic capabilities (Figure and holmes paper reference).
- Single and Cross wire constant temperature anemometry and calibration unit (TSI).
- Laser Doppler Velocimetry (5W) for which a nebulizer was built to seed oil particles in the air (TSI).
- A Nickel-Chrome smoke wire was built for flow visualization by using a variable power supply.
- General purpose load cells of different ranges.
- Multi-axial, 6 degrees of freedom load cells (JR3) this are used for forced balance building models as well as for bridge section static testing.
- Signal conditioners (8 ch.) analogue filters and data acquisition system (32 ch.).
- Dynamic section model testing rig (see section for further details).
- Static section model testing rig (see section for further details).
- A pressure line was setup to be used with different instrumentation such as the hotwire calibrator, pressure system, nebulizer ... as well as with particular pneumatic tools and machinery.
- Pitot tubes (3) for measuring reference wind speeds using high resolution differential pressure transducer.

### 3.1.5 Wind Tunnel II

Wind Tunnel II was built approximately a year before WTI. It is a 1:5 scaled replica of WTI except for what respect to the aerodynamics of the turbomachine<sup>34</sup>. It was built with the main purpose of testing the performance of key components of the wind tunnel such as the contraction. It was also found helpful in characterizing the effect of the inlet and outlet flow conditions (distances to the wall, columns and such) and evaluating their effect in the overall performance. Velocity profiles were measured at both ends and along the test section in WTII with simulated WTI surroundings (see picture). Such information was found useful for confirming the final design of the settling chamber elements: honeycombs and screens. As shown in Figure (Mans & Terrés-Nícoli, 2004) the scaled wind tunnel was found useful in determining that a storage room positioned at the

---

<sup>34</sup> the diameter is close to the corresponding a 1:5 scale, 460mm compared to 447.6mm

lower right corner of the room in **Figure** acting as a deflector would have a good effect on the wind tunnel performance as well as will make more storage space available. It is therefore proposed for future development that this room is built.

Wind Tunnel II is built entirely transparent for teaching and flow visualization purposes. Made of PVC glass it is easier to maintain since it is more flexible and can be welded, compared to the more transparent but more rigid acrylic.

Once Wind Tunnel I has been built, the replica is left for use in small scale research, teaching and given that it can be fully dismantled, attending fairs and shows such as the International Boat Show in Barcelona (**picture?**).

## 3.2 New CEAMA Section model test system

A new section model test rig was built at CEAMA new boundary layer wind tunnel I. The system was designed configurable for both dynamic and static section model testing. It was benchmarked with the testing of both the Third Millennium Bridge, Expo 2008, Zaragoza and the Storebael Bridge, Danmark.

In this section, the section model test is introduced and framed within the current practices in bridge aerodynamics. The details of the new dynamic and section model test rigs are given thereafter. Finally the two models design and results are present.

### 3.2.1 Section model testing

Section model testing is an efficient tool for studying the fundamentals of the aerodynamics of two-dimensional or line-like structures. These include medium and long span bridges, cables, medium and high-rise chimneys and towers. Its methodology is based on the experimental investigation of the flow structure interaction of a segment of the structure, which allows for somewhat large scales, normally in the range of 1:40-1:100 (ASCE, 1999), (Hjorth-Hansen, 1992), (King J. P., 2003).

Different testing techniques have been developed ever since the first section model tests in the Tacoma aftermath (Farquharson, Aerodynamic Stability of Suspension Bridges with special reference to the Tacoma Narrows Bridge, 1952). The section model can be basically set-up stationary or dynamic. When stationary, the forces are measured at the fixed ends and the corresponding aerodynamic coefficients are calculated upon them for different angles of attack, normally from  $-10$  to  $+10^\circ$ . See, for example, (Cigada, Falco, & Zasso, 2001).

In the dynamic configuration, a model with calibrated generalized mass and inertia is mounted on a dynamic system where the damping and vertical and torsional stiffnesses are properly scaled (see section 3.3). The model is then left to respond freely to wind loading. Forces and responses can be measured simultaneously and aeroelastic instabilities and response to turbulent wind (buffeting) is investigated. A useful approach in the investigation of stability is the formulation based on functions named **aerodynamic derivatives** (Scanlan

& Tomko, 1971). The study of these derivatives can identify wind speeds and modes of negative aerodynamic damping, indicator of vortex induced vibration, galloping or flutter. Such functions can be obtained through free vibration tests in which an initial displacement is given to the model and the consequent decay is measured after it. Alternatively the model can be forced to oscillate at particular frequencies and the derivatives are obtained upon the ratio of the motion-induced force and the actual oscillation. More recently, system identification techniques are being used systematically to solve simultaneous equations for a given initial displacement and rotation simultaneously (Sarkar, Jones, & Scanlan, 1992).

The dynamic testing of section model requires matching of certain dimensionless quantities:

- Reynolds number (Re): Represent the ratio of the inertial forces in the fluid over the viscous force:

$$\text{Re} = \frac{U \cdot D}{\nu}$$

where  $U$  is the free stream wind speed,  $D$  the body's dimension that controls the flow geometry and  $\nu$  is the kinematic viscosity, normally  $1.5 \cdot 10^{-5} \frac{\text{m}^2}{\text{s}}$ .

Strict Reynolds number scaling is not possible, however section models are significantly better off compared to full aeroelastic models. The effect of the mismatch is not easy to quantify but is anticipated minor in the case of shapes without rounded shapes. In order to minimize these effects and to ensure that all attached flow was turbulent, the surface of the model is normally roughened with sand. The Re in the case of circular geometries, such as handrails and members of central and edge barriers, Re effects are handled by selecting the diameter of the tubes so that an equivalent force effect are modeled.

- Cauchy number (Ca): represents the ratio of the elastic to fluid inertia forces. It can be written as a reduced velocity,

$$\text{Ca} = \frac{U}{f \cdot B}$$

where  $f$  is the natural frequency of the structure and  $B$  the deck width.

- Density ratio: The models are designed to match the same material to air density of the prototype. This is important for dynamic similarity; having same density in model and prototype means that forces exerted by the wind are scaled down by the geometry only.
- Structural Damping: Structural damping is difficult to predict and has been proven to have a strong effect on the amplitudes of the vortex - induced oscillations (Frandsen J. B., 1999). Consequently tests are normally carried out for a number of ratios starting with a the lowest possible.

Both static and dynamic forces can alternatively be obtained by integration of the measured pressure field around the deck. This technique though more complicated allows investigating the geometry of the pressure field that leads to the corresponding aerodynamic forces.

The effect of turbulent intensity in the response for a given mean wind speed (buffeting) as well as in the different aeroelastic phenomena is normally investigated. Precise simulation of the frequency distribution and scales of the turbulent structure is complicated at the scales that are managed in section model testing. This is recognized as a matter in which further knowledge is needed (King J. P., 2003), (Tanaka H. , Similitude and modeling in bridge aerodynamics., 1992). Nevertheless there are formulations available that let interpret the effect and account for it to some extent (Davenport & King, 1982).

The sectional forces are then incorporated into the structural analysis through its dynamical characteristics. Clearly, the comparison to the full structure becomes less sustainable the more three-dimensional the structures are. Consequently the two-dimensionality of the flow and the model have to be treated carefully in the experimental design. An aspect ratio of 4-5 is recommended thereby (ASCE, 1999), (King J. P., 2003).

The larger scale of section models makes it easier to examine different configurations of deck geometries, railings or aerodynamic devices. Given the productive and economical nature of this methodology it is systematically used to select and discard geometries and detail decks by simple comparison. It is valued as a reliable tool to detect and avoid instabilities such as galloping, vortex induced vibration, torsional divergence or flutter.

### 3.2.2 Test Rig frame

The system is designed so that it is fully located out the wind tunnel test section. This simplifies all the mounting, calibration and adjusting procedures. It also let use the full width of the test section, 2.15m, which as mentioned before allows preferable larger model' aspect ratios. The model in both dynamic or static test setup is connected to the rig by pins through slots in the test section windows. Therefore, such design requires that the system is air sealed to avoid the undesired jets that would occur otherwise through the slots in the glass.

The range of inertias and stiffness of the sprung system in dynamic section model test can vary. The simulation of the free response in such configuration focuses in the vertical and torsional fundamental modes of the section model. The excitation of inertias of any other source or section model mode is therefore undesirable. Consequently the frame system that supports the interchangeable static and dynamic rigs is designed sufficiently stiff attending at its dynamic analysis. The structure is basically a set of two frames at both sides of the test section connected by a set of four beams and two tensioning crosses above and below it (see drawing 11 App. A). Each frame is tightly fixed to the floor by a set 2L plates on each column. Four beams connect each frame column. Two of the are fixed to provide the corresponding stiffness and the other two are adjusted according to the project needs. A rubber air sealing profile lets the frames lean tightly onto the test section windows. As shown in (drawing #12 App. A), the adjustable beams are set close together when the rig is

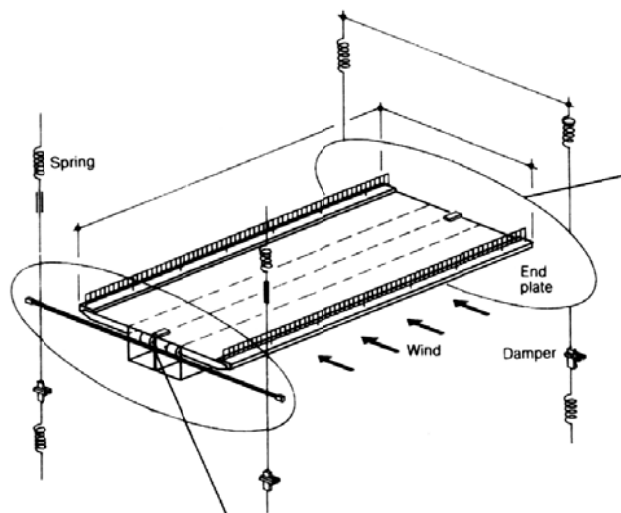


configured for static testing and separated according to the project needs for the dynamic test configuration.

All the structural members are made of extruded aluminum profiles including railings for connecting bolts, which provided the desired flexibility of these multipurpose systems.

### 3.2.3 Dynamic section model testing rig

A section model dynamic testing rig is designed so that models are setup to freely vibrate under wind loading. The dynamic similarity of the simulation requires that the modal mass and mass momentum of inertia of the vibrating system is matched to the targeted scaled values. Consequently, the rig must be capable to carry ballast at adjustable distances to the centre of rotation so that the model's inertia topped up to targeted values. **Figure** shows a typical section model rig configuration. Interchanging the springs located above and below the model configures the vertical stiffness. The torsional is adjusting by changing the separation between the springs. The force at each of the four springs alignment is measured by means of load cells located at the bottom. The modal responses, vertical displacement and rotation, are calculated upon the corresponding generalized stiffness obtained through dynamic calibrations (see **Section** ).



The damping shall be adjusted as well. This has been achieved traditionally by connecting a vane to each side support and letting it oscillate solidarity within an oil tank. More recently, adjustable miniature pneumatic or electromagnetic dashpots are being used. Pneumatic dashpots were used in the present design.

Normally the study of wind induced response via section model testing will focus on the vertical and torsional modes only. The along wind or drag response is therefore restrained. This constrain must applied with no limitation to the vertical and torsional modes. It can be achieved with the use of long wires (see **Section**) that connected to the centre of rotation from a point upstream restrain such response with little induced lift. A more compact



solution inspired in BLWTL's state of the art rig was used here. The system is based on short leaf springs and bearings that allow rotation with little added vertical stiffness (drawing #12, App. A).

### 3.2.4 Static section model testing rig

A device was designed to measure the wind-induced forces at the ends of the model. Lift, Drag and Torsional Aerodynamic coefficients ( $C_L$ ,  $C_D$ ,  $C_M$ ) can be obtained upon the measurement of the corresponding forces and torque ( $F_L$ ,  $F_D$ ,  $M_M$ ). These forces are averaged from the values at each end measured by means of high frequency multiaxial, six-degrees-of-freedom load cells. The study of the aerodynamic coefficients is typically carried for a range of angle of attacks  $\pm 10^\circ$ . Therefore the system is designed so that it can be precisely rotated. The rotation is executed driving the inertia disk with a vertical ball screw using a stepper motor. The motor is equipped with a gearbox so that the available power allows performing fast rotations as required in forced oscillation tests. The rotating disk serves as a reference for the multiaxial load cell and is consequently provided with the sufficient mass and mass momentum of inertia. The torque transmission is achieved by a mecha-lock press fit connection and a shaft to the load cell base. A low friction shaft collar allocated within an aluminum plate supports the rotating system. The plate is eventually fixed to the wind tunnel test frame. Drawing #13, presents a back and side view of the resulting design.

## 3.3 Section models design

The details and challenges pertaining to the design of the two section models used in the present work are presented in this section. The work focuses in two bridges: The Storebaelt Bridge in Denmark and the Third Millennium Bridge in Spain. The main properties of each are summarized in the attached **tables**. Further details regarding both structures can be found in **Appendix**.

Both Bridges are 21<sup>st</sup> Century structures that share an innovative design but quite different in nature. The Storebaelt is a line-like or bidimensional deck whereas the Thrid Millenium Bridge is three-dimensional. Both decks have significantly aerodynamic shapes that the author hesitates to call "bluff".

The model design starts upon the section model testing theory (Section 3.2.1) and the consideration of a number of prototype factors:

- the inertia (both  $m$  and  $mmi$ )
- the modal analysis
- the targeted test wind speed range or wind speed scale which determines the velocity scale and hence the wind speed resolution

- geometry of the deck with respect to complexity and the consideration of possible construction methodologies and materials.

Based on these, the geometric scale is selected as a compromise of the desired aspect ratio, the resulting weight of the model, the wind tunnel section blockage<sup>35</sup> and the feasibility of modeling geometric details at that scale (Terrés-Nicoli J. M., 2002) (Hjorth-Hansen, 1992,). A scale of 1 to 70 was chosen for both models. The geometric scale and other similarity parameters are defined in the table below.

Parameter		Storebaelt	Third Millenium
Length	$\lambda_L = \frac{L_P}{L_M}$	1:70	1:70
Density	$\lambda_\rho = \frac{\rho_P}{\rho_M}$	1	1
Mass	$\lambda_M = \frac{M_P}{M_M} = \lambda_\rho \cdot \lambda_L^3$		
Mass Momenmtum of inertia	$\lambda_{MMI} = \frac{MMI_P}{MMI_M} = \lambda_M \cdot \lambda_L^2$		
Velocity	$\lambda_V = \frac{V_P}{V_M} = \lambda_L \cdot \lambda_f$	Varies (see table)	
Frequency	$\lambda_f = \frac{f_P}{f_M}$	Varies (see table)	
Damping	$\lambda_\xi = \frac{\xi_P}{\xi_M}$	1	1

where  $L_p$  is a certain length in the prototype and  $L_m$  is the corresponding length in the model. Similarly  $\rho$  is the deck density,  $V$ , the wind speed,  $f$ , the frequency, and  $\xi$  is the damping ratio as a fraction of the critical.

The models are hence designed at that scale with a lower mass and mmi than the corresponding targets. This allowance let cope with the mass of the sprung system and also match the target mmi by adding masses at certain distances to the centre of rotation. The model is dimensioned with a selection of materials and following construction process ensuring that it will be sufficiently stiff compared to the targeted sprung system stiffness. In other words, if the model bending modes are any close to the simulated modes (sprung system frequencies), such model inertia will get excited and the results contaminated.

The Reynolds number based on the size of the handrails and circular tubes of side and central barriers is about 1,500,000 for the design wind speed of the prototype and 1,000 for the model. Due to the difference in the Re number, the drag coefficient is expected to be

<sup>35</sup> vaules lower that 5% are recommended ASCE. (1999). *Wind Tunnel Model Studies of Buildings and Structures*. (N. Isyumov, Ed.).

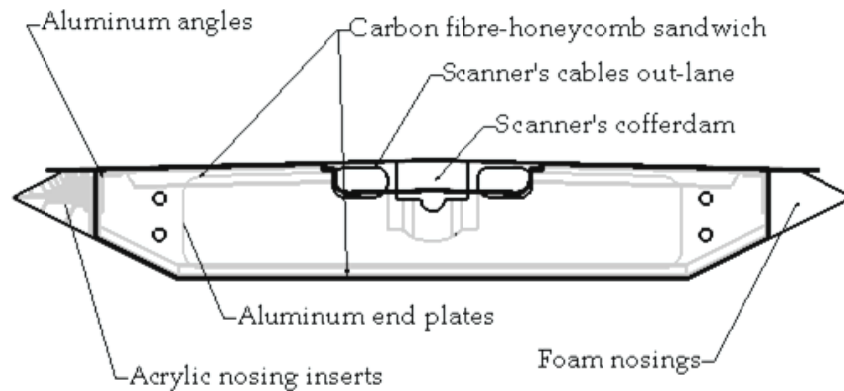
smaller in the prototype-scale than in the model-scale. Therefore the model railings should be undersized by a factor of the drag coefficients of prototype over the model's one ( $C_{DP}/C_{DM}$ ). This would make them too small in size to model individually, so the equivalent drag and blockage effect were included in the design of the support posts. The surface of the models was roughened with calibrated size sand grain. The whole models were painted black to minimize light reflection when carrying out laser technique measurements.

### 3.3.1 The Storebaelt Bridge 1:70 section model

The new section model was designed to **measure pressure** on the surface. A set of 11 pressure scanners had to be installed inside the model and they had to be easily removable. A central channel under the top layer was made to house the scanners and all the tubes and wires connected to them. The scanners, together with these accessories, had to be tight so that they would move when the model was undergoing vibration. Scanners are insensitive to accelerations parallel to their internal diaphragms; thus, they were located the sensitive axis of the transducer in the restrained direction to avoid any induced error due to the accelerations.

Storebaelt Prototype Properties	
m (kg/m):	23687
mmi (kg-m <sup>2</sup> /m):	2.50E+06
lift freq <sup>36</sup> . (Hz):	0.097
torsion freq <sup>37</sup> . (Hz):	0.270
damping <sup>38</sup> $\xi$ (%)	0.26
main span, L (m)	1624
deck width, B (m):	31
depth (m)	4.4
chord to depth ratio	7

not  
with  
drag



Storebaelt Model Properties	Target	Actual <sup>39</sup>
Model m (kg/m):	4.83	3.668
Model mmi (kg-m <sup>2</sup> /m):	0.10416	0.0324

<sup>36</sup> frequency of the first vertical mode of vibration with the lowest frequency

<sup>37</sup> frequency of the first torsional mode of vibration with the lowest frequency

<sup>38</sup> came from full-scale measurements at lock-in (vertical mode) [17]

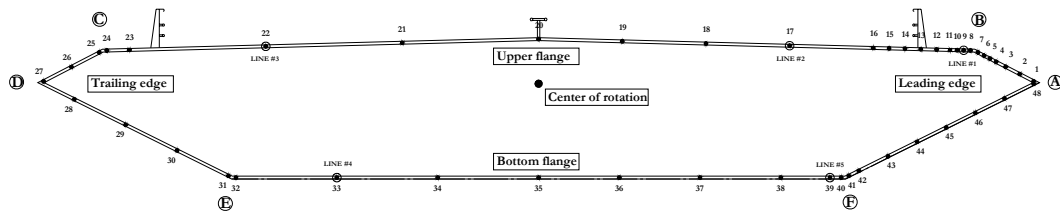
<sup>39</sup> as built, before adding lumped masses.

Model M (kg):	10.31	7.826
Model MMI (kg·m <sup>2</sup> ):	0.22225	0.0692
Radius of Gyration (m):	0.1468	0.137
Center of gravity	Y' (m)	0.000
	X' (m)	0.039

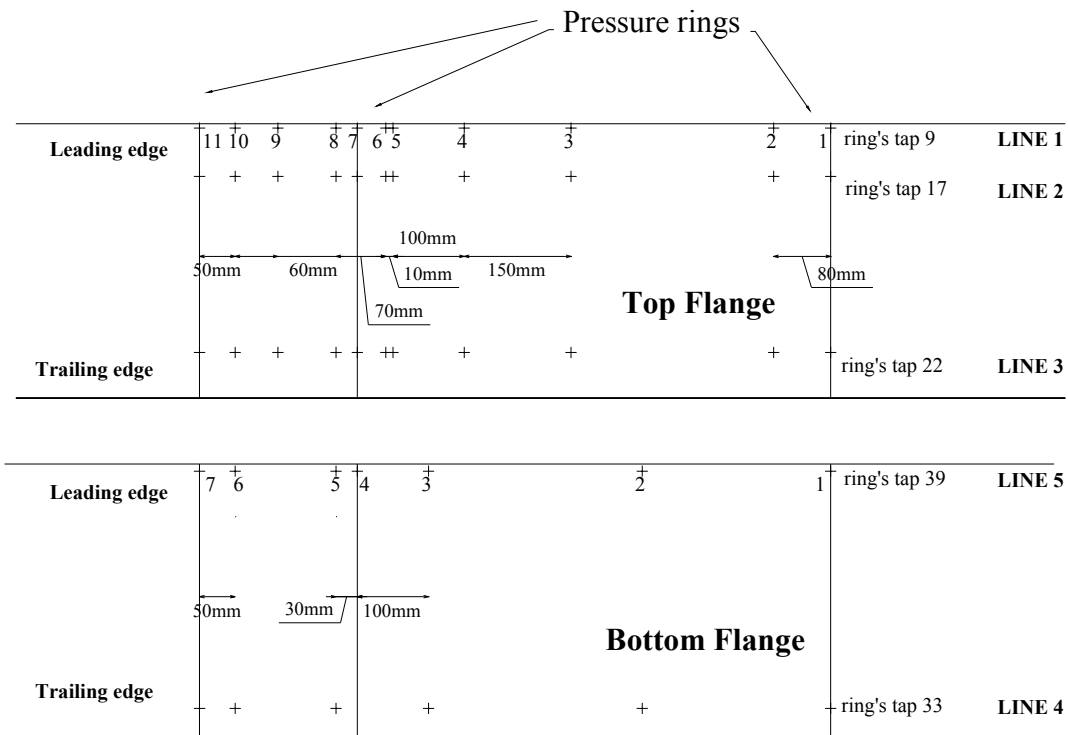
The total mass of the scanner inside the model reached a value of over 10% the target mass. Consequently the model had to be designed lighter than normally but still as stiff. The deck was made of a carbon fiber - cardboard

sandwich laminated with the help of a foam mould. **Figure** shows a typical cross section of the model. Further design details are available in (Terrés-Nicoli J. M., 2002).

The pressure tap layout is shown in **Figures and** .



Placing two accelerometers, one at the end plate and the other at the midspan section, the stiffness of the model was checked. The resulting frequencies for the bending and torsional modes were 42Hz and 48Hz clearly over the highest sprung configuration of 9.78Hz and 6.33Hz.

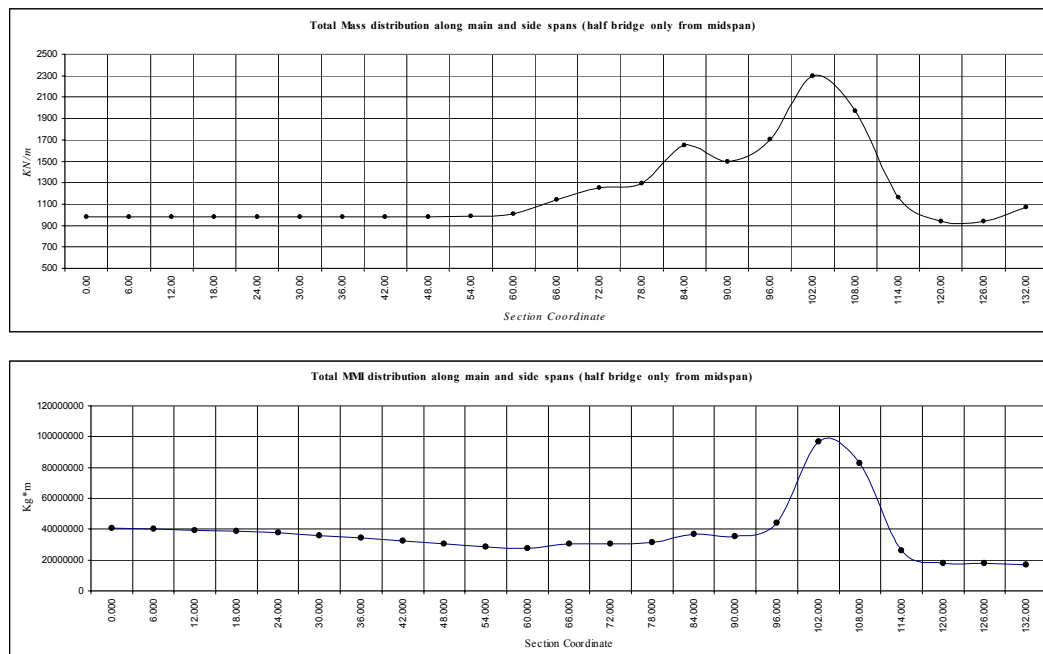


### 3.3.2 The Third Millenium Bridge 1:70 section model

The Third Millenium Bridge with a 216 m main span is not such a two-dimensional structure and consequently the scaling parameters should be selected with great care. The mass distribution along the span varies rapidly compared to long span bridges (see Figure). Consequently the generalized mass defined as:

$$M^* = \int \Phi_1(x) \cdot \Phi_1(x) \cdot m(x) dx = m \cdot L$$

where  $M^*$  is the generalized mass,  $MMI$  the generalized mass moment of and  $\Phi_1(x)=1$  for  $0 \leq x \leq L$ , the vertical lift mode shape differ from the mass per unit length. Question remains on how much arch inertia is actually moved in, for example, torsional modes. A comparison between section model and full scale observed response may answer the question.



Consequently, a generalized mass per unit length is calculated considering the spanwise variation of the mass and the geometry of the mode shape. The resulting value is listed in table

The table below present a summary of the prototype bridge dimensions.

Third Millenium Bridge, Zaragoza, Spain. Cable Stayed, Arch – Boxstring.		
Length	27 + 216 + 27 m	27, side spans. 216 main span.
Chord	42.9 m	Measured in between the side barriers
Depth	3.27m (*)	Midspan.
	6.421m (**)	Midspan, projected.
Chord to depth ratio	13.12 (for *)	
	6.68 (for **)	
Arch height	35.7 m	Over deck at midspan

The main frequencies obtained from the structural modal analysis are listed below table.

Mode nº	Frecq.(Hz)	Shape
1	0.42	Assymetric flexion
2	0.61	Symetric flexion
3	0.72	Symetric torsion
4	0.91	Symetric flexion (3 sines)
5	1.21	Symetric flexion (2 sines)
6	1.53	Assymetric torsion

The prototype characteristics and scales are listed below,

Third Millenium Bridge Prototype Properties			
<b>Damping</b>		0.001	(log decrement)
<b>Mass (min)</b>	Deck/midspan	76544,578	kg/m
<b>Mass (max)</b>	Tablero, arco, pendolas/clave	98087,7	kg/m
<b>MMI (inercia mín torsión)</b>	Tablero/clave	14587135,293	kg-m <sup>2</sup> /m
<b>MMI (inercia máx torsión)</b>	Tablero, arco, pendolas/clave	41385305,303	kg-m <sup>2</sup> /m
<b>Centre of rotation.</b> Obtained from the modal analysis	Measure at midspan from the bottom line of the diaphragm.	1.7360	m
<b>SCALES</b>		Per unit length values	
$\lambda_L = \frac{L_m}{L_p}$	0,0143 (1/70)		
$\lambda_M = \frac{M_m}{M_p}$	2,92E-06	$\lambda_m$	0,000204082
$\lambda_{MMI} = \frac{MMI_m}{MMI_p}$	5,95E-10	$\lambda_{mmi}$	4,16E-08

Given the considerable scaled mass and the complex curved geometry, the model had to be built in carbon fibre composite laminated using a high density curved complex mould (Figure).

Third Millenium Bridge 1:70 section model properties	
Mass per unit length (Kg/m), m	15,621
MIM (per unit length, Kg·m <sup>2</sup> /m)	0,60754416
Mass (Kg),	33,330
MIM (Kg·m <sup>2</sup> )	1,296256221
Radius of gyration (m)	0,197
Centre of gravity (m)	
X <sub>cg</sub> (m)	0.000
Y <sub>cg</sub> (m)	0.0324
Centre of rotation (m)	0.0249

Aluminum fiber composite diaphragms were inserted between the monolithic carbon fiber composite shell of the twin boxes. The canopies along the span were made of polyamide (laser synthesized). Located at the midspan of the model were the corresponding leading and trailing edge pressure modules. These modules allowed for the measurement of the

leeward and windward pressure field by means of short tubes connected to electronic scanners inside the twin boxes. **Figure** shows the windward and leeward pressure tap distribution.

### 3.4 Experimental Set-up

Different experimental set-ups for static and dynamic tests were used in both BLWT I and II at The University of Western Ontario and the CEAMA BLWT I. The **table** attached present a summary of the different dynamic test configurations of the Storebaelt Bridge.

I	Targetted phenomena	Vertical Mode	Torsional Mode	Velocity scale
II	VIV -Torsional	<b>2.28 Hz</b>	<b>6.33 Hz</b>	<b>2.98</b>
III	VIV - Torsional	<b>3.38 Hz</b>	<b>9.04 Hz</b>	<b>2.05</b>
IV	VIV - Vertical	<b>9.78 Hz</b>	n/a	<b>0.69</b>
V	Flutter	<b>1.24 Hz</b>	<b>3.47 Hz</b>	<b>5.45</b>
VI	Flutter	<b>1.78 Hz</b>	<b>4.98 Hz</b>	<b>3.81</b>

Test programs include simultaneous load (pressure) and response measurements, as well as limited hotwire velocity measurements in the near wake. Standard static and dynamic calibration for both vertical and torsional modes were performed prior to each test. Further details regarding the typical setup and procedures are available in (Terrés-Nicoli J. M., 2002).

# Chapter 4:

## Mechanisms of Vortex Induced Vibration

### 4.1 Introduction

The literature on the mechanisms of vertical vortex-induced vibration of bluff bodies is vast, [1], while relatively less research has been carried out for the torsional vortex-induced response. Many of the vortex-induced motions described in the literature are induced by the fluctuating surface pressure field induced by the shedding of vortices into a vortex street. However, the vortex-induced response of bluff bodies can involve other types of vortex structures such as motion induced vortices or vortices traveling across bodies with long chord lengths [2,3]. The case of modern bridge decks can be quite different from typical Kármán vortex shedding, involving streamlined shapes with blunt edges, long afterbodies and oscillating leading and trailing edges. The aerodynamics of these shapes have not been fully resolved.

There have been some attempts to classify bluff bodies for vortex-induced response regarding their cross-sectional shape [2,3,4]. For example, Matsumoto [3] classified the response of square, rectangular and hexagonal cross sections with symmetrical nosings. Different mechanisms are involved in the vortex-induced response depending on cross sectional shape.

There have been a number of bridges which are known to have suffered problems related to vortex-induced oscillations [5]. Among these are the Tokyo Bay Bridge in Japan, with a maximum span of 240 m, and the Kessock Bridge in the U.K. which exhibited the previously unobserved torsional vortex-induced response. The Storebaelt Bridge in Denmark is the focus of the present work. The Storebaelt Bridge exhibited unacceptably large amplitude vertical oscillations under the effect of remarkably low turbulence intensity wind (as low as 2%) [6]. The cross section of the Storebaelt is similar to many other modern long span suspension bridges, so it is the aim of this work to provide some insights into the mechanisms of the complex fluid-structure interaction responsible for the torsional



vortex-induced response. An extended report of this research can be found in Terrés-Nicoli, 2002, [5]. The mechanisms involved with the lift mode will also be reported elsewhere [7].

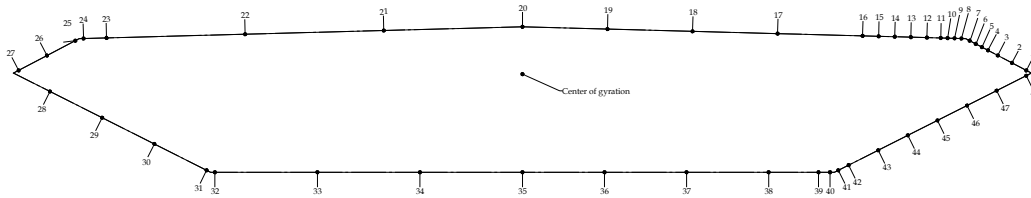


Figure 4-2. Cross section of the model showing the pressure tap layout for one of the “rings” of taps.

## 4.2 Experimental work

A 1:70 scale section model was built and tested in smooth ( $I_u=0.5\%$ ), uniform (1.0%), stationary flow in Boundary Layer Wind Tunnel I at the University of Western Ontario, Figure 4-1 shows a sketch of the model with the taps locations. The model design of carbon fibre with a paper honeycomb sandwich permitted allocating electronic pressure scanners inside the relatively light model. Rigs of different stiffnesses were set-up for the different type of response, allowing comparisons with experimental results already available in the literature.

### 4.2.1 Model Response: Displacements

Vertical displacements and rotation of the model were obtained for all the tests using of a set load cells, as described in Chapter 2. Three different spring system were set up. Two of these, rig 1 and rig 3, were to investigate the vortex-induced response, the other was to investigate the flutter limit. The entire set-up in the tunnel was checked by comparing the present data with previous experiments at different scales and different laboratories. For the vortex-induced response, the stiffer set-up allowed the acquisition of pressure time series for all stages of the build up phases (for both increasing and decreasing wind speeds). The hysteresis in the response was investigated with the softer set-up.

#### 4.2.1.1 Aeroelastic instabilities

The response of the model until the flutter limit wind speed for  $0^\circ$  angle of attack was investigated. The vertical and torsional responses are presented in Figure [4-1]. RMS values for the rotation for wind speeds higher than 50 m/s (f.s.) are not to be trusted since some measured values were found equal to the maximum voltage of the acquisition system. These were not repeated due to time constraints.

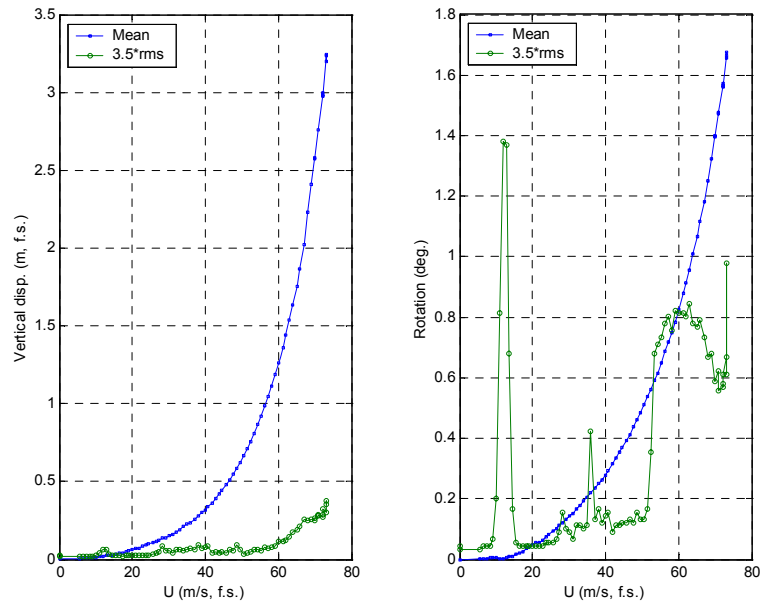


Figure [4- 1]: General response observed in the sectional model from 0 until flutter stability wind speed.

The response is characterized by an increasing mean positive rotation with increasing wind speed. The model exhibited clear signs of instability at a full scale wind speed of 73 m/s. The instability is a coupled torsional and vertical motion. The resulting motion was clearly observed as a rotation about a longitudinal axis approximately 1.2 m (f.s.) upstream of the leading edge. This flutter limit is compared with that found by others Table [4-1]. Clearly, the present experiments are consistent with the earlier ones.

The onset of “Flutter Instability” is defined here as when the response changed from random to periodic just prior to the instability. This was identified through the examination of the “peak factor”, defined as the ratio of the largest observed reading during the sample period to the RMS of the sample. A normal, random signal has a peak factor of about 3.5, while a sinusoid has peak factor of  $\sqrt{2}$ . A peak factor of less than 2 was selected as the criteria to terminate the run. A peak factor of 3.5 is commonly assumed in Gaussian processes, thus, 3.5 times the RMS value was plotted.

Even though each of the results presented in Table [4-1], were obtained with different values of structural damping, the flutter limit did not change much. Computer numerical simulations have predicted values for the flutter limit in this range. Frandsen [17] found the flutter limit for the bridge, as built, with the guide vanes, to be 65 m/s. This, to the author’s knowledge, is the only estimate of the flutter limit for the bridge as built available in the literature, without the benefit of experimental validation.

	Model Scale	Iu (%)	Damping (% of critical)	Flutter limit (m/s)
BLWTL sectional model (present)	1:70	0.5	0.33	73.3

BLWTL taut strip model (1991)	1:300	6	1.5	72
DMI (1990)	1:80	0	1	73.9
DMI full aero (1992)	1:200	6	0.5	70

Table [4- 1]: Comparison of observed flutter limit in different experiments.

Three torsional vortex-induced oscillation peaks can be observed in Figure [41] at full-scale wind speeds of 11.9, 28.3 and 36.0 m/s. With the given wind speed resolution of the present set-up the vertical peak does not appear.

#### 4.2.1.2 Vortex-induced response

The vortex-induced response was first investigated using a softer rig (rig 1). Figure [4-2] shows normalized vertical displacements and rotation. A vertical vortex-induced response peak was detected at reduced wind speed of  $V_r=1.34$  (4.1 m/s, f.s.). Two torsional vortex induced response peaks were observed at  $V_r$  of 1.74 and 2.49 respectively.

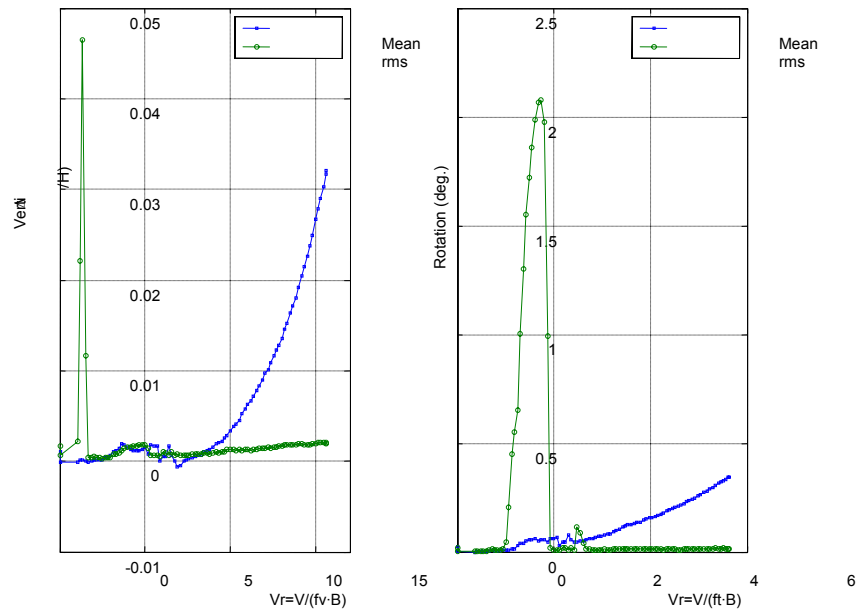


Figure [4- 2]: Vertical and torsional vortex induced response observed in rig 1.

With the resolution of this rig, the lock-in range, especially for the vertical response was found to be narrower than what was found in previous research and full-scale monitoring (see Chapter 1). In addition, it was not possible to measure pressure for any of the build-up phases for either vertical or torsional vortex-induced response due to potential measurement errors due to low wind tunnel speeds. A detailed study could not be conducted using this set-up and thereby a stiffer rig was set-up. This new rig (#3) was

designed so that the maximum wind speed in the wind tunnel would coincide with the end of the plateau range of the torsional response.

Figure [4-3] shows vertical and torsional response of the model mounted on rig 3/1 using an increasing wind speed.

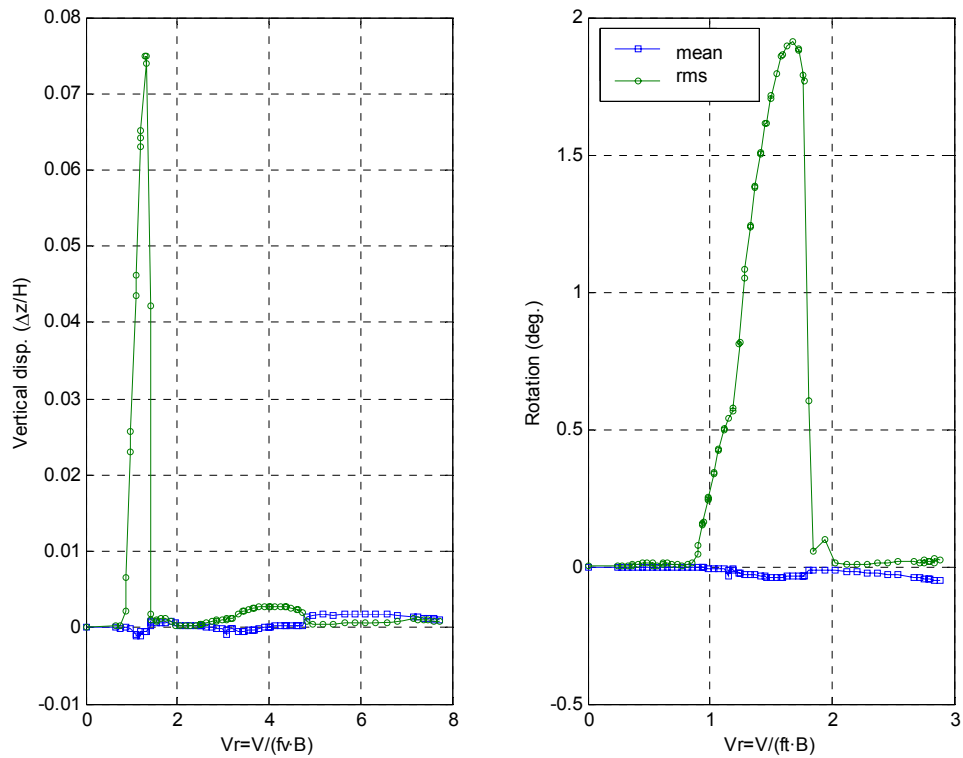


Figure [4- 3]: Vertical and torsional vortex induced response observed in rig 3.

The sample time for each data point was 90 s, which is three times that used for data in Figure [4-2]. More data points were also acquired. The vertical response peaked at  $V_r=1.31$  (4.0 m/s f.s.). The maximum amplitude was significantly higher than found for the softer rig. The rotation shown in Figure [4-3], reached its maximum amplitude at  $V_r=1.68$ . The higher structural damping in the torsional mode of the stiffer set-up could be pointed as the cause of the lower amplitudes reached. It can be observed that the second torsional peak seems to approach a lower wind speed, falling into the lock-in range of the primary one.

#### 4.2.1.1.1 Vertical vortex-induced response

Figure [4-4] shows the different vertical response found when the critical wind speed ( $V_{cr}$ ) was approached from a higher wind speed (decreasing WS) compared to that when it was approached from a lower wind speed (increasing WS).

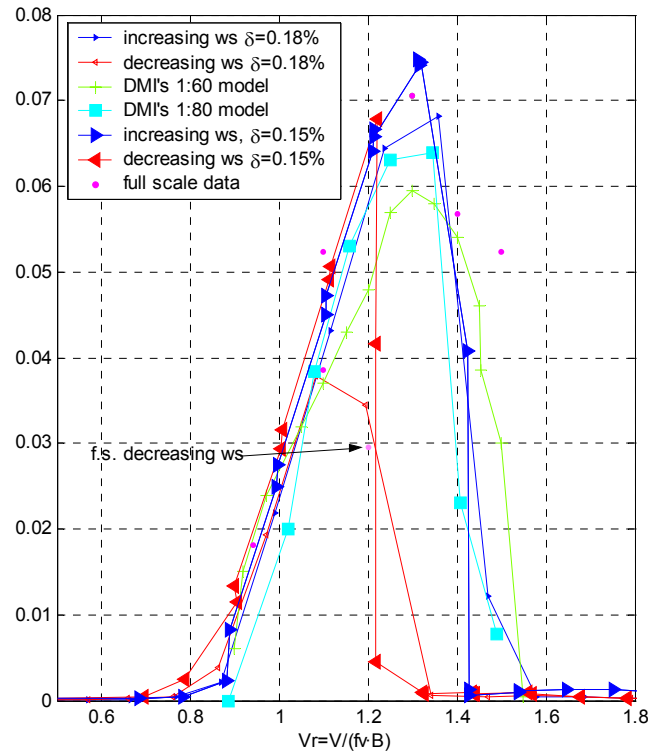


Figure [4- 4]: Vertical vortex-induced response. Observed response for two different damping ratios compared with DMI's results and full scale measurements.

It is observed that  $V_{cr}$  is smaller ( $V_r = 1.22$ ) for decreasing wind speed compared to that for increasing wind speed ( $V_r = 1.31$ ). The maximum amplitude observed was smaller when the wind speed was decreased.

The onset wind speed of the vortex-induced oscillations will be referred to as  $V_{or}^+$  when the critical wind speed was approached from lower wind speeds (increasing wind speed) and as  $V_{or}^-$  when the critical wind speed was approached from higher wind speeds (decreasing wind speed). In advance, the super index “+” will be used for increasing wind speed and “-” for decreasing wind speed. For instance,  $V_{cr}^+$ , denotes the critical wind speed for the case of increasing wind speed.

Rig 3 was set-up in the tunnel when a second campaign of experiments (rig 3/2) was carried out. A slightly higher damping ratio of  $\delta=0.18\%$  was measured compared to the  $0.15\%$  measured in the previous set-up (rig 3/1). Results of both set-ups are presented in Figure [4- 4]. The onset reduced velocity of the vertical vibrations  $V_{or}^+$ , was  $=0.88$  for the lower damping case and  $V_{or}^+=0.87$  for the higher damping. The critical wind speeds,  $V_{cr}^+$  were  $1.31$  and  $1.36$ . These differences are probably due to a slight shift in the wind speed steps

for the fan controller from those in the earlier run, combined with a relatively coarse resolution (response measured for less reduced wind speed steps within the same range). A smaller maximum amplitude was observed, possibly due to the slightly higher structural damping measured ( $\delta=0.18\%$  compared to  $\delta=0.15\%$ ) or the coarse velocity resolution. The effect of this was more significant for a decreasing wind speed than for an increasing one.

The presented results are also compared in Figure [4-4] to other section model studies carried out at DMI and in full-scale monitoring [15]. Results from the different studies, including full-scale, are all in reasonably good agreement. This is also the case for the response to a decreasing wind speed where only full-scale and the present results were available<sup>40</sup>. The differences between maximum amplitudes for the different section model tests might be due to different values of the structural damping ratio and turbulence levels in the wind tunnels. The highest maximum amplitude,  $\frac{\Delta z}{H} = 0.075$  (Figure [4-4]) was observed for the minimum structural damping ratio in all the experiments available. The maximum normalized full scale amplitude was reported by Frandsen [15].

Figure [4-5] shows how the critical wind speed found fits into Komatsu & Kobayashi's [29] results for rectangular cylinders. Note that the reduced velocity in this plot is calculated using the depth of the section; hence,  $V_r=9.5$ . It can be observed that the critical response matches with the case, for

$$V_{cr} = 1.2 \frac{B}{H} + 0.5 \quad (3.1)$$

and the work done by the pressure at the upper surface changes from negative to positive at the quarter point of the width from the trailing edge [29]. Assuming that a similar pattern occurs at the bottom surface for vertical vibration, this would explain the success of the guide vanes installed after construction in reducing the vertical vortex-induced oscillations.

---

<sup>40</sup> See response for a decreasing wind speed at  $V_r = 1.2$ . The full-scale measurement at a decreasing wind speed is in good agreement with what was observed in the experiments.

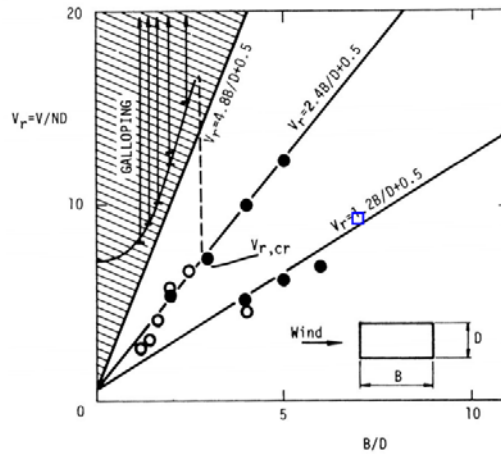


Figure [4-5]: Critical wind speed observed for rectangular cylinders (from Komatsu & Kobayashi [29]). The present experiment is indicated with a  $\square$ .

## 4.2.2 Torsional vortex-induced response

A large amplitude, highly fluctuating rotation was observed when the model was tested in each of the rigs. In the softer one (rig 2) two additional peaks were observed as noted earlier (Figure [4-1]). The rotation response observed was characterized by a relatively wide lock-in range (0.95-1.85) and significantly different response curves for decreasing and increasing wind speeds.

### 4.2.2.1 Hysteresis study

The rate at which the response built up was studied in rig 1. This could be interpreted as a study of the rate at which an increment in the energy of the incoming flow is transformed in an increment of the amplitude of the oscillations. Figure [4-6] shows the observed response for different sample times, 90, 60 and 30 seconds (left, centre, right respectively). These times would be approximately 3000, 2000 and 1000 seconds in full scale, since the time scale is given by,

$$\lambda_T = \frac{1}{\lambda_f} = \frac{f_m}{f_p} = \frac{9.033}{0.271} = 33.33 \quad (3.2)$$

It is observed that the onset and critical velocities were not affected by the change in the sample time. The amplitudes of maximum oscillations were not affected in the response to an increasing incoming wind speed. In contrast, for a

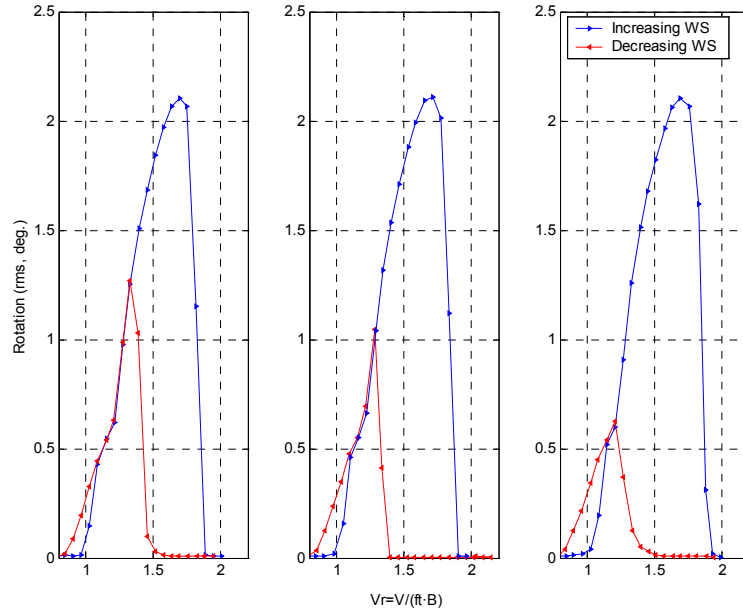


Figure [4- 6]: Observed torsional vortex induced response for different sample times, 90, 60 and 30 s (left, center and right, respectively).

decreasing wind speed it was found that the maximum amplitudes of oscillation are clearly sensitive to the build-up time; lower amplitudes for  $V_{cr}^-$  were found for the lower sample times. The increase in the amplitude with sample time ( $t$ ) is presented in Figure [4-7]. It can be observed that the amplitude of  $V_{cr}^-$  as a fraction of  $V_{cr}^+$  grows rapidly with sample time and tends to an asymptotic value of approximately 0.9.

As has been mentioned, the set-up in rig 1 did not allow acquiring pressure time series due to high measurements errors at low wind tunnel speeds. Therefore, the model was set-up in rig 3. A structural damping of  $\delta=0.33\%$  was measured in the first set-up in rig 3. The torsional responses from rig 1 and rig 3 are compared in Figure [4-8].



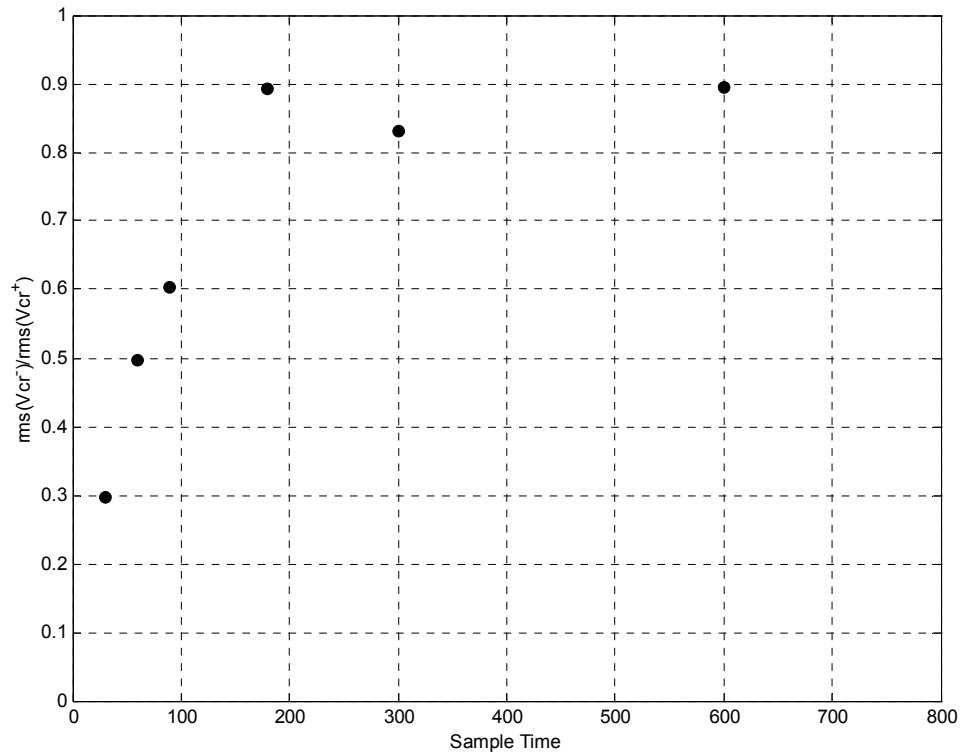


Figure [4- 7]: Variation in the response amplitude with the sample time.

The amplitude of oscillations at  $V_{cr}$  are reduced by 0.1 due to the increase in  $\delta$  by 60%. Again, for the higher  $t_c$  case, the amplitude of oscillations at  $V_{cr}^-$ , increase with respect to the amplitude at  $V_{cr}^+$ . For  $t_c=180$  (not shown), the response at low  $V_i$  coincides for increasing and decreasing wind speeds. The onset wind speeds ( $V_{or}^+$  and  $V_{or}^-$ ) are the same in both cases.

The torsional response is compared to that obtained in the tests of the 1:80 section model at DMI, in Figure [4-9]. Amplitudes from DMI experiments were less than half of those observed in the present research. Only response to an increasing wind speed is available, to the author's knowledge. A coarser velocity increment, lower sample time, a higher structural damping, and Reynolds number effects might be pointed out as the reason for these differences.

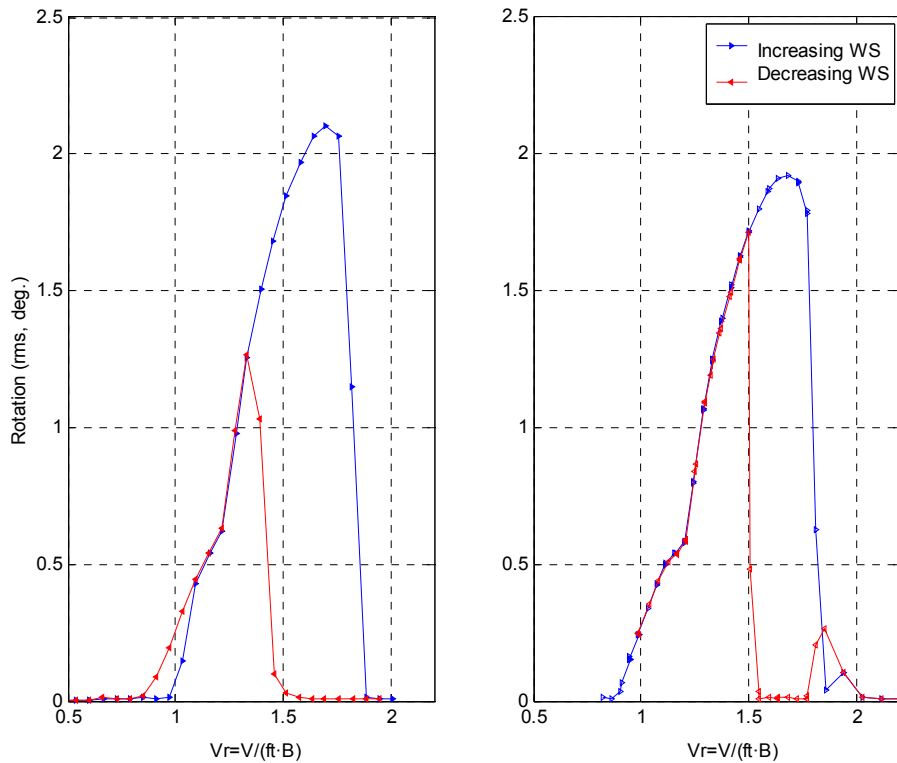


Figure [4- 8]: comparison of torsional response in rig 1 (left) and rig 3/1 (right).

The effect of the history of the loading on the response was studied. Figure [4-9] shows the amplitudes of the rotation observed when the wind speed was increased to a certain wind speed from zero very rapidly. At this wind speed, the response was sampled in three consecutive 90 s blocks. For  $V_r < 1.5$ , the rms values of the last two samples were the same. Thus, the stationary state was then reached some time between 90 and 180 seconds. The stationary<sup>41</sup> state [65] reached was, in any case, close to the amplitude of the other experiments in which wind speed was increased gradually. For  $V_r = 1.5$ , the stationary state was only reached during the last sample. No oscillations were observed within the 3 samples when the wind speed was increased up to a  $V_r > 1.5$  or likewise  $V_r > V_{or}^-$ .

#### 4.2.2.2 Description of the torsional response domains

All the observed torsional responses discussed to this point are presented together in Figure [4-10]. The onset wind speeds labeled “1” ( $V_{or}^+$ ) and “6” ( $V_{or}^-$ ) are similar for all tests. However, between these, different paths could be obtained by changing the sample time, the rate of change in the wind speed and the sign of this rate. In contrast, it appears that in the range of  $V_r$  bound by “5”, “6”, “3” and “4”, only two solutions are possible for a

<sup>41</sup> Stationary here, should be understood in terms of second order statistics for the last 90 seconds. Higher order statistics are not available.

given structural damping; one if the wind speed is increasing; and the other (no oscillation) if the wind speed is decreasing.

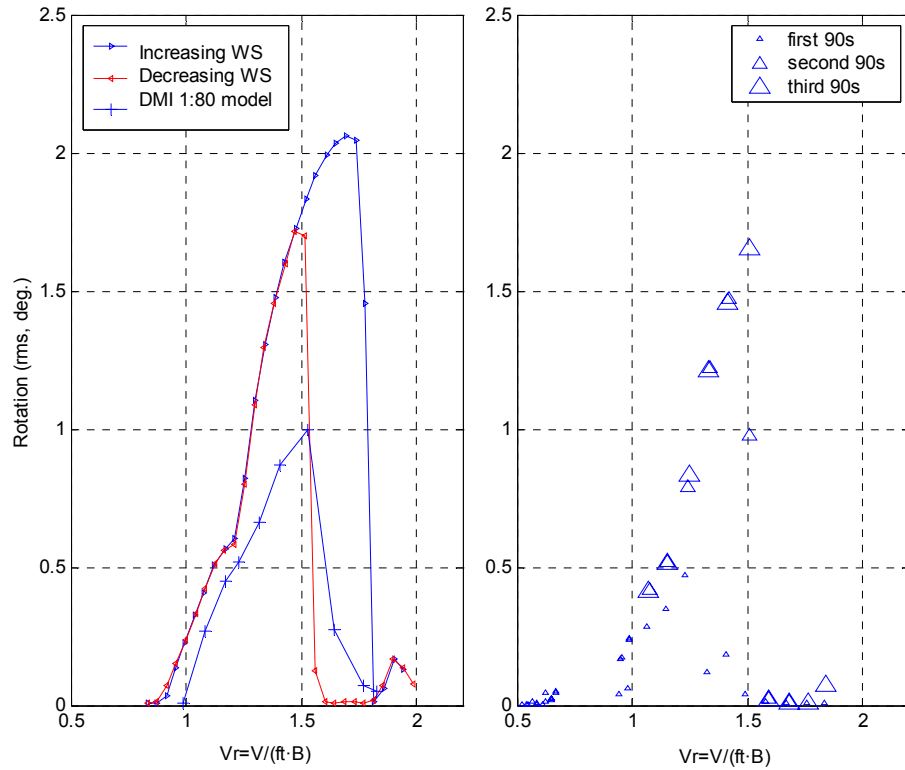


Figure [4- 9]: Left, comparison of torsional vortex induced response in rig 3/2 and DMI results. Right, study of the effect of the rate and magnitude of change of wind speed in the response.

At “2”, the slope of the response curve changes. One could think about it in terms of energy. Part of the energy in the incoming flow is transformed through the fluid-structure interaction into motion of the model. These mechanisms are still poorly understood in the literature. After “2”, for an increasing wind speed, the rate at which the energy of the incoming flow is transformed into motion appears to be greater since the response increases at a greater rate. One could infer that at this inflection in the curve, the energy transfer mechanism from the flow to the structure has changed and that a significant change also occurs in the flow field around the bridge deck. This is investigated in Chapters 4 and 5.

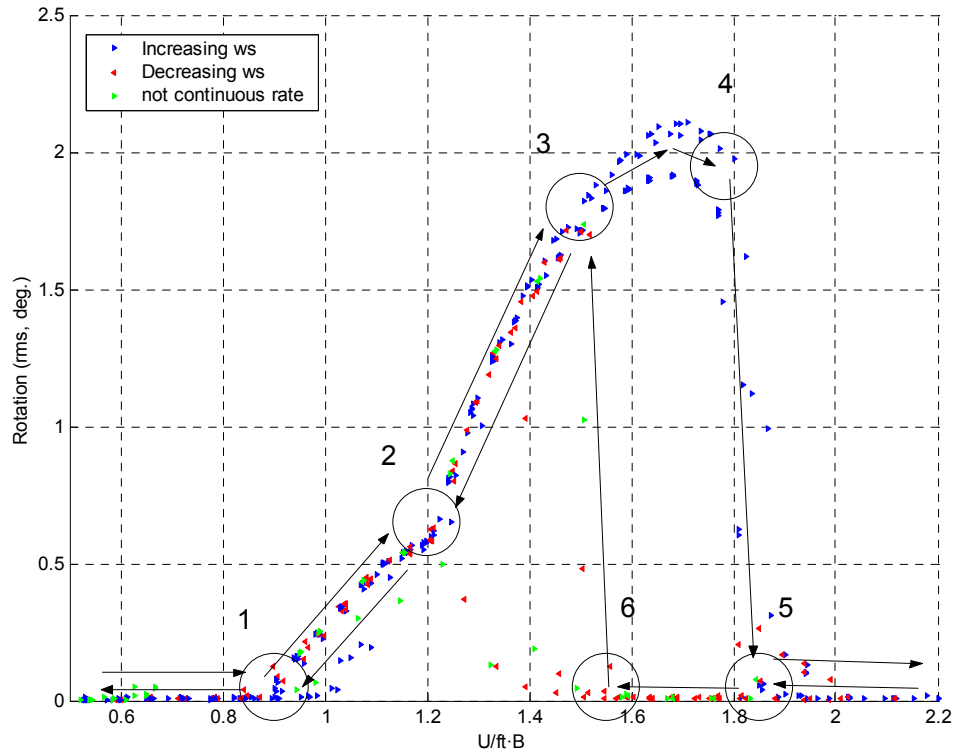


Figure [4- 10]: Torsional vortex induced response domain from the present experiments.

The torsional vortex-induced response of the present experiments is superimposed in the domain proposed by Shirashi & Matsumoto [30], and is presented in Figure [4-11]. Their research classified the vortex-induced response into three groups. The star corresponds to the torsional response and the circle for the vertical. The torsional response as determined in the current experiments, follows:

$$V_{\alpha} = 1.67 \frac{B}{H}. \quad (3.3)$$

Equation (3.3) was derived in [30] assuming that separated vortices from the leading edge reach the trailing edge after  $\Delta t = ((2n-1)/2)T_v$  with  $n=1,2,3,\dots$  where  $T_v$  is the period of the oscillation. According to this classification, the present bridge would belong to that called Group 2. Group 2 corresponds to those bridges where motion is induced by the combined action of motion induced vortices and Kármán vortices. However, Group 2 corresponds to rectangular deck cross sections and Group 3 to hexagonal ones, so the classification may be too simple.

$$\frac{V_{cr} B}{D}$$

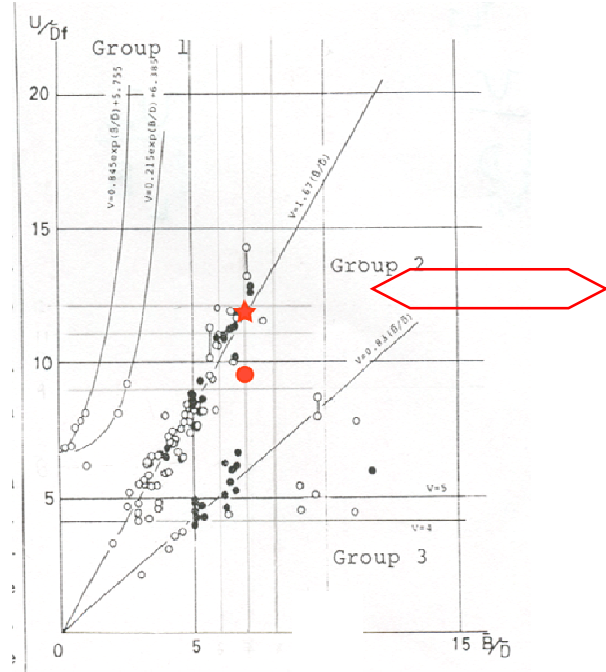


Figure [4- 11]: Observed vertical and torsional vortex-induced response in the domain proposed by Shirashi and Matsumoto [30]. The star and larger circle represent, respectively, the torsional and vertical response in the present experiments.

The onset wind speed for vertical and torsional vortex-induced vibrations,

$$V_{or} = \frac{U_{ov}}{Bf_v} \quad , \quad V_{or} = \frac{U_{ot}}{Bf_t} \quad , \quad (3.4)$$

respectively, were the same, being about 0.9. In equation (3.4),  $U_{ov}$  and  $U_{ot}$  are the model-scale onset wind speeds of the vertical and torsional vortex-induced vibrations respectively.

The measured force was divided onto in-phase and out of phase component in order to investigate the energy transfer capabilities of the system. The procedure followed is summarized below,

Let  $d(t)$  be the instantaneous vertical non-dimensional displacement defined as a fraction of the bridge's deck thickness at the center line,  $D$ .  $d(t)$  can be defined as the sum of two components,

$$d(t) = \langle d \rangle + d'' \quad (1.1)$$

where  $\langle d \rangle$  is the phase averaged periodic displacement and  $d''$  the random component. Let's assume that the phase averaged displacement ( $\langle d \rangle$ ) can be represented as,

$$\langle d \rangle = \widehat{\langle d \rangle} \cos(2\pi f_L \langle t \rangle) + \bar{d} \quad (1.2)$$

where  $\widehat{\langle d \rangle}$  is half the phase averaged amplitude of the response,  $f_L$  is the response frequency,  $\langle t \rangle$  is the corresponding phase averaged time with  $\langle t \rangle \in [0, T]$  (where  $T = \frac{1}{f_L}$ ) and  $\bar{d}$  is the mean vertical displacement.

The lift coefficient,  $C_L(t)$ , is defined as:

$$C_L(t) = \frac{F_L(t)}{\frac{1}{2}\rho U^2 B} \quad (1.3)$$

where  $F_L$  is the lift force,  $U$ , the free stream wind speed,  $\rho$ , the air's density and  $B$  the bridge's deck width measured from the leading edge to the trailing edge. It is assumed that the phase average of it can be represent as,

$$\langle C_L \rangle = \widehat{\langle C_L \rangle} \cos(2\pi f_L \langle t \rangle + \phi) + \overline{C_L} \quad (1.4)$$

where  $\widehat{\langle C_L \rangle} = (\langle C_L \rangle_{\max} - \langle C_L \rangle_{\min})/2$  and  $\phi$  is the phase angle by which the lift load lead the response. It is remarked that  $\widehat{\langle C_L \rangle}$ ,  $\widehat{\langle d \rangle}$  and  $\phi$  are unknown, not continuous, functions of the reduced wind speed defined as for example,

$$\phi = \begin{cases} \phi_1(V_r^+) & \forall V_r > 0 \\ \phi_2(V_r^-) & \forall V_r < 0 \end{cases} \quad (1.5)$$

$C_L(t)$  is obtained as a result of the integration of the pressures measured around the bridge's deck at each pressure tap  $i$ . If it is assumed that the pressure coefficient at tap "i" varies harmonically, it can be represented as,

$$\langle C_{p_i} \rangle = \widehat{\langle C_{p_i} \rangle} \cos(2\pi f_L \langle t \rangle + \phi_i) + \overline{C_{p_i}} \quad (1.6)$$

one can then define  $\langle C_{p_i} \rangle$  as the sum of two components,

$$\langle C_{p_i} \rangle = \langle C_{p_i}^I \rangle + \langle C_{p_i}^O \rangle \quad (1.7)$$

where,  $\langle C_{p_i}^I \rangle$  and  $\langle C_{p_i}^O \rangle$  are the in-phase and out-of-phase, phase averaged pressure coefficient at tap “i” defined as,

$$\begin{aligned} \langle C_{p_i}^I \rangle &= \overline{\langle C_{p_i}^I \rangle} \cos(2\pi f_L \langle t \rangle) + \overline{C_{p_i}^I} \\ \langle C_{p_i}^O \rangle &= \overline{\langle C_{p_i}^O \rangle} \cos(2\pi f_L \langle t \rangle + \frac{\pi}{2}) + \overline{C_{p_i}^O} \end{aligned} \quad (1.8)$$

whith  $\overline{\langle C_{p_i}^{I,O} \rangle}$  being  $(\langle C_{p_i}^{I,O} \rangle_{\max} - \langle C_{p_i}^{I,O} \rangle_{\min})/2$  respectively and defined as:

$$\begin{aligned} \overline{\langle C_{p_i}^I \rangle} &= \overline{\langle C_{p_i} \rangle} \cos(\phi_i) \\ \overline{\langle C_{p_i}^O \rangle} &= \overline{\langle C_{p_i} \rangle} \sin(\phi_i) \end{aligned} \quad (1.9)$$

which are the projections on the horizontal and vertical axis of the corresponding vector,  $\langle C_{p_i} \rangle$  in the phase diagram (see Figure).

It follows by combining Eqns. (1.8) and (1.9) that,

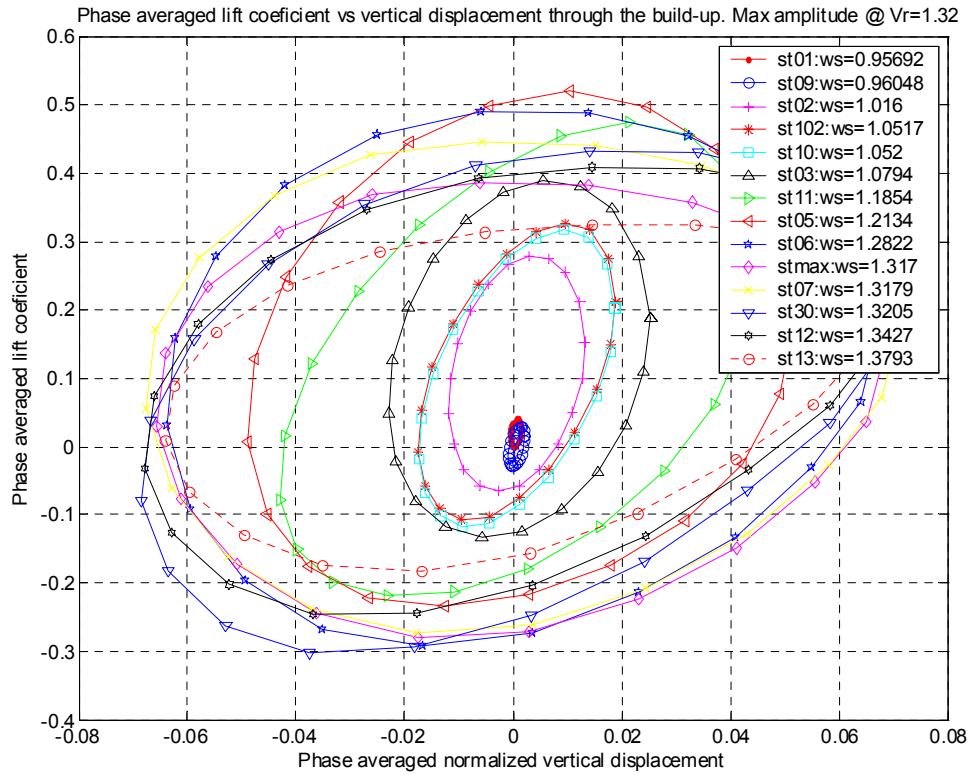
$$\begin{aligned} \langle C_{p_i} \rangle &= \overline{\langle C_{p_i}^I \rangle} \cos(2\pi f_L) + \overline{C_{p_i}^I} - \overline{\langle C_{p_i}^O \rangle} \sin(2\pi f_L) + \overline{C_{p_i}^O} = \\ &= \overline{\langle C_{p_i} \rangle} \cos(\phi_i) \cos(2\pi f_L) + \\ &+ \overline{C_{p_i}^I} - \overline{\langle C_{p_i} \rangle} \sin(\phi_i) \sin(2\pi f_L) + \overline{C_{p_i}^O} = \\ &\overline{\langle C_{p_i} \rangle} \cos(2\pi f_L \langle t \rangle + \phi_i) + \overline{C_{p_i}^I} + \overline{C_{p_i}^O} \end{aligned} \quad (1.10)$$

Which proves that the components defined as in (1.8) checked the definition of  $\langle C_{p_i} \rangle$  in (1.7) and the mean are related as,

$$\overline{C_{p_i}} = \overline{C_{p_i}^I} + \overline{C_{p_i}^O} \quad (1.11)$$

The work done by the pressure at each tap will be the sum of the work done by each component, in-phase and out-of-phase. It is known that the work done by a force acting at the same frequency and in-phase with the response is null (see for example Hartog, D). One might expect this pressure ( $\langle C_{p_i}^I \rangle$ ) to be caused by the actual relative body's motion. Therefore all the work is done by the out-of-phase component and will be positive if the corresponding force at tap "i" or negative if it is negative.

The Figure below presents the evolution of the loading response diagrams throughout the built up phase. The fascinating capability of the system transferring energy from the flow around into body motion is exhibited.





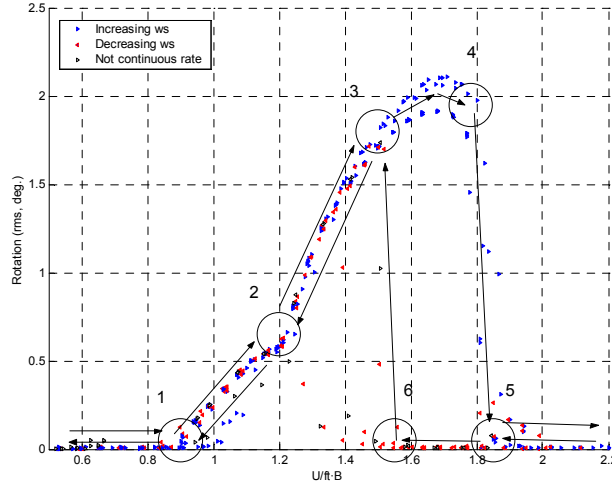


Figure 4-13. Measured torsional responses at different increasing and decreasing wind speeds and set-ups.

Figure 4-12 presents the measured responses for the torsional mode versus the reduced velocity,

$$V_r^{+/-} = \frac{U}{f_t \cdot B}$$

where  $U$  is the mean wind tunnel speed,  $f$  is the torsional natural frequency and  $B$  is the deck width (chord). Increasing wind speeds are denoted with the superscript “+”, while decreasing are “-”. Different responses were observed when the critical wind speed was approached from lower wind speeds compared to that when it was approached from higher wind speeds.

### The onset of the oscillations

Figure 4-13 shows that a nearly sinusoidal response was observed at the onset of the torsional oscillations. This occurred at a reduced wind speed of  $V_r^+=0.9$  when the critical wind speed was approached from lower wind speeds (increasing wind speed) and at  $V_r^-=1.6$  for decreasing wind speeds (Figures 4-13(a) and 4-13(b)). Figures 4-13(c) and 4-13(d) present spectra of the torsional response at the onset wind speeds, for both increasing and decreasing wind speeds. The figures show distinct peaks at different frequencies. The peak at 9 Hz, corresponds to the torsional natural frequency. The peak at 11.4 Hz occurred when the critical wind speed was approached by increasing the wind speed ( $V_r^+=0.9$ ), while the peak at 21.9 Hz occurred when the critical wind speed was approached by decreasing the wind speed ( $V_r^-=1.5$ ). These two peaks correspond to a Strouhal number of  $St=0.20$ , where  $St$  is defined as:

$$St = \frac{n \cdot D}{U}$$

$n$  is the vortex shedding frequency, and  $D$  is the depth. Values of  $St$  around this value have been obtained for the vertical vortex-induced oscillations using a numerical simulation with a very fine mesh [8, 9], however other authors have reported lower values. The final peak at 27 Hz is the second harmonic of the torsional natural frequency. Comparable energy was observed, respectively, for the onset wind speeds in the lift coefficient and response at the above mentioned two frequencies.

Figures 4-14(a) and 4-14(b) show the spectra of pressure coefficients measured at the trailing edge for the onset wind speeds. These spectrum show a peak at 11.4 and 21.9 Hz respectively consistent with the above mentioned for the response, associated with the same Strouhal number of 0.20. Spectra of pressure coefficients measured at other locations on the bridge section or at same location, but with larger amplitude oscillations, did not produce these peak frequencies. In addition, a peak at 21.9 Hz, for  $V_r^+=1.6$ , can be observed in the spectrum of hot wire measurements recorded near the trailing edge (Figure 4-14(c)). Therefore, it appears that vortex shedding at the trailing edge may be responsible for the response at onset wind speeds.

The correlation between the pressure on the upper flange at the trailing edge and the moment coefficient shown in Figure 4-14(d) is also consistent with the hypothesis of having vortex shedding at the trailing edge causing the onset of the oscillations. The correlation of the pressure at the trailing edge with the moment coefficient ( $\rho_{p27m}$ ) increases up to a certain wind speed around  $V_r^+=1.2$  and then decreases as the response builds up and another driving mechanism takes over (which will be described below). However, one would expect the onset for increasing wind speed to occur near the wind speed that matches the natural frequency to the Strouhal number (i.e.,  $V_r^+=0.7$ ), in contrast with the observed  $V_r^+=0.9$ . It appears that at  $V_r^+=0.7$  there is not sufficient energy in the fluctuations to get the deck moving. This hypothesis was testing in the wind tunnel by matching the  $f$  and  $n$  and then exciting the deck manually. When this was done, onset began.

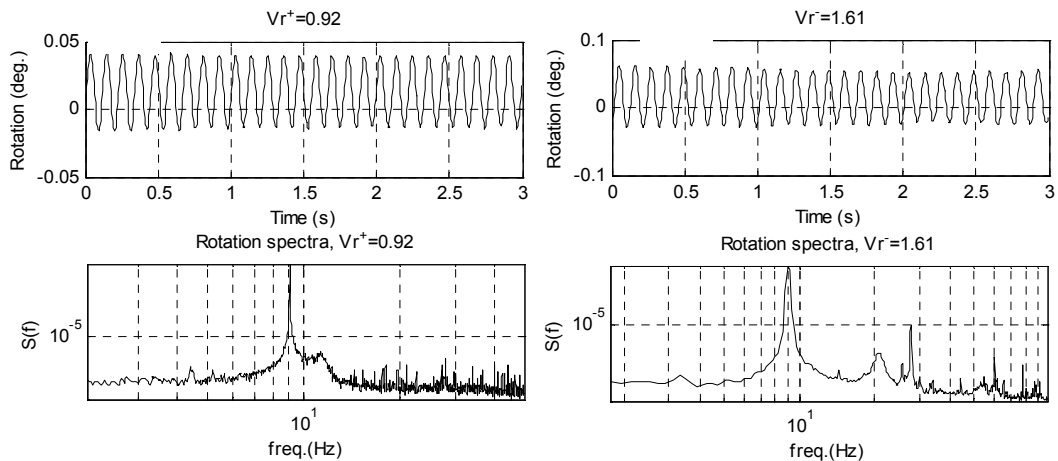


Figure 4-14. (a) and (b) show the torsional response at the lower and upper onset wind speeds, respectively (c) and (d) present the spectra of such responses.

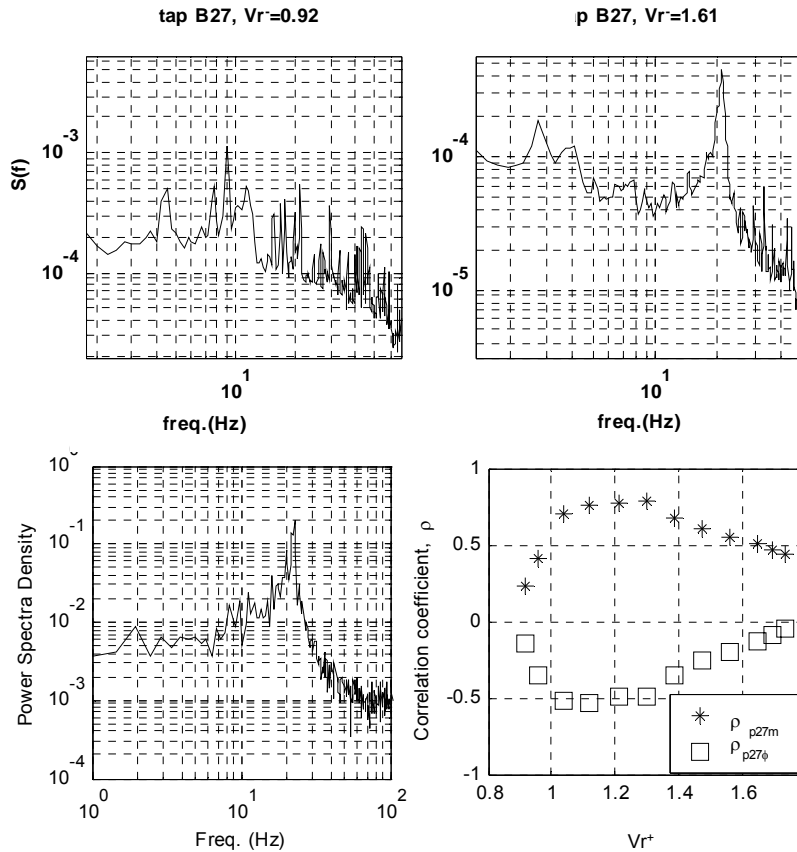


Figure 4-15. (a) and (b) show the spectra of the pressure on the upper flange of the leading edge near the onset of the oscillations for increasing and decreasing wind speed respectively. (c) presents the spectra of the v-component of the velocity in the near wake near the onset of the oscillations for decreasing wind speed. (d) correlation of the pressure on the upper flange of the trailing edge and the moment coefficient and the torsional response.

## BUILD-UP MECHANISMS

### 4.1 Maximum amplitude oscillations

Significant hysteresis can be observed in Figure 4-12. The maximum amplitude rotations (rms,  $\tilde{\phi} = 2.1$ ) are observed for a critical reduced wind speed of  $V_r^+ = 1.7 = V_{cr}^+$ . In sharp contrast, no response is observed for the same wind speed when it was approached from higher wind speeds. The largest amplitudes between points “3” and “4” could only be reached, no matter the sampling time, by following the path “1” - “2” - “3”. In contrast, several statically stationary states of response within  $V_r^+ = 0.9$  and  $V_r^+ = 1.5$  (“1” and “3”) could be reached. Harmonic oscillations at the model’s natural frequency were observed within the considerable range of  $0.9 \leq V_r^+ \leq 1.8$ , and small amplitude ones at the first harmonic frequency (18Hz) within a small range around  $V_r^+ = 1.9$ .

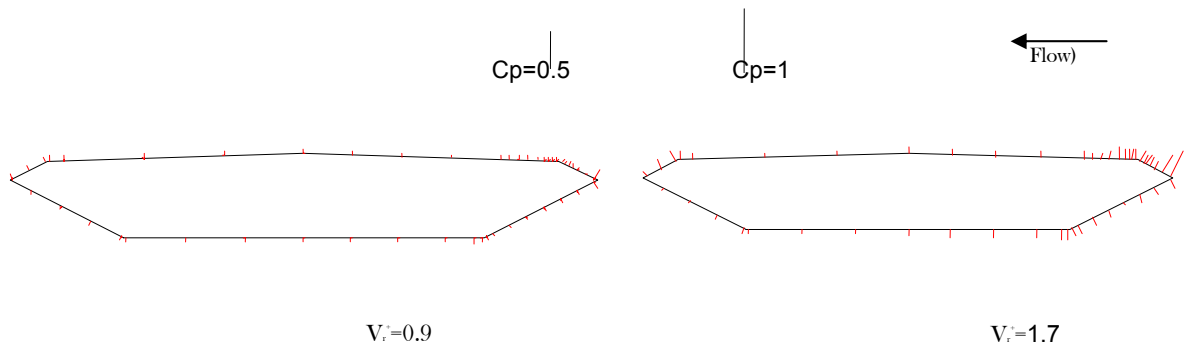


Figure 4-16. Root mean square (rms.) pressure coefficient for a reduced wind speed of (a) 0.9 and (b) 1.7.

Figure 4-15 shows the fluctuating (rms.) surface pressure distribution around the deck at maximum amplitude oscillations compared to that at the onset of the oscillations. Highly fluctuating pressure is observed at the leading edge's upper flange, especially near the edge. Mean negative pressure (suction) areas are observed at the upper flange's leading edge's upper and bottom corner and on the upper flange of the trailing edge. One can associate these with separated flow zones.

#### 4.2 Surface pressure field

The study of the pressure field utilized the phase averaging technique [9], with the rotation as the reference signal. Figure 4-16 shows the phase averaged pressure coefficient of a tap near the leading edge on the upper surface during the build-up for increasing wind speeds. This figure shows the remarkably high fluctuating pressure on the leading edge's upper flange through the build up stages of the response. It is observed that during the higher amplitudes oscillations there is a small change in phase with respect to the rotation, which is within the resolution of the phase averaging technique. For maximum amplitudes oscillations, the pressure coefficient varies from about -1 to +1. The pressure field on this particular area plays a major role in the build up of higher amplitude oscillations. In fact, negative pressures (suction) in this area of the deck are observed for wind speeds higher than that corresponding to the inflection point in the response curve. This could explain why the loading path "1" - "2" - "3" is required to reach maximum amplitude oscillations, since a certain amplitude of motion may be needed to cause separation near the edge.

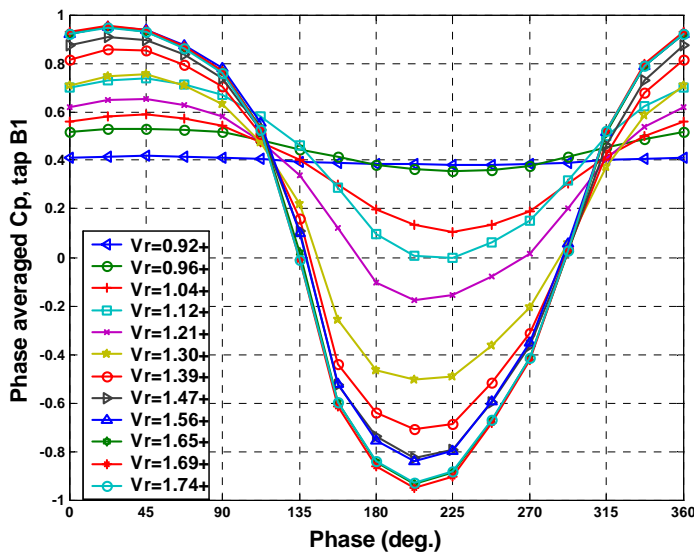


Figure 4-17. Phase averaged pressure coefficient on the upper flange near the leading edge through the build-up phases of the response for increasing wind speed.

The phase between the loading (moment coefficient) and the response (rotation) remains unchanged ( $180^\circ$ ) through the build up phases of the response, in contrast with the constant  $90^\circ$  degrees phase of a typical resonant mechanical response [10].

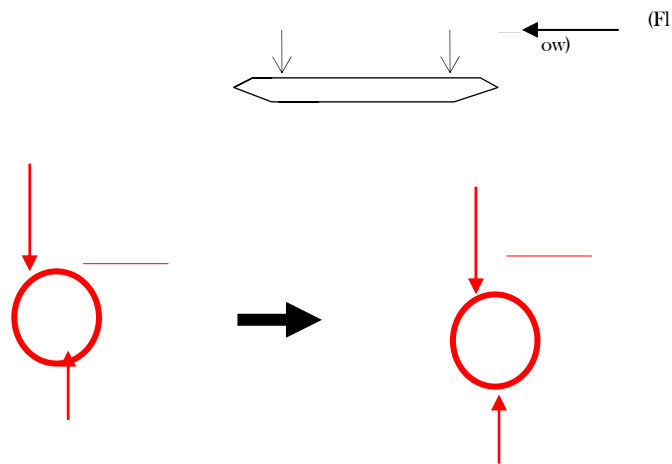


Figure 4-18. Phase averaged contribution (per cent) of the pressure at every tap around the deck to the moment coefficient for phases 10 ( $180^\circ$ , nose down) and 20 ( $360^\circ$ , nose up) of the rotation.

To investigate the mechanisms involved in the development of higher amplitude oscillations, the contribution of each phase-averaged pressure coefficient for each tap around the deck to the phased averaged moment coefficient was

determined. It was found that there is a considerable contribution to the maximum (positive) moment coefficient around the separation at the leading edge's upper corner (tap 16) which shifts through half a rotation cycle to the trailing edge's upper corner (tap 23), see Figure 4-17. A vortex traveling between these two locations may be associated with it. One can observe (Figure 4-18) that the phase with respect to the rotation of the pressure around tap 16 remains unchanged through the build up phases while that of tap 23 changes through it, reaching a phase difference of approximate  $180^\circ$ , within the cycle. A convective velocity could be obtained for the vortex moving over the upper surface, i.e.,

$$\rightarrow U_{\text{conv}} = 0.88U$$

The correlation coefficient between the pressures at these two locations decreased through the build up phases of the response, reaching values of around -0.8 for maximum amplitude oscillations. This is consistent with the hypothesis of traveling vortices from the leading edge.

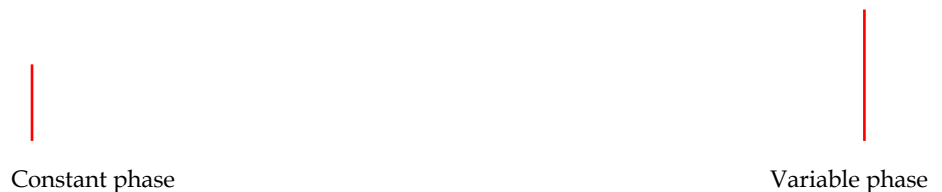


Figure 4-19. Phase averaged pressure coefficients through the build-up of the response for increasing wind speed, at the upper corner of the leading edge (left) and upper corner of trailing edge (left)

## Conclusions

Several conclusions can be made from the present study:

- The classification of deck cross sections for vortex-induced vibration may need to be based on the detailed deck shape.

- Significant hysteresis was observed in the vortex-induced response. This is due to changes in the flow structures.
- The onset of the oscillations could be due to vortex shedding at the trailing edge. Further flow information would be needed to confirm this.
- The magnitude of the maximum amplitude oscillations is related to the separation of the flow near the leading edge of the upper flange, and the resulting loading changes.
- Maximum amplitude oscillations are controlled at the leading edge.
- A vortex advected by the flow from the leading edge plays a role in the synchronization of the higher amplitude oscillations.

# Chapter 5

## Vortex induced vibration of bridge beams under construction

Vortex induced vibration of a bridge deck has been investigated in the previous chapter 4 as the driving mechanism of the response of the full bridge. This phenomenon was also described in chapter 2 as responsible for the response of structural members such as cables and pylons. The present chapter focuses on an observed full scale vibration of bridge beams under construction, leading to a partial collapse. Along wind - VIV is presented as the cause of the vibration.

### 5.1 Summary

Severe vibration under wind loading of a particular type of slender precast beams has been reported by manufacturers in a number of occasions and sites. A case study is presented here to explain the possible driving mechanism and proposed remedies are provided. The vibration event scope of this chapter was noticed and therefore observed and recorded for a few days prior to the failure, which enlightened the analysis.

The chapter has been divided into four sections. In the first place, (5.2) a characterization of the Bridge local winds is presented, indicating both intensity and direction thereof; estimating the probability of wind-induced integrity failure of the beams as well as to the winds that specifically caused the undesired vibration. The probability of occurrence of a wind that would cause the vibration is estimated to be 11%. Subsequently, static loads and stability to overturning and sliding have also been evaluated. This study has been made for both the wind conditions causing the failure as well as for the conditions required by the standard. Design loads relative to the requirements set forth in the standard, are far more stringent than the ones present the day the structural failure occurred. Findings indicate that the beams are stable to



overturning and sliding under collapse conditions, even without struts. Bracing is necessary to withstand the pseudo-static overturning loads required by the standard. In any event, the beam has been found to withstand wind-induced pseudo-static stresses under project conditions, that is, the prevailing conditions at the time of the vibration.

The aeroelastic phenomenon responsible for the vibrations that caused the collapse is analyzed in section 5.5. The vortex shedding from the leeward face of the web starts up a fluctuating horizontal drag force at a frequency close to that of the beam's fundamental mode. Such loading triggers a resonant response and, consequently unacceptable vibrations. This phenomenon has been confirmed through numeric simulation, yielding results that match the analytical formulation. Given the repetition and amplitude of the oscillations during several hours, fatigue has been identified as the cause resulting in the damage that initially triggered the collapse. A precise estimate of the vibrations' amplitude can only be made through a wind tunnel test of an aeroelastic or sectional model of the beams. The legislation in force does not require testing for aero-elastic phenomena of structural components or bridges with a span below 200m.

Last, a few courses of action have been proposed for the future. The preferable course of action is placing clothes pieces on the leeward faces of extreme beams to dissipate the vortices originating the vibration. Numeric simulation has been used to prove the effectiveness of these devices in suppressing the fluctuating forces. An additional proposal is placing steel profiles at the ends to protect against the possibility of the clothes been pulled off. At the end, a few simple measures have been indicated to monitor wind speed and vibration of the structural component to favor control and effective operation.

## 5.2 Case Scenario

Severe vibration was observe for days leading to the failure of 6 of the 10 beams that had already been set, and were simply resting in place braced on to a double prop at both ends and on both sides on the piers of the Bridge under construction. The 10 beams were laid in place waiting for the construction on site of the slab over them. Figure 5.1 enclosed below shows a part of the Bridge indicating, and distinctly highlighting in the plan, the beams over which the slab had already been built (in blue), the 4 beams still in place that withstood the effect of wind (in green) as well as the 6 collapsed beams (in red).

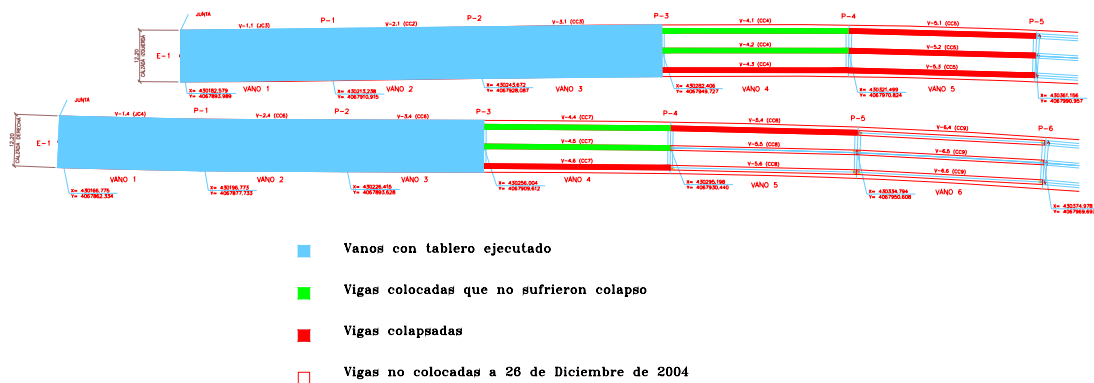


Figure 5.1: Plan layout of both the collapsed beams, as well as of the weather-resisting beams with the constructed slab over them.

Included herein is the study of the effect of wind on the Bridge beams under construction to determine the cause of the unwanted vibration. The mechanisms through which the wind may have caused the failure to occur will also be identified and described. Last, future measures are proposed to ensure the stability of these beams under wind conditions.

### 5.3 Climate analysis: Wind

To determine the effects of the wind causing the collapse, the wind weather conditions prevailing at the time of the event need to be analyzed. This section will describe the weather conditions originating the winds prevailing in the region as well as the specific air circulation characteristics and patterns at the Bridge site. Likewise, - for illustration purposes only - wind intensity records (average wind speed, gusts and mean direction and gust direction) from neighboring weather stations are also included.

#### 5.3.1 Mesoscale - general circulation in the region

Weather conditions may be described using the isobar map study of the day of the event, shown in Figure 5.2 enclosed below. The Bridge location in Figure 5.2 has been indicated with a blue dot.

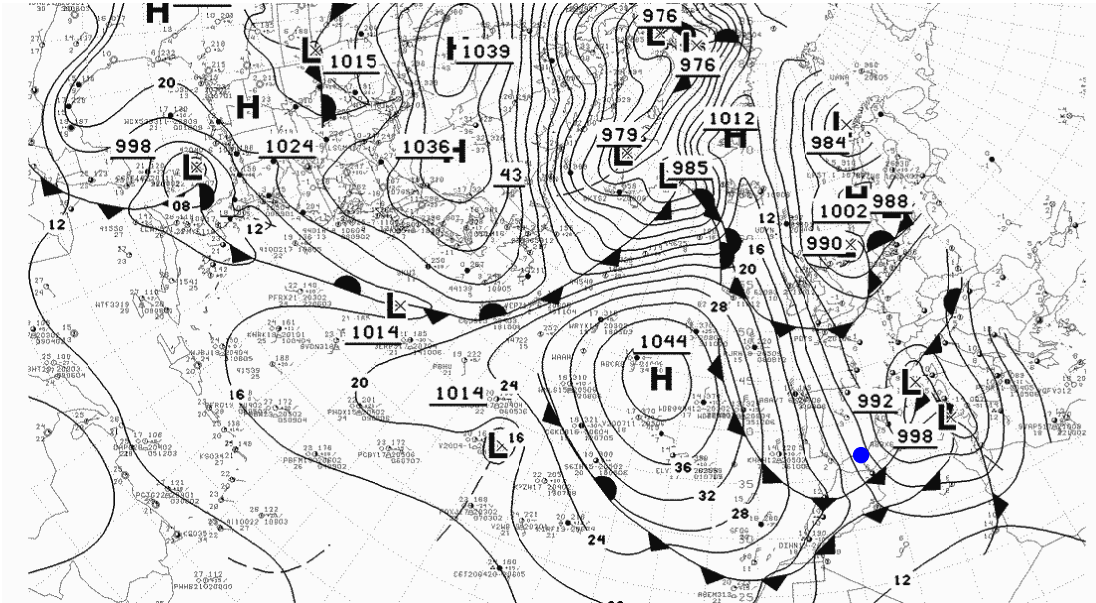


Figure 5.2: Surface isobar map of the days of the vibration. The blue dot indicates the Bridge location.

The general circulation in the region is governed by the presence of a low-pressure system to the north of the Azores Islands dominating an important high-pressure zone (1044mb), by the presence of an anticyclone formation in the Mediterranean (992-998mb) and by a cold front formed between them. The Bridge is located between the following estimated coordinates: 36.77° North Latitude and 3.77° West Longitude. Isobars in the area, as indicated and plotted in the figure, appear parallel therefore the effect of centrifuge forces generating the wind leading to a balanced wind may be deemed negligible: Geostrophic wind, blowing parallel to the direction of the isobars. This is a weather situation common to wintertime in the zone governed by a South Atlantic low-pressure system. Thus, the general direction of wind circulation in the area, as indicated and shown in the figure will roughly be in the NW direction. The magnitude of this wind speed can be calculated on the basis of the prevailing pressure gradient according to the following equation (see for example, (Holmes J. D., 2001):

$$V_g = \frac{1}{\rho f} \frac{\delta p}{\delta n} \quad (5.1)$$

where  $\rho$  is the air density (1.23 Kg/m<sup>3</sup>),  $f$  is the Coriolis parameter,

$$f = 2 \cdot \Omega \cdot \sin \varphi \quad (5.2)$$

and  $\Omega$ , the angular velocity of the rotation of the earth and  $\varphi$  the location's latitude. In (5.1),  $p$ , is the atmospheric pressure and  $n$  the distance measured in the normal direction to the isobar lines.

Thus, for the map situation plotted in Figure 5.2 and for the site, results indicate that the prevailing geostrophic wind velocity is **NW30.7 m/s (NW110.5 km/hr)**. This is the wind velocity originated by the atmospheric pressure gradient, beyond the boundary layer over the terrain, at an altitude where wind is not affected by the friction against the surface of the earth. At this altitude, the thickness of the boundary layer, may be of about 200 m (calm sea) to 1000 m (a dense urban area), depending on the type of surface of the earth or the sea. For the case location, the estimation is that the boundary layer thickness is **z<sub>g</sub>=400m**. Therefore, as altitude drops, wind velocity decreases too until it becomes nil close to the surface of the earth, at the so-called zero effective height (for the land to be studied **z<sub>0</sub>=0.5m**). The mechanism to account for this variation with decreasing altitude (z) may be described, under low-pressure conditions, using the well-known exponential law ( (Spanish Ministry of Public Works, 1995), (Davenport A. , 1961)):

$$V(z) = V_g \left( \frac{z}{z_g} \right)^\alpha \quad (5.3)$$

where  $\alpha$  is an exponent that depends on the type of terrain ( $\alpha=0.32$ ). In this manner, a representative mean velocity may be calculated at a 10 meter height,  $V(10) = V_{10}$  based on the geostrophic wind velocity previously calculated using the isobar map. This therefore works out to **V<sub>10</sub>=9.43m/s (34Km/hr, Force 5** in the Beaufort scale. The mean velocity corresponding to the bridge slab height is worked out in the same manner **V<sub>30</sub>=15.78m/s (56.82Km/hr, Force 7)**. As height decreases relative to the geostrophic wind height, a direction variation occurs in the order of 3-4° (Eckman spiral) which may be considered negligible in the study herein relative to the effects that the local topography at the Bridge site will have over the intensity and direction of the wind. The effects of the local topography over the geostrophic wind are analyzed next.

The annual probability in the area, in the scalar regime, of surpassing this mean velocity is 90%. However, as shown further ahead, the combined effect of wind velocity and direction is responsible for the structural vibration. Thus, the NW wind direction in this area has a probability of surpassing this intensity threshold (> 9.43m/s) of approximately 0.75, with the NW component wind having a 0.0344 probability. Therefore the wind blowing on the day of the event has an annual probability of occurrence of 2.5% (Spanish Ministry of Public Works, 1995). In any event, as shown below, the directions of the N, WNW, NW, NNW, NE and NNE winds may lead to the same phenomenon. Therefore the sum of overpass probabilities of the intensity threshold for every individual direction, (1-F, with F=0.8, 0.6, 0.7, 0.75, 0.84, 0.84 respectively) combined with the probability of wind blowing from each direction (0.0197, 0.0576, 0.0344, 0.0139, 0.0484, 0.0155) yields a probability of occurrence of a wind equal or greater than 9.43m/s in any of these four sectors of 5%:

$$\begin{aligned}
& P(V_{10} > 9.4\text{m/s}, 292.5 < \theta < 45) = \\
& = \sum_{\theta_i} (1 - F(\theta_i, 9.4)) \cdot P(292.5 < \theta_i < 360) = 0.049 = 5\% \quad (5.4)
\end{aligned}$$

As described in the following section, winds in these directions are accelerated by the funnel effect. This effect is fundamentally for winds with the S component, given the proximity of the coastline. However, the winds with SSE and SSW component will have a normal incidence on the beam. Similarly, the following equation is used,

$$\begin{aligned}
& P(V_{10} > 9.4\text{m/s}, 135 < \theta < 45) = \\
& = \sum_{\theta_i} (1 - F(\theta_i, 9.4)) \cdot P(135 < \theta_i < 45) = 0.063 = 6.3\% \\
(0.5)
\end{aligned}$$

As shown further ahead, this velocity of approximately 9.5 m/s corresponds to the wind intensity threshold that may originate the vibrations responsible for the collapse. In this manner, since we are dealing with separate events, the result found is that the annual probability of occurrence of a wind with the direction and intensity resulting in this phenomenon is of 11.3%. (2% correlates with the winds which, specifically, caused the vibration):

$$\begin{aligned}
& P(V_{10} > 9.4\text{m/s}, 135 < \theta < 45 \text{ ó } 292.5 < \theta < 45) = \\
& P(V_{10} > 9.4\text{m/s}, 135 < \theta < 45) + P(V_{10} > 9.4\text{m/s}, 292.5 < \theta < 45) = 11.3\% \\
(1.12)
\end{aligned}$$

which would correspond to a reasonable return period given the temporary nature of exposure to risk (construction).

### 5.3.2 Micro scale – local winds field

Due to the surface of the earth effect, the wind originated by the presence of pressure gradients at extreme heights is modified in direction and intensity. Turbulence intensity will increase considerably as altitude decreases. Local topography, hills, river basins, vallies ... may originate drastic changes in wind direction and velocity which may have important effects on structures located in the surroundings of these topographic features. The effects of topography on local winds are so complex that American standards ANSI A58.1-72&82 and ANSI/ASCE 7-88 (Metha, 1998) do not recommend a procedure to evaluate the effect and are limited to warning the engineer about the risk indicating the wind tunnel test as the only procedure to estimate the local winds field. The European ENV 1991-2-4:1995 standard (European Committe for Standarization, 2001) states that in vallies, 1 shall be taken as the topographic coefficient (it is not taken into account) unless no velocity increase is expected due to funnel effect.

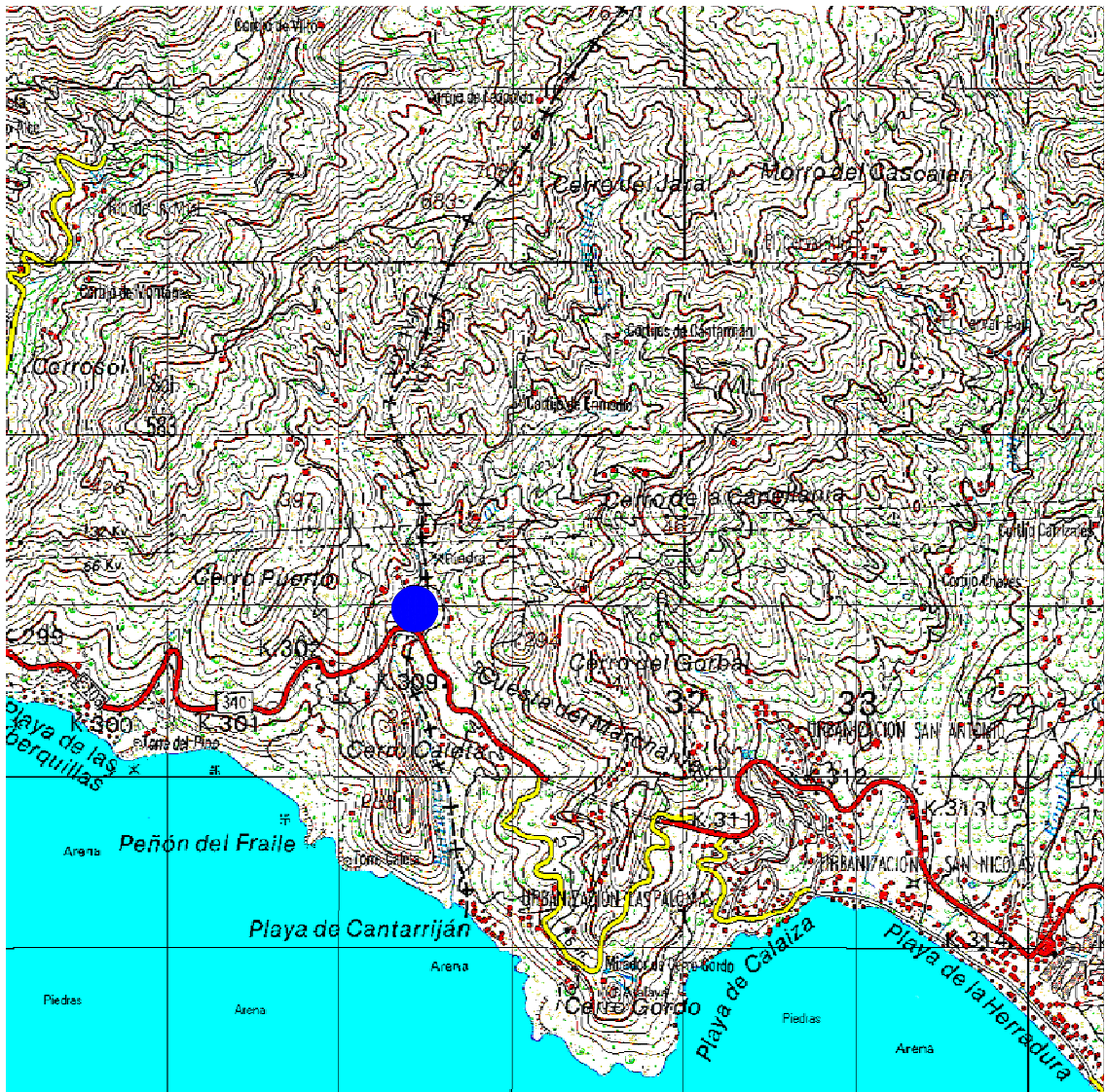


Figure 5.3: General topography in the Bridge area.

Figure 5.3 attached herein includes a large-scale topographic drawing of the Bridge location. As shown in the figure, local topography is extremely complex, reaching elevations over 1000m only a few meters away from the coastline. Specialized literature and in-force international regulations allow *isolated* topographic features such as vallies, hills or river basins to be evaluated. However, it is not possible to accurately evaluate the effect of wind intensity and direction in a topography as complex as this without resorting to experimental studies using the wind tunnel test of the boundary layer.

The Bridge runs across the gully at an elevation of 50m, wedged between two mounts of 467m and 411m to the East and another two of 391m and 238m to the West. However, the valley opens in the N and NW direction thus originating a funnel effect or Venturi for these wind directions. It is possible see how, at 200m heights in the NW direction, the valley opens up to elevations close to 800 m. When descending to the 50m elevation the valley closes up to 300m. In addition, for the N wind case with



the W component, the mean descending flow through the valley in that direction encounters the above mentioned Hills located to the E of the gully with elevations over 400m which favors the acceleration in question. The effect of this contraction on the increase of the velocity of winds with the N-NW component will be considerable, and it can be estimated to be of at least 20%. It is thus possible to consider the gradual de-acceleration of wind to be negligible when descending through the valley, with a mean slope of 12% while going from 200 to 50 m.

The contraction details causing the acceleration of winds in these directions are shown in Figure 5.4 below.

Locally, in the gully the flow is expected to de-accelerate at the gully close to the banks on both sides of the Bridge due to the effect of friction against the land in such a manner so that higher velocities will occur in the center of the valley and higher ones too will also occur on the E side for the wind directions in question. Close to the sides, turbulence intensity will be stronger, which, as explained further ahead, has an attenuating effect over the mechanism originating the vibration. This is in full

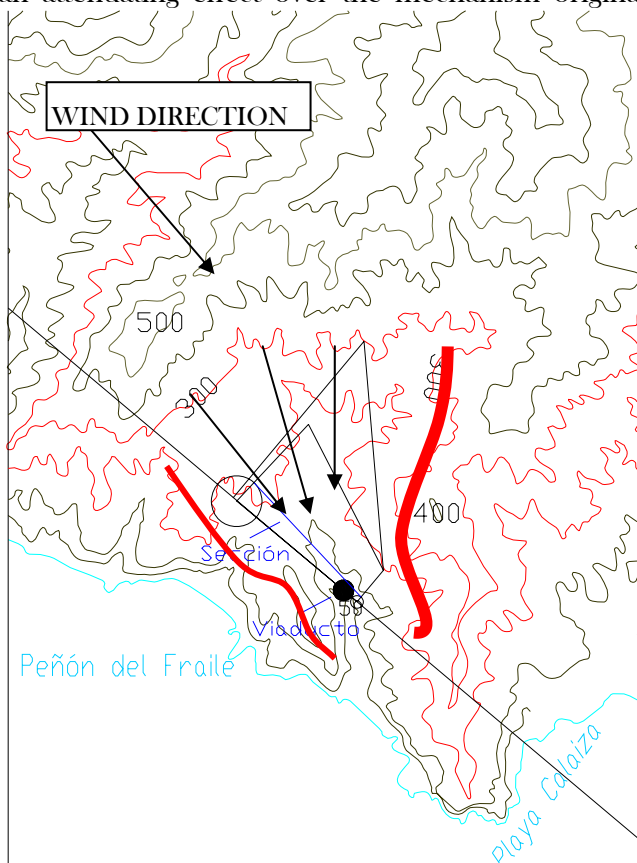


Figure 5.4: Schematic of the topography near the bridge for estimating funnelling effect.

agreement with the location of the beams that withstood the wind effect and the ones that collapsed, see Figure 5.1. At the same time it also indicates that the remaining beams still to be installed are the beams with the highest exposure to wind effects.

In addition to the meteorological wind described herein, winds of a thermal nature may be added, in the direction of the valley: both valley and sea breezes. The most unfavorable case in the study herein would be at midnight during the hot season (late Spring early Fall) the time when the valley breeze in the direction of the sea will blow due to the fast cooling of the earth relative to the water leading to an air temperature gradient both onshore and offshore and therefore to a

pressure gradient. Winds of this type have been of up to 8m/s (Plate, 1982).

### Recorded wind measurements

For the analysis herein, wind measurements have been taken from the different meteorology stations available in the area.

In the area covered by this study, there are two agro-climate meteorology stations reporting to the Consejería de Agricultura y Pesca, Junta de Andalucía:

- Almuñecar meteorology station. Station code number 9.
- Vélez-Málaga meteorology station. Station code number 2.

Given the location and relative low height of anemometers, as well as the time resolution of the available data, these measurements have been estimated not to be representative and have been disregarded for the study herein.

The results from the GFS model have been studied, the Global Forecast System<sup>29</sup> for the Costa del Sol, for the day the collapse occurred, having the following velocities and directions for the average wind, at a 10m altitude, see Table 1.

Hora CET 26dec2004	8h	11h	14h	17h	20h	23h
Velocidad (m/s)	11.2	12.3	10.2	10.7	10.7	9.8
Dirección	NW	NW	NW	NW	NW	NW

Table 5.1: Wind intensity and velocity output ( $V_{10}$ ) of the GFS model for the site area

The findings are that the model output is in agreement with the velocity determined in the previous analysis of 9.4 m /s.

Likewise, the data from the model for day of the event shows that the wind velocity decreases up to the 6m / s and rolls in the N direction.

Last, the measurements from two near-by stations of the National Meteorology Institute were taken<sup>30</sup>. Such will be referred to as Station A and B, located near the shore to West and East of the site respectively.

Table 5.2 attached herein includes a summary of wind and average direction measurements for both stations and for 10 minute periods for the day the collapse occurred. As explained further ahead, the average wind data is the data of interest in the phenomenon and not the maximum wind data, which can be used as an indication of the gust factor, but which is not the wind controlling the flow around the beams, responsible for the vibration.

STATION A	STATION B
26-dic-04	
HOUR WINDSPEED (Km/h) DIRECTION (°)	HOUR WINDSPEED (Km/h) DIRECTION (°)

<sup>29</sup> The Global Forecast System is produced by the National Centers for Environmental Prediction (NCEP) a section of the NOAA (National Oceanic and Atmospheric Administration), NWS (National Weather Service), USA. It is run every 6 hours with a special resolution of 55 km and a time resolution every 3 hours based on recent actual measurements.

<sup>30</sup> Note: The information presented herein has been provided unofficially for the present purpose by INM - Andalucía Oriental.



0	29	270	0	13	310
1	22	270	1	14	310
2	22	270	2	15	280
3	20	280	3	15	280
4	17	280	4	13	300
5	20	270	5	21	310
6	15	280	6	15	300
7	17	280	7	22	310
8	13	280	8	22	310
9	10	290	9	22	320
10	12	290	10	13	320
11	12	310	11	12	330
12	11	320	12	19	330
13	13	310	13	22	320
14	15	320	14	29	320
15	24	280	15	28	320
16	22	290	16	25	310
17	26	300	17	15	320
18	12	310	18	13	320
19	17	280	19	14	300
20	19	310	20	22	310
21	17	310	21	14	330
22	9	330	22	12	340
23	11	320	23	22	320

Table 5.2: Hourly (10 minutes) average measurements wind direction and intensity from the nearby meteorological stations.

Maximum average winds occur in at 05:00 PM and at 02:00 PM with mean directions of 300 and 320 degrees respectively. The maximum gust data has been taken in both stations: 57 and 72 Km/hr with 290 and 340° directions respectively. These measurements, somewhat higher at 8m/s, are in agreement with the previous meteorology analysis taking into account the possible local effects in the stations' measurements.

Given the data gathered and, considering the wind directions and velocities identified in the previous paragraph as the cause of the vibrations, the conclusion is that during the month of the event, primarily around the approximate time and date on which the vibration was observed, there were 8-10 hours of winds with these characteristics. Thus, as will be explained further ahead, the beams had been subject to vibration prior to the time of failure.

### 5.3.3 Summary

Based on different sources of information: station measurements and numeric simulations and using different methodologies, the estimation has been made that the average wind velocity prevailing in the area was of approximately  $V_{10}=9$

m/s at the time the collapse occurred. The mean direction of that wind was NW. Likewise the wind at the slab level has been estimated to be of approximately 16m/s (**56.5 Km/hr**). This prevailing wind measured on the one hand in the coast and reduced from the geostrophic wind to a 400m height on the other, is believed may have amplified itself by at least 20% because of the local topography and due to the funnel effect or Venturi, thus concluding that the average velocity of the wind acting upon the Bridge under construction has been estimated to be **68 Km/hr (daily maximum average<sup>31</sup>)**. The winds within the risk directions (N and S components) and intensities have been studied, determining that the annual probability of occurrence is moderate, of 11.3%. Finally, the beams located in the central sections and close to the E side have been identified as the beams with the highest sensitivity to the effects of local wind.

## 5.4 Pseudo-static analysis

This section presents the calculation of the pseudo-static thrust exercised by the wind over the beam. This analysis helps to determine the wind load on the beam as a static load though; consideration is given to the variability associated to wind due to the atmospheric turbulence as well as to structural damping. Wind conditions required by standards will also be taken into account as well as collapse conditions. Finally, the stability of the beam will be evaluated vis a vis the wind load. This analysis does not take into account the dynamic characteristics of the beam and therefore no consideration is given to any kind of fluid structure dynamic interaction. These effects are analyzed in section 5.5.

### 5.4.1 Beam Aerodynamics

In the first place, the geometric characteristics of the typical Beam have been identified and summarized in Figure 5.4. Small differences among the different beams with which curve superelevations are formed (and/or any other minor detail) are considered negligible from the aerodynamics point of view. For the purposes of the study herein, the characteristics of the beam shall be the ones listed in Figure 5.4. The beam length considered in the study is of 44.23m and, therefore the inertia is of 2063 Kg/m.

Listed below are the aerodynamic load coefficients defined according to the following expression:

---

<sup>31</sup> Understood as the highest of the 24 hourly average values corresponding to that day

$$F_{L,D} = A C_{L,D} \cdot \frac{1}{2} \rho V^2 \quad (1.13)$$

Where  $F_L$  is the force in the normal direction to flow, vertically assumed, (axis and in absence of vibration), hereinafter supporting force,  $F_b$  is the force in the direction of flow, horizontally assumed (axis and in absence of vibrations), hereinafter called the drag force,  $A$  is the body's projection area according to the respective axis,  $\rho$  is the air density of  $1.2\text{Kg/m}^3$  and  $V$  is the velocity of wind acting on the beam.

Given the transverse rigidity (vertical) of the beam, supporting forces are expected to be negligible relative to the weight itself, in the order of  $10^6\text{N}$ . Likewise, aerodynamic torsion<sup>32</sup> forces shall not be taken into account because they are considered negligible relative to static moments.

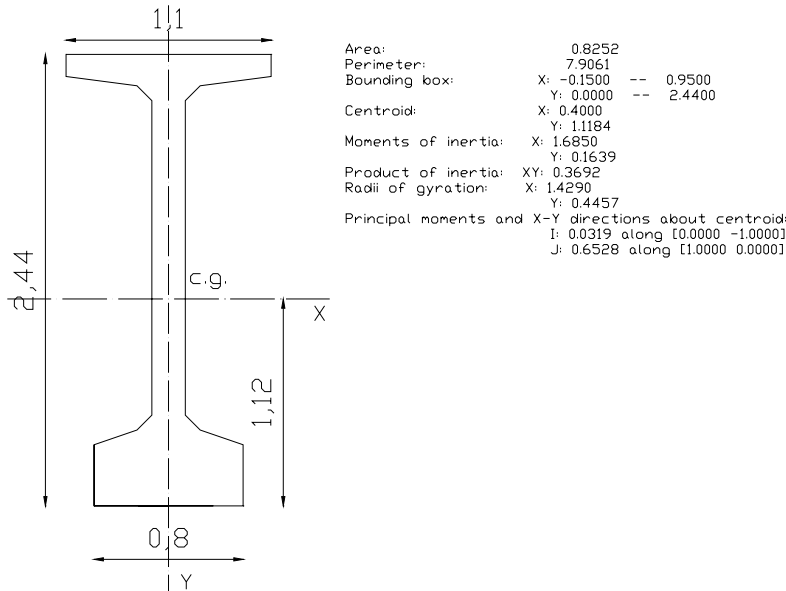


Figure 5.5: Typical beam geometric characteristics that are the purpose of the study.

The wind load caused by the drag aerodynamic force shall be studied. To this end, the normal wind direction relative to the beam shall be considered (most unfavorable and probable given the boxing of the valley). In section, wind of a constant direction shall be considered and paralleled to the X axis. For double-T beams with height-width ratios in the order of 2 the aerodynamic coefficient calculated is ( $0^\circ$  angle of attack):

- ROM 0.4 [ (Spanish Ministry of Public Works, 1995)] :  $C_b=2.05$

<sup>32</sup> Moment aerodynamic coefficients are not available for this geometry. Wind tunnel tests are required to determine such.

- Canadian constr. Standard [ (National Research Council of Canada, 1995)]<sup>33</sup>:  $C_D=2.05$
- IAP98 [ (Spanish Ministry of Public Works, 1998)]:  $C_D=2.2$
- Eurocode 1991- 2-4 [ (European Committee for Standardization, 2001)]:  
 $C_D = 2.0 \psi = 1.56$  , applying a slenderness ratio.

According to IAP98 the simplified calculation shall not be applicable since there are spans of over 40m, (Spanish Ministry of Public Works, 1998) paragraph 3.2.3.2.1 (h). Below, aerodynamic drag forces shall be studied according to different standards for their recommended velocities, namely, in all cases, greater than the forces that occurred during the collapse event described in section 1.

## 5.4.2 Standards review

A calculation is included below of the pseudo-static load required by the EUROCODE, volume 2-4 and as well as the Instructions about actions to be considered in the IAP98 road bridges project. In addition, the beam has been tested following the Canadian standard providing for the inclusion of dynamic response effects (never aero elastic phenomenon).

### 5.4.2.1 ENV 1991-2-4:1995

Below is the calculation of the drag force ( $F_D$ ) on the beam according to the Euro code formulation.

$$F_D = q_{ref} \cdot C_e(z_e) \cdot C_d \cdot C_f \cdot A_{ref} \quad (1.14)$$

where:

$$\begin{aligned} C_d &= 0.925 \text{ is the dynamic coefficient,} \\ C_f &= C_{f0} \cdot \psi_\lambda = 2.078 = 1.56, \text{ coeficiente de fuerza} \\ \psi_\lambda &\text{ es el coeficiente de reducci3n por esbeltez} \end{aligned} \quad (1.15)$$

$$q = \frac{1}{2} \rho V_{ref}^2 = 345.6 \text{ Pa, presi3n din3mica de referencia con } V_{ref} = 24 \frac{\text{m}}{\text{s}} \quad (1.16)$$

---

<sup>33</sup> The Canadian standard incorporates more information for the estimation of wind effects such as for example the variation of aerodynamic coefficient with angle of attack for galloping effect, see section 5.4.2.2

The 24 m/s reference velocity has a return period of 50 years or a 2% annual overpass probability.

$$C_e(z) = C_r^2(z) \cdot C_t^2(z) \cdot \left( 1 + \frac{7 k_t}{C_r(z) \cdot C_t(z)} \right), \text{coeficiente de exposición} \quad (1.17)$$

This coefficient includes both the effects of local topography ( $C_t$ ) as well as the height the beam<sup>34</sup>  $C_r$  is placed at. The effect of local topography can only be quantified for isolated topographic features. The Euro code states that for valleys this coefficient “may be taken to be 10 provided an increase of velocity is not expected to happen due to the funnel effect. In structures or bridges located in valleys with steep hillsides consideration should be given to any increase in wind velocity due to the funnel effect”. Thus, according to the specific analysis made in section 1.2 the coefficient used is  $C_t(z) = 1.20$ .

For the area in question with rural soil and a complex topography this can be estimated using the well-known logarithmic law given the fact that the height ( $z=50\text{m}$ ) does not go beyond the surface sub layer of the boundary layer (100m), which works out to,

$$k_t = 0.23 \text{ y } z_o = 0.5. \text{ Así } C_r(z) = k_t \cdot \ln\left(\frac{z}{z_o}\right) = 1.06 \quad (1.18)$$

Which yields an exposure coefficient equal to  $C_e(z) = C_e(50) = 3.67$ , replacing in (0.11)

The drag force is calculated using the (0.8) equation, which works out to  $F_D = 197,261.22 \text{ N}$ .

#### 5.4.2.2 Spanish Road Bridge Design Standard, IAP-98

Last, the drag force has been calculated using the IAP98 Spanish standard formulae.

The drag force is calculated according to its definition, equation (0.3). Contrary to the Euro code, this methodology builds-in the dynamic effect of the load using a gust factor ( $C_g$ ) in addition to a risk factor ( $C_r$ ) providing for the use of calculation velocities with a shorter return period in the case of temporary loads as in the case we are studying. The study herein, analyzes the load on the beams that did not collapse, a temporary situation given the fact that the slab over these beams had been built. For these cases, the proposal in the standard is a  $C_r = 0.84$  risk reducing factor

---

<sup>34</sup> Since the reference velocity used is consistent with a 10 m altitude and the beam is placed at 50, see section 1. The velocity corresponds to the mean ten-minute value and to a flat area, unprotected from wind.

equivalent to a 4 year return period. The  $C_g$  gust factor is calculated using the following expression,

$$C_g = \sqrt{1 + \frac{7k_t}{C_z \cdot C_t}} = 1.54 \quad (1.19)$$

where  $C_s$ ,  $C_z$  y  $k_t$  follow the same definition stated in the Euro code.

The reference velocity is also equivalent to 24m/s according to the isotacs map.

Therefore the calculation velocity is calculated using:

$$V_{cal} = C_t \cdot C_r \cdot C_z \cdot C_g \cdot V_{ref} \quad (1.20)$$

which is equal to  $V_{cal} = 39.5\text{m/s}$ , therefore the drag force, using a 2.2 drag coefficient in the manner and as indicated above, is equal to:

$$F_b = 227,823.6\text{N} \quad (1.21)$$

very much in agreement with the results found at an earlier stage using the Canadian standard, building-in the dynamic nature of loads and damping.

#### **5.4.2.3 NBC 1995 - Part 4 Canadian Standard (National Research Council of Canada, 1995)**

This section focuses on estimating the drag force using the Canadian methodology, which is considered to be one of the most developed standards by the international community for the evaluation of wind effects on civil works structures. In this specific case, the standard allows the pseudo-static calculation to include the turbulence effect, introducing a peak factor and the structural damping effect.

The drag force is calculated using the formulae developed by Davenport (Davenport A. , The application of statistical concepts to wind loading of structures. , 1961),

$$F_D = K \cdot C_D \cdot q \cdot C_g \cdot C_e \cdot A \quad (1.22)$$

where:

- **K** is an aerodynamic slenderness coefficient, equivalent to **K=0.75** for a >20 slenderness

- **C<sub>D</sub>=2.05**, drag coefficient as stated above

- **q=345.6 Pa** is the dynamic load calculated pursuant to the Euro code

- **C<sub>e</sub>=0.9**, exposure coefficient according to type of terrain

- **A=107.9 m<sup>2</sup>**, the projected area

**C<sub>g</sub>** es el coeficiente de respuesta dinámica, factor de efecto de ráfaga

$$C_g = 1 + g_p \left( \frac{\sigma}{\mu} \right) \quad (1.23)$$

where **g<sub>p</sub>** is a wind peak factor which we may consider to be around **3.6**, since turbulence may be adjusted to a Gaussian process. **σ** is the quadratic mean value of the dynamic load and **μ** is the mean dynamic load. The quotient between them can be calculated based on the fundamental mode frequency of structural vibration and damping,

$$\frac{\sigma}{\mu} = \sqrt{\frac{K}{C_{eH}} \left( B + \frac{sF}{\xi} \right)} \quad (1.24)$$

where:

- **K** is a factor depending on the type of terrain **K=0.12**.

- **C<sub>eH</sub>** is an exposure factor to the beam altitude

- **B** is a background turbulence component relying on the **B=1.3** aerodynamic slenderness.

- **s** is a scale reduction factor depending on the fundamental mode frequency (1.31 as shown further ahead in section 6) **s=0.8**.

- **F** is a gust energy content factor varying with the fundamental mode frequency and the mean velocity relative to the project altitude, **F=0.07**

- **ξ** is the structural critical damping factor, estimated to be 5% pursuant to the design calculation annex and around 2% according to (National Research Council of Canada, 1995). Loads are estimated for both damping values.

Therefore for the gust effect the following is calculated,

$$\begin{aligned}\frac{\sigma}{\mu} &= 0.57 (\beta = 0.05) \\ \frac{\sigma}{\mu} &= 0.74 (\beta = 0.02)\end{aligned}\tag{1.25}$$

Last the drag force,

$$\begin{aligned}F &= 188,857.34\text{N} (\beta=0.05) \\ F &= 226,628.64\text{N} (\beta=0.02)\end{aligned}\tag{1.26}$$

very much in agreement with the results found using the Eurocode formulae. The estimate herein however, turns out to be less conservative and builds-in the dynamic nature of loads. A load has been identified that is approximately 20% higher for the case with the lowest structural damping value.

Since the active/passive reinforcement characteristics are not known, no stricter loads are expected to be required other than the ones that are mandatory for ultimate limit statuses stated in the EHE standard, given the relative magnitude of the static stresses caused by the wind effect.

### 5.4.3 Pseudo-static load in the collapse event

The pseudo-static load applied by wind on the beams at the time the collapse occurred has been estimated using the same methodology described in this section but based on the wind velocity calculated in paragraph 4, 4, 68Km/h =18.9m/s (see paragraph 4.3). The result is that the corresponding drag force is equivalent to,

$$F_D = 120,000\text{N}\tag{1.27}$$

calculated using the Canadian pseudo-static methodology, with a structural damping factor of 2% and which is equal to approximately 50% of the value required by the standard.

### 5.4.4 Stability Analysis



Upon determining the load magnitude produced by the wind thrust, the study proceeds to estimate the beam's stability vis a vis said magnitude, overturning and sliding.

#### 5.4.4.1 Overturning

Overturning stability is analyzed by establishing a balance between the stabilizing and the unstabilizing moments: the moment produced by the drag force and the moment created by the weight itself ( $8.94 \cdot 10^5 \text{N}$ ).

In the first place, stability is analyzed relative to the wind on the day the collapse occurred.

The drag force is considered to have been applied at an intermediate altitude of the projected area,  $2.44/2=1.22\text{m}$  above the support. In such a manner that the overturning moment it causes shall be equivalent to:

$$M_v = F_D \cdot 1.22 = 146,400 \text{ N}\cdot\text{m} \quad (1.28)$$

The most unfavorable case considered has been rotating relative to one of the supporting neoprene ends. Thus, the stabilizing moment will be equivalent to:

$$M_e = P \cdot 0.2 = 178,800 \text{ N}\cdot\text{m} \quad (1.29)$$

The stabilizing moment works out to be longer so that the system is stable and the beam does not overturn under these load conditions and without consideration to the stabilizing moments caused by the support struts mounted for this purpose.

Therefore the beam is found to be stable to overturning caused by the pseudo-static thrust of the wind that led to the collapse event. In addition the beams were mounted on two struts with a 10tn allowable load on both sides which lead to a stabilizing moment which shall not be taken into account in this study.

For a calculation load with a 50-year return period estimated above, the assistance provided by the struts will be necessary, which is equivalent to:

$$M_v = F_D \cdot 1.22 = 277,944 \text{ N}\cdot\text{m} \quad (1.30)$$

The stabilizing moment of the weight does not vary relative to the previous  $M_{ep}=178,800 \text{ N}\cdot\text{m}$  case. We shall now consider the stabilizing effect of the struts. The

10tn<sup>35</sup> allowable sagging load provides a horizontal component equal to 4.4tn = 44,000N creating a stabilizing moment equivalent to  $\frac{1}{2} M_{\text{ep}}=44,000 \cdot 2.2=96,800 \text{ N}\cdot\text{m}$  for each end, accounting for a total of  $M_{\text{ep}}=193,600 \text{ N}\cdot\text{m}$ . Therefore the total stabilizing moment shall be equivalent to,

$$M_c = 178,800 + 193,600 = 372,400 \text{ N}\cdot\text{m} \quad (1.31)$$

Following the reverse procedure, the wind velocity that would lead to that overturning moment and would actually cause the beam to overturn can be calculated only to offer some guidance. Thus, said velocity is found to be of 108.5 km/hr as a reference, which would be equivalent to 115.0 km/h mean wind velocity at the bridge altitude (therefore gusts in the order of 200km/h).

#### 5.4.4.2 Sliding

To analyze sliding stability due to the effect of the drag aerodynamic force, the study has referred to the neoprene calculation annex (RTE, 2004), where they are found to withstand 15tn loads. In the case of the wind drag force, each neoprene should withstand  $F_D/2=113,911 \text{ N} < 150000 \text{ N}=15\text{tn}\cdot\text{f}$ .

In all cases the 2-dimension stress status in the neoprene would be:

$$\begin{aligned} \sigma_z &= \frac{P_z}{A_z} = \frac{-45 \cdot 10^4}{10 \cdot 40^2} = -28.1 \text{ Kg} / \text{cm}^2 \\ \tau_{xy} &= \frac{P_x}{A_z} = \frac{11.4 \cdot 10^4}{10 \cdot 40^2} = 7.13 \text{ Kg} / \text{cm}^2 \end{aligned} \quad (1.32)$$

The main stresses on the elastomer can be calculated on the basis of this two stresses:

The main stresses are equivalent to:

---

<sup>35</sup> As confirmed by the sponsor the allowable load of struts is, sagging allowable load =10tn.

$$\begin{aligned}
\overline{\sigma_1} &= 1.7 \frac{\text{kg}}{\text{cm}^2} \\
\overline{\sigma_2} &= 29.7 \frac{\text{kg}}{\text{cm}^2} \\
\overline{\tau_{\max}} &= \frac{\overline{\sigma_2} - \overline{\sigma_1}}{2} = 15.71 \frac{\text{kg}}{\text{cm}^2}
\end{aligned}
\tag{1.33}$$

Stresses which in all cases are lower than the maximum admissible stresses indicated in the above mentioned annex (RTE, 2004). The conclusion is that the beams are perfectly stable to sliding induced by the pseudo-static thrust of the calculation wind (T=50 years).

#### 5.4.4.3 Summary

Wind pseudo-static loads have been studied for the wind conditions required by standards, far more stringent than the ones causing the failure:

##### PSEUDO ESTATIC LOAD ACCORDING TO STANDARDS

IAP98	<b>227.823,6N</b>	No damp., dynamic type
ENV 1991-2-4:1995	<b>197.261,22N</b>	No damp., non dynamic
NBC-95	<b>188.857, 34 N</b>	5% damp., dynamic type
NBC-95	<b>226, 628.64 N</b>	2% damp., dynamic type

The reference wind, if applied pursuant to standards, should be equivalent to an average wind of **115 Km/h** on the beam. Note should be taken of the fact that, given the magnitude, unless corroborated according to assembly, the values found should not jeopardize the ELU set forth in EHE.

For the event conditions, the estimated load is **120.000N**, close to 50% of the load required by the standard.

Last, the overturning and sliding stability has been corroborated and the beams have been found to be stable without the need of struts under event conditions. However, in the case of overturning, the beams have been found to need struts for the conditions required by the standard.

## 5.5 Aeroelastic Study

In this section the structural response is analyzed due to the wind-structure dynamic interaction. This dynamic interaction, via different mechanisms which may

take place with low velocity wind, may lead to vibrations that may jeopardize the structure's integrity or service.

There are different aeroelastic phenomena occurring on bridges and on bridge structural components that are very different in nature: the classic or stall flutter, galloping, wake galloping, torsion divergence and vortex-induced vibration. A brief description of these phenomena on bridges can be found in Chapter 1 or (Simiu & Scanlan, 1996).

The mechanic nature of the beams in question is characterized by a high vertical rigidity and a relatively high lateral flexibility. The slab to be built on site over the beam heads provides the bridge's lateral rigidity.

Transverse galloping takes place when the structure experiences a variation between the supporting aerodynamic coefficient and the angle of attack subsequently leading to instability. The variation in the apparent angle of attack takes place due to the transverse vibration of the body itself. The approaching flow will flow in approximately horizontal directions, therefore, since the beam provides a high transverse resistance to flow (restricted vertical mode), there will be no variation in the apparent angle of attack. Thus, vibrations caused by transverse galloping may be ruled out. The 4.65m distance between beam axis, barely amounts to 2 D, where D is the beam height equivalent to D=2.44. Therefore, a free wake shall not occur between beams allowing us to rule out slipstream or wake galloping too. The distribution of fallen beams and the lay-out of the beams that withstood are in full agreement with this statement.

Similarly, since there are mode frequencies that are so different, considerable resistance to torsion, there will be no coupling between modes or torsion vibrations; therefore flutter and torsion discrepancy can also be ruled out.

Given the evidence found by direct observation of harmonic vibrations in the lateral bending mode (sway) on the days of the event, it is believed that vortex-induced vibration was the driving mechanism.

### 5.5.1 Beam dynamic characteristics

For the purposes of this analysis the frequencies and forms of fundamental vibration modes involved need to be estimated.

Both vertical ( $EI_y$ ) and lateral rigidity ( $EI_x$ ) can be estimated on the basis of the inertias stated in Figure 5.5,

$$\begin{aligned}EI_y &= 5.509 \cdot 10^9 \text{ Nm}^2 \\EI_x &= 5.664 \cdot 10^{10} \text{ Nm}^2\end{aligned}\tag{1.34}$$

Beams are assumed to be simply resting at both ends. The vertical vibration modes are calculated from rigidity and geometry (RTE, 2004). Thus, the fundamental vibration mode will be a harmonic (half sine) frequency mode:

$$\begin{aligned}
y_{\text{ver1}}(x, t) &= \phi(t) \cdot \sin \frac{\pi x}{L} \\
f_{\text{ver1}} &= \frac{\pi^2}{2 \pi} \sqrt{\frac{EI_x}{m L^4}} = 4.21 \text{ Hz}
\end{aligned} \tag{1.35}$$

Where  $m$  is the mass per length unit  $m=2063\text{Kg/m}$  and  $L$  is the beam length,  $L=44.23\text{m}$ .

The second vertical mode will be:

$$\begin{aligned}
y_{\text{ver2}}(x, t) &= \phi(t) \cdot \sin \frac{2 \pi x}{L} \\
f_{\text{ver2}} &= \frac{(2 \pi)^2}{2 \pi} \sqrt{\frac{EI_x}{m L^4}} = 39.48 \text{ Hz}
\end{aligned} \tag{1.36}$$

It is an asymmetric mode including a full sine.

To study the horizontal vibration modes, orthogonal and decoupled from the vertical modes, the same formulae used above may be used because the difference in mode is only related to gravity acceleration. Since gravity is a static load it is not involved in the vibration mode, which has been determined by rigidity, inertia ( $m$ ), geometry and support conditions. However, the deformation status will be different given the fact that weight is orthogonal to vibration in the lateral bending mode. Therefore the following occurs,

$$\begin{aligned}
z_{\text{hor1}}(x, t) &= \phi(t) \cdot \sin \frac{\pi x}{L} \\
f_{\text{hor1}} &= \frac{\pi^2}{2 \pi} \sqrt{\frac{EI_y}{m L^4}} = 1.31 \text{ Hz}
\end{aligned} \tag{1.37}$$

This therefore indicates that the lateral bending vibration mode ( $f_{\text{hor1}}=1.31 \text{ Hz}$ ) is the beam fundamental vibration mode. The mode frequency close to 1 Hz is usually taken as indicative of the order of magnitude of the structure threshold especially sensitive to vibration by wind effect. Given the flexibility, a specific study of the effect of wind is recommended, as well as a study of the buffeting section due to turbulence caused by the pseudo-static loads estimated in section 5.4. The second lateral vibration mode will be,

$$z_{\text{hor2}}(x, t) = \phi(t) \cdot \sin \frac{2 \pi x}{L}$$

$$f_{\text{hor2}} = \frac{(2 \pi)^2}{2 \pi} \sqrt{\frac{EI_y}{m L^4}} = 5.24 \text{ Hz}$$

(1.38)

In the horizontal modes, the assumption used is that the ends are simply resting to be on the safe side in the vibration analysis because it leads to lower mode frequencies. However, given the neoprene supports and the struts, there might be a considerable moment at the base, at the ends of the beam. Thus, as a guide only, the modal frequency has been estimated corresponding to the lateral bend with embedded supports, 2.98 Hz.

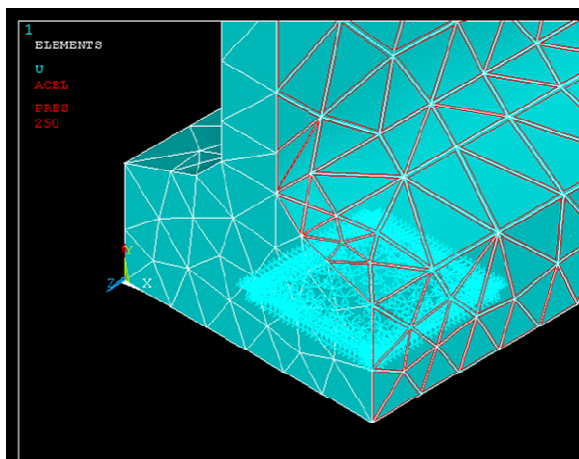


Figure 5.6: Close-up of the support model, including the neoprene blocks.

As stated above, given the support specific conditions, (neoprene support on the bottom face and the junction of the web with the head) a modal analysis vis a vis the horizontal action is difficult to do. The calculation of mode frequencies is extremely important to study the aero elastic phenomenon. It is for this reason that a mode analysis has been made using numeric simulation, with the purpose of corroborating the abovementioned frequencies.

In this analysis, the supports have been modeled (see Figure 5.6) as well as the restrictions on struts. Figure 5.7 attached herein shows a view of the one deformed in the estimated fundamental vibration mode corresponding to (1.1Hz), according to the above calculation, a symmetric lateral bend. Given the support conditions, a stronger inertia is expected to mobilize relative to the simply resting case assumed before, with an ideal symmetric support (1.31Hz). Thus, the figure shows a small rotation of the head in combination with bending. This is in full agreement with the lower mode frequency found, given the higher inertia mobilized in the mode.

In Table 5.3 below, the first 9 modes found in the analysis are shown:

Mode	Frec. (Hz)	Description
1	1.1	Symmetric lateral
2	3.12	Asymmetric lateral bending
3	3.80	Symmetric vertical bending

4	4.64	Symmetric Torsion
5	6.33	Asymmetric lateral bending
6	9.27	Asymmetric Torsion
7	10.57	Asymmetric vertical bending
8	10.81	Symmetric Torsion
9	14.26	Asymmetric Torsion

Table 5.3: Mode analysis results using numeric simulation.

The fundamental vibration frequencies (lateral bend) of the beam are **1.31 and 1.1 Hz** when considering ideal symmetric supports and specific supports, respectively.

FREQ=1.098  
DMX =.005269

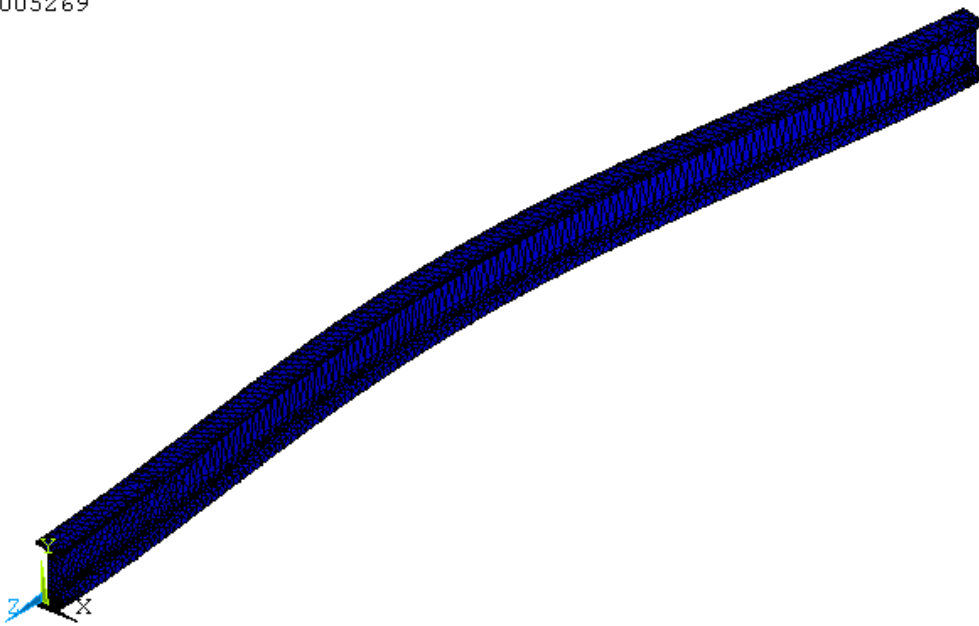


Figure 5.7: View of the deflected beam in lateral vending (mode 1)

## 5.5.2 Vortex Induced Vibration analysis via vortex shedding

Vortex-induced vibration is responsible for major problems in structures and structural members in civil engineering. This type of vibration is associated to flexible structures or structural members and to bluff forms or non aerodynamic forms. Rightly so, there are a significant number of bridges that have experienced vortex-induced vibrations generated by the air flow (see Chapter 4)<sup>36</sup>. The most studied case

---

<sup>36</sup> In May 1998, a few days before the opening, the then longest bridge worldwide (1624m clearance), the Storebaelt Bridge in Denmark, experienced vortex-induced vertical vibrations on the slab that were almost half a meter in

is the phenomenon that may occur in any (flexible enough) structure having a bluff form, non aerodynamic or with sharp edges.

### 5.5.2.1 Description of the phenomenon

A 2-dimension body with a non aerodynamic form, bluff or sharp-edged in midst of a normal direction flow to the axis creates high circulation in the leeward direction when the flow separates away (boundary layer) from the surface of the body. Due to the circulation, the opposite direction on either side of the axis, flow rotational structures shall be formed on the leeward face of the object. These vortices will recirculate without traveling if the wind velocity is low. The higher the velocity the bigger the vortices, until a specific size is reached relative to the body size causing it to detach and to travel with the flow medium. As soon as vortex shedding occurs, one vortex gives way to the development of another one on the opposite side and direction until the later separates away from the body and a new cycle begins. In this manner, vortex shedding generated in the leeward direction of the body alternates on either sides of the axis. Vortex shedding involves a sudden change in the pressures field on the leeward face, so that alternative vortex shedding originates a pressure field that fluctuates with the frequency at which detachments take place. Figure 5.8 shows vortex shedding in the wake of a cylinder. This formation of vortices in the wake is normally called the Von Karman Street. The frequency at which vortex shedding takes place is known to vary linearly with the mean velocity of the incident flow.

The resulting field of pressures on either side of the axis has an important transverse component and a component in the direction of the flow. If the body is flexible the fluctuating pressures thus originated will cause the body to vibrate in the harmonic

form (monochromatically). Should the frequency at which vortices are emitted coincide with the frequency of the body's transverse vibration mode, a resonance problem will occur. In that case, the vibration amplitude will grow enormously up to a limit that will depend on the geometry, the mass and the degree of structural damping. The load cycle will take place for as long as the wind velocity producing vortex shedding continues in the frequencies close to the structural mode frequencies and their harmonic ones. With these vibrations the structure

may be subject to important stresses and in addition lead to material fatigue in the structure or structural member.

Figure 5.8: Smoke visualization of the vortex shedding in the wake of a cylinder.

---

amplitude. The bridge was closed and had to be modified with aerodynamic deflectors. (see Chapter 1 and 4)



As stated above, vibration due to vortex shedding is a resonance response. However, it is a self-limiting vibration because its amplitude will grow through resonance until the distortion that the body itself produces in the surrounding flow is such that it breaks the synchronization status and therefore the frequency of vortex shedding. At that point in time, the vibration vanishes and it may reappear if the wind velocity decreases again. By and large vibration will occur within a range of velocities in which the synchronization will take place. This range varies as the characteristics of the body (shape ...), flow and damping change.

The study has found that for this type of vibration to occur, a certain bi-dimensionality in the flow is necessary as well as a normal direction of the flow to the body's axis. Similarly it is a particularly sensitive phenomenon to changes in body geometry and in the turbulence intensity of the approaching flow (decreasing amplitude with increasing intensity).

The transverse component of the pressure fluctuating field induced by vortex shedding has the same frequency,  $n$ , than the vortex shedding cycle, namely, it has a maximum value in one direction when vortex shedding takes place on that side and a maximum one in the opposite direction when there is vortex shedding on the opposite side, completing a full detachment cycle. However, the longitudinal component in the flow direction does not change its sine width the vortex on either side so that the frequency at which this component fluctuates shall be  $2n$  (see, for example (Blevins, Flow induced vibration, 1986).

In terms of effects on bridges, the applicable standard IAP98 states that “in bridges with a span below 200m, vibration due to vortex shedding should not be checked”. In any event neither does the standard make any reference to the effect on structural members during construction.

### 5.5.2.2 Analysis

To study the possibility of vibration caused by vortex shedding, the frequency needs to be determined at which said emission will take place in the case of the Bridge beams. The frequency at which the detachment takes place shall be dependant on, as stated above, the velocity, linearly changing with it. It will also depend on the size of the normal body relative to the flow and this can be calculated using the Strouhal number common to the shape of the body which is defined as:

$$St = \frac{nD}{V} \quad (1.39)$$

where  $n$  is the frequency at which the vortex shedding takes place,  $D$  the normal dimension relative to the body flow and  $V$  the free mean velocity. The Strouhal number is experimentally estimated. For the double-T shape, Eurocode (European Committee for Standardization, 2001) and ROM0.4 (Spanish Ministry of Public

Works, 1995) state:  $St=0.144$ . For further accuracy, Blevins (Blevins, Flow induced vibration, 1986):  $St=0.144$  is used for the case of the double-T slenderness in question. This a-dimensional constant has been estimated using numeric simulation for the Bridge beams.

Reynolds number,  $Re$ , is used to know whether the velocities range matches the one at which the stationary recirculation takes place or if a vortex shedding will occur instead. In this case, for a 10 m/s velocity the following is used:

$$Re = \frac{V \cdot D}{\nu} = 1.47 \cdot 10^6 \quad (1.40)$$

where  $\nu$  is the cinematic viscosity of air. The estimated  $Re$  is reasonable for vortex shedding. Thus, Figure 5.9 attached herein shows vortex shedding for a wind velocity of 11m/s.

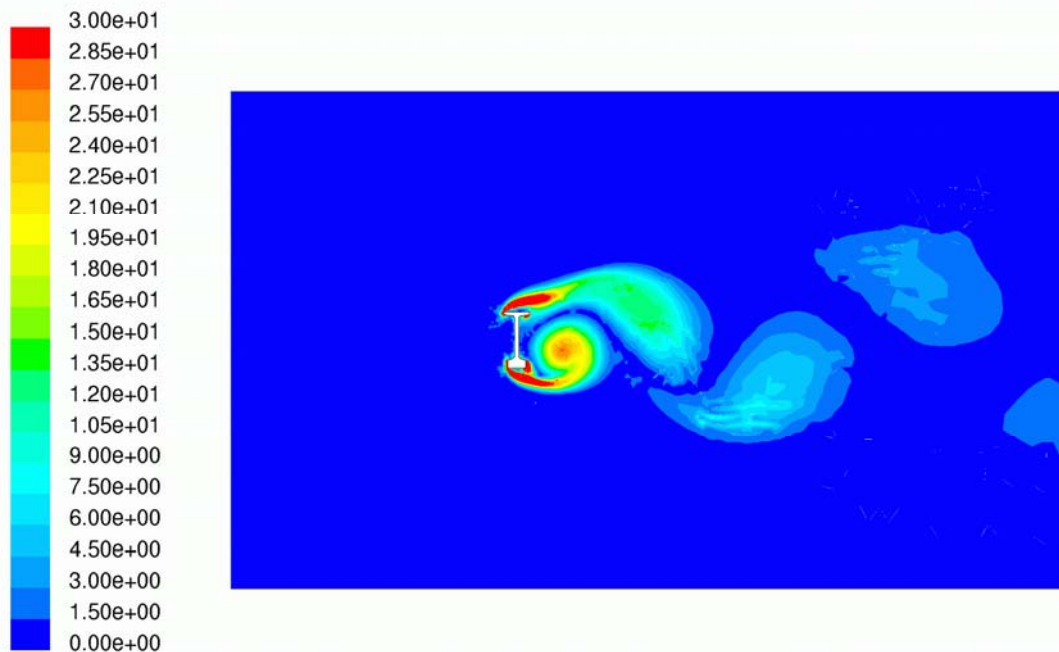


Figure 5.9: Vorticity field for an 11m/s wind velocity.

Using the (0.29) equation the wind velocity can be calculated at which resonance will occur if vortex shedding frequency is equal to half the lateral bend mode frequency, because as stated above, the load frequency in the flow direction is twice the vortex shedding speed.

$$V_{\text{resonancia}} = \frac{\frac{1}{2} f_{\text{hor1}} \cdot D}{St} = \frac{\frac{1}{2} 1.31 \cdot 2.44}{0.144} = 11.1 \text{ m/s} = 39.95 \text{ Km/h} \quad (1.41)$$

As of wind velocities of about 40 Km/h a resonant response will occur, and lateral bending vibrations might be reached with significant amplitudes.

Similarly, if we consider a mode frequency of **1.1Hz**, calculated with a mode analysis, the velocity that will originate the resonance response is of **9.3 m/s**. Therefore, for this specific support conditions (neoprenes and struts) a resonance response will occur starting at  $9.3\text{m/s} = \mathbf{34\text{ Km/h}}$ .

Using numeric simulation the drag coefficient in terms of time has been calculated and it is presented in Figure 5.9. The study has found that **the drag coefficient clearly fluctuates around the 1.34 Hz frequency** which is consistent with the St number used in the previous mathematical analysis.

Using the velocity field shown on Figure 5.11, at one instant of the shedding cycle, vortex geometry can be described at the time the shedding occurs, which will be of special interest when studying the vibration dissipating measures. The corresponding velocity fields to the different shedding phases can be found in the Appendix II.

The maximum amplitude response may be roughly estimated as a reference, using the cylinder case (Blevins, Flow induced vibration, 1986), based on a mass-damping parameter though it does not specifically fit the shape of the Beam.

$$\frac{1}{\pi^2} \frac{2 m (2 \pi \xi)}{\rho D^2} = 7.17 \quad (1.42)$$

where  $\xi$  is the estimated critical damping factor, which as stated above is 2%.

A non-dimensional amplitude is calculated based on this coefficient,

$$\frac{A}{D \gamma} = 0.015; \frac{A}{D} = 0.0196 = 2\%; A = 5\text{cm} \quad (1.43)$$

In this type of vibration the study has found that the so-called aerodynamic damping turns negative, which added on to the structural damping causes the total effective damping on the movement to be lower, therefore causing the amplitude to increase. The damping factor is difficult to estimate unless it is experimentally calculated in a wind tunnel test.

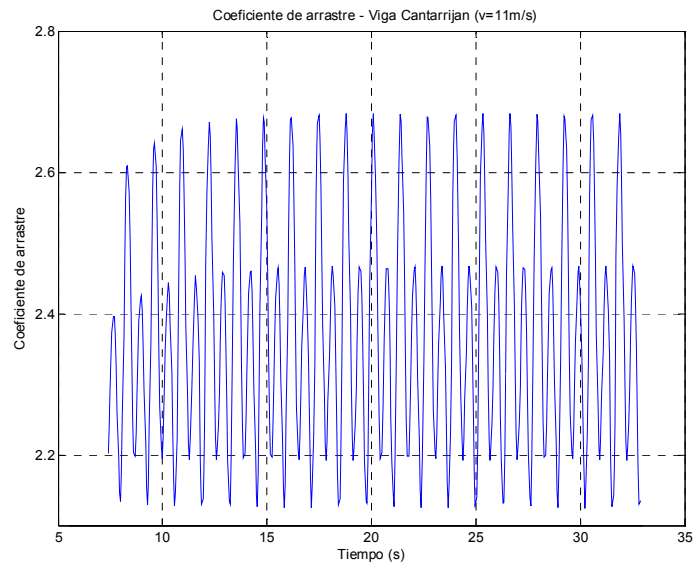


Figure 5.10: Drag coefficient time series calculated using numeric simulation.

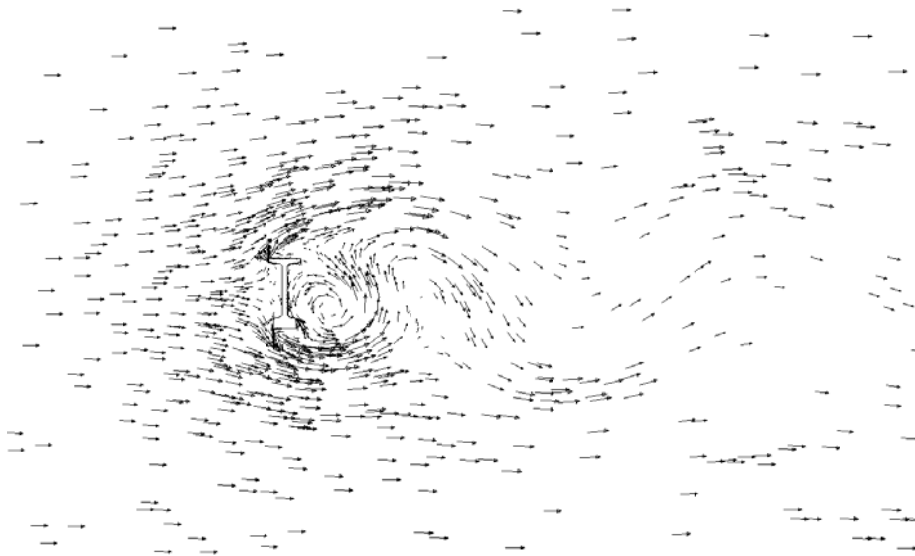


Figure 5.11: Vector velocities field for a flow velocity of 11m/s calculated with numeric simulation.

## Equivalent Force

Below an equivalent static force is calculated using the methodology in the Canadian standard NBC-1995 (National Research Council of Canada, 1995). This equivalent force is calculated using the following equation:

$$F_{ce} = \frac{C_1}{\sqrt{\lambda} \cdot \sqrt{\xi - C_2 \cdot \frac{\rho D^2}{m}}} q D \quad (1.44)$$

where  $C_1 = 3$  is a slenderness-related parameter,  $\lambda = 18.1$ ,  $C_2 = 0.6$  and the remaining parameters have been defined in advance. The result is that the equivalent static load per longitudinal meter is,

$$F_{ce} = 593.87 \text{ N/m} \quad (1.45)$$

for a previously calculated velocity of 11.1 m/s.

With a dynamic analysis of the response for twofold the estimated amplitude, the total calculated inertia force is of **31,317.6 N**, which would be consistent with 708.04 N/m which in turn is a conservative estimate.

However, the limiting nature of the vibration is given by the maximum displacement by the dynamic interaction in resonance.

According to the wind analysis submitted, there are between 8 and 10 hours prior to the time when the vibration occurred during which the vibration should have occurred. For a mode frequency of 1.1Hz this timeframe would be consistent with almost 40,000 cycles of discontinuous vibration. Thus, fatigue has been identified as the probable cause of failure.

### 5.5.3 Summary

After covering the static calculations in the previous section, this section has focused on the dynamic phenomenon resulting in beam vibrations. The study has found that precisely, at velocities of an order of magnitude similar to the ones that occurred the day the failure happened (see section 3), resonant vibration may have been experienced in the lateral bend due to vortex shedding. Therefore this aero elastic mechanism has been identified as the cause of the vibrations that lead to failure (fatigue). Such mechanism is also referred to as along wind or in-line vortex induced vibration.

From the analysis the conclusion may be drawn that these vibrations will occur for local wind directions in the direction of the valley, (see section 5.3, N-NW and S-SE component winds). The wind intensity that will cause these vibrations is as low as 34 Km/hr over the bridge, which is consistent with a 5 Force approximately at 10 m high in the coast, a force that is relatively probable for these directions.

The mechanism described herein is consistent with the lay-out of the beams that fell as well as with the order in which they fell (see Figure 5.1) since only the beams with a free wake in the leeward direction were forced with this mechanism.

The buffeting effect due to turbulence on site might facilitate the synchronization of the harmonic vibrations described herein.

The neoprene supports conveying an embedding moment vis a vis the lateral vibration, account for the slight rocking movement combined with the significant harmonic vibration identified the day after the failure occurred, consistent with the vibration mode estimated with numeric simulation in section 5.5.1. In addition, the pair of vortices, given the non symmetric geometry relative to the X axis, is not symmetric, therefore the pressure induced by each one of them will be different thus mildly contributing to a torsion mode.

## 5.6 Proposed Action

Proposed course of action for future practice follows two different options.

### 5.6.1 Aerodynamic

A simple way to prevent this phenomenon from occurring is to place hanging clothes fastened on to the web of the beams at the extremes, in the third central part of the beam, to stop circulation and, therefore preventing the vortex formation and shedding. This methodology would eliminate the “source” mechanism causing the vibration<sup>37</sup> and at the same time it is simple and not costly. This effect can be easily achieved with a single central stretch or two shorter ones as proposed in the attached schematic. In no case shall it be less than 1.75 m high.

The dissipating effectiveness of the mechanism has been corroborated using numeric simulation. Thus, Figure 5.13 attached herein shows the vortex-induced pressure field, with and without the proposed clothes in place. Clearly, by placing these clothes, the variable nature of the leeward pressures is reduced, if not eliminated. Last, the drag force induced on the beam equipped with clothes has also been corroborated. This time series (Figure 5.14) clearly shows that there is no oscillation therefore resonance cannot occur.

### 5.6.2 Structural

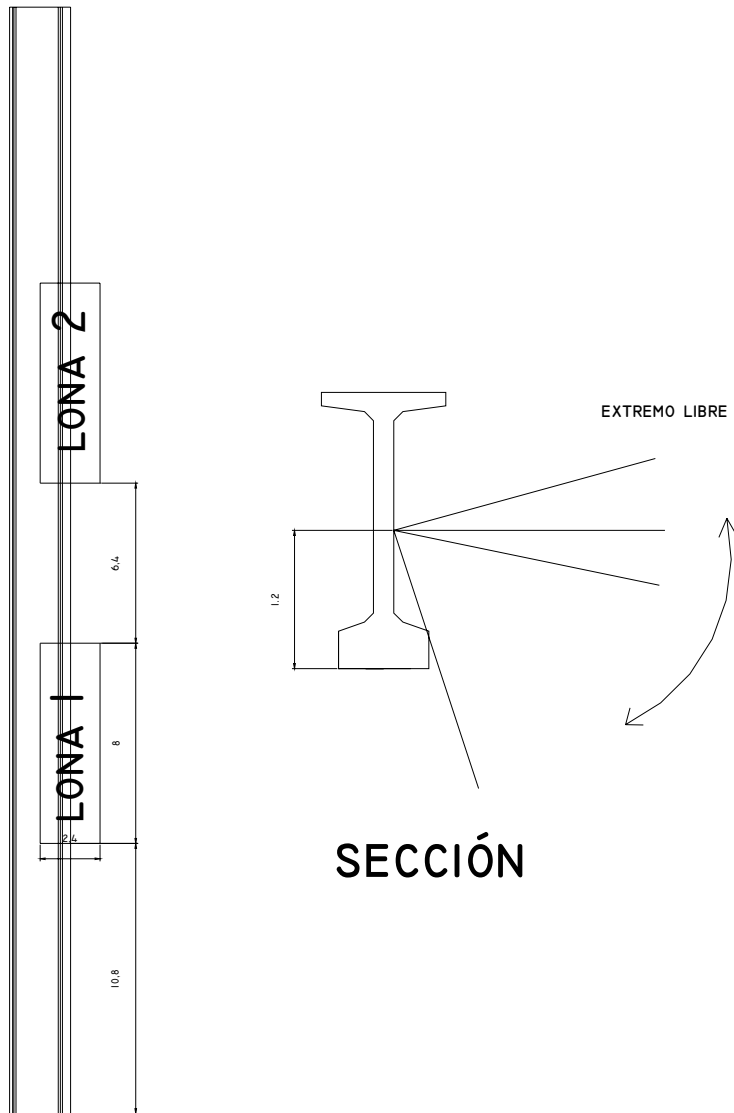
The structural response can be improved by increasing the damping factor or the rigidity:

---

<sup>37</sup> In certain aviation structures, rigid forms called “splitter plates” are frequently used.

- The former would involve placing dampers such as viscous (oil) fluid tanks, preferably of a small size on the beams to be installed to be removed at the time the slab is built.
- By modifying the transverse vibration mode with tie rods between beams from head to head. The profiles should be rigidly linked to the heads because should there be any play vibration might be initiated and lead to increasingly stringent loads due to the effect of resonance and to the high inertia of beams. The study has found that, for example, by distributing 3 profiles in an asymmetric manner (see Figure attached) the initiation of vibration would be prevented. In this example, the corroboration is made by buckling front axial 3 IPN160 profiles in A52 distributed at  $1/3, 1/5$  and  $1/4$  of the length and asymmetrically.

With this mechanism the transverse bend vibration mode in every beam has been changed by increasing the natural frequency and preventing the resonance response from occurring up to significantly higher velocities which will depend on the final distribution of profiles and tie rods.



## PERFIL

Figure 5.12: Clothes of the "splitter plate" type to dissipate vibrations.



Figure 5.13: Vortex induced pressure field, with and without clothes

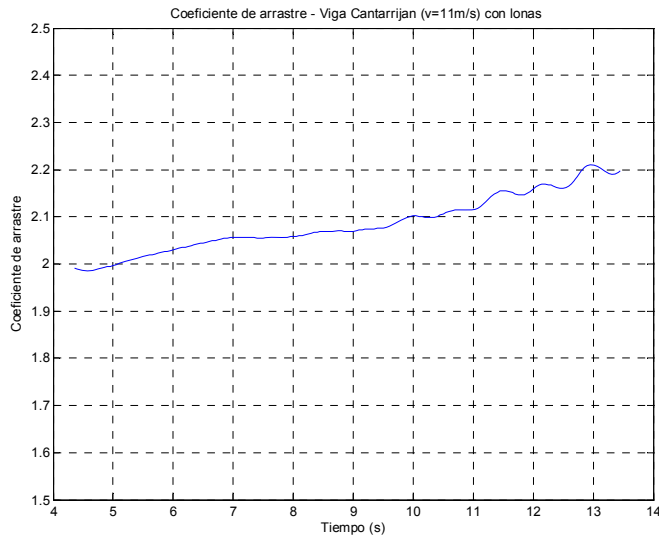


Figure 5.14: Time series of the drag coefficient on the beams with the proposed clothes.

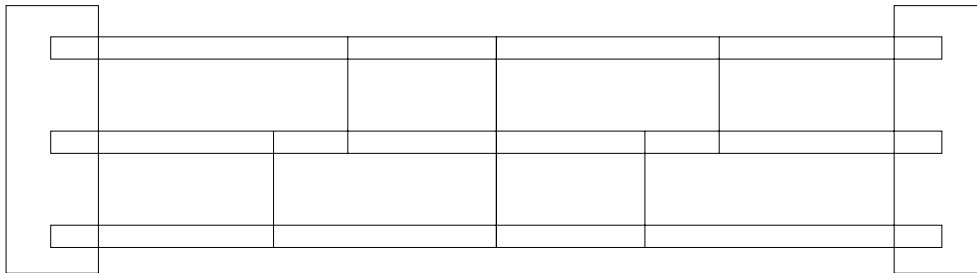


Figure 5.15: An example of a proposed profile lay-out.

### 5.6.3 Monitoring

The proposal is to monitor vibrations as well as wind conditions which would facilitate real-time and ongoing control and prediction of anomalies.

#### 5.6.3.1. Real time measurement of local wind

Permanent measurement of wind and direction in the centre of the valley transmitted on an ongoing basis with a wireless system to a control post. An intensity threshold could be set for specific directions as on site warning system (audio signal and/or light signal) and via SMS text messages to technicians in charge.

#### 5.6.3.2. Real time measurement of structural response

An accelerometer permanently transmitting to the same control post, would provide quantitative information about the vibration level, rejecting false alarms and thus increasing control and operation effectiveness. Likewise, this measurement will facilitate the determination of the real structural damping factor and the intrinsic aerodynamic factor of these beams in this vibration mode.

## 5.7 Conclusions

Evidence has been presented to conclude that the cause that drove the collapse of 6 beams freely placed on the pillars, was the lateral bending along wind vibration induced by vortex shedding. Likewise, the way in which they were placed was consistent with applicable current technical standards. This is a rare phenomenon, because of its nature and because of the clear temporary nature of the vulnerability thereof (from the setting of the beam on the piers through the construction of the slab). However, the wind velocity necessary to cause this phenomenon has been estimated to be relatively probable. Thus, a proposal has finally been made for future practice including two courses of action: a structural one, increasing the rigidity or the damping factor and an aerodynamic one, preventing the initiation of the mechanism causing the vibration. Last, a monitoring control is proposed of velocity, wind direction and vibration to enhance safety and operation effectiveness during construction.



# Chapter 6

## Conclusions, recommendations and future work

The main objective of this research was to investigate the mechanisms of the complex flow-structure interaction in torsional vortex-induced oscillations of a quasi-streamlined bridge deck. The case study was the Storebælt Bridge in Denmark.

### 6.1 Structural response

The response to different wind loading histories was studied (Chapter 3). The results obtained were consistent with previous investigations from different laboratories with different types of models and full-scale monitoring. The main findings are summarized below:

- It was observed that the wind speed resolution of the test is important.

A coarse resolution can lead to non-conservative estimations of the amplitude of the response. It is recommended that, for a detailed study of the vortex-induced response of streamlined bridges, the resolution be as high as possible. This resolution would be given by the wind tunnel speed range and carefully designing the stiffness of the model. The use of a specific spring system for each particular response is recommended.

- The sample time for each wind tunnel wind speed, depending on the velocity scale, affects the amplitude of the response. This is of greater effect for the case of decreasing wind speeds.
- The considerable effect of the structural damping in the vortex-induced response was observed. It is recommended that the response with the lowest structural damping values possible be used, due to the uncertainty in the estimation of the prototype values.
- The amplitudes observed in the model, when locked-in vortex-induced response for decreasing wind speeds were the same as for an increasing wind speed; both curves collapse within the range  $V_{or}^+ - V_{or}^-$ . A decreasing wind speed monitored in full-scale (by others) was consistent with the present experiments. The onset wind speeds for the response to decreasing wind speeds was within the plateau range for increasing wind speeds.

The hysteresis in the response and the significant sensitivity observed to different parameters has been described. Therefore, a combined study of the evolution of the wind velocity field in the event of a storm and the subsequent evolution of the bridge response is necessary. For instance, in study of the evolution of a bridge's response to a hurricane passing. The real wind field to which bridges are subjected, differs from the stationary wind speeds of the wind tunnels.

The observed responses in these experiments were located in two domains available in the literature for classifying the shapes of bodies for vortex-induced vibration. It was found that in these classifications, the response of the Storebaelt Bridge would correspond to that of a rectangular shape. Therefore, a classification of bridge deck shapes for vortex-induced vibration may need to include detailed deck shape information.

## 6.2 Mechanisms of the flow-structure interaction

Simultaneous surface pressures and responses were measured for different build-up phases, with increasing and decreasing wind speeds. Spectral, phase-averaging, and correlation studies provided some insight into the flow-structure interaction (Chapter 4-7).

The torsional vortex-induced oscillations seem to start due to vortex-shedding from the trailing edge (Figure [5-18]). Strengthened separation bubbles develop with increasing wind speed at the leading edge's upper and lower flanges, where the flow recirculates. A vortex structure, associated with the separation bubble on the upper flange may be advected downstream. One could associate that with motion-induced vortices that may originate due to the oscillations of the tip of the leading edge. Note that, the larger the amplitudes, the faster the leading edge moves. The flow around the tip remains attached up to a certain relative velocity (of the tip with respect to the air). Then, separation occurs and a vortex at the tip may form. This vortex on the upper flange near the leading edge, would form for wind speeds higher than a certain one (point labeled "2" in Figure [3-10]) given that suctions on this location were observed for those wind speeds only (Figure [6-9]). At the wind speed for point "2", the response curve presents an inflection point. For higher wind speeds, amplitudes of oscillation grow at a greater rate for the same wind speed increments. In the range of wind speeds from inflection point in the response curve to the maximum amplitude oscillations wind speed, a motion-induced forcing mechanism seems to control the response, instead of the above mentioned Kármán vortices (Figures [7-6]-[7-8]).

This vortex generated at the tip of the leading edge, plays a major role in the forcing mechanism. Actions to suppress or reduce torsional vortex-induced vibrations in such a type of streamlined bridge deck should be carried out at this location.

## 6.3 Future work

A similar study to this presented here should be carried out for the vertical vortex-induced oscillations.

Further research is needed to fully understand the mechanisms of the synchronization and confirm what has been speculated about the flow field. Therefore, the velocity field around the deck should be obtained. The author is planning on carrying out PIV (Particle Image Velocimetry) measurements in the near future.

The identification of the mechanisms of the flow-structure will aid in the understanding and evaluation of the aerodynamic damping and aerodynamic admittance. Mathematical models available could be refined and adjusted to predict

less conservative values of the maximum amplitude of oscillations or which require fewer experimental parameters.

To mitigate the vertical induced oscillations exhibited by the Storebaelt Bridge, guide vanes were installed at the sharp edges of the bottom surface. The study of effect of these devices was not considered in this investigation. A study of their effects on the torsional vortex-induced response, as well as on the flutter limit, should be considered.

# References

AG Davenport Wind Engineering Group. (2007). *Wind Tunnel Testing: A General Outline*. The University of Western Ontario, Boundary Layer Wind Tunnel Lab. . London, On: Boundary Layer Wind Tunnel Lab. .

ASCE. (1999). *Wind Tunnel Model Studies of Buildings and Structures*. (N. Isyumov, Ed.) ASCE.

Barlow, J., Rae, W. H., & Pope, A. (1999). *Low-Speed Wind Tunnel Testing* (3rd Edition ed.). Canada: John Wiley & Sons.

Batill, S. H. (1984). Aerodynamic Design of Three Dimensional Subsonic Wind Tunnel Inlets. *American Institute of Aeronautics and Astronautics Journal (AIAA)*, 24 (2), 268-269.

Battista, R. a. ( 2000). Reduction of vortex-induced oscillations of Rio-Niteroi bridge by dynamic control devices. *Journal of Wind Engineering and Industrial Aerodynamics*, 273-288 Vol 84,.

Bearman, P. (1984). Vortex Shedding from Oscillating Bluff Bodies. *Annu. Rev. Fluid Mech*, 16, 195-222.

Bearman, P. (1984). Vortex Shedding from Oscillating Bluff Bodies. *Annu. Rev. Fluid Mech*, 16, 195-222.

Bendat, J. a. (2000). *Random Data, Analysis and Measurement Procedures*. 3rd Ed. . Wiley Inter-Science. .

Billah, K. (1989). *A Study of Vortex-Induced Vibration*. PhD Thesis. USA: John Hopkins University.



Bishop, R., & Hassan, A. (1963). The lift and drag forces on a circular cylinder in a flowing fluid. *Proceedings of the Royal Society London Ser.*, (pp. 32-50). London.

Blackburn, H. M., Govardhan, R., & Williamson, C. (2000). A complementary numerical and physical investigation of vortex-induced vibration. *Journal of Fluids and Structures*, *15*, 481-488.

Blackburn, H., & Henderson, R. (1999). A Study of two-dimensional flow past an oscillating cylinder. *Journal of Fluid Mechanics*, *385*, 255-286.

Blevins, R. (1986). *Flow induced vibration*. Krieger.

Blevins, R. (1990). *Flow induced vibration* (Second Edition ed.). Krieger Publishing Company.

Blevins, R., & Iwan, W. (1974, September). A Model for Vortex Induced Oscillation of Structures. *Journal of Applied Mechanics*, 581.

Brika, D. a. (1993). Vortex-induced vibrations of a long flexible circular cylinder. *Journal of Fluid Mechanics*, *250*, 481-508.

Cantwell, B. a. (1983). An experimental study of entrainment and transport in the turbulent near wake of a circular cylinder. *Journal of Fluid Mechanics*, *136*, 321-374.

Cataldo, J. A. (1991). *Determinación del campo de Velocidades Medias en las inmediaciones de una entrada acampanada*. Instituto de Mecánica de los Fluidos e Ingeniería Ambiental. Montevideo: Facultad de Ingeniería.

CBR. (1998.). *Measurements of Vortex Shedding Excitation*. Technical Report.

CBR. (1998). *Measurements of Vortex Shedding Excitation*. Technical Report.

CEN . (2004). *Eurocode 2: Design of concrete structures - Part 1-1: General rules and rules for buildings*. CEN European Committee for Standardization.

Cermak, J. (1971). Laboratory Simulation of the Atmospheric Boundary Layer. *AIAA Journal*, *9*(9), 1746-1754.

Cigada, A., Falco, M., & Zasso, A. (2001). Development of new systems to measure the aerodynamics forces on section models in wind tunnel testing. *Journal of Wind Engineering and Industrial Aerodynamics*, *89*, 725-746.

Corless, R. M. (1993.). Mathematical modelling of the combined effects of vortex-induced vibration and galloping. Part II. *Journal of Fluids and Structures* *7*, 825-848.

Counihan, J. (1967). The simulation of the atmospheric boundary layer in a wind tunnel. *Atmospheric Environment*.

Csanady, G. (1964). *Theory of turbomachines*. Waterloo, ON, CANADA: Mc Graw-Hill.

Chyu, W., & Rockwell, D. (1994). Timing of vortex formation from an oscillatory cylinder. *Physic of Fluids* , 6 (11), 3677-3682.

Davenport, A. (1961). *A Statistical Approach to the Treatment of Wind Loading on Tall Masts and Suspension Bridges, PhD Thesis*. Bristol, UK: The University of Bristol.

Davenport, A. K. (1992). Taut strip model tests. *Proc. of Aerodynamics of Large Bridges*. (pp. 113-124). Bakelma, Rotterdam. : A. Larsen (Ed.).

Davenport, A. (1961). *PhD Thesis. A statistical approach to the treatment of wind loading of tall masts and suspension bridges*. Bristol, U.K.: The University of Bristol.

Davenport, A. (1961). The application of statistical concepts to wind loading of structures. . 19, pp. 449-71. Proceedings, Institution of Civil Engineers .

Davenport, A., & Isyumov, N. (1967). *The Application of the Boundary Layer Wind Tunnel to the Prediction of Wind Loading* (Proc. of the Int. Res. Sem. ed., Vol. 1). (U. o. Press, Ed.) Ottawa, Ontario, Canada: N.R.C. Canada.

Davenport, A., & King, J. (1982). *A Study of Wind Effects for the Sunshine Skyway Bridge Tampa, Florida - Concrete Alternative*. The University of Western Ontario, Faculty of Engineering Science Research Report, London.

Davenport, A., Isyumov, N., King, J., Novak, M., Surry, D., & Vickery, B. (1985). BLWT II: The design and performance of a new boundary layer wind tunnel. *Proc. 5th U.S. National Conference on Wind Engineering* . Lub-bock, Texas.

Davies, M. (1976). A comparison of the wake structure of a stationary and oscillating bluff body, using a conditional averaging technique. *Journal of Fluid Mechanics* , 75 (2), 209-231.

Den Hartog, J. (1984). *Mechanical Vibrations*. Dover Publications Inc.

DMI and SINTEF. (1993). *Wind Tunnel Tests, Storebaelt, East Bridge. Detailed Design Suspension Bridge Section Model Tests*.

DMI. ( June 1998.). *Wind Tunnel Study of Vortex Shedding Mitigating devices for the Storebaelt East Bridge* .

Dyke, M. V. (1982). An album of fluid motion. . *The Parabolic Press* . , 42-59.

Ehsan, F. a. (1990). Vortex-induced vibrations of flexible bridges. *Journal of Engineering Mechanics, ASCE, Vol. 116, No. 6* , 1392-1411.

European Committe for Standarization. (2001). *Eurocode 1: Basis of design an actions on structures. Part 2-4 Actions on structures: Wind Actions*.

Fang, F. (1997). A design method for contractions with square end sections. *ASME Journal of Fluids Engineering* , 454-458.

Fang, F., Chen, J., & Hong, Y. (2001). Experimental and analytical evaluation of flow in a square to square wind tunnel contraction. *Journal of Wind Engineering and Industrial Aerodynamics*, 247-262.

Farell, C. Y. (1992). *Experiments on Turbulence Management using screens and honeycombs*. University of Minnesota, Department of Civil and Mineral Engineering. Minneapolis: University of Minnesota.

Farquharson, F. B. (1952). Aerodynamic Stability of Suspension Bridges with special reference to the Tacoma Narrows Bridge. Washington: University of Washington, Engineering Experiment Station, .

Farquharson, F. B. (1952). Aerodynamic Stability of Suspension Bridges with special reference to the Tacoma Narrows Bridge. Washington: University of Washington, Engineering Experiment Station, Bull. .

Frandsen J.B., M. A. (1999). Finite element simulation of wind induced bridge motion. *Proc. of Computational Methods for Fluid-Structure Interaction.*, (pp. 271-282.). Tapir, Forlag, Trondheim, Norway.

Frandsen, J. (2001.).

Frandsen, J. B. (1999). *Computational Fluid-Structure Interaction Applied to Long-Span Bridge Design*. . PhD Thesis. Cambridge University .

Frandsen, J. (2004). Numerical bridge deck studies using finite elements. Part I: Flutter. *Journal of Fluids and Structures*, 19, 171-191.

Frandsen, J. (2001). Simultaneous pressures and accelerations measured full-scale on the Great Belt East suspension bridge. . *Journal of Wind Engineering and Industrial Aerodynamics* 89, 95-129.

Frandsen, J. (2001). Simultaneous pressures and accelerations measured full-scale on the Great Belt East suspension bridge. *Journal of Wind Engineering and Industrial Aerodynamics*, 89, 95-129.

Fujino, Y. a. (1012-1025). Wind-induced vibration and Control of the Trans-Tokyo Bay Crossing Bridge. . *Journal of Structural Engineering, ASCE* 128 (8) , 1012-1025.

Fujino, Y., & Yoshida, Y. (2002). Wind-induced vibration and Control of the Trans-Tokyo Bay Crossing Bridge. *Journal of Structural Engineering, ASCE* 128 (8) , 1012-1025.

Govardhan, R., & Williamson, C. (2000). Modes of vortex formation and frequency response of a freely oscillating cylinder. *Journal of Fluid Mechanics*, 420, 85-130.

Groth, J. J. (1988). Turbulence reduction by screens. *Journal of Fluid Mechanics*, 197, 139-155.

Hangan, H. K. Simultaneous characterization of wake velocities, pressures, loading, displacements and accelerations for a dynamic bridge deck model. . *Americas Conference on Wind Engineering, Session W1C, Clemson, US*.

- Hartlen, R. T. (1970). Lift oscillator model of vortex induced vibration. *Proceedings of the American Society of Civil Engineers* , (pp. 577-591.).
- Hartlen, R., & Currie, I. (1970). Lift oscillator model of vortex-induced vibration. *Journal of the Engineering Mechanics Division* , *EM 5*, 577-591.
- Hjorth-Hansen, E. (1992.). Section Model Tests. . *Proc. of Aerodynamics of Large Bridges*. (pp. 94-112.). Bakelma, Rotterdam.: A. Larsen (Ed.) .
- Holmes, J. a. (1987). Optimization of dynamic-pressure measurement systems. . *Journal of Wind Engineering and Industrial Aerodynamics*. *25* , 249-273.
- Holmes, J. D. (2001). *Wind Loading of Structures*. Spon Press.
- Holmes, J. D. (2001). *Wind Loading of Structures*. Spon Press.
- Hunt, J., & Fernholtz, H. (1975). Wind Tunnel Simulation of the Atmospheric Boundary Layer: A report on Euromech 50. *Journal of Fluid Mechanics* , *70* (3), 543-559.
- Hussain, A. K., & Ramjee, V. (1976). Effects of the Axisymmetric Contraction Shape on Incompressible Turbulent Flow. *Transactions of ASME, Journal of Fluids Engineering* , 58-69.
- Idelchik, I. (1986). *Handbook of hydraulic resistance*. Berlin, Germany: Springer Verlag.
- Irwin, H. (1981). The Design of Spires for Wind Simulation. *Journal of Wind Engineering and Industrial Aerodynamics* , *7*, 361-366.
- Ito, M. (1992). Wind Engineering of Larges Bridges in Japan. In A. Larsen (Ed.), *Proc. of Aerodynamics of Large Bridges* (pp. 71-83). Rotterdam: A.A. Bakelma.
- J.P.C., K. (2002). *The University of Western Ontario*. Ontario: Phd Thesis in progress.
- Jensen, M. (1958). *The Model-Law Phenomena in Natural Wind*. Copenhagen, Denmark: The Danish Technical Press.
- Jensen, M., & Niels, F. (1963). *Model Scale Tests in Turbulent Wind* (Vol. Part I). (T. D. Press, Ed.) Copenhagen, Denmark.
- Khalak, A., & Williamson, C. (1999). Motions, forces and mode transitions in vortex-induced vibrations at low mass-damping. *Journal of Fluids and Structures* , *13*, 813-851.
- King, J. e. (December 1990.). *A Study of Wind Effects for The Storebaelt Bridge Tender Design*. The University of Western Ontario. : BLWT-IR-S67-1. Boundary Layer Wind Tunnel Laboratory. .
- King, J. K.-N. ( Aug 2001.). *A study of wind effects for The Tsing Lung Bridge, Hong Kong*. London, Ontario, Canada: Final Report of Phase 2, G3 section model tests. BLWT-SS33-2001, BLWT,.

King, J. K.-N. (May 2001). *A study of wind effects for The Tsing Lung Bridge, Hong Kong*. London, Ontario, Canada.: Final Report of Phase 1, G3 section model tests. BLWT-SS28-2001, BLWT,.

King, J. (n.d.). Not published research material. London, Ontario, Canada.

King, J. P. (2001).

King, J. P. (2003). *The Aerodynamics of Long Span Bridges. PhD. Thesis*. London, Ontario, Canada: The University of Western Ontario.

King, J. (n.d.). *The Boundary Layer Wind Tunnel Laboratory Home Page*. Retrieved from <<http://www.blwt.uwo.ca/facil/facil.htm>>.

King, J., Larose, G., & Davenport, A. (1990). *A Study of Wind Effects for The Storebaelt Bridge Tender Design*. The University of Western Ontario, Boundary Layer Wind Tunnel Laboratory.

Komatsu, S. a. (1980,). Vortex-induced oscillations of bluff cylinders. *Journal of Wind Engineering and Industrial Aerodynamics*. 6, , 335-362.

Komatsu, S., & Kobayashi, H. (1980). Vortex-induced oscillations of bluff cylinders. *Journal of Wind Engineering and Industrial Aerodynamics* , 6, 335-362.

Koumaoutsakos, P., & Leonard, A. (1995). High resolution simulations of the flow around an impulsively started cylinder using vortex methods. *Journal of Fluid Mechanics* , 296, 1-38.

Kumarasena, T. S. (1989). Deer Isle Bridge: Field and computed vibrations. *Journal of Struc. Eng., ASCE 115(9)* , 2313-2328.

Larsen, A. (1993). A generalized model for assessment of vortex-induced vibrations of flexible bridges. . *Proceedings of the 7th U.S. Conference on Wind Engineering*. , (pp. . 383-392.).

Larsen, A. a. (1997). Aeroelastic analysis of bridge girder sections based on discrete vortex simulations. . *Journal of Wind Engineering and Industrial Aerodynamics*, 67-68, , 253-265.

Larsen, A. (1993,). Aerodynamic aspects of the final design of the 1624m suspension bridge across the Great Belt. . *Journal of Wind Engineering and Industrial Aerodynamics 48* , 261-285.

Larsen, A. E. (2000). Storebaelt Suspension Bridge-Vortex Shedding excitation and mitigation by guide vanes. . *Journal of Wind Engineering and Industrial Aerodynamics 88* , 283-296.

Larsen, A. e. (1999). Vortex shedding excitation of the Great Belt East Bridge. *10th International Conference on Wind Engineering*. (pp. 947-954.). Copenhagen, Denmark: In A. Larsen et al., editor.

Larsen, A., & al., e. (1999). Vortex shedding excitation of the Great Belt East Bridge. *10th International Conference on Wind Engineering*. (pp. 947-954.). Copenhagen, Denmark: In A. Larsen et al., editor.

Larsen, A., & Walther, J. Discrete vortex simulation of flow around five generic bridge deck sections. *Journal of Wind Engineering and Industrial Aerodynamics*, 77 & 78, 591-602.

Larsen, A., Esdahl, S., & Andersen J., E. (2000). Storebaelt Suspension Bridge-Vortex Shedding excitation and mitigation by guide vanes. *Journal of Wind Engineering and Industrial Aerodynamics* 88 , 283-296.

Lumley J.L., M. J. (1967, December). Reducing Water Tunnel Turbulence by means of a honeycomb. *Transactions of the ASME - Journal of Basic Engineering* , 764-770.

Lyn, D. a. (1994,). The flapping shear layer formed by flow separation from the forward corner of a square cylinder. *Journal of Fluid Mechanics*, 267, , 353-376.

Mans, M., & Terrés-Nícoli, J. (2004). *Hotwire Study within and around CEAMA WTII in WTI simulated conditions*. CEAMA, Wind Engineering Division. Granada: Univeristy of Granada.

Marris, A. (1964). A review of vortex streets, periodic wakes and induced vibration phenomena. *Journal of Basic Engineering, Transactions of ASME* , 185-193.

Matsuda, K. e. (2001). An investigation of Reynolds number effects on the steady and unsteady aerodynamic forces on a 1:10 scale bridge deck section model. . *Journal of Wind Engineering and Industrial Aerodynamics* 89 , 619-632.

Matsumoto, M. (1999). Recent study on bluff body aerodynamics and its mechanism. *Wind Engineering into the 21st Century*, 67-78.

Matsumoto, M., Shirashi, N., Shirato, H., Stoyanoff, S., & Yagi, T. (1993). Mechanism of and turbulence effect on vortex-induced osillations for bridge girders. *Journal of Wind Engineering and Industrial Aerodynamics* , 49, 467-476.

McDonald, J. e. (2001,). Vortex-induced vibrations of the Second Severn Crossing Cable-stayed bridge—full-scale and wind tunnel measurements. . *Proc. Of the institution of Civil Engineers* 152 issue 2, (pp. 123-134.).

Melaragno, M. (1998). *Preliminary Design of Bridges for Architects and Engineers*. Marecl Dekker.

Metha, K. y. (1998). *Guide to the use of the wind load provisions of ASCE 7-95*. ASCE Press.

Mills, R., Sheridan, J., & Hourigan, K. (2002). Response of base suction and vortex shedding from rectangular prisms to transverse forcing. *Journal of Fluid Mechanics* , 461, 25-49.

Mills, R., Sheridan, J., & Hourigan, K. (2003). Particle Image Velocimetry and Visualization of natural and forced flow around rectangular cylinders. *Journal of Fluid Mechanics* , 478, 299-323.

Miyata, T., Miyazaki, M., & Yamada, H. (1983). Pressure distribution measurements for wind induced vibrations of box girder bridges. *Journal of Wind Engineering and Industrial Aerodynamics*, 14, 223-234.

Morel, T. (1975). Comprehensive Design of Axisymmetric Wind Tunnel Contractions. *ASME Journal of Fluids Engineering*, 225-233.

Nakamura, Y., & Nakashima, M. (1986). Vortex Excitation of Prisms with elongated rectangular, H and T cross-sections. *Journal of Fluid Mechanics*, 163, 149-169.

National Research Council of Canada. (1995). *Nacional Building Code. Structural Commentaries*. Canadian Commission on Building and Fire Codes. Ottawa: National Research Council of Canada.

Naudascher, E., & Rockwell, D. (2005). *Flow Induced Vibrations*. Mineola, NY, USA: Dover Publications.

Naudascher, E., & Wang, Y. (1993). Flow Induced Vibrations of Prismatic Bodies and Grids of Prisms. *Journal of Fluids and Structures*, 4, 341-373.

Okajima, A. (1982). Strouhal Numbers of rectangular cylinders. *Journal of Fluid Mechanics*, 123, 379-398.

Ostenfeld K. H., L. A. (1992). Bridge Engineering and aerodynamics. *Proc. of Aerodynamics of Large Bridges* (pp. 3-22). Rotterdam: Bakelma.

Ostenfeld, K. H. (1986). *Bridge Projects for the Great Belt Crossing. Strait Crossings*. . Bakelma, Rotterdam. : R. Klinge (Ed.).

Owen, J. e. (1996). The prototype testing of Kessock Bridge: response to vortex shedding. *Journal of Wind Engineering and Industrial Aerodynamics*, 60, , 91-108.

Parker, R., & Welsh, M. (1983). Effects of sound on flow separation from blunt plates. *International Journal of Heat Fluid Flow*, 4, 113-128.

Parkinson, G. (1974). Mathematical Models of Flow-Induced Vibrations. In E. Naudascher (Ed.), *Flow Induced Structural Vibration* (pp. 81-127). Berlin: Springer.

Parkinson, G. (1989). Phenomena and modeling of flow-induced vibrations of bluff bodies. . *Progress in Aerospace Science* 26, 169-224.

Plate, E. (1982). *Engineering Meteorology: Fundamentals of Meteorology and their application to problems in Environmental and Civil Engineering*. (E. Plate, Ed.) Elsevier.

Plate, E. (1982). *Engineering Meteorology: Fundamentals of methodology and their applications to problema in environmental and civil engineering*. (E. Plate, Ed.) Amsterdam: Elsevier Scientific Pub. Co.

Plate, E. (1982). Wind-Tunnel modeling of wind effects in engineering. In E. Plate, *Engineering Meteorology: Fundamentals of methodology and their applications*

to *problema in environmental and civil engineering* (pp. Ch. 13, pp.573-639). Amsterdam: Elsevier Scientific Publishing Company.

Ramjee, V., & Hussain, A. K. (1976). Influence of the Axisymmetric Contraction Ratio on Free Stream Turbulence. *Transactions of ASME. Journal of Fluids Engineering*, 506-515.

Reinhold, T. A. (1992). Wind tunnel tests for the Great Belt Link. *Proc. of Aerodynamics of Large Bridges*. (pp. 255-268.). Bakelma, Rotterdam.: A. Larsen (Ed.) .

Ricciardelli, F. d. (2002). Pressure distribution, aerodynamic forces and dynamic response of box bridge sections. . *Journal of Wind Engineering and Industrial Aerodynamics*, Vol. 90, , 1135-1150.

Robertson, I., Sherwin, S., & Bearman, P. (2003). *International Journal for Numerical Methods in Fluids*, 43, 1239-1256.

Rockwell, D. (1998). Vortex-Body Interactions. *Annu. Rev. Fluid Mech.* 30, , 199-229.

Rohsko, A. (1954.). *On the development of turbulent wakes from vortex streets*. National Advisory Committee for Aeronautics, NACA Tech Report 1191.

Roshko, A. (1954). *On the drag and shedding frequency of two dimensional bluff bodies*. National Advisory Committee for Aeronautics (NACA). Washington: NACA.

Royal Aeronautical Society. Engineering Science Data Units. (1980). *Performance of conical diffusers in incompressible flow. ESDU data items #73024 Amend. B*. London: Royal Aeronautical Society.

RTE. (2004). *Design Proeject. Cantarrijan Highway Bridge. Appendix #13, substructure calculations*.

Saathoff, P., & Melbourne, W. (1997). Effects of free stream turbulence on surface pressure fluctuations in a separation bubble. *Journal of Fluid Mechanics*, 337, 1-24.

Saffman, P. (1995). *Vortex Dynamics*. Cambridge, UK: Cambridge University Press.

Sarkar, P., Jones, N., & Scanlan, R. (1992). System Identification for Estimation of Flutter Derivatives. *Journal of Wind Engineering and Industrial Aerodynamics*, 1243-1254.

Sarpkaya, T. A. (2004). A critical review of the intrinsic nature of vortex-induced vibrations. *Journal of Fluids and Structures*, 19, 389-447.

Sarpkaya, T. (1979). Vortex Induced Oscillations. *Journal of Applied Mechanics*, 46, 241-258.

Scanlan, R. H. (1951.). *Introduction to the study of aircraft vibration and flutter*. . Macmilliam.



Scanlan, R., & Tomko, J. (1971). Airfoil and Bridge Deck Flutter Derivatives. *J. Eng. Mech. Div., ASCE*, 97, . , 1717-1737.

Scruton, C. .. (1948). Severn Bridge Wind Tunnel Tests. *Surveyor*, 107. No. 2959. , p. 555.

Schewe, G., & Larsen, A. (1998). Reynolds number effects in the flow around a bluff bridge deck cross section. . *Journal of Wind Engineering and Industrial Aerodynamics* , 829-838.

Schlichting, H., & Gersten, K. (2001). *Boundary Layer Theory* (8th Edition ed.). Bochum, Germany: Springer-Verlag.

Schubaber, G. S. (1948). *Aerodynamic Characteristics of Damping Screens*. National Advisory Committee for Aeronautics. NACA.

Selberg, A. (1961.). Oscillation and aerodynamic stability of suspension bridges. *Acta Polytechnica Scandinavica. Civil Engineering and Building Construction Series No. 13*.

Shirashi, N. a. (1983). On classification of Vortex Induced Response and its application for bridge structures. *Journal of Wind Engineering and Industrial Aerodynamics*, 14 , 419-430.

Shirashi, N., & Matsumoto, M. (1983). On classification of Vortex Induced Response and its application for bridge structures. *Journal of Wind Engineering and Industrial Aerodynamics*, 14 , 14, 419-430.

Simiu, E. a. (1996). *Wind effects on structures. 3rd ed.* . John Wiley & Sons, Inc. .

Simiu, E., & Scanlan, R. (1996). *Wind Effects on Structures* (3rd Edition ed.). New York, US: Wiley-Interscience.

Spanish Ministry of Public Works. (1995). *Recommmendations for the design of Maritime Structures. Climatic loads II: Wind*. (Vols. ROM 0.4-95). Spain: Ports Authority.

Spanish Ministry of Public Works. (1998). *Road Bridge Design Actions*. Department of Road Transportation.

Structurae. (n.d.). *Storebaelt Bridge File*. Retrieved from Structurae: <http://www.structurae.de/en/structures/data/str00031.php>,

Tan Atichat, J. N. (1982). Interaction of free stream turbulence with screens and grids. *Journal of Fluid Mechanics* , 114, 501-528.

Tanaka, H. (1992). Similitude and modeling in bridge aerodynamics. *Proc. of Aerodynamics of Large Bridges*. (pp. 83-94.). Bakelma, Rotterdam: A. Larsen (Ed.) .

Tanaka, H. (1990). *Similitude and modeling in wind tunnel testing of bridges. Bluff Body Aerodynamics and its applications.* . Elsevier.

Tanaka, H. (1992). Similitude and Modelling in Bridge Aerodynamics. . *Proc. of Aerodynamics of Large Bridges*. (pp. 83-91). Bakelma, Rotterdam: A. Larsen (Ed.).

Tanaka, H., & al., e. (1999). Aerodynamic Design of the Great Belt East Bridge. *Long-Span Bridges and Aerodynamics*. (pp. 203-230.). Springer-Verlag,.

Terrés-Nicoli, J. (2006). *Design of Section Model Bridge Test Rig*. CEAMA, Sección de Ingeniería del Viento. Granada: Grupo de Dinámica de Fluidos Ambientales.

Terrés-Nicoli, J. M. (1999). *Study for the design of low speed wind tunnel* (1st Edition ed.). (M. A. Costas, Ed.) Granada, Spain: Universidad de Granada.

Terrés-Nicoli, J. M. (2002). *Torsional Vortex Induced Response of The Storebaelt Bridge*. *MESc Thesis*. London, Ontario, Canada: The University of Western Ontario.

Terrés-Nicoli, J. M., & Losada Rodríguez, M. A. (2002). *Low Speed Aerodynamic Wind Tunnel*. *The University of Granada*. Granada, Spain: Grupo de Puertos y Costas.

Terrés-Nicoli, J. (2002). *The torsional Vortex-Induced Vibration of the Storebaelt Bridge*. *Master of Engineering Science Thesis*. . The University of Western Ontario.

Theodorsen, T. (1935.). *General Theory of aerodynamic instability and the mechanism of flutter*. National Advisory Committee for Aeronautics. Technical Report 496.

Theodorsen, T. (1940.). *General Theory of aerodynamic instability and the mechanism of flutter*. . National Advisory Committee for Aeronautics. Technical Report 452.

Uberoi, M. (1956). Effect of Wind Tunnel Contraction on Free-Stream Turbulence. *Journal of the Aeronautical Sciences* , 754-764.

Van der Pol, B. (1920). A theory of the amplitude of free and forced oscillation. *Radio review 1* , 701-716.

Venture., D. a. ( May 1993. ). *Wind Tunnel Tests, Storebaelt, East Bridge*. . Detailed Design Suspension Bridge Section Model Tests.

Venture., D. a. (May 1990.). *Wind Tunnel Tests, Storebaelt, East Bridge*. . Tender Design Tests.

Venture., D. a. (March 1993. ). *Wind Tunnel Tests, Storebaelt, East Bridge*. *Tender Evaluation, Suspension Bridge*. *Alternative Sections*. .

Vickery, B., & Basu, R. (1983). Across-wind vibrations of structures of circular cross-section. Part I. Development of a mathematical model for two-dimensional conditions. *Journal of Wind Engineering and Industrial Aerodynamics* , 12, 49-73.

Vickery, B., & Steckley, A. (1993). Aerodynamic Damping and Vortex Excitation on an Oscillating Prism in Turbulent Shear Flow. *Journal of Wind Engineering and Industrial Aerodynamics*.

Walther, R. (1999). *Cable Stayed Bridges. 2nd edition.* . Thomas Telford .

Wardlaw, R. L. (1992). The improvement of the aerodynamic performance. . *Proc. of Aerodynamics of Large Bridges* (pp. 59-70.). Bakelma, Rotterdam: A. Larsen (Ed.) .

Williamson, C. (1997, ). Advances in our understanding of vortex dynamics in bluff body wakes. . *Journal of Wind Engineering and Industrial Aerodynamics*, 69-71, 3-32.

Williamson, C., & Govardhan, R. (2004). Vortex-induced vibrations. *Annual Rev. Fluid Mech* , 36, 413-455.

Wyatt, T. (2003). AG Davenport Wind Engineering Symposium. Discussion. . Technical session B: wind effects on bridges. . *ournal of Wind Engineering and Industrial Aerodynamics* , 91, 1559-1563.

Zdravkovich, M. M. (1996). Different modes of vortex shedding: . *An overview Journal of Fluids and Structures* 10, 427-437.

Zdravkovich, M. M. (1997). *Flow around Circular Cylinders: Vol 1: Fundamentals* (Vol. 1). Oxford Science Publications.



CEAMA BOUNDARY LAYER WIND TUNNEL I  
UNIVERSITY OF GRANADA

Scale	N	Revision / Issue	Date

Date  
**January 2003**  
Drawing #  
**1**

Designed and  
Engineered by :  
José M<sup>o</sup> Terrés-Nicolí  
[www.terresnicoli.com](http://www.terresnicoli.com)

General View

TÚNEL AERODINÁMICO  
CEAMA  
UNIVERSIDAD DE GRANADA



CEAMA BOUNDARY LAYER WIND TUNNEL I  
UNIVERSITY OF GRANADA



Date  
**January 2003**

Designed and  
Engineered by :  
**José M<sup>a</sup> Terrés-Nicolí**  
[www.terresnicoli.com](http://www.terresnicoli.com)

Scale	N	Revision / Issue	Date

General view from entrance

Drawing # **2**

UNIVERSIDAD DE GRANADA

CEAMA

TUNNEL I

UNIVERSIDAD DE GRANADA

CEAMA

TUNNEL I

UNIVERSIDAD DE GRANADA

CEAMA

TUNNEL I

UNIVERSIDAD DE GRANADA

CEAMA

TUNNEL I

UNIVERSIDAD DE GRANADA

CEAMA

TUNNEL I

UNIVERSIDAD DE GRANADA

CEAMA

TUNNEL I

UNIVERSIDAD DE GRANADA

CEAMA

TUNNEL I

UNIVERSIDAD DE GRANADA

CEAMA

TUNNEL I

UNIVERSIDAD DE GRANADA

CEAMA

TUNNEL I

UNIVERSIDAD DE GRANADA

CEAMA

A B C D E F G H

1 2 3 4 5 6 7 8





CEAMA BOUNDARY LAYER WIND TUNNEL I  
UNIVERSITY OF GRANADA



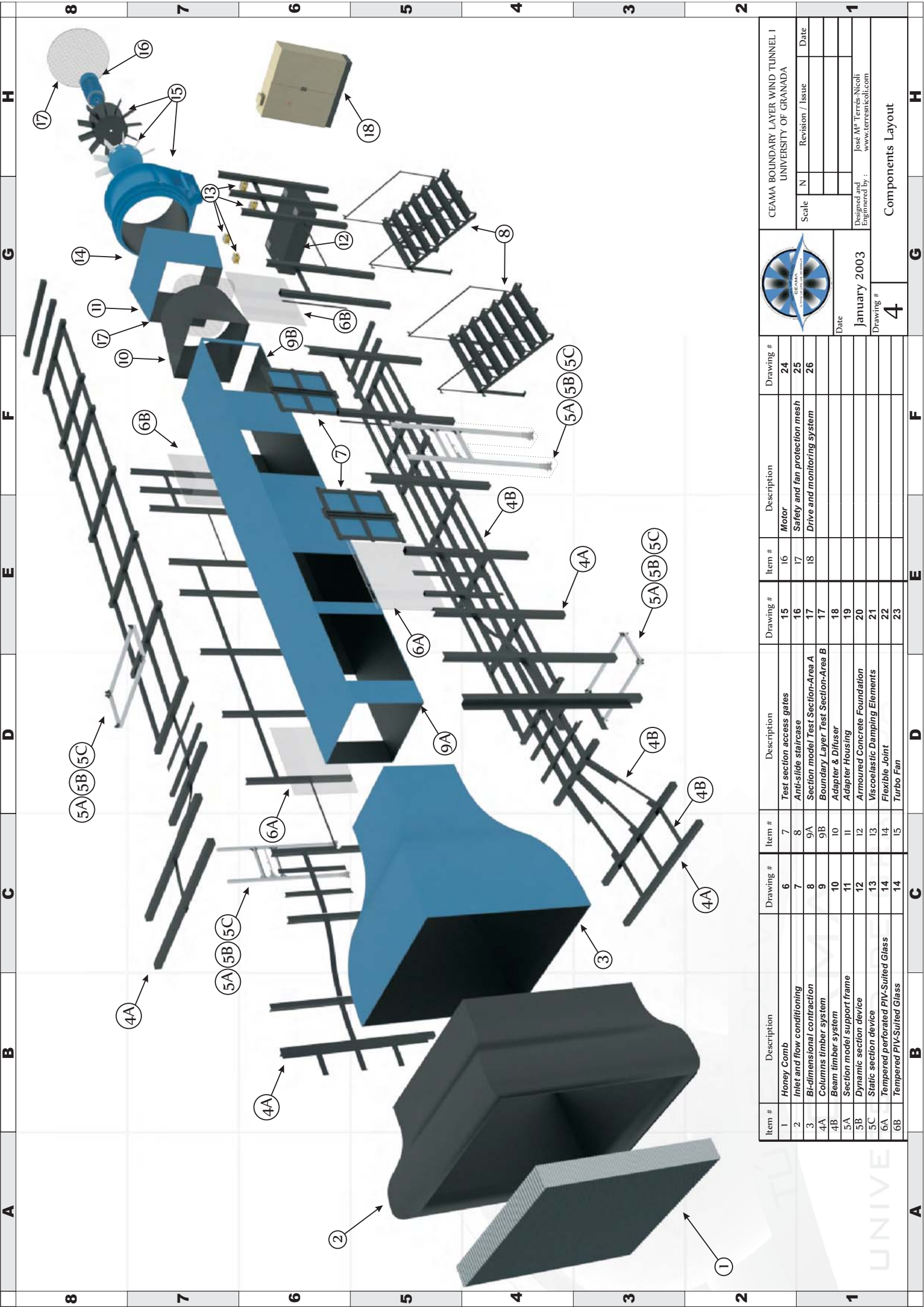
Scale	N	Revision / Issue	Date

Date  
**January 2003**  
Designed and  
Engineered by :  
José M<sup>a</sup> Terrés-Nicoli  
[www.terresnicoli.com](http://www.terresnicoli.com)

Drawing #  
**3**

General view from control room

TUNNEL I  
CEAMA  
UNIVERSIDAD DE GRANADA



Item #	Description	Drawing #	Item #	Description	Drawing #	Item #	Description	Drawing #
1	Honey Comb	6	7	Test section access gates	15	16	Motor	24
2	Inlet and flow conditioning	7	8	Anti-slide staircase	16	17	Safety and fan protection mesh	25
3	Bi-dimensional contraction	8	9A	Section model Test Section-Area A	17	18	Drive and monitoring system	26
4A	Columns timber system	9	9B	Boundary Layer Test Section-Area B	17			
4B	Beam timber system	10	10	Adapter Housing	18			
5A	Section model support frame	11	11	Adapter Housing	19			
5B	Dynamic section device	12	12	Armoured Concrete Foundation	20			
5C	Static section device	13	13	Viscoelastic Damping Elements	21			
6A	Tempered perforated PIV-Suited Glass	14	14	Flexible Joint	22			
6B	Tempered PIV-Suited Glass	14	15	Turbo Fan	23			

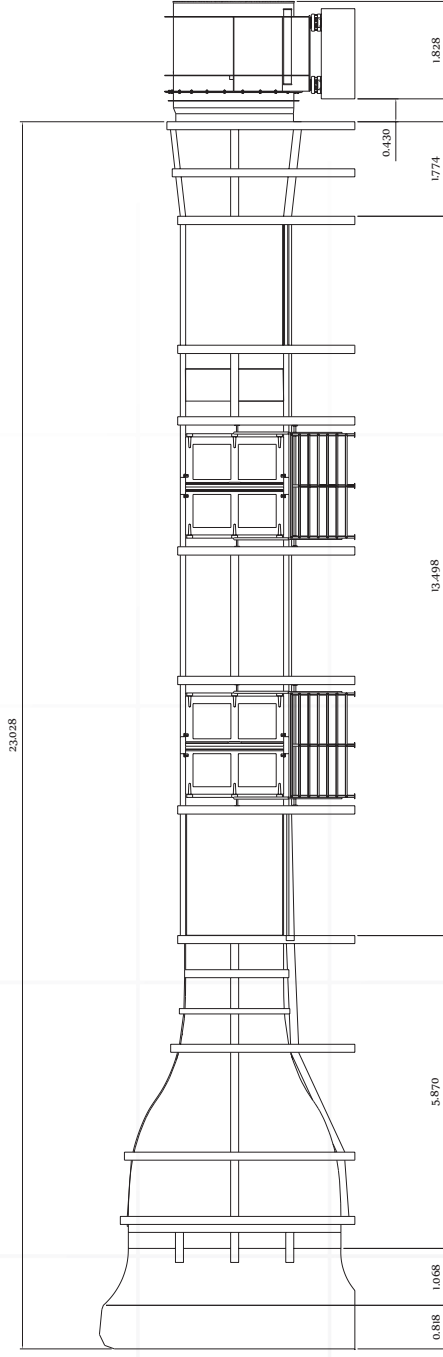
CEAMA BOUNDARY LAYER WIND TUNNEL I  
UNIVERSITY OF GRANADA

Scale: \_\_\_\_\_  
Revision / Issue: \_\_\_\_\_  
Date: \_\_\_\_\_

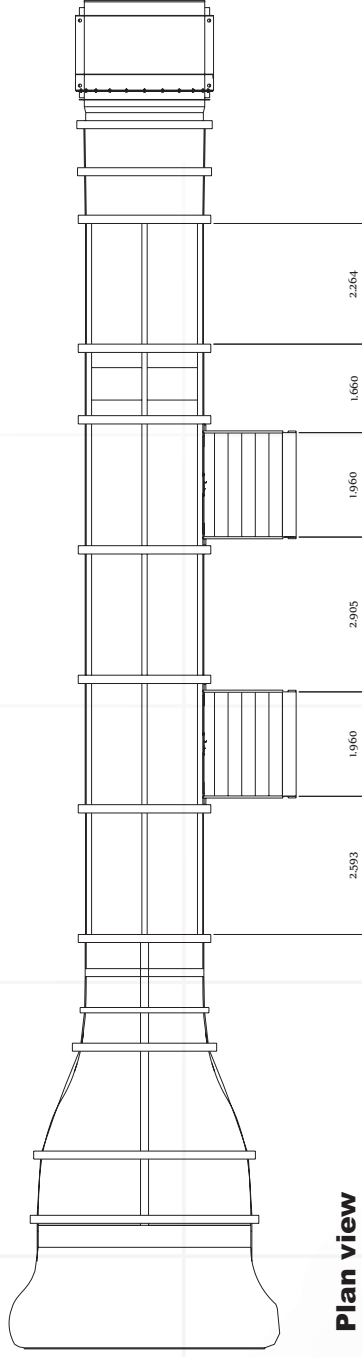
Designed and Engineered by: **José M<sup>a</sup> Torres-Nicoli**  
www.torresnicoli.com

Date: **January 2003**  
Drawing #: **4**

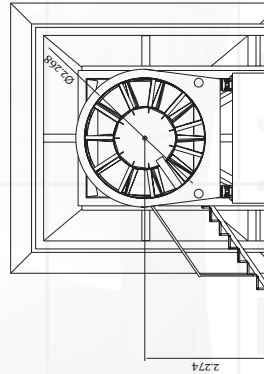
Components Layout



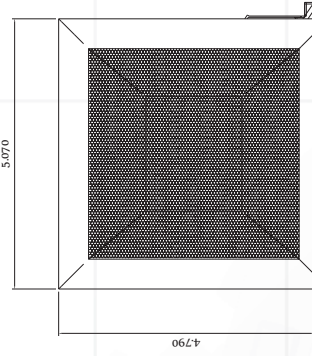
**Side view**



**Plan view**



**Rear view**



**Front view**



CEAMA BOUNDARY LAYER WIND TUNNEL I  
UNIVERSITY OF GRANADA

N	Revision / Issue	Date

Scale  
**1:100**

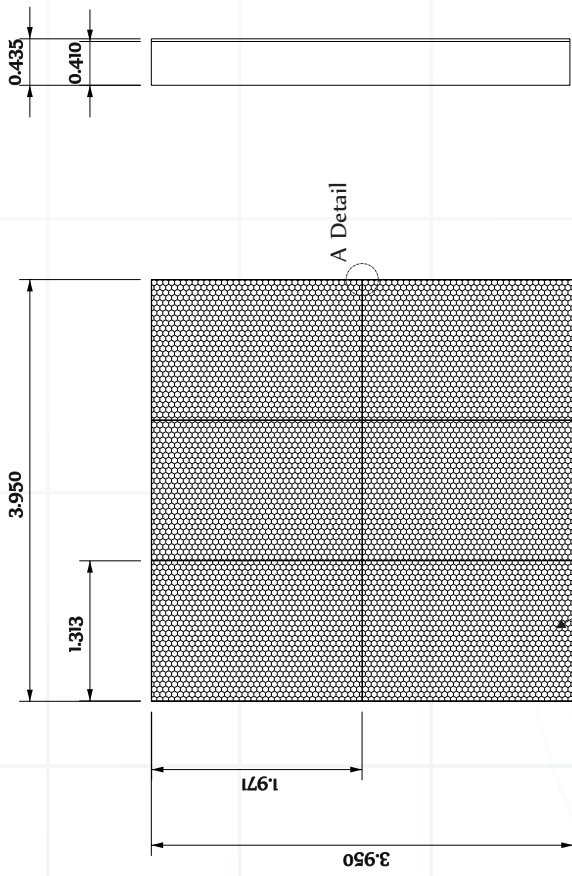
Date  
**January 2003**

Designed and Engineered by :  
**José M<sup>a</sup> Terrés-Nicoli**  
[www.terresnicoli.com](http://www.terresnicoli.com)

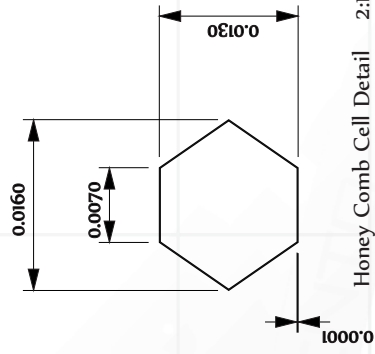
Drawing #  
**5**

General dimensions

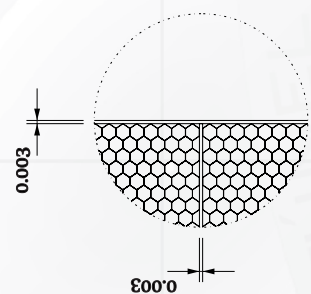




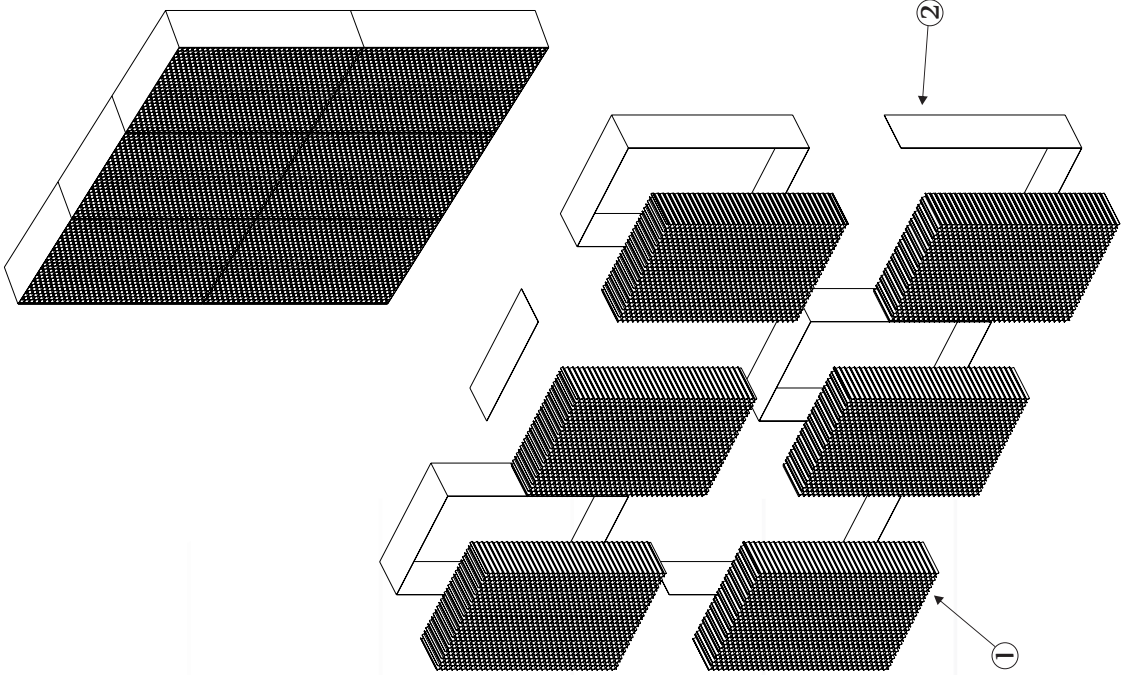
A Detail



Honey Comb Cell Detail 2:1 Scale




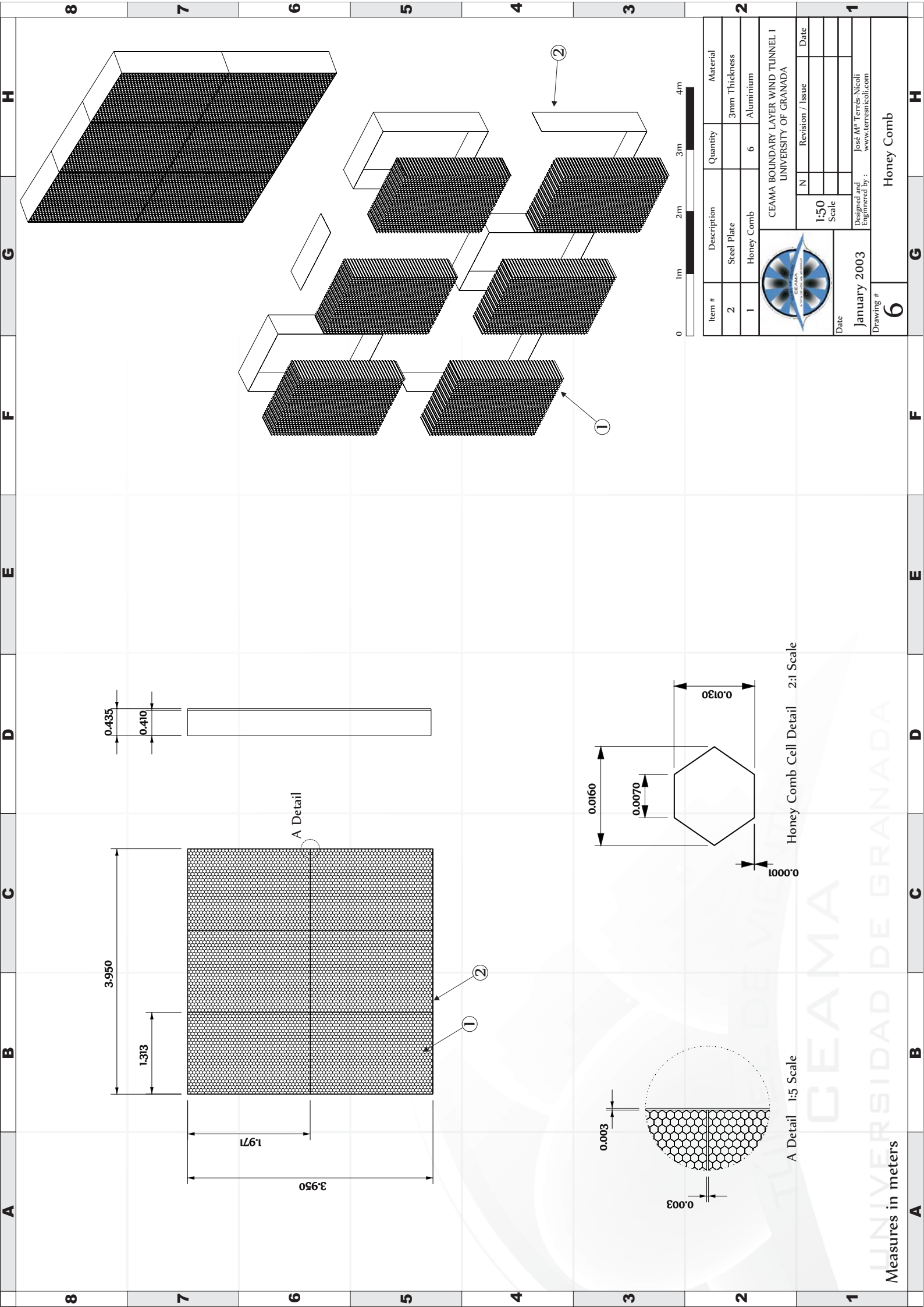
A Detail 1:5 Scale

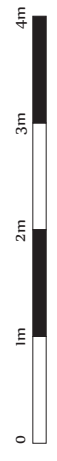
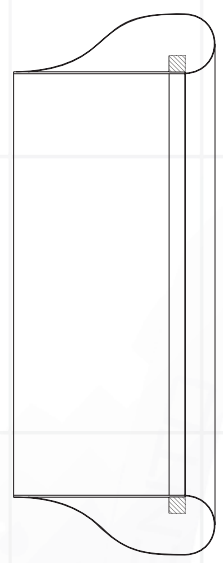
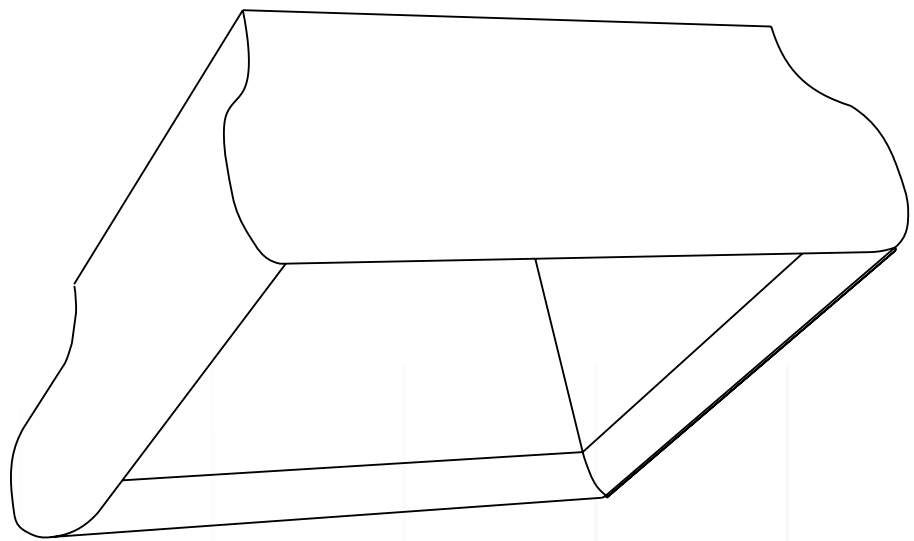
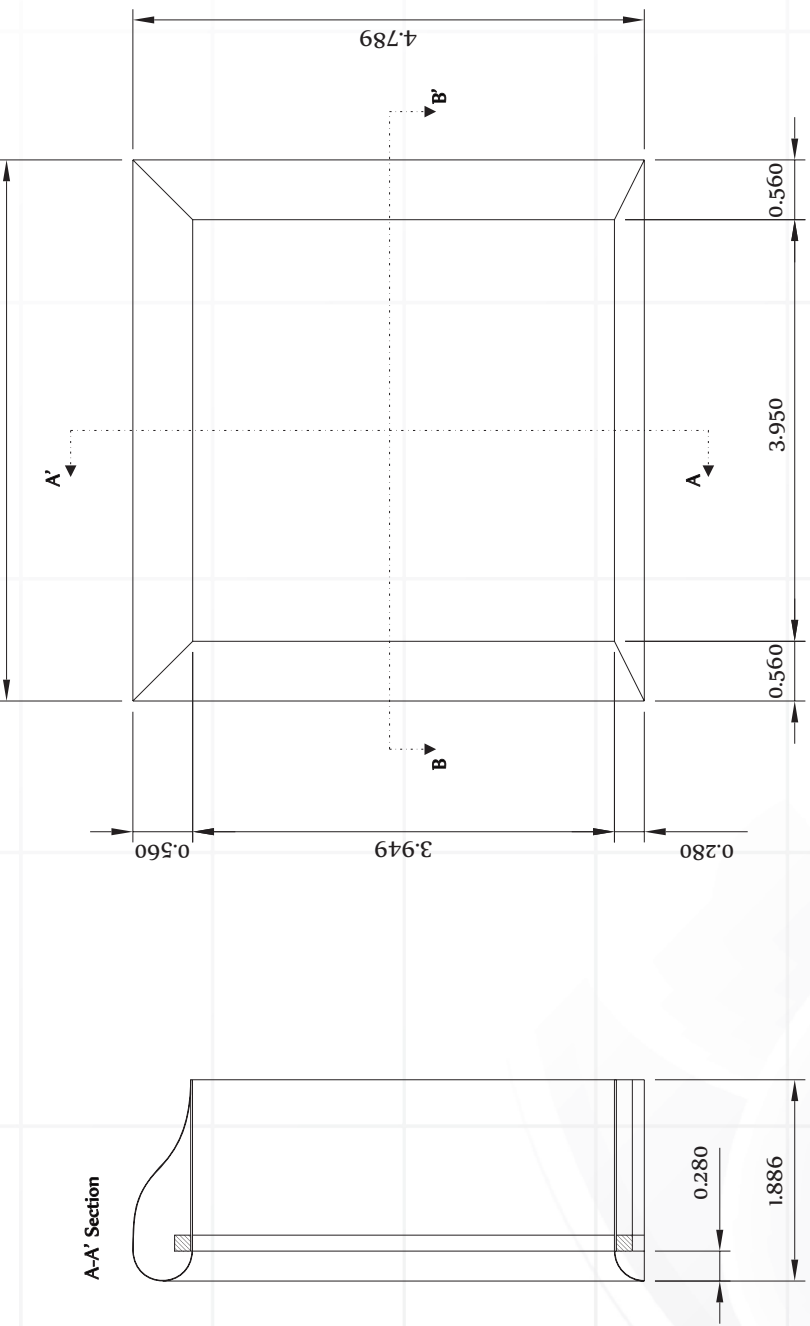


Item #	Description	Quantity	Material
2	Steel Plate		3mm Thickness
1	Honey Comb	6	Aluminium

		CEAMA BOUNDARY LAYER WIND TUNNEL I	
		UNIVERSITY OF GRANADA	
Date	January 2003	Revision / Issue	Date
Scale	1:50		
Designed and Engineered by :	Jose M <sup>a</sup> Terrés-Nicoli www.terresnicoli.com		





CEAMA BOUNDARY LAYER WIND TUNNEL I  
UNIVERSITY OF GRANADA

N	Revision / Issue	Date

1:50  
Scale

Date  
**January 2003**

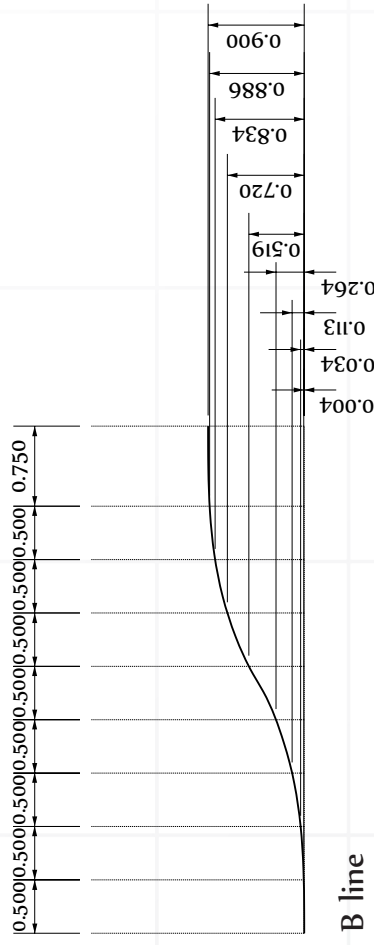
Designed and  
Engineered by :  
José M<sup>a</sup> Terrés-Nicoli  
www.terresnicoli.com

Drawing #  
**7**

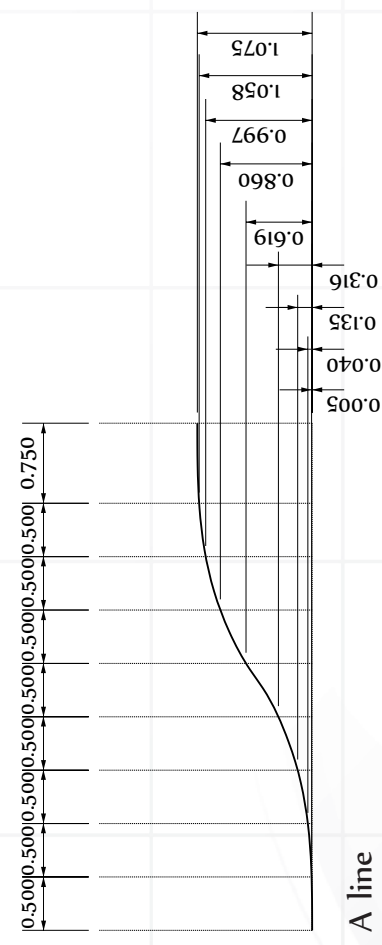
Inlet and Flow Conditioning

Measures in meters

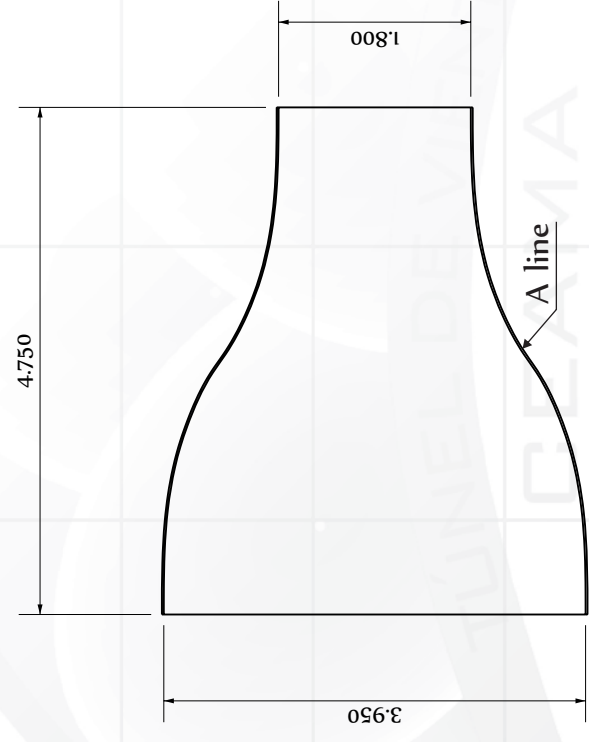
TÚNEL DE VIENTO  
CEAMA  
UNIVERSIDAD DE GRANADA



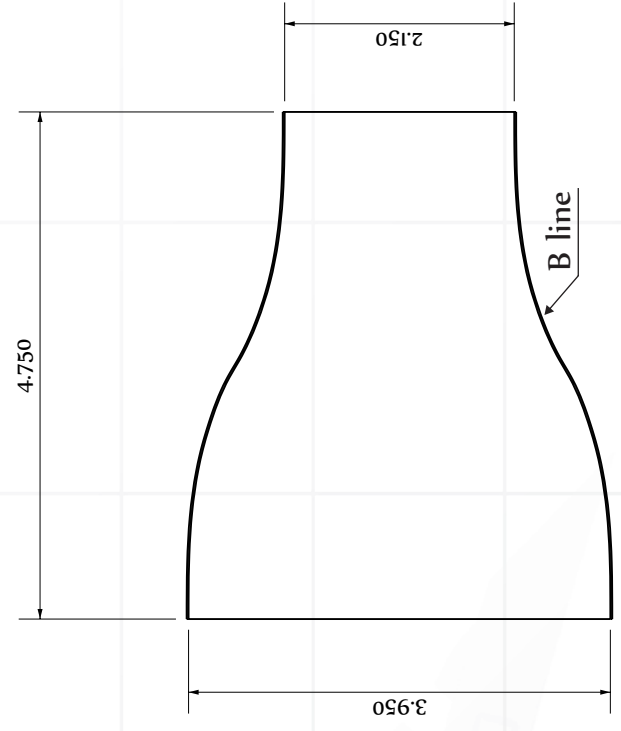
B line



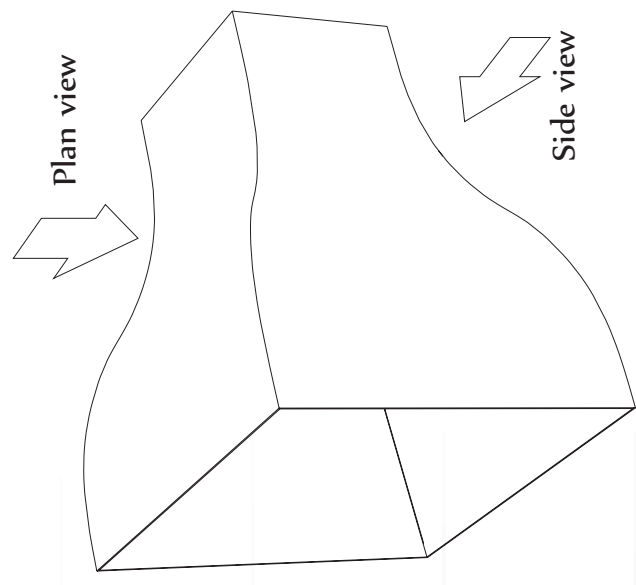
A line



Side view

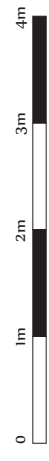


Plan view



Plan view

Side view



CEAMA BOUNDARY LAYER WIND TUNNEL I  
UNIVERSITY OF GRANADA

N	Revision / Issue	Date

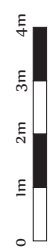
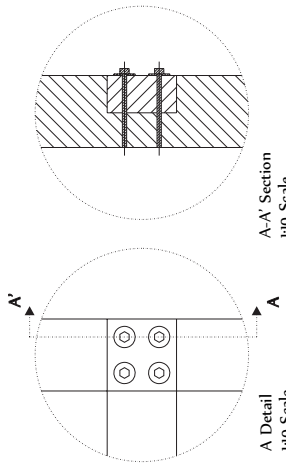
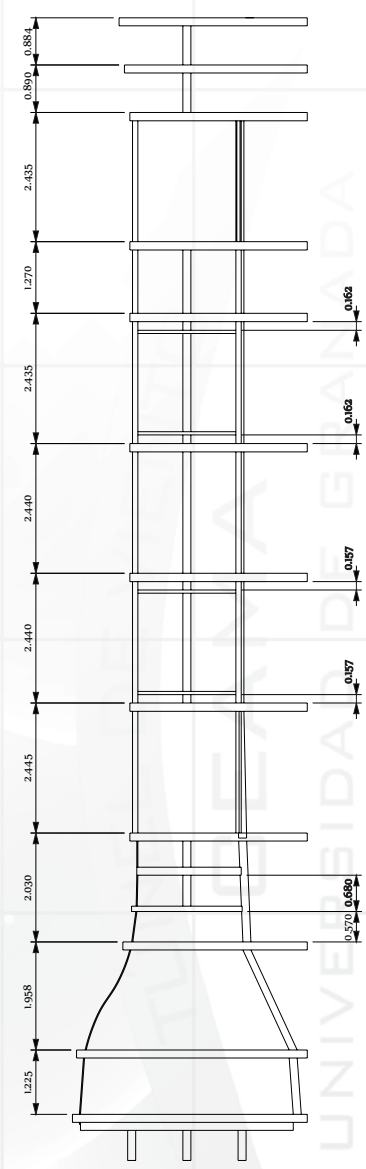
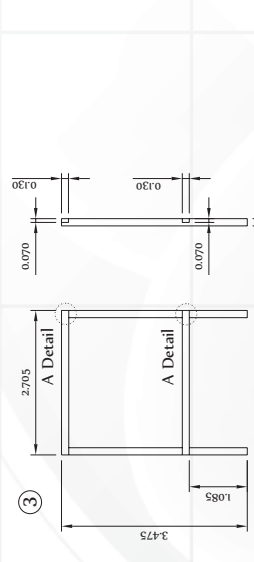
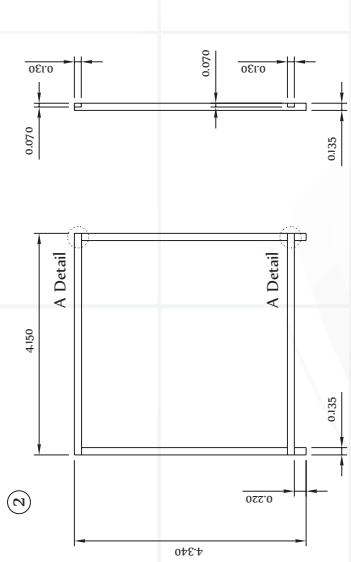
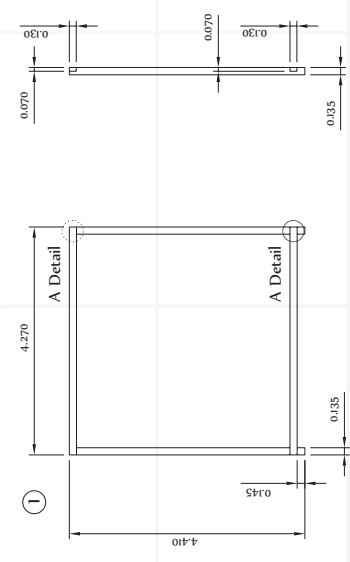
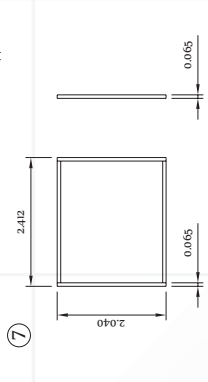
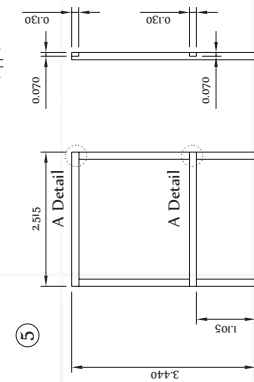
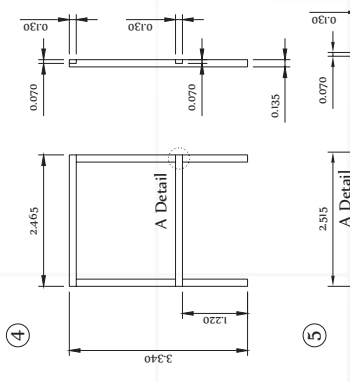
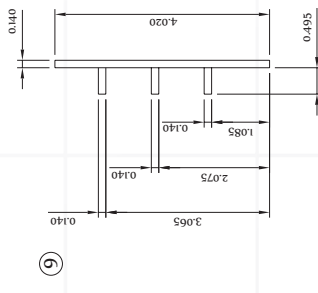
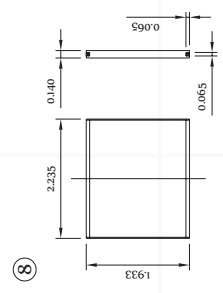
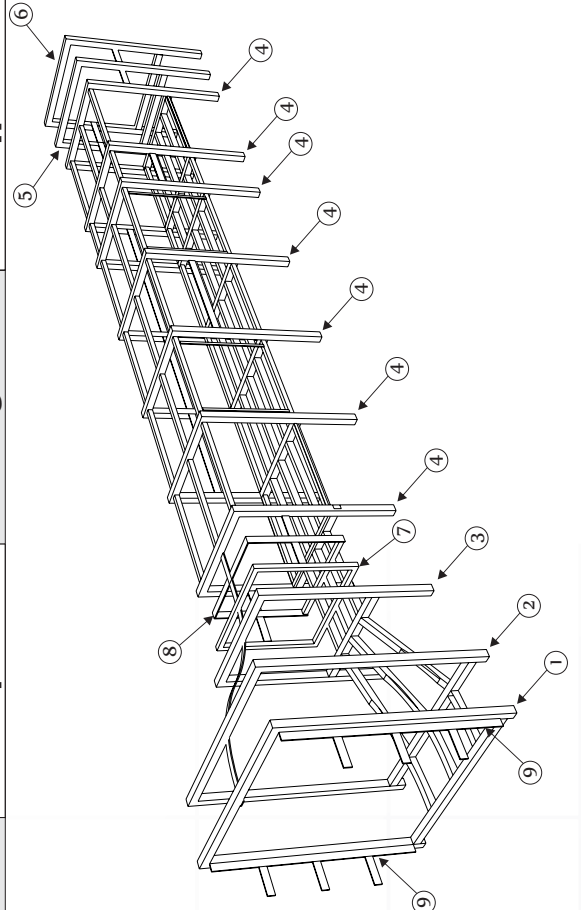
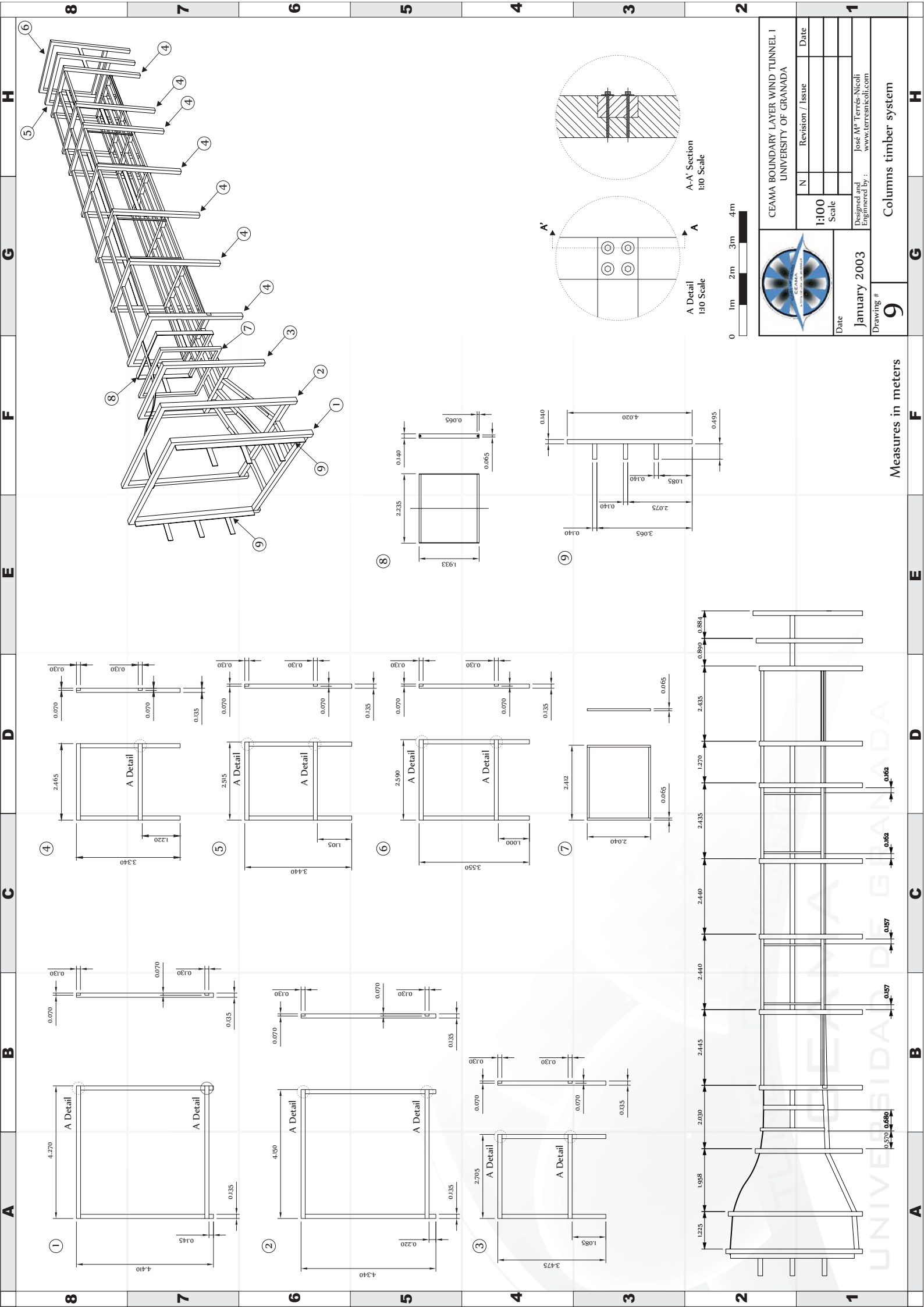
1:50  
Scale

Date  
January 2003  
Designed and  
Engineered by :  
José M<sup>a</sup> Terrés-Nicoli  
www.terresnicoli.com

Drawing #  
**8**  
Bi-dimensional Contraction

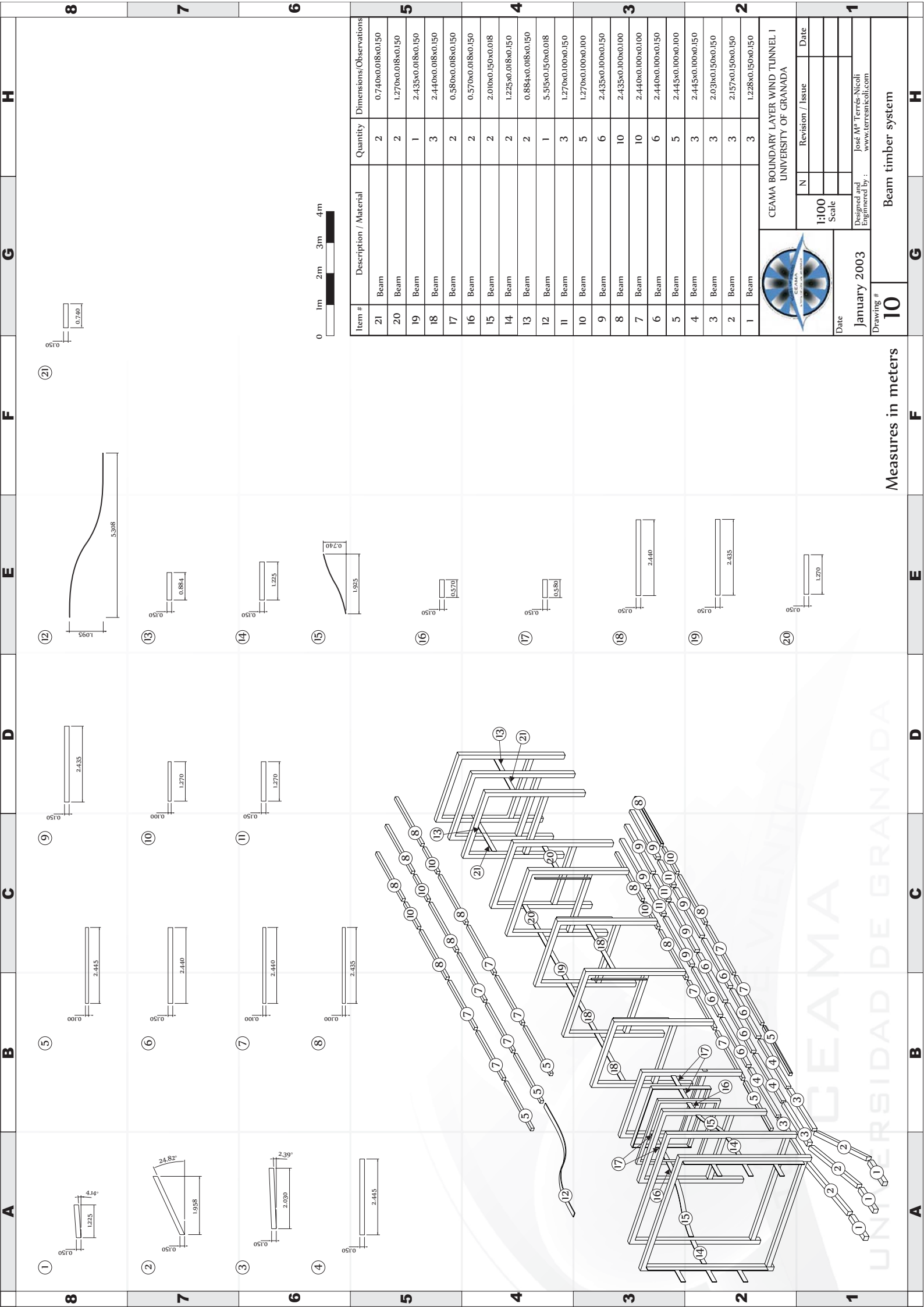
Measures in meters

UNIVERSIDAD DE GRANADA



		<b>CEAMA BOUNDARY LAYER WIND TUNNEL I</b> UNIVERSITY OF GRANADA	
Date <b>January 2003</b>	Drawing # <b>9</b>	Scale <b>1:100</b>	Revision / Issue _____
		Date _____	Date _____
Designed and Engineered by : <b>José M<sup>a</sup> Terrés-Nicolí</b> <a href="http://www.terresnicoli.com">www.terresnicoli.com</a>		<b>Columns timber system</b>	

Measures in meters



Item #	Description / Material	Quantity	Dimensions/Observations
21	Beam	2	0.740x0.018x0.150
20	Beam	2	1.270x0.018x0.150
19	Beam	1	2.435x0.018x0.150
18	Beam	3	2.440x0.018x0.150
17	Beam	2	0.580x0.018x0.150
16	Beam	2	0.570x0.018x0.150
15	Beam	2	2.010x0.150x0.018
14	Beam	2	1.225x0.018x0.150
13	Beam	2	0.884x0.018x0.150
12	Beam	1	5.515x0.150x0.018
11	Beam	3	1.270x0.100x0.150
10	Beam	5	1.270x0.100x0.100
9	Beam	6	2.435x0.100x0.150
8	Beam	10	2.435x0.100x0.100
7	Beam	10	2.440x0.100x0.100
6	Beam	6	2.440x0.100x0.150
5	Beam	5	2.445x0.100x0.100
4	Beam	3	2.445x0.100x0.150
3	Beam	3	2.031x0.150x0.150
2	Beam	3	2.157x0.150x0.150
1	Beam	3	1.228x0.150x0.150



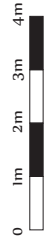
CEAMA BOUNDARY LAYER WIND TUNNEL I  
UNIVERSITY OF GRANADA

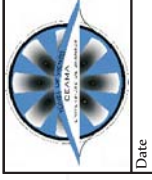
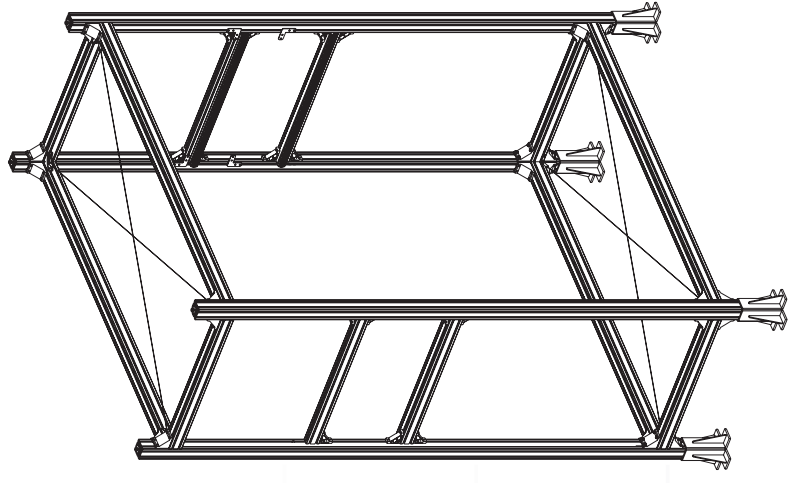
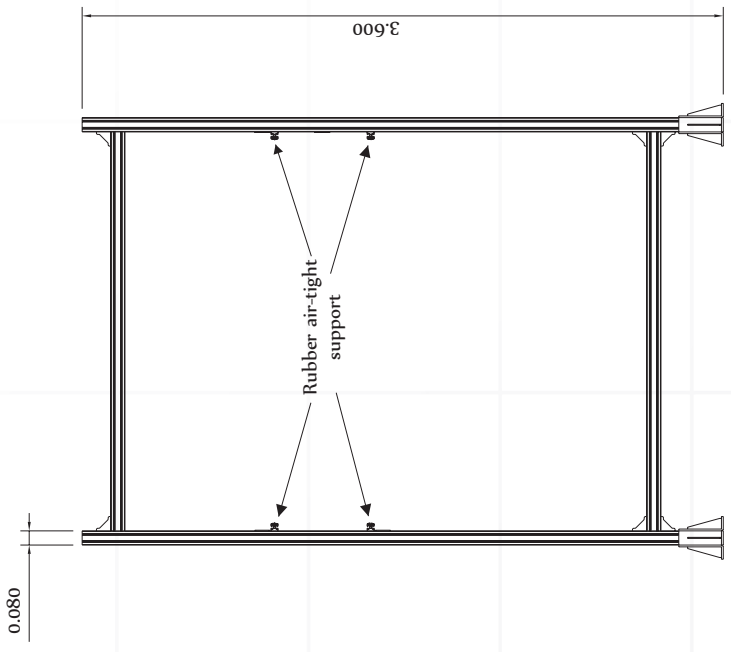
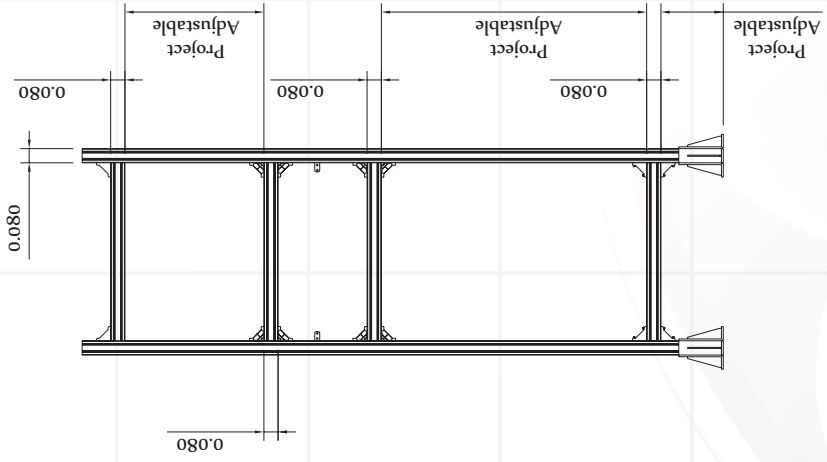
Date: **January 2003**  
 Scale: **1:100**  
 Revision / Issue: \_\_\_\_\_ Date: \_\_\_\_\_

Designed and Engineered by: **José M<sup>a</sup> Terrés-Nicoli**  
[www.terresnicoli.com](http://www.terresnicoli.com)

Drawing # **10** Beam timber system

Measures in meters





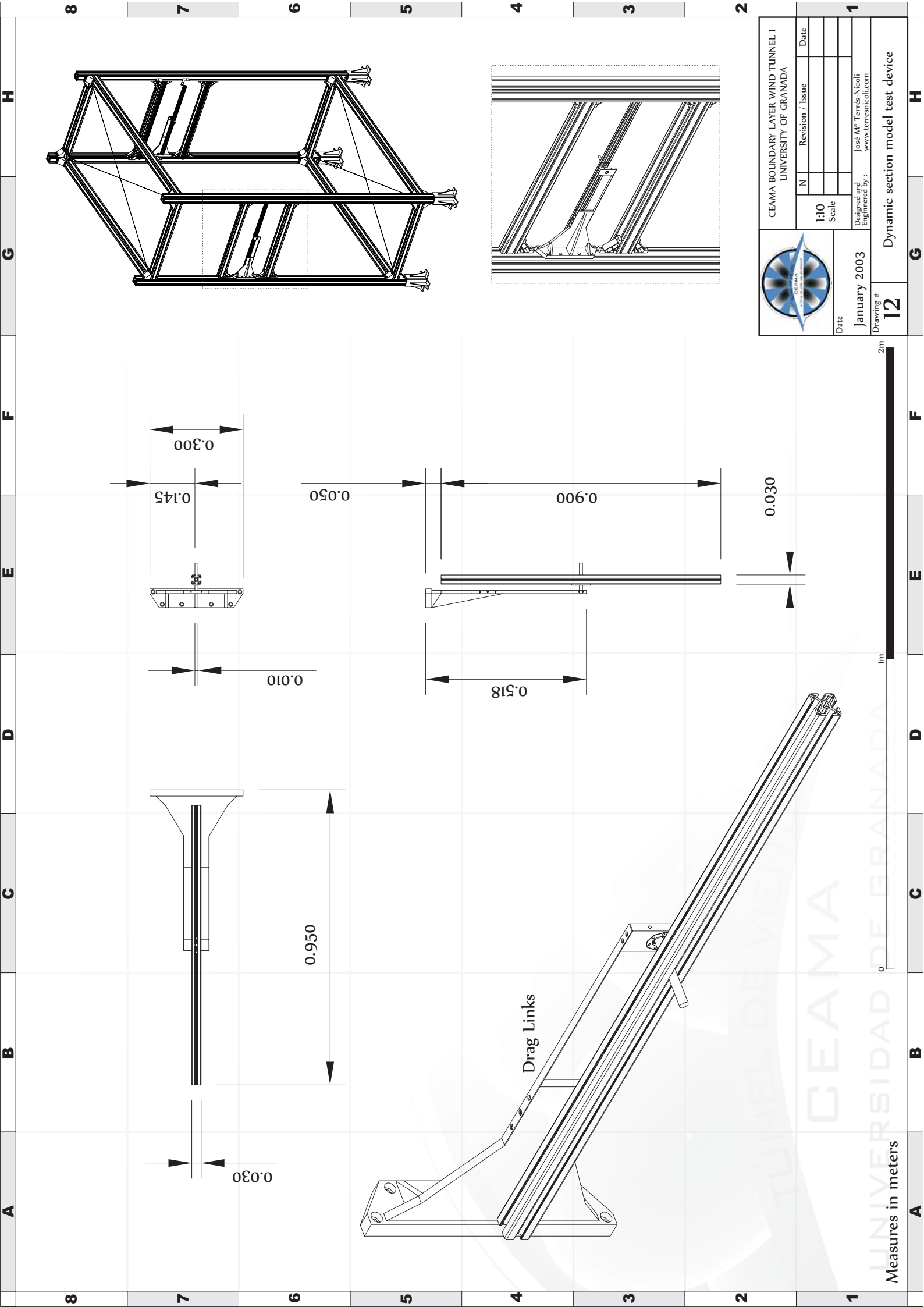
CEAMA BOUNDARY LAYER WIND TUNNEL I  
UNIVERSITY OF GRANADA

N	Revision / Issue	Date

1:30  
Scale

Date  
January 2003  
Designed and  
Engineered by :  
José M<sup>a</sup> Terrés-Nicoli  
www.terresnicoli.com

Drawing #  
**11**  
Section model support



CEAMA BOUNDARY LAYER WIND TUNNEL I  
UNIVERSITY OF GRANADA

N	Revision / Issue	Date

Scale  
1:10

Date  
January 2003  
Designed and  
Engineered by :  
José M<sup>a</sup> Terrés-Nicoli  
www.terresnicoli.com

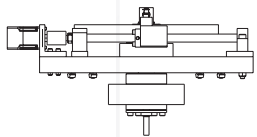
Drawing #  
**12**  
Dynamic section model test device



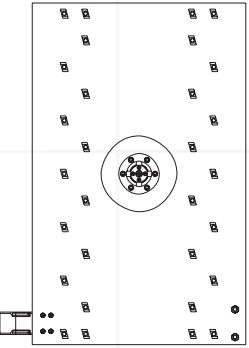
Measures in meters



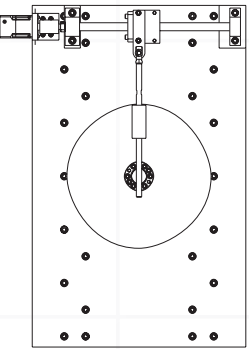
Side view



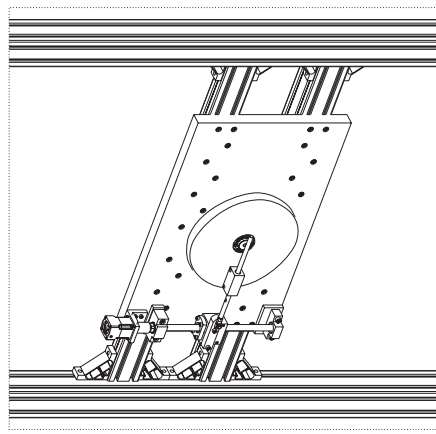
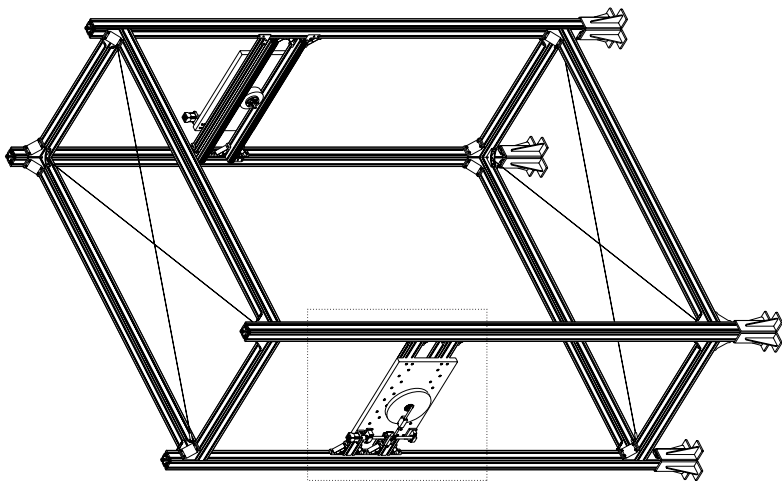
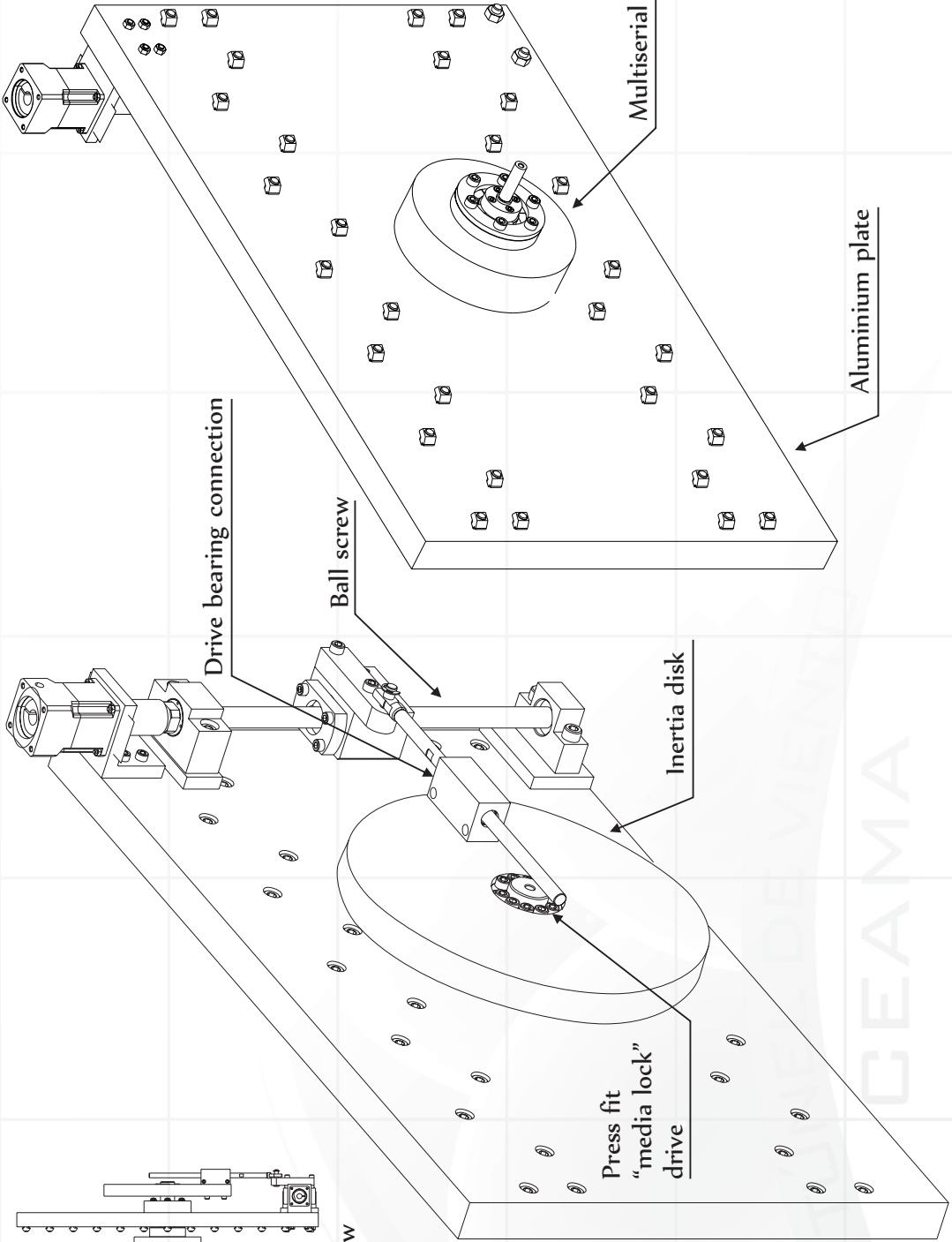
Front view



Back view



Plan view



Measures in meters



CEAMA BOUNDARY LAYER WIND TUNNEL I  
UNIVERSITY OF GRANADA

N	Revision / Issue	Date

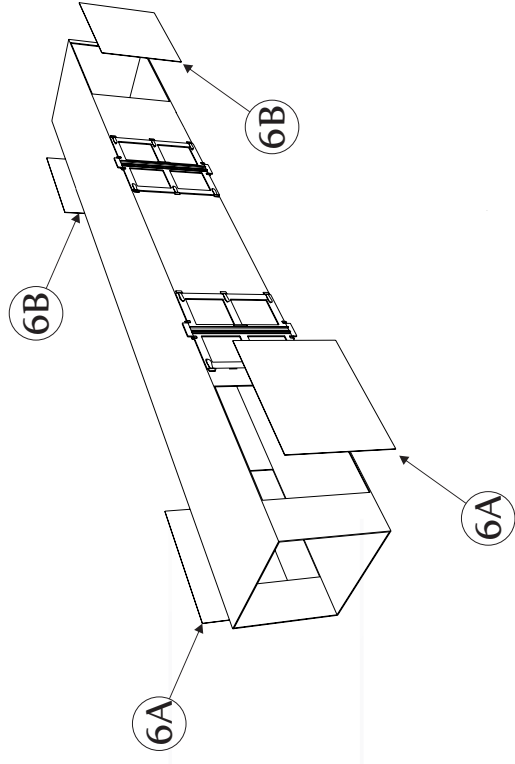
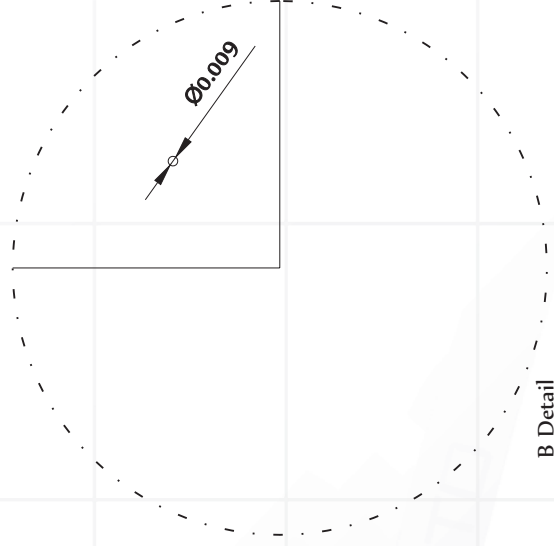
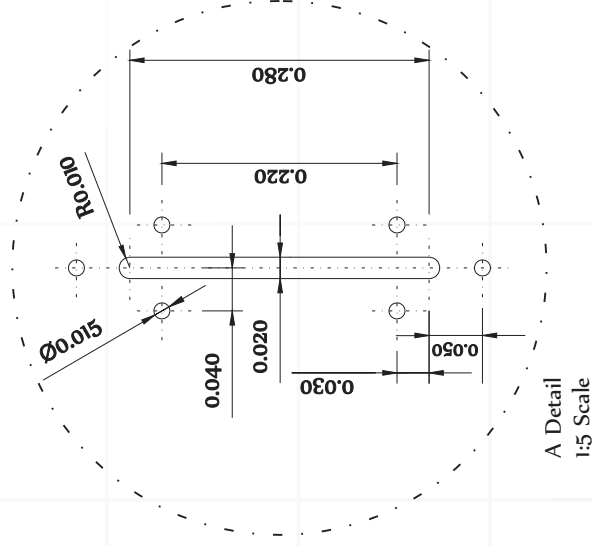
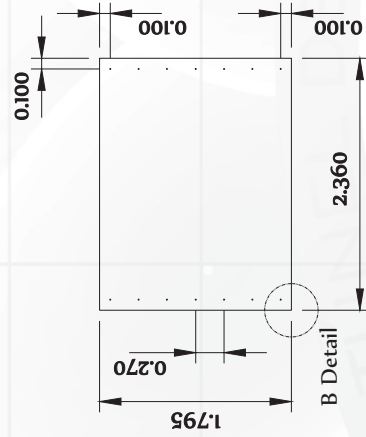
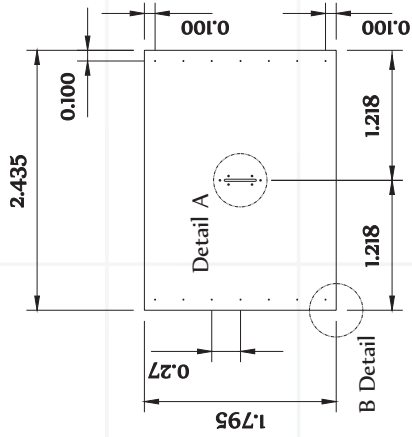
1:10  
Scale

Date  
January 2003  
Designed and  
Engineered by :  
José M<sup>a</sup> Terrés-Nicoli  
www.terresnicoli.com

Drawing #  
**13**

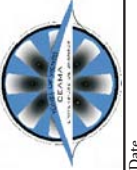
Static section model test device



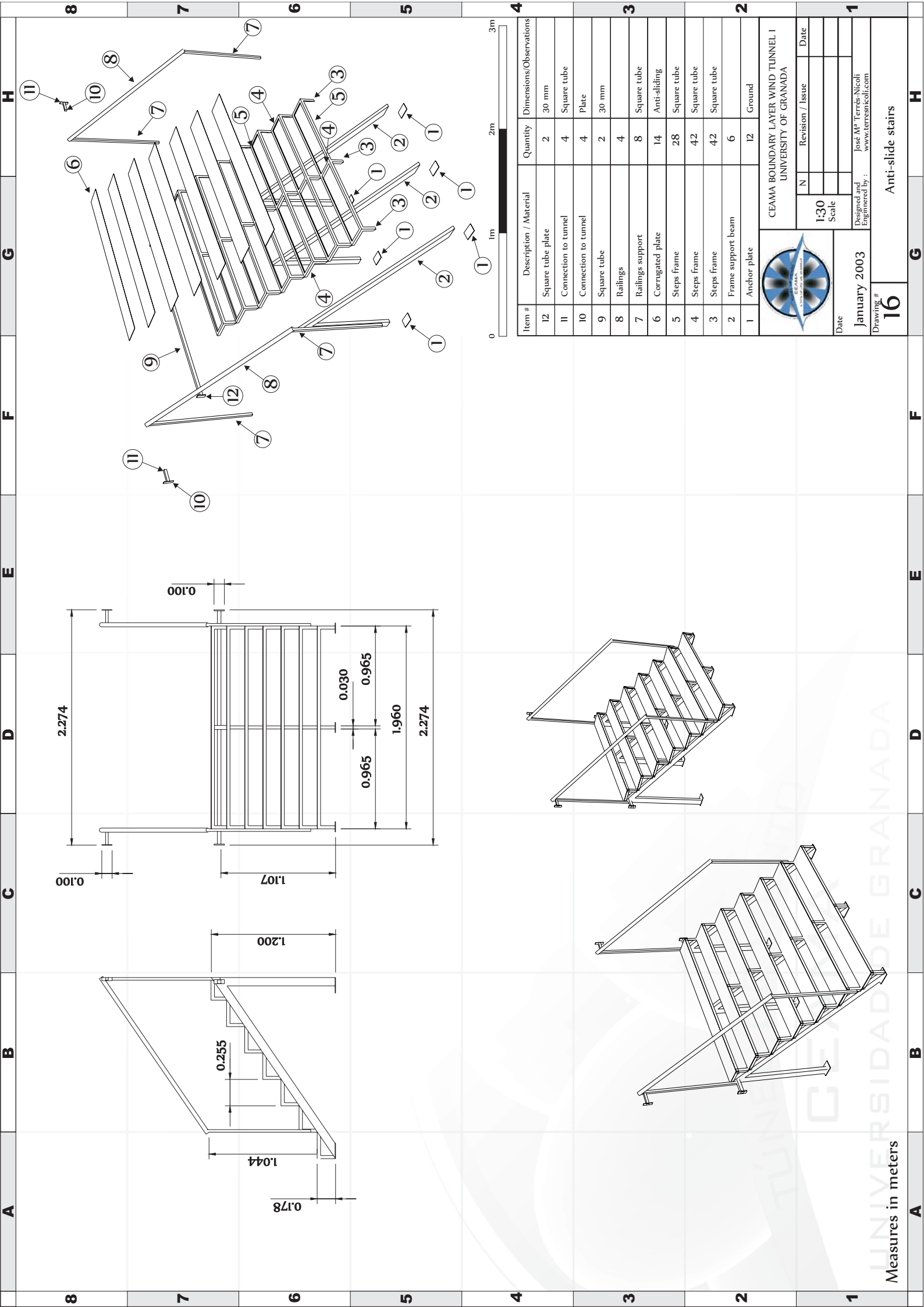


Item #	Description / Material	Quantity	Dimensions/Observations
6B	Tempered PIV-Suited Glass	1	Thickness 8mm
6A	Tempered perforated PIV-Suited Glass	1	Thickness 10mm


  

		<b>CEAMA BOUNDARY LAYER WIND TUNNEL I</b> UNIVERSITY OF GRANADA	
Date	January 2003	Scale	1:50
Designed and Engineered by :	Jose M <sup>a</sup> Terrés-Nicoli	Revision / Issue	
	www.terresnicoli.com	Date	
Drawing #	14	Tempered PIV-Suited Glass	





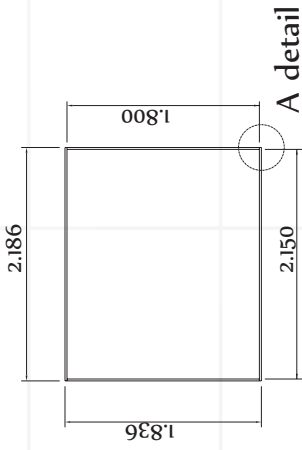
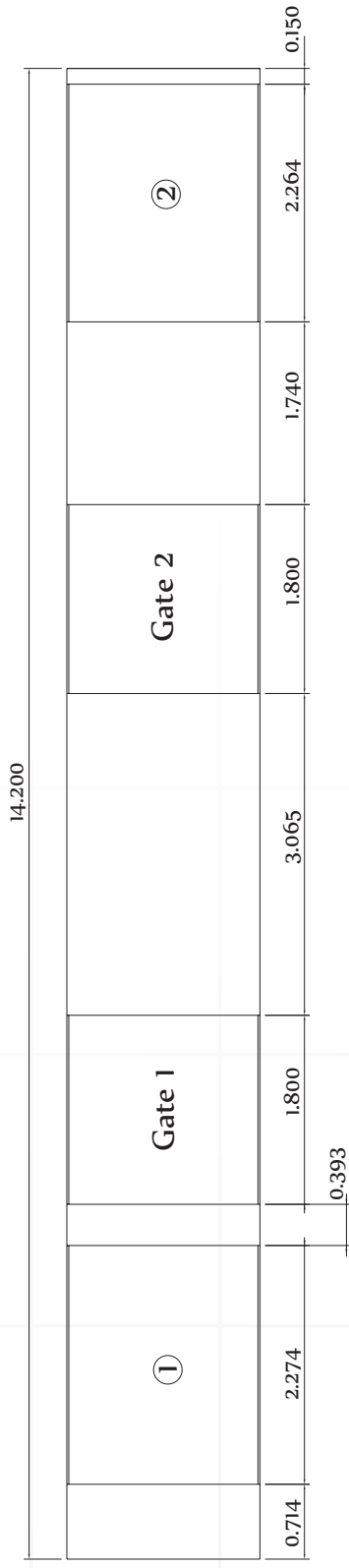
Item #	Description / Material	Quantity	Dimensions/Observations
12	Square tube plate	2	30 mm
11	Connection to tunnel	4	Square tube
10	Connection to tunnel	4	Plate
9	Square tube	2	30 mm
8	Railings	4	
7	Railings support	8	Square tube
6	Corrugated plate	14	Anti-sliding
5	Steps frame	28	Square tube
4	Steps frame	42	Square tube
3	Steps frame	42	Square tube
2	Frame support beam	6	Square tube
1	Anchor plate	12	Ground


  
 CEAMA BOUNDARY LAYER WIND TUNNEL I  
 UNIVERSITY OF GRANADA

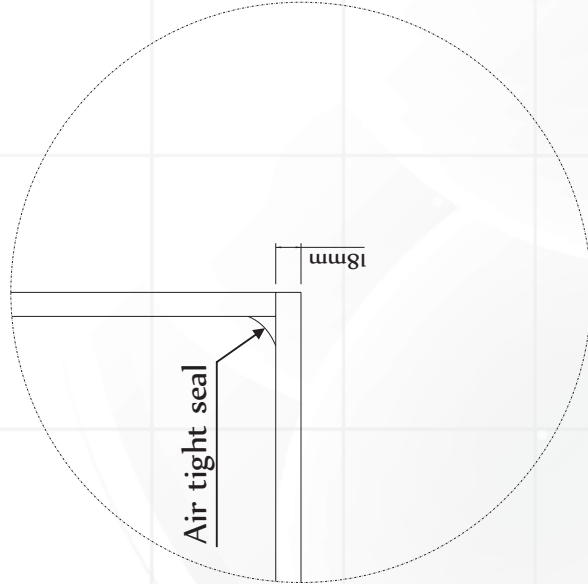
Date: **January 2003**  
 Drawing # **16**

Scale: **1:30**  
 Revision / Issue: \_\_\_\_\_ Date: \_\_\_\_\_

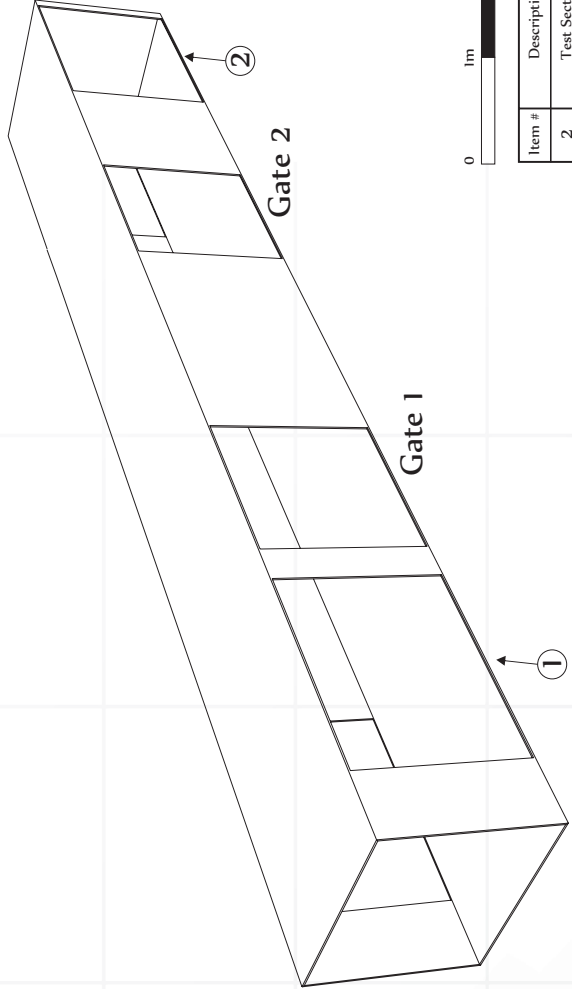
Designed and Engineered by: **José M<sup>a</sup> Terrés-Nicoli**  
[www.terresnicoli.com](http://www.terresnicoli.com)



A detail

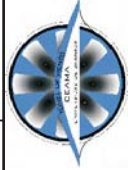


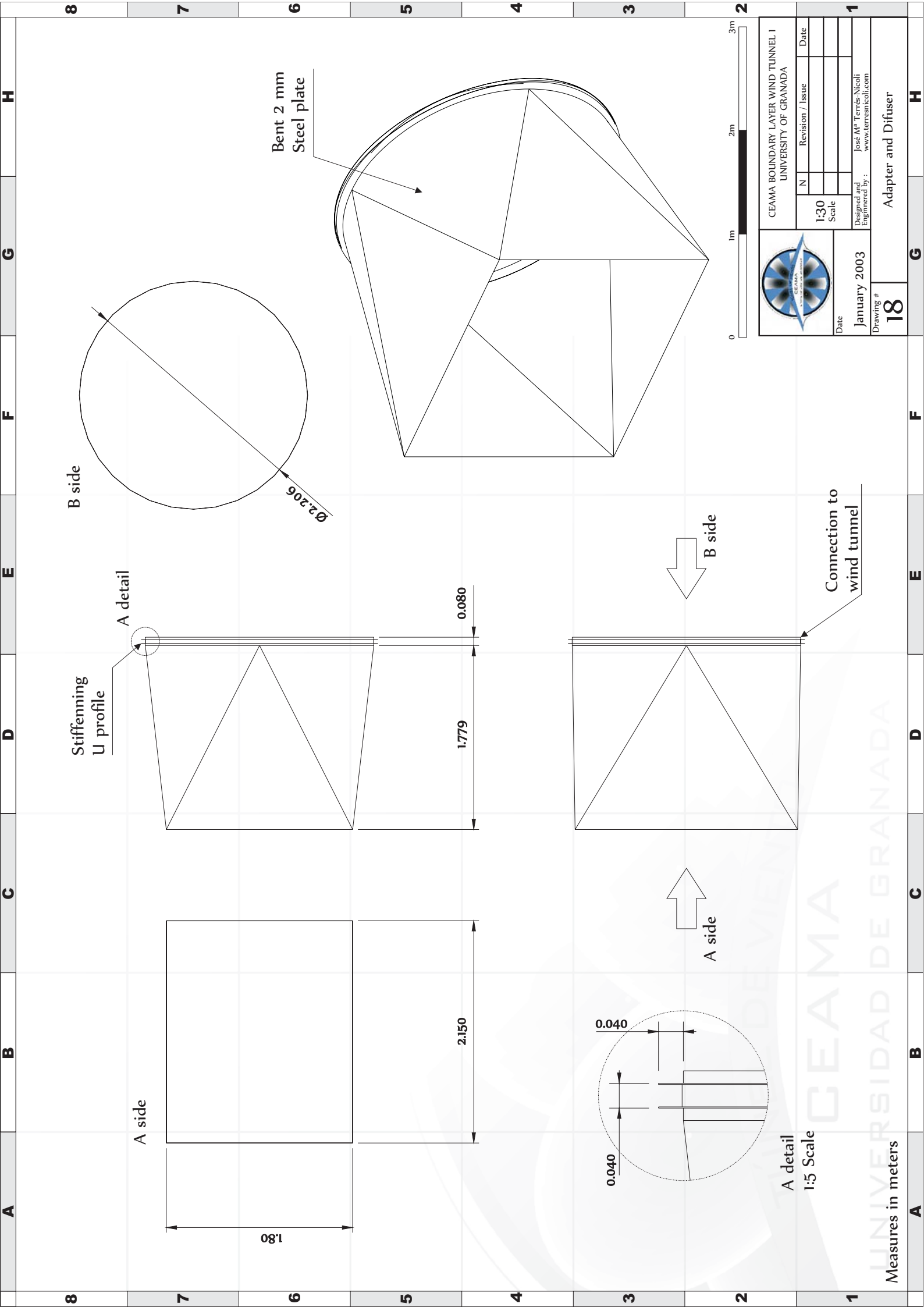
A detail  
1:4 Scale



Item #	Description / Material	Quantity	Dimensions/Observations
2	Test Section Area B	1	Boundary Layer Area
1	Test Section Area A	1	Section Model Area

CEAMA BOUNDARY LAYER WIND TUNNEL I UNIVERSITY OF GRANADA			
	N	Revision / Issue	Date
	1:50	Scale	
Date	January 2003		
Designed and Engineered by :	José M <sup>a</sup> Terrés-Nicoli www.terresnicoli.com		
Drawing #	17		



B side

Bent 2 mm  
Steel plate

Stiffening  
U profile

A detail

A side

180

2.150

1.779

0.080

0.040

0.040

A side

B side

Connection to  
wind tunnel



CEAMA BOUNDARY LAYER WIND TUNNEL I  
UNIVERSITY OF GRANADA

N	Revision / Issue	Date

1:30  
Scale

Date  
January 2003

Designed and  
Engineered by :  
José M<sup>a</sup> Terrés-Nicoli  
www.terresnicoli.com

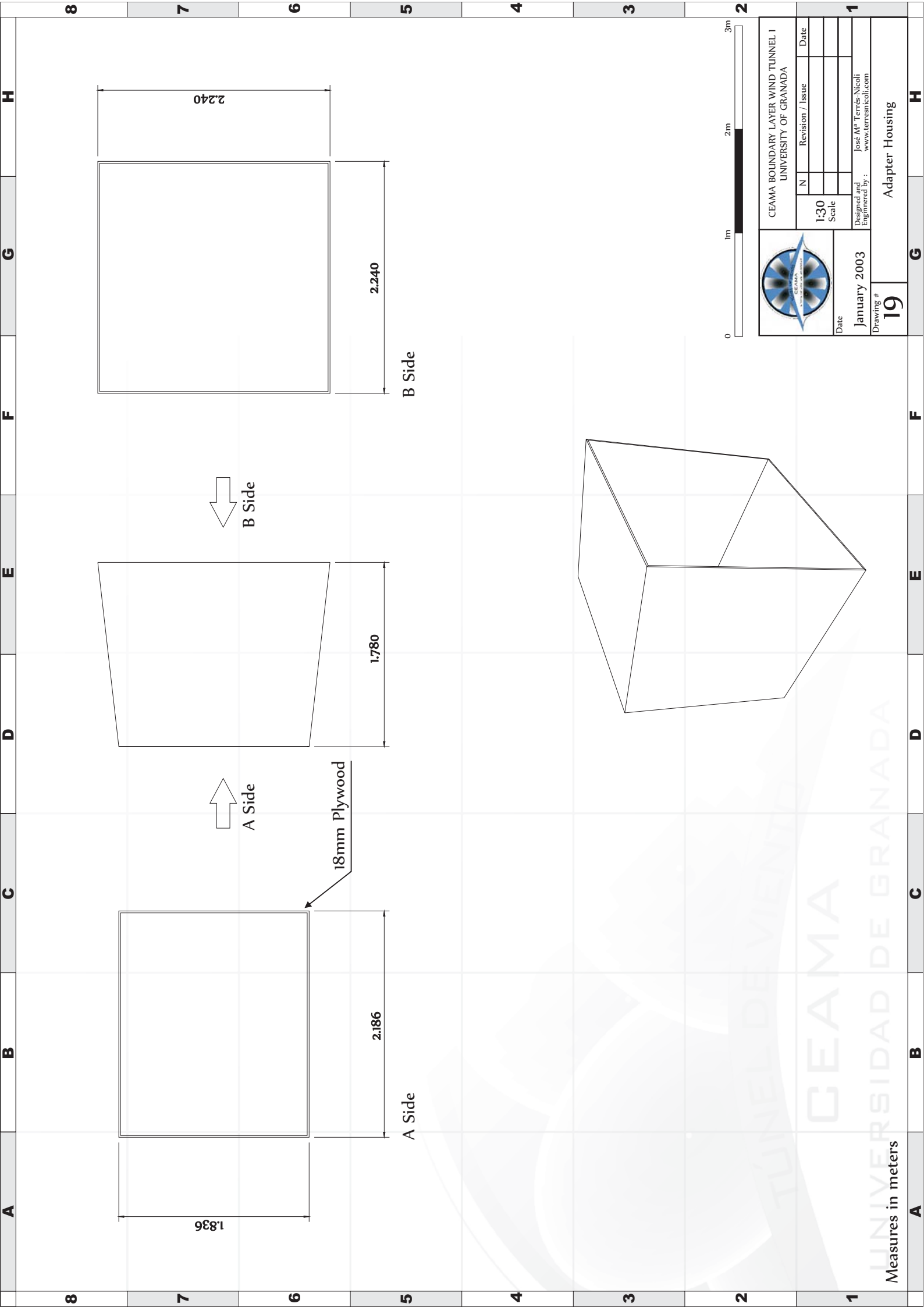
Drawing #  
**18**

Adapter and Diffuser

Measures in meters

UNIVERSIDAD DE GRANADA

CEAMA



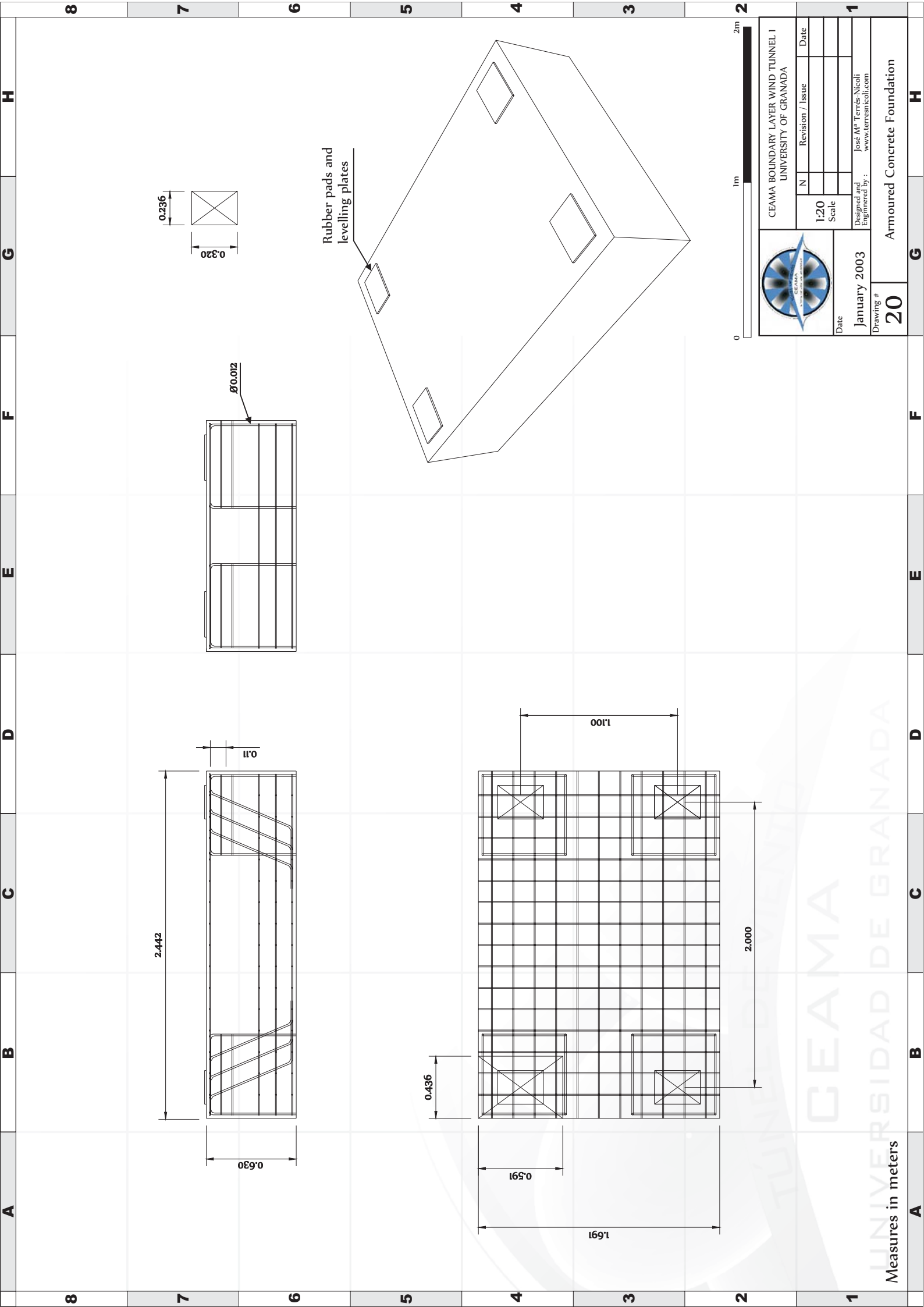
CEAMA BOUNDARY LAYER WIND TUNNEL I  
UNIVERSITY OF GRANADA

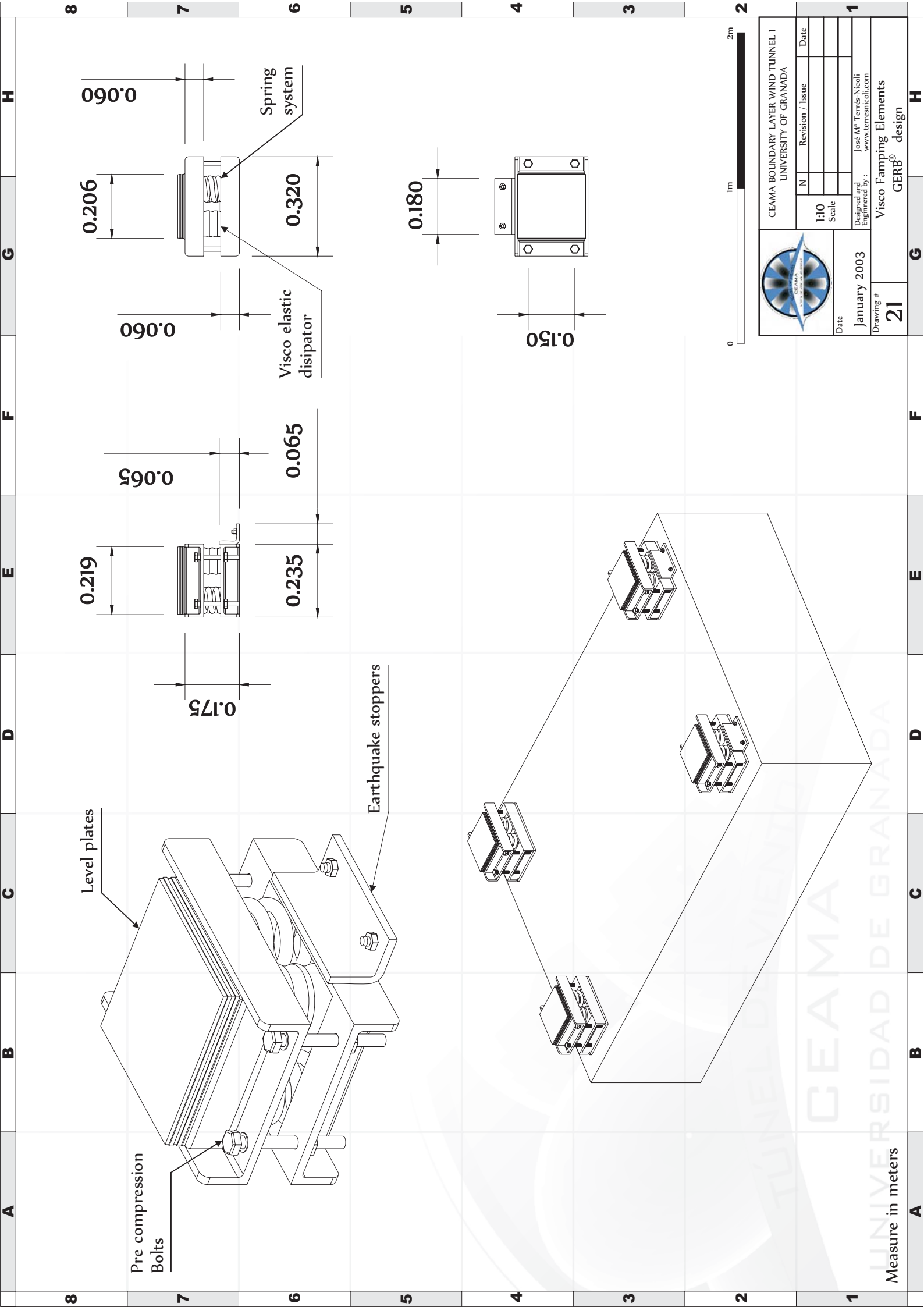
N	Revision / Issue	Date

1:30  
Scale

Date  
January 2003  
Designed and  
Engineered by :  
José M<sup>a</sup> Terrés-Nicoli  
www.terresnicoli.com

Drawing #  
**19**  
Adapter Housing





Level plates

Pre compression Bolts

Earthquake stoppers

0.090

0.206

0.060

0.065

0.219

0.175

0.235

0.065

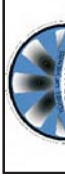
Visco elastic dissipator

Spring system

0.320

0.180

0.150



CEAMA BOUNDARY LAYER WIND TUNNEL I  
UNIVERSITY OF GRANADA

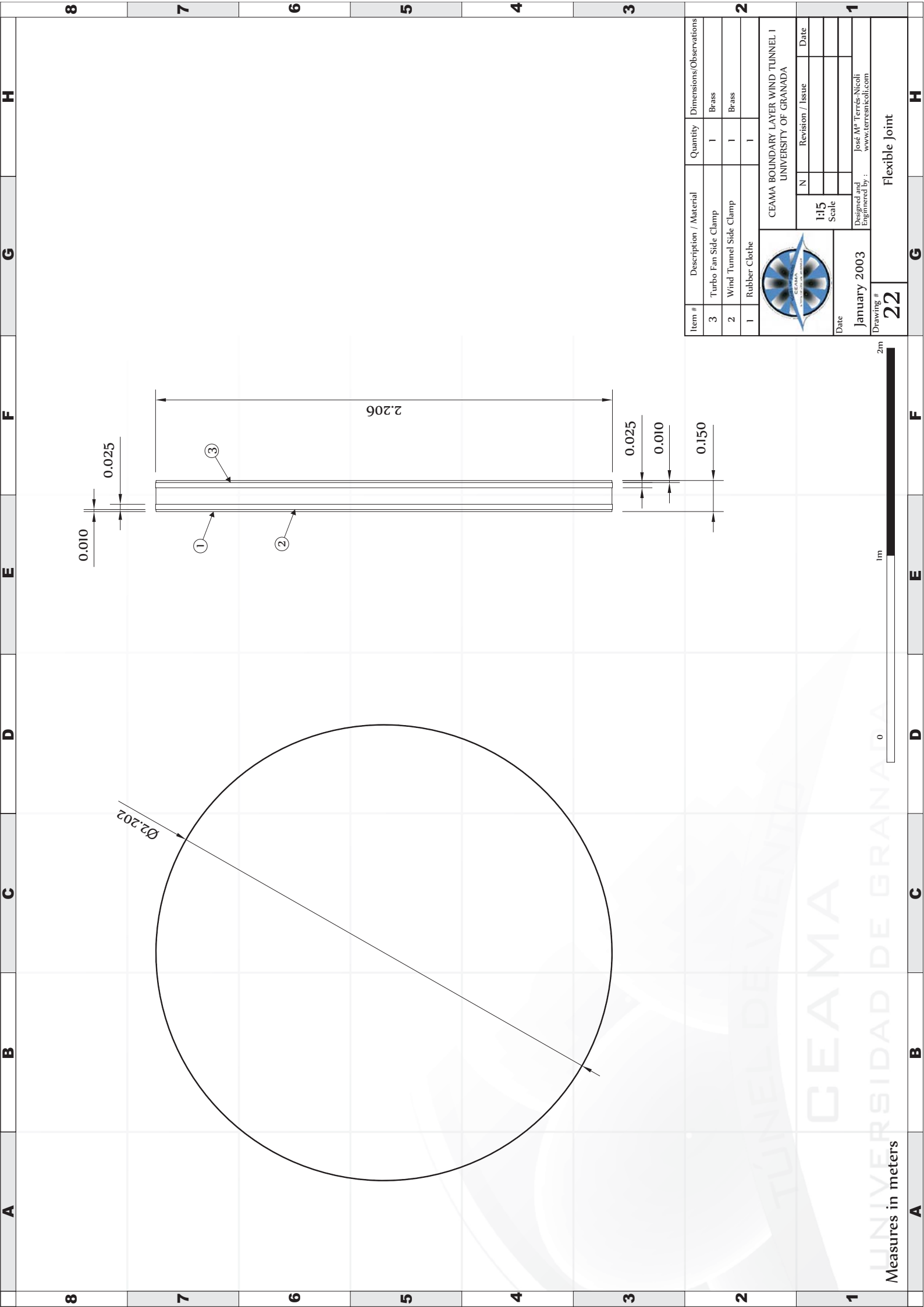
Date	January 2003	
	Designed and Engineered by :	Jose M <sup>a</sup> Terrés-Nicoli www.terresnicoli.com
Scale	1:10	
	Revision / Issue	Date

Drawing # **21**  
Visco Famping Elements  
GERRB<sup>®</sup> design

Measure in meters


TUNEL VIENTO  
UNIVERSIDAD DE GRANADA  
CEAMA





Item #	Description / Material	Quantity	Dimensions/Observations
3	Turbo Fan Side Clamp	1	Brass
2	Wind Tunnel Side Clamp	1	Brass
1	Rubber Clothe	1	

		CEAMA BOUNDARY LAYER WIND TUNNEL I UNIVERSITY OF GRANADA	
Date	January 2003	Scale	1:15
Designed and Engineered by :	Jose M <sup>a</sup> Terrés-Nicoli	Revision / Issue	
	www.terresnicoli.com	Date	

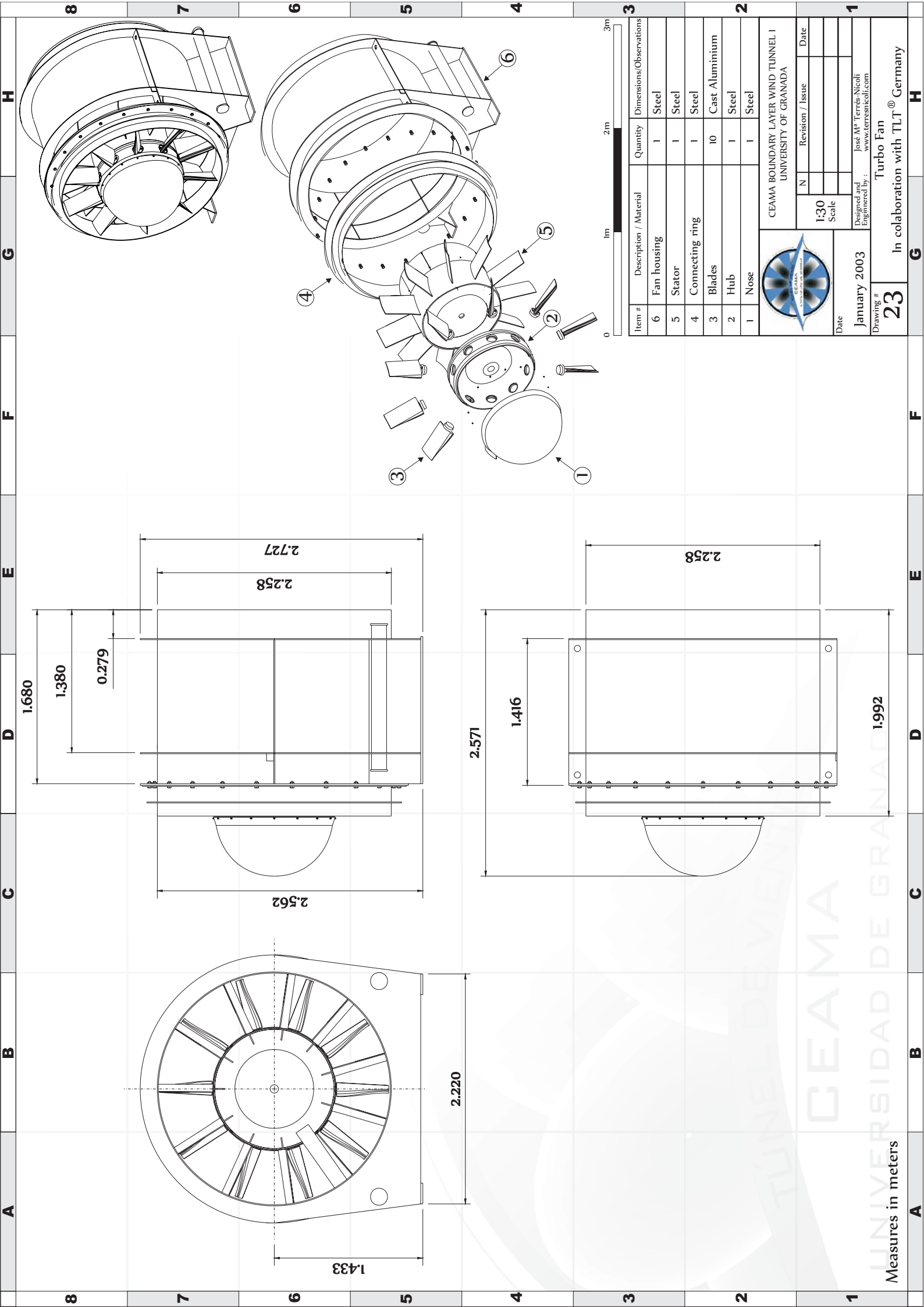
Drawing #	22	Flexible Joint
-----------	----	----------------

Measures in meters

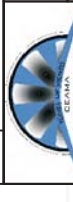
0

1m

2m



Item #	Description / Material	Quantity	Dimensions/Observations
6	Fan housing	1	Steel
5	Stator	1	Steel
4	Connecting ring	1	Steel
3	Blades	10	Cast Aluminium
2	Hub	1	Steel
1	Nose	1	Steel



CEAMA BOUNDARY LAYER WIND TUNNEL I  
UNIVERSITY OF GRANADA

Date		Revision / Issue		Date	
January 2003					
Designed and Engineered by : José M <sup>a</sup> Terrés-Nicoli					
www.terresnicoli.com					

Turbo Fan  
In collaboration with TLT<sup>®</sup> Germany

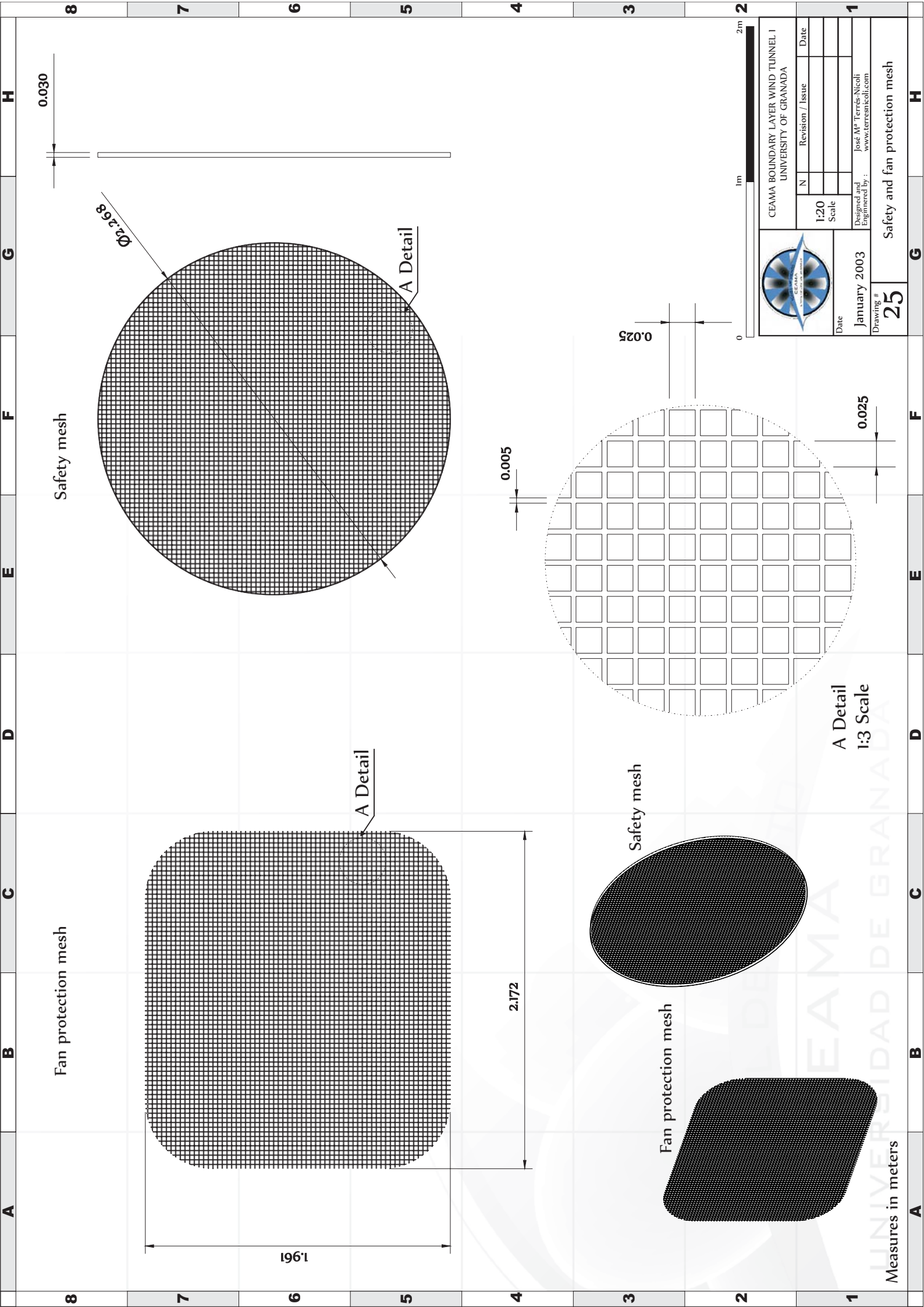
23  
Drawing #

Measures in meters


TUNEL DE VIENTO  
CEAMA

UNIVERSIDAD DE GRANADA





CEAMA BOUNDARY LAYER WIND TUNNEL I  
UNIVERSITY OF GRANADA

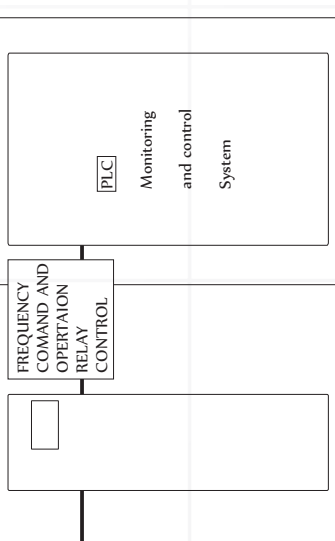
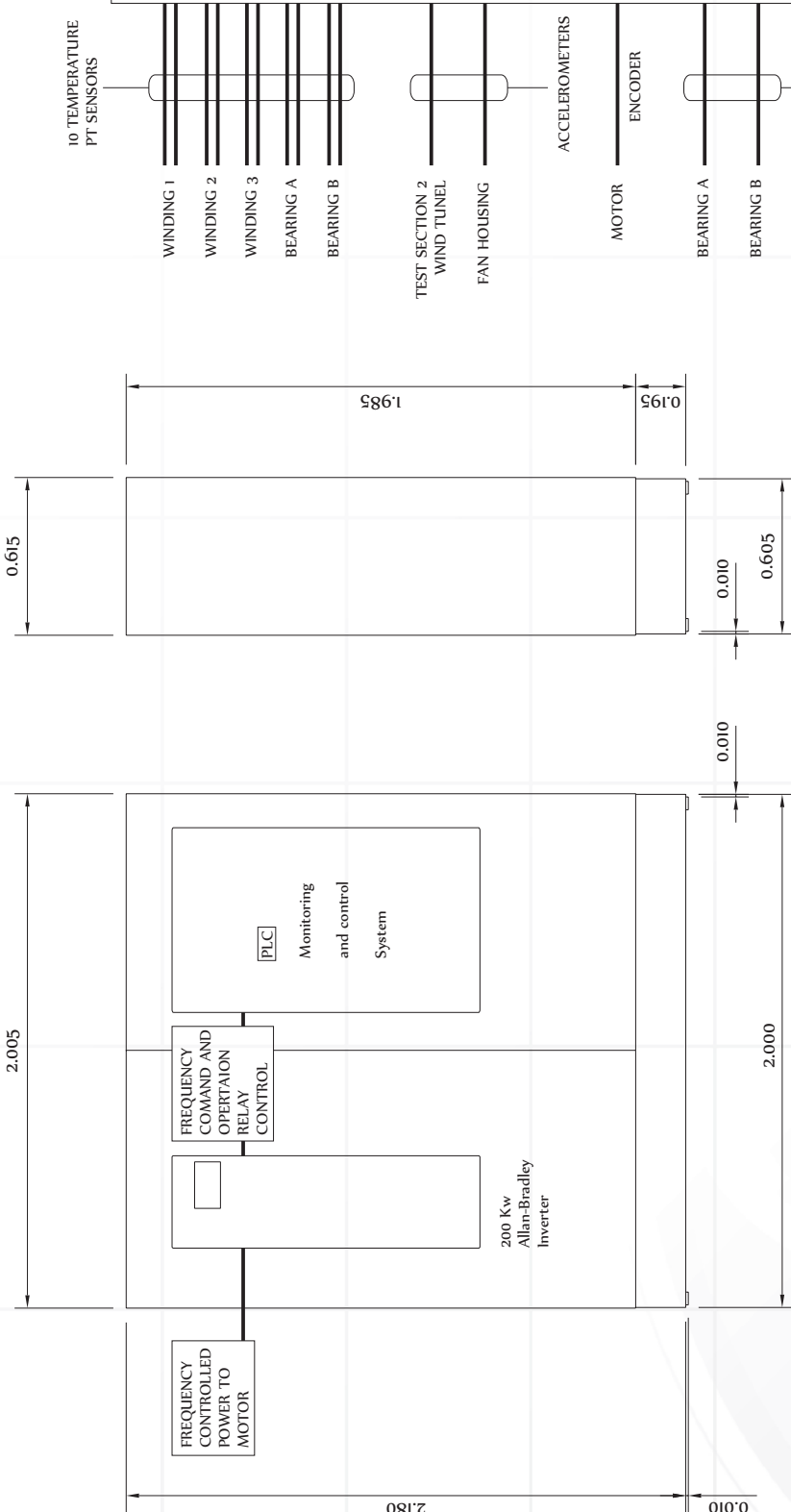

 Date: January 2003  
 Scale: 1:20  
 Revision / Issue: N  
 Designed and Engineered by: José M<sup>a</sup> Terrés-Nicoli  
 www.terresnicoli.com

Drawing # **25**

Safety and fan protection mesh

Measures in meters

# WIND TUNNEL MOTOR



MONITORING OUTPUT TO CONTROL COMPUTER

CONTROL COMMAND FREQUENCY COMPUTER



CEAMA BOUNDARY LAYER WIND TUNNEL I  
UNIVERSITY OF GRANADA

N	Revision / Issue	Date
1	See attached picture for clarification	April 2004

1:20  
Scale

Date  
January 2003

Designed and Engineered by :  
José M<sup>a</sup> Terrés-Nicoli

Drawing #  
**26**

Drive and monitoring system



Measures in meters

# Appendix 2

## Phase ensemble-averaging

### A2.1 Description of the technique

#### A2.1.1 Introduction

Chaos and vorticity are often associated with systems that involve turbulent flows. In these flows there are some larger scale, identifiable, regular structures, often referred to as coherent structures. Coherent structures are distinct from the random ones. There are different ways to decompose signals in such systems. In a turbulent flow field, one can decompose, for example, a velocity component into a mean (non-fluctuating) and a random or fluctuating component as follows,

$$\mathbf{u} = \bar{\mathbf{u}} + \mathbf{u}' \quad (\text{A2.1})$$

This is usually referred to as the Reynolds decomposition, where  $\bar{\mathbf{u}}$  is the mean (or global mean) and  $\mathbf{u}'$  is the fluctuating component. The global mean is defined as,

$$\bar{\mathbf{u}} = \frac{1}{N} \sum_{i=1}^N \mathbf{u}_i \quad (\text{A2.2})$$

where  $N$  is the length of the record or, more properly, the number of data points in the time history.

One can decompose the fluctuating part into a regular or periodic component associated with coherent structures and a random, non-periodic component,

$$\mathbf{u} = \bar{\mathbf{u}} + \tilde{\mathbf{u}} + \tilde{\tilde{\mathbf{u}}} \quad (\text{A2.3})$$

this is normally called the triple decomposition, where  $\bar{\mathbf{u}}$  is the global mean as in (A2.1),  $\tilde{\mathbf{u}}$  is a coherent or periodic mean and  $\tilde{\tilde{\mathbf{u}}}$  is the random component. The so called phase average is one of the ways to decompose  $\tilde{\mathbf{u}}$  and  $\tilde{\tilde{\mathbf{u}}}$ . An application of phase averaging to a velocity field is presented in [70,71].

### A2.1.2 Description

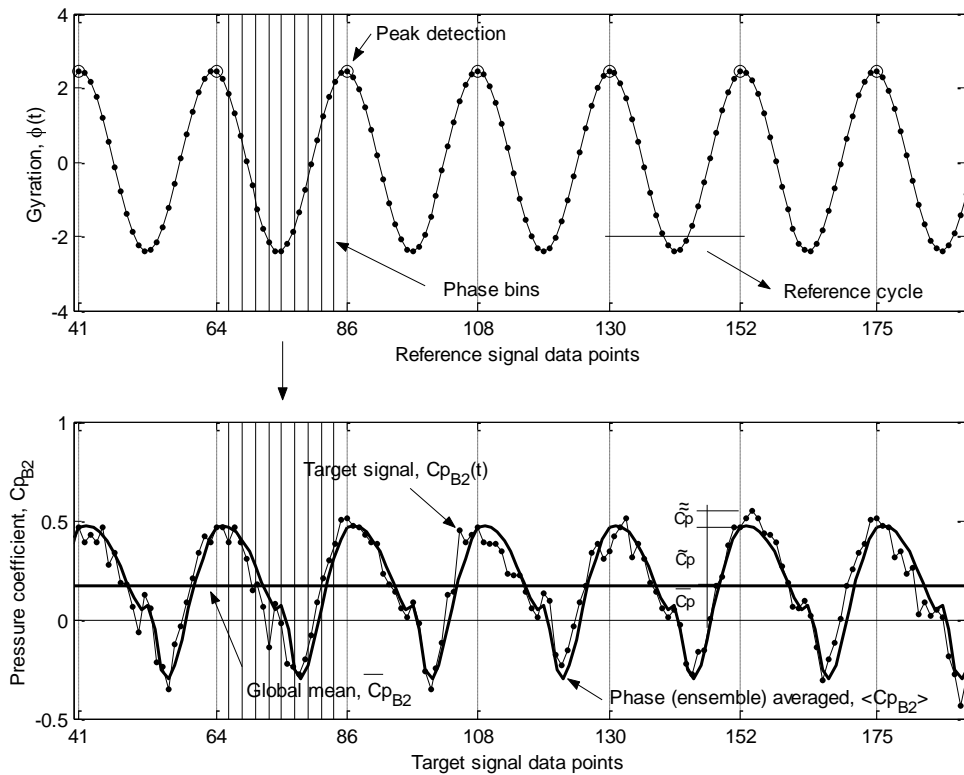
The periodic component  $\tilde{\mathbf{u}}$ , in (A2.2) can be defined as,

$$\tilde{\mathbf{u}} = \langle \mathbf{u} \rangle - \bar{\mathbf{u}} \quad (\text{A2.4})$$

where  $\langle \mathbf{u} \rangle$  is the phase averaged velocity and  $\bar{\mathbf{u}}$  is the global mean. The term phase average should not be understood as mean over the phase, but rather as an ensemble-mean at constant phase. To carry out the phase averaging, one must select a reference signal which contains a reasonable “clean” periodic component. This reference will permit dividing the data from each other signal into a number of populations at equal phase. The target signal for which we wish to obtain a phase average is first divided into segments of the length of the reference period (from the reference signal). Once the number of phase bins is decided, each of the above mentioned segments can be divided in bins. One can then average the values within one of the bins and then ensemble average this value, i.e.,

$$\langle \mathbf{u} \rangle_j = \frac{1}{N_j} \sum_{z=1}^{N_j} \mathbf{u}_z \quad \text{for } j=1,2,\dots, \text{number of phase bins} \quad (\text{A2.5})$$

where  $N_j$  ( $N_j \subset N$ ) is the population of the data points of phase  $j$ . Figure [A2-1] shows an example of an actual application from the current analysis. The upper plot, the reference signal is divided in periods with a peak detection algorithm. This allows the division into bins of each correspondent segment of time series of the target signal.



**Figure [A2-1]: Upper, rotation used as reference signal for the phase averaging. Lower, example of phase averaged pressure coefficient (tap B2). This plot corresponds to maximum amplitude oscillations.**

The original time series and the phased average, repeated for every (periodic) segment, are compared in the Figure [A2-1].



The use of phase averaging in complex signals systems allows isolating the coherent, or repetitive part of it, while disregarding the randomness due to turbulence. It, thus, simplifies the system considerably and allows observations of the critical behaviour.

One could compare the output phase averaged signal with that resulting of filtering the original data. Even though they could coincide in certain cases, they are different by definition since the phase average intends to pick out coherent structures that might happen at whatever frequency or frequencies. For instance, if one had low pass filtered the target signal in the lower plot in Figure [A2-1], it would have missed the peak detected in the fifth bin by phase averaging, a real and repetitive feature of the data.

### **A2.1.3 Application**

The present study focuses on the complex interaction of an unsteady flow field and a moving bridge deck. At certain wind speeds (see section 3.1) this interaction results in large harmonic torsional oscillations. The surface pressure field around the deck was studied to bring some insights into the flow-structure interaction. Hence the surface pressure signals were phase averaged with the rotation of the deck as reference signal. It was found that, in fact, this reference period was governing all target signals. Thus, the phase differences and amplitudes of the coherent pressure coefficients around the deck could be studied.

The rotation signal was divided into periods using a peak detection algorithm to locate the local time maxima. The condition to determine whether a data point was a local maximum or not was that it was larger than the data point after it and before it. An example of the result of the peak detection can be observed in Figure [A2-1]. In some tests the reference signal presented more than two local maximums per cycle. In these cases, the reference signal had to be low pass filtered digitally at 15Hz before carrying out the phase averaging analysis (the natural torsional frequency was  $f_t=9.03\text{Hz}$ ). An average of 22 data points per cycle and 5500 cycles were available for each signal. The number of cycles to perform the phase averaged was decided, after a sensitivity analysis, to be about 2000 cycles. The number of bins was decided in order to achieve the maximum resolution possible, given that the number of cycles was sufficient so that there was no need to have more than one data point per phase bin and cycle. A number of 20 phase bins was used typically. Thus, the phase resolution was  $18^\circ$ .

## **A2.2 Algorithm development**

### **A2.2.1 Description of the algorithm**

An algorithm was implemented in Matlab V6.1 R12. This was a function called from a main program written to compute all analyses presented in the thesis. A flow diagram of this algorithm is presented in Figure [A2-2].

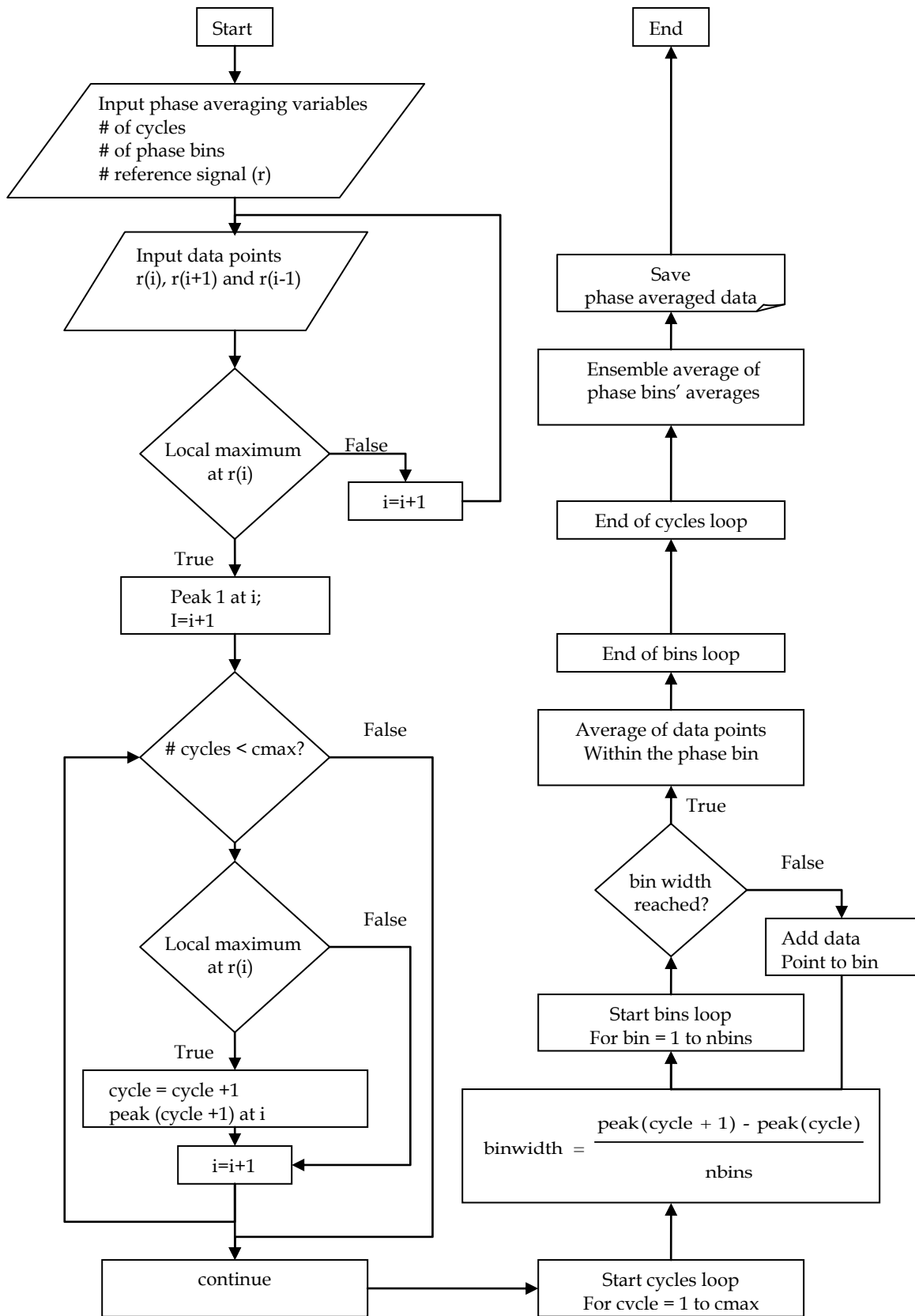


Figure [A2- 2]: Flow chart of the phase averaging algorithm

### A2.2.2 Testing the software

As a result of each pressure test, there was one time history file per pressure scanner. Typical analysis focused on the surface pressures around the deck for a particular ring or over a certain line along the span (see Figures [2-18] and [2-19]). The scanner files were combined to form ring and lines time history files. A known artificial set of scanner time histories was created in order to test the file management and every function of the analysis software.

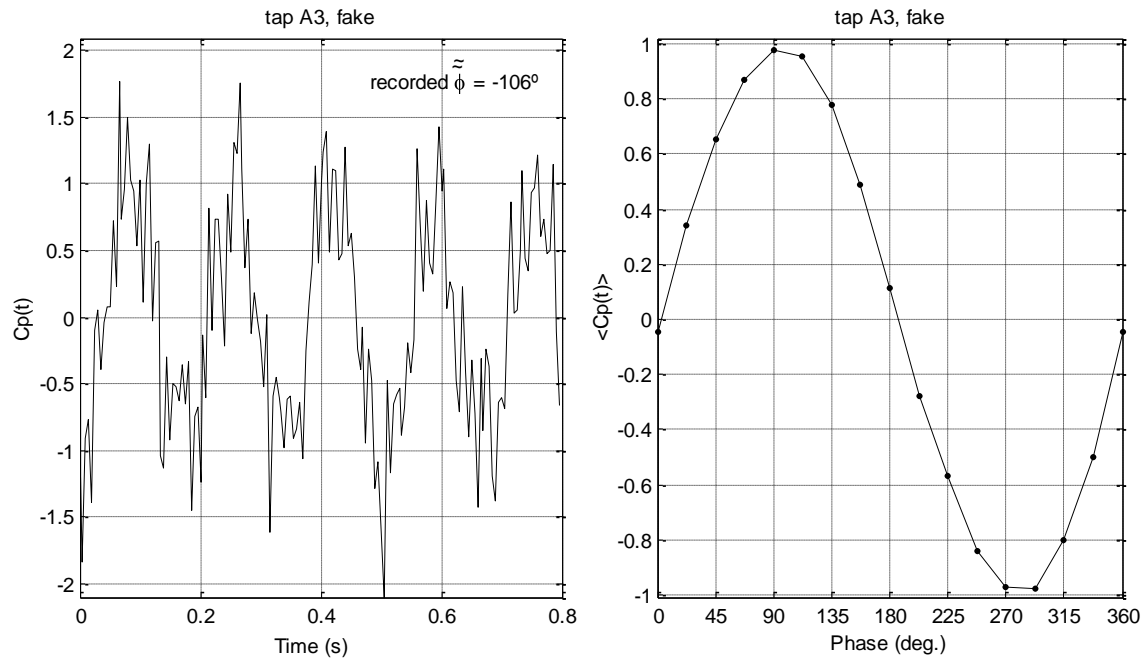
The artificial time series for each tap was,

$$y_i(t) = \sin(6\pi t + \tilde{\phi}_i) + \frac{1}{2}\tilde{a}(t), i = 1, 2, \dots, 176 \quad (\text{A2.6})$$

where  $\tilde{\phi}_i$  and  $\tilde{a}(t)$  are a random phase (with respect to the reference) and amplitude respectively.  $\tilde{\phi}_i$  and  $\tilde{a}(t)$  are Gaussian variables with 0 mean and variance of 1. The values of the  $\tilde{\phi}_i$  were recorded in a file. Figure [A2-3], left shows a sample of the created time history for tap A1 and the phase averaged obtained. The artificial signal was sampled at the same frequency as the actual data. The recorded random phase for tap A3 was  $-106^\circ$ . The phase averaging was carried out using 900 cycles and with a resolution of 16 bins. Figure [A2-3], right, shows the resulting phase averaged pressure coefficient. It can be observed that as it was expected the phase averaged maximum and minimum amplitudes are +1 and -1 given that  $a(t)$  has 0 mean. The phase with respect to the reference in the

phase averaged  $C_p$  is within the range  $90-112.5^\circ$  given the resolution of

$$\frac{360^\circ}{16} = 22.5^\circ .$$



**Figure [A2- 3]: Sample of the artificial time history created for tap A3 (left) and the resulting phase averaged cycle (right)**

These results confirmed that the file management and analysis software and the phase averaging algorithm were performing as expected.

### A2.3 Results

The presented algorithm was applied to the pressure signals, aerodynamic coefficients and response signals. The sensitivity of the resulting ensemble averages was studied. Figure [A2-4] shows a comparison between the obtained phase averaged  $C_p$ s at tap B2 for  $V_r^+=1.30$ . If one compares the ensemble averaged  $\langle C_p \rangle$  around the maximum in this figure, it can observe that the

differences for 2000 cycles with respect to 4000 are small. Hence, to save computing time phase averages were obtained typically for 2000 cycles.

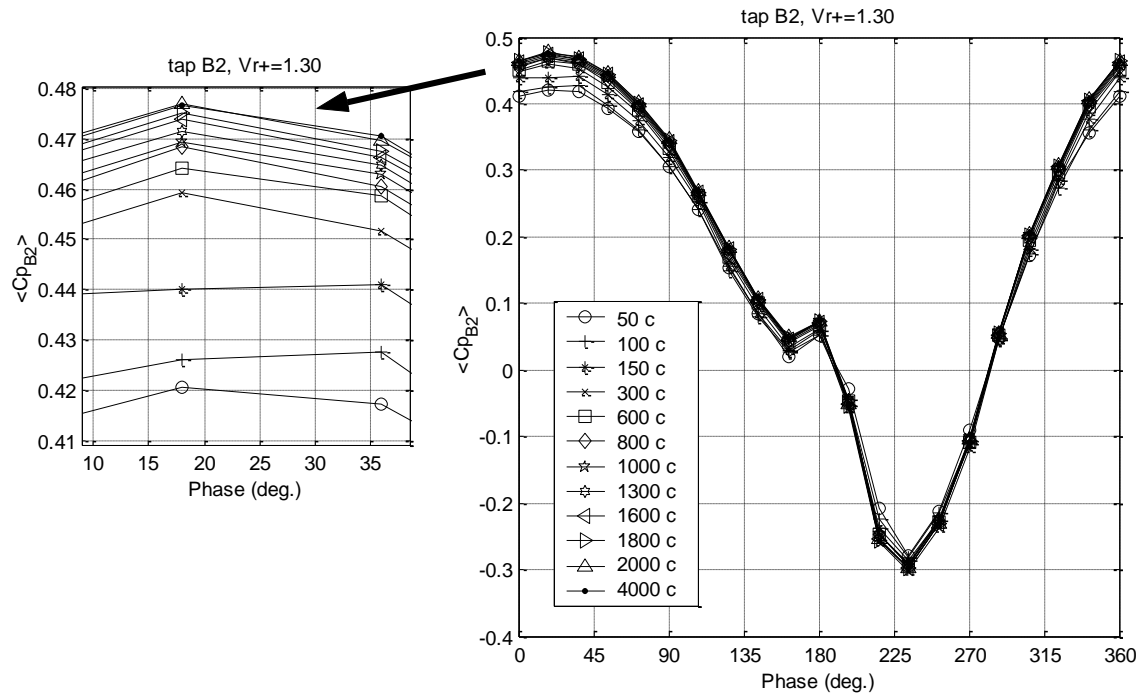


Figure [A2- 4]: Comparison of phase averaged  $\langle C_p \rangle$  for different number of cycles

In order to avoid missing higher frequency coherent structures it was decided to aim for a resolution as high as possible in the phase averages; hence, for resolution and simplicity 20 bins were typically used. Figure [A2-5] shows a comparison of the phase averaged  $C_p$  at tap B2 for  $V_r^+ = 1.30$  for different number of phase bins or resolutions. In this figure one can observe that when the cycles were divided into 8 or 10 bins the peak at  $180^\circ$  was not picked out.

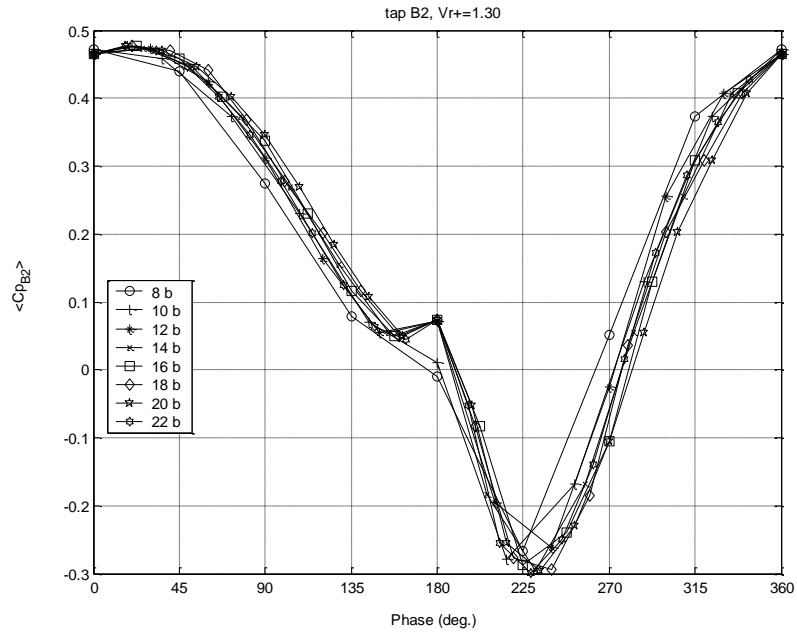


Figure [A2- 5]: Comparison of phase averaged  $\langle C_{p_{B2}} \rangle$  for different number of phase bins

# Appendix 3

## The Storebælt Bridge

The Storebælt Bridge (also known as the Great Belt Bridge (East)) is part of a rail and road fixed link across the Storebælt Strait (18 km) between the Danish islands of Funen and Zealand. The suspension bridge links the islands of Sprogø and Zealand (see Figure [A1-1]).

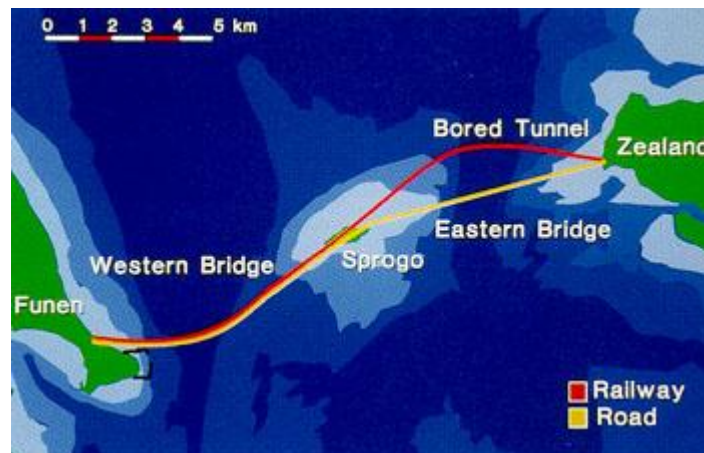


Figure [A1- 1]: Location of the Storebælt Bridge, part of the fixed link across the Storebælt Strait [69].

A view of the bridge under construction is shown in Figure [A1-2]. When the bridge was built, in 1998, it was the longest span in the world. Now days, only the Akashi Kaikyo, with a main span of 1991 m, is longer. It is though, the longest suspension bridge with a continuously suspended structure; the towers have two struts and no supporting. The unfettered passage of the deck through the towers is of an exceptional simple and elegant design.





Figure [A1- 2]: View of the Storebælt's main span under construction [75].

The bridge's deck is suspended of two main cables anchored by the gravity of the two side triangular blocks. The main cables are attached to deck at the midspan by triangular clamps. The suspension bridge has a main span of 1,624 m and two side spans of 535m each. Geometrical details are presented in Figure [A1-3]).

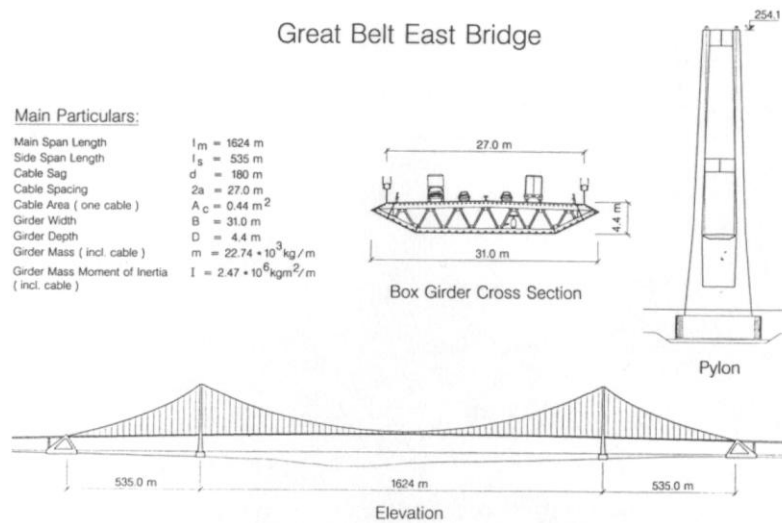


Figure [A1- 3]: Geometrical details of the Storebælt East Bridge [35].